AD_____

Award Number: DAMD17-99-1-9571

TITLE: Molecular Mechanisms of Soft Tissue Regeneration and Bone Formation in Mice: Implication in Fracture Repair and Wound Healing in Humans.

PRINCIPAL INVESTIGATOR: Subburaman Mohan, Ph.D.

CONTRACTING ORGANIZATION: Loma Linda Veterans Association for Research and Education
Loma Linda, CA 92357

REPORT DATE: April 2008

TYPE OF REPORT: Final

PREPARED FOR: U.S. Army Medical Research and Materiel Command
Fort Detrick, Maryland 21702-5012

REPORT DOCUMENTATION PAGE

Form Approved
OMB No. 0704-0188

1. REPORT DATE	2. REPORT TYPE	3. DATES COVERED
14-04-2008	Final	1 OCT 99 - 14 MAR 2008

4. TITLE AND SUBTITLE
Molecular Mechanisms of Soft Tissue Regeneration and Bone Formation in Mice: Implication in Fracture Repair and Wound Healing in Humans.

5a. CONTRACT NUMBER

5b. GRANT NUMBER
DAMD17-99-1-9571

5c. PROGRAM ELEMENT NUMBER

6. AUTHOR(S)
Subburaman Mohan, Ph.D.

Email: subburaman.mohan@med.va.gov

5d. PROJECT NUMBER

5e. TASK NUMBER

5f. WORK UNIT NUMBER

7. PERFORMING ORGANIZATION NAME(S) AND ADDRESS(ES)

Loma Linda Veterans Association for
Research and Education
Loma Linda, CA 92357

8. PERFORMING ORGANIZATION REPORT NUMBER

9. SPONSORING / MONITORING AGENCY NAME(S) AND ADDRESS(ES)
U.S. Army Medical Research and Materiel Command
Fort Detrick, Maryland 21702-5012

10. SPONSOR/MONITOR'S ACRONYM(S)

11. SPONSOR/MONITOR'S REPORT NUMBER(S)

12. DISTRIBUTION / AVAILABILITY STATEMENT
Approved for Public Release; Distribution Unlimited

13. SUPPLEMENTARY NOTES

14. ABSTRACT

The primary goal of the proposed work is to identify genes which play an anabolic role in bone and soft tissue function and to clarify the function of these genes. Three hypotheses have been proposed: 1) The high bone density gene in chromosome 1 in our CAST/B6 congenic mice can be cloned; 2) Genes that regulate soft- and hard-tissue regeneration can be identified by using appropriate mouse strains that exhibit differences in regeneration; and 3) ENU mutagenesis, applied to our mouse model, will lead to the identity of genes that regulate soft and hard tissue function. During the last funding period, we have proposed several specific objectives for each of the above-mentioned hypotheses. As disclosed in the progress report, we have successfully accomplished all of the specific objectives. Our work during the first year of the funding period has resulted in two manuscripts in press, two published manuscripts, and three abstracts. We believe that the successful accomplishment of the proposed studies will provide a better understanding of the molecular mechanisms involved in hard- and soft-tissue regeneration and will provide a framework for future development of therapies for hard and soft tissue injuries.

15. SUBJECT TERMS
Soft- and hard-tissue regeneration; bone density; gene function; cDNA microarray analysis; congenic mice; QTL analysis; mouse genetics; musculoskeletal genes

16. SECURITY CLASSIFICATION OF:			17. LIMITATION OF ABSTRACT	18. NUMBER OF PAGES	19a. NAME OF RESPONSIBLE PERSON
a. REPORT	b. ABSTRACT	c. THIS PAGE			USAMRMC
U	U	U	UU	201	19b. TELEPHONE NUMBER *(include area code)*

Table of Contents

Page

I. General Introduction

The primary goal of the project funded by the U.S. Army is to identify genes which play an anabolic role in bone tissue and soft tissue function, particularly during regeneration, and to clarify the function of these genes. To accomplish this goal, we have proposed 3 technical objectives during the funding period. These 3 Technical Objectives are as follows:

A. Technical Objective 1:

Studies proposed in the first technical objective are designed to employ state-of-the-art molecular biotechniques to identify the gene located in mouse chromosome 1 that is involved in the regulation of peak bone density.

B. Technical Objective 2:

Our second technical objective has been focused on identifying the key genes that are involved in soft tissue repair/regeneration using inbred strains of mice as model systems.

C. Technical Objective 3:

The goal of our third technical objective is to identify and characterize novel genes, using ENU mutagenesis techniques and to elucidate the function of known genes that play a key role in the metabolism of bone and soft tissue.

Our progress for the technical objective1 is described below.

A. TECHNICAL OBJECTIVE 1: TO CLONE THE GENE REGULATING PEAK BONE DENSITY ON CHROMOSOME 1 IN THE CAST/B6 CONGENIC MICE.

1- INTRODUCTION

Our long-term goal in this study is to identify the genes involved in the acquisition of peak bone mineral density (BMD) and evaluate the functions of those genes. Such genes are particularly relevant to determine both one's risk of fractures resulting from battlefield injury and to corresponding gene therapy treatment for such fractures.

Osteoporosis is characterized by loss of bone mass and strength, often resulting in bone fractures even from minor trauma. According to the National Osteoporosis Foundation, osteoporosis is estimated to be the major public health threat in United States, producing disability and excess mortality through the development of fracture. It has been recently reported that approximately 17 billion dollars were spent in the US to treat over 2 million fractures in 2005. Furthermore, due to the aging population in US, the health care cost to treat osteoporosis is expected to increase to $25 billion in 2025 (Simonelli, 2008) and the cost in human suffering and lost productivity is incalculable. The major cause of osteoporosis related fracture is compromised bone strength, which is largely determined by BMD, geometric architecture and quality. Therefore, identifying mechanisms to improve any of these aspects would be important for prevention and treatment of osteoporosis.

Our studies have concentrated on the identification of mechanisms that contribute to bone strength by affecting peak BMD, since low peak BMD has been established as an important risk factor for osteoporosis. Because heritability studies in humans and experimental animals have shown that approximately 70% of variation in peak BMD can be accounted by genetic variations among individuals (Shen et al., 2003 and Ioannidis et al., 2004), focuses in a number of laboratories including ours have been directed towards identifying genes that regulate peak BMD. Genetic linkage studies in both humans and animal models have provided convincing evidence that peak BMD variation is determined by large number of genes with a modest or small effect size rather than by few genes of major effect as it was originally thought. Thus, elucidating the genetic basis for BMD variation could lead to identifying potential preventive measures that would lower the risk of developing osteoporosis and bone fracture. Accordingly, genome-wide linkage screens for new genes underlying BMD variability have been launched both in humans (Devoto et al., 1998; Niu et al., 1999; Shen et al., 2004) and in mice (Beamer et al., 1999; 2001; Klein et al., 1998; Bouxsein et al., 2004) and several genetic loci responsible for BMD variations have been identified at different Chromosomes.

Since it is now widely recognized that many human diseases can be modeled in the mouse. Studies have been carried out in mice to examine the relationship between bone density and bone strength (Kaye et al., 1995; Jamsa et al., 1998). These analyses mainly focused on bone density as a primary parameter to determine bone strength. Therefore in our studies to identify new genes involved in bone density and bone strength, we have used mouse model and we combined several strategies including development of congenic mice to confirm the effect of the QTL on BMD and bone strength, fine mapping of the BMD QTLs, generation of subcongenic lines of mice carrying different regions of the identified QTL for phenotype characterization, expression profiling of the genes present in the QTL region and sequence polymorphism analyses to identify genes that regulate BMD variation. In this report we have summarized the accomplishments performed during the funded period (1999-2008).

2- BODY

1) Development of congenic mice to confirm the effect of the QTL in chr 1 on the BMD variation.

In previous studies (Beamer et al., 1999), Genetic loci that contribute to femur volumetric bone mineral density (vBMD) were identified at several chromosomes from the cross between C57BL/6J (B6), the low BMD mice, and CAST/EiJ (CAST), the high BMD mice. Of the four BMD QTLs, we focused on Chromosome 1 BMD QTL because this QTL exhibits the highest LOD score in the B6 x CAST F2 intercross female progeny and a syntenic region in human chromosome 1q21-q43 carries a BMD QTL which has been reported in independent studies using human populations humans (Koller et al., 2000 and Ralston, 2002) which shows the importance of Chr 1 in BMD variation.

We have successfully developed and characterized the congenic strains that contain the QTL gene. The initial congenic strain, designated B6.CAST-1T, that was made carried a large region of chr 1 from CAST that contained the BMD QTL, while the rest of the genome was B6 in composition. We characterized the skeletal phenotype of B6.CAST-1T congenic and B6 control mice to confirm the presence of BMD QTL in this chromosomal region. Then, gene expression profiling was used to determine the mechanism by which chr 1 QTL regulates BMD.

a. Breed heterozygous pairs into homozygous mice and then create additional subcongenic lines. To produce the subcongenic strain, we crossed congenic B6.CAST-1 (N7) mice with the B6 mice to produce N8F1 mice. Next, N8F2 mice were produced by intercrossing N8F1 mice and were genotyped in the QTL region. Individuals with a crossover genotype between B6 and CAST in the QTL region were selected for further crosses. Finally, progenies with smaller chromosomal region from CAST were intercrossed to produce homozygous subcongenic lines.

A total of nine subcongenic strains were produced and bred for homozygosity. They covered different portions of the original QTL region and overlapped with each other. The region of CAST chromosome transferred into B6 background for a representative 3 congenic lines are shown in **figure 1.**

b. Determine the size of CAST chromosome in each subcongenic line by PCR amplification of informative markers. The size of the CAST chromosome in different subcongenic strains in **Figure 1** were determined by molecular markers. The initial B6.CAST-1T congenic strain contains a chromosomal region from *D1mit10* to *D1mit511* on Chr 1 from CAST. In order to breed subcongenic lines, 25 additional markers were eventually selected for our genotyping. **Fig. 1** lists the molecular markers that we used in genotyping the subcongenic strains as well as the CAST chromosomal region carried by each congenic. PCR-based genotyping with microsatellite markers was performed, as described previously (Beamer et al., 1999; Gu et al., 1999). DNA from F_2 progenies of subcongenic strains and B6 mice was extracted from either a piece of tissue from ear punch or a tail tip using the QIAmp Tissue Kit (Qiagen, Chatsworth, CA). PCR was conducted on a DNA engine tetrad from MJ Research Inc. (Watertown, MA). PCR products were separated in 7% polyacrylimide gel and visualized with Ethidium Bromide under UV light.

NCBI (Mb)	Markers	C168-185	C166-193	C100-193
80.3	D1mit216	B	B	B
133.2	D1mit30	B	B	C
155.95	D1mit451	B	B	C
156.77	D1mit14	B	B	C
157.36	D1mit268	B	B	C
162.33	D1mit106	B	B	C
165.2	D1mit453	B	B	C
166.7	D1mit57	B	B	C
167.3	D1mit145	B	C	C
168.03	D1mit370	B	C	C
169.04	D1mit112	C	C	C
171.86	D1mit113	C	C	C
172.8	D1mit149	C	C	C
173.134	D1mit206	C	C	C
174.76	D1mit150	C	C	C
175.77	D1mit403	C	C	C
176.6	D1mit166	C	C	C
177.8	D1mit115	C	C	C
178.96	D1mit315	C	C	C
180.87	D1mit509	C	C	C
184.6	D1mit152	B	C	C
185.82	D1mit407	B	C	C
187.3	D1mit459	B	C	C
-	D1mit17	B	C	C
193	D1mit511	B	B	B

Figure.1. The regions of CAST chr 1 transferred from CAST mice onto B6 background, for the three congenic sublines. The genotyping data for every marker are represented with "B" referring to homozygous b6/b6, "C" referring to cast/cast and "-" for data not available. The names of the congenic lines are at the top. We used a letter "C" followed by the proximal and distal limits of cast alleles carried by the congenic sublines in megabases. The grey squares denote the CAST chromosomal regions carried by each congenic subline.

c. Compare the phenotype of the congenic sublines with the B6 control mice.

Based on data from our previous studies that showed rapid acquisition of vBMD peaked at approximately 16 weeks, resulting in significant higher density values in the CAST females compared to the B6 females (Beamer et al., 1999), we chose this time point as the age at which to measure our phenotypes. We analyzed 10-14 female mice from the B6 line and from each congenic at 16 weeks of age. Body weights were recorded at necropsy. Bones collected were stored in 1 x PBS buffer supplemented with 0.05% sodium azide. Their lengths were measured with digital calipers (Stoelting, Wood Dale, IL, USA). Then, isolated femurs were assessed using the peripheral quantitative computed tomography (pQCT) system from Stratec XCT-RESEARCH (Norland Medical System, Fort Atkinson, WI, USA), operating at a resolution of 0.07 mm. Isolated femurs were scanned at nine locations symmetrically located around the midpoint, 11% of the femur length apart and covering the entire length. **Figure 2** shows the femur vBMD evaluated at the mid-diaphysis region of the femurs (average of slices 4 and 5). Analyses of the scans were performed using manufacturer-supplied software program (Stratec Medizintechnik GMBH Bone Density Software, version 5.40C).

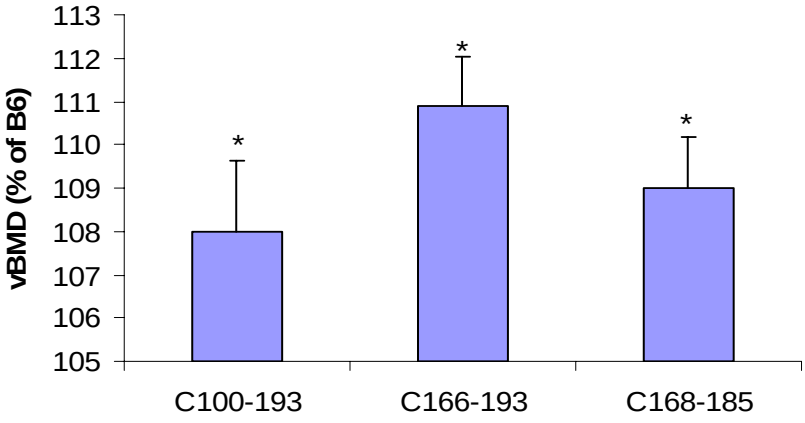

Figure.2. Femoral vBMD at the mid-diaphysis of the three congenic strains of mice; C168-185, C166-193 and the initial congenic C100-193 compared to B6 control mice. Each congenic is presented with a "C" letter referring to the cast allele, followed by the position (in megabases) of the two markers flanking the donated CAST segment according to NCBI (build 35). We designated the congenic B6.CAST-1D1mit216-D1mit511 as C100-193 which indicates the approximate proximal and distal megabase limits known for the CAST chromosomal region, the congenic B6.CAST-1D1mit370-D1mit152 designated as C168-185 and B6.CAST-1D1mit57-D1mit511 represented as C166-193. Data are expressed as a percentage of B6 and are mean + SEM. * $P<0.05$ as evaluated after ANOVA test. n=10-14.

Femur vBMD was significantly higher in the three congenic strains of mice compared to the B6 control mice which confirmed the presence of gene(s) that regulate vBMD in the chromosome 1 BMD QTL. Therefore, we decided to generate more congenic sublines of mice to narrow down the size of the BMD QTL in chr 1.

Because CAST progenitor mice are considerably smaller than the B6 mice (-64% compared to B6 mice, data not shown), we evaluated the body weights of these congenics to determine if a body weight phenotype co-segregates with mid-diaphyseal vBMD. **Figure 3**

shows that subline C168-185 of mice showed significantly greater body weight (8%) compared to B6 control mice (**Fig. 3**), and femur length was similar in all congenics compared to B6 control mice. Moreover, the adjustment for body weight or femur length did not affect the significance of femoral vBMD change (data not shown). This provided evidence that body weight is not responsible for the vBMD variation introduced by CAST donated segments.

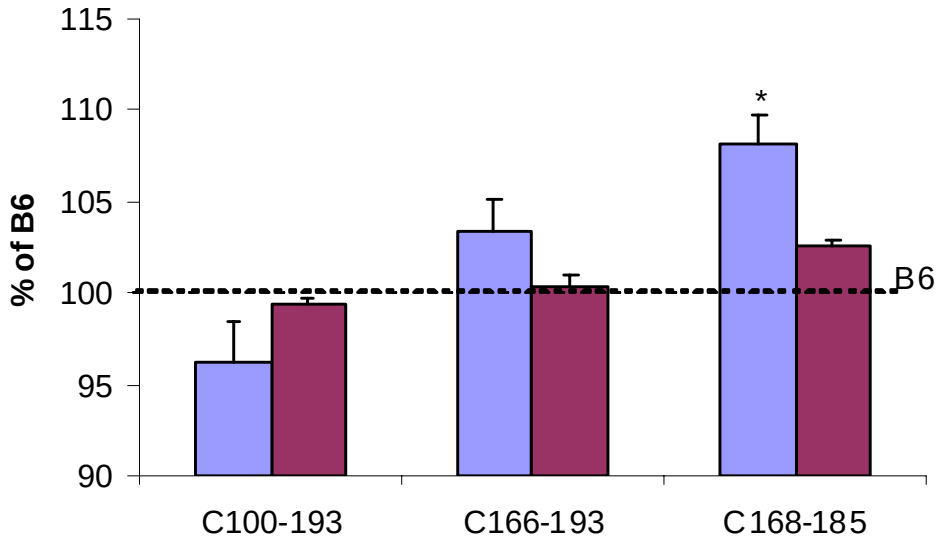

Figure 3. Femur length and body weight from the three congenic strains of mice. Data are expressed as a percentage change from B6 and are mean ± SEM, *P<0.05 congenic *vs* B6. n=10-14.

d. Expression profile evaluated by Microarray techniques

In order to get insights on the mechanisms by which the QTL in chr 1 regulates BMD, we have used commercial and in-house microarray techniques to determine the genes and/or molecular pathways that could be involved in regulating BMD.

d.1. Commercial microarray.

The probe labeling and microarray hybridization were performed by Incyte Genomics, where 0.2 μg purified mRNA from B6.CAST-1T and from B6 were each utilized at a concentration of 50 ng/μl to hybridize the mouse GEM I microarray chips, which contained 8,734 accessions (genes and ESTs). The sequences were selected from the UniGene database based on clustering algorithms developed at Incyte Genomics. A single IMAGE consortium clone that matched the 5′ end of each cluster was selected.

The mRNA from the B6.CAST-1T congenic and B6 mice was labeled with Cy5 and Cy3, respectively, and hybridized simultaneously onto the same microarray set. The level of expression of each gene or EST was measured by relative intensity of the fluorescence of the dyes, which was used in the comparison between B6.CAST-1T congenic and B6 mice. Detailed information of these clones and the hybridization procedure can be obtained from http://www.genomesystems.com.

d.2. Expression levels and patterns of total 8,734 genes on microarray chips in the mouse femur

Before evaluating the expression of genes in the QTL region, we evaluated the femur for the expression of all 8,734 genes on the GEM I microarray chips. Interestingly, we found that the majority of the gene accessions (which were not selected for bone tissues) in the Incyte Genomics microarray chips were expressed in the mouse femur. If a conservative critical threshold of light intensity of 1,000 relative units was used, 58% of the accessions in the chips were expressed at a detectable level. In contrast, if a more liberal threshold of 400 relative units was used, 88% of the accessions were considered detectable in the mouse femur. Among the detectable accessions, 93 genes and ESTs had fluorescence signals higher than 10,000 relative units. By searching literature, as of 25 July 2000 from the PubMed, we found that 31 of these 93 gene accessions have been reported to have their function and/or expression in the musculoskeletal system (data published in Gu et al., 2002). Thus, neither a function nor expression in the bone has been reported previously for the remaining two-thirds of these genes.

d.3. Comparison of genome wide (8,734 genes) expression of genes in the mouse femur in B6.CAST-1T congenic and B6 mice

Most of the gene accessions on the GEM I microarray chips were expressed at similar levels in B6 and B6.CAST-1T congenic mice. Because the difference between the congenic and B6 mice is only in the QTL region, we anticipated that the gene expression pattern in the congenic mice should be very similar to that in the parental B6 mice. Comparison of expression levels of the 8,734 genes and ESTs in B6 and the congenic mice by analysis of variance (ANOVA) indicated that the gene expression of the two mouse strains had a similar pattern ($P=0.47$; **Fig. 4**). The difference in expression of the majority of the genes (92%, 8,007 out of 8,734 genes and ESTs) in these two strains was within ±1.5-fold. Of special interest was that we identified 283 genes and ESTs (i.e. 3%), the difference in the expression of which were equal to or greater than 1.8-fold between B6 and congenic mice (data not shown). Of these 283 accessions, only 114 are known genes or ESTs that are similar to known gene sequences (data published in Gu et al., 2002).

d.4. Preparation of customized cDNA chips with a cDNA microarrayer.

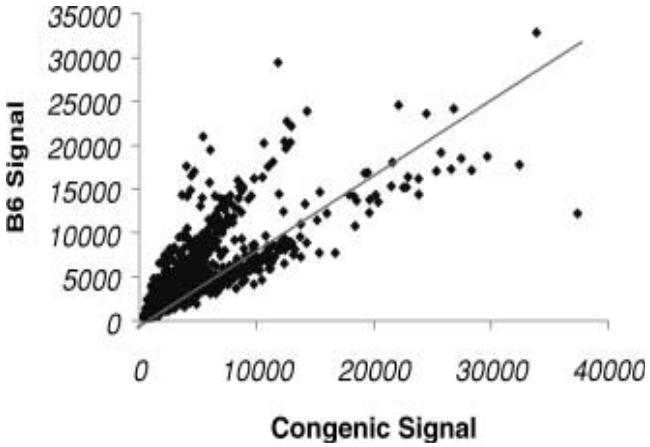

Figure 4. **Relative expression signal levels of 7,724 gene accessions that have relative light signals higher than 400 on GEMI microarray chips in the femora of C57BL/6J and B6.CAST-1T congenic mice.** The *y axis* represents relative signal level of an accession of B6 mice and the *x axis* represents the signal level of congenic mice. The difference in the expression of the majority of the genes between these two strains was within ±1.5-fold. While most genes and ESTs were expressed at less than 10,000 relative units, a few were expressed at between 10,000 and 40,000 relative units.

Due to the expense of commercial microarray, we were not able to reproduce our data using the commercial 8,734 gene accessions. However, in order to gain some information on the reproducibility of our findings, we selected two genes [procollagen, type I and osteoblast-specific factor 2 (Osf2)] showing up-regulation, and one EST that represents a gene (Ras-binding protein SUR-8) showing down-regulation in the congenic mice for further study in our in-house microarray. Fragments of ESTs and known genes at a concentration of 200–300 ng/μl were mixed in 50% dimethyl sulfoxide and spotted onto CMT-GAPS-coated slides (Corning, Corning, N.Y.). The chips were then hybridized by using 50 μg each of total RNA from B6.CAST-1T and B6 labeled with Cy5 and Cy3 dye (Amersham Pharmacia, Piscataway, N.J.) respectively. Hybridization was conducted with five replicates for each gene. The experiment was repeated with RNA of congenic and B6 mice labeling with alternative dyes (Cy5 for B6 and Cy3 for B6.CAST- 1T). Quantification of signal was conducted using a Scan Array 4,000 (GSI Lumonics) and images were acquired with its ScanArray software. Data of gene expression level were obtained through ImaGene Software, version 4.1, and analyzed with ANOVA (Worley et al. 2000).

d.5. Identify and confirm the differentially expressed candidate genes.

RNA was extracted from femurs isolated from Fourteen week-old female B6 and B6.CAST-1 mice in order to identify potential genes for bone formation/resorption.

Our commercial microarray results showed increased expression of Osf2 and procollagen type 1 α1 and decreased expression of the EST that represents the Ras binding protein SUR8 in

the congenic animals compared with the B6 mice. By examining the data of our in-house microarray experiment (**Table 1**), we found that: 1) the expression of Osf2 and procollagen type 1 α1 was expressed significantly higher in B6 than in congenic mice; 2) the EST that represents Ras-binding protein SUR-8 was expressed lower in B6 than in congenic mice; and 3) the expression level of control (ribosomal protein S5) between B6 and the congenic mice was similar (**Table 2**). This result agrees with the major finding of the commercial microarray that relates to the expression patterns of genes of bone formation and resorption between congenic and B6 mice.

Table 1. Known bone-related genes differentially expressed in C57BL/6J and congenic mice of 14 weeks.

Strain	***Procollagentype 1, alpha 1***	***Osteoblast specific factor 2***	***ESTs, Represent Ras***	Ribosomal protein S5
B6	*89764 ± 3809	*6167 ± 498	**17260 ± 1822	7631 ± 122
B6.CAST-1T	37560 ± 969	3223 ± 177	22838 ± 2092	7189 ± 185
B6/Cong	2.38	1.90	0.75	1.01

P<0.001; **P=0.08

Table 2. Genes differently expressed between B6 and congenic mice at 14 weeks detected by in-house microarray analysis.

	Fold change B6 vs Congenic	Potential function
Genes related to bone formation		
ESTs, (represent RAS-related protein RAB-6)	+1.9	Involvement of Ras/Raf/AP-1 in the BMP-4 signaling pathway
Catenin beta	+2.2	Important to activity of osteoblast (Luegmayr et al. 2000)
Osteoblast-specific factor 2	+2.9	Associated with the bone extracellular matrix after secretion by osteoblasts and participates in cell adhesion and/or cell communication
Procollagen, type I, alpha 1	+3.1	Bone formation
Procollagen, type V	+2.5	
Procollagen, type XI	+2.4	Stabilize cartilage fibrils
Genes related to bone resorption		
ESTs, represent latent	–3.9	
ESTs, present Ras-binding protein SUR-8	–2.1	

d.6. Complete the analysis of gene expression experiments using commercial and in-house microarray assays and search for candidate genes.

We selected the candidate genes by comparing the results of commercial microarray and in-house microarray. We identified the genes located in the human genome that are syntenic to the QTL region on mouse chromosome 1 and evaluated their known functions. In addition, we identified the open reading frame of known DNA sequences of the human genome that are

syntenic to the QTL region on mouse chromosome 1 for future studies with the positional candidate genes approach.

We compared the gene expression pattern between the congenic and the B6 mice in order to identify candidate genes for bone density. The criteria for a significant differential expression were that both the data from commercial and in-house microarray agreed and the results could be duplicated. In addition, of the bone formation genes reported in the previous report, we have found genes and EST that showed difference in the expression between B6 and congenic mice. **Tables 3 and 4** report only the 4 ESTs and 2 known genes that were differentially expressed between the congenic mice and the control mice and with the expression signal was above 2000 (**Tables 3 and 4**). These genes will be further analyzed.

Table 3: ESTs up-regulated in the femur from the congenic mice (data from commercial microarray and in-house microarray:

Gene ID/expression ratio Cong/B6	Femur 14 weeks	Femur 6 weeks	Function	Reference
ESTs similar to AA404014	1.5*	3.54	diadenosine triphosphate hydrolase (Fhit). Tumor supressor	Asensio AC. et al., (2000)
ESTs, AA015542.1	1.57*	3.25	No homology with any known gene	
ESTs AA273950.1	1.76*	2.6	_	_

*same results as from commercial microarray

Table 4: Genes and ESTs differentially expressed in Femur from The B6 wild type mice:

Gene ID/expression ratio Cong/B6	Femur 14 weeks[a]	Femur 6 weeks[b]	Function	Reference
EST AA437635.1	0.50	0.86	No significant homology with any known gene	-
Histone H2A.Z AA466087.1	0.41	2.9	Regulates transcription of certain genes under specific cell growth conditions	Adam et al., **(**2001)
Eosinophil-associated ribonuclease 2 AA510161.1	0.44	1.36	Likely participate in skin lesion development in Churg-Strauss syndrome.	Drage et al., (2002)

[a]: means that the differential expression is similar to the result achieved from commercial microarray. [b]: data have been duplicated in-house.

e. Serum level of ALP and IGF-I in B6 and congenic mice

Biochemical markers were measured using serum from animals at 14 weeks of age to determine the level of bone formation markers in the B6.CAT-1T congenic and the B6 control mice.

Table 5 shows that the level of serum ALP, a bone formation marker, in the congenic mice was only 73% of that of B6 mice, suggesting that bone formation of the congenic line was significantly lower than that of the B6. Because serum IGF-I levels have been shown to be elevated in a mouse strain of high bone density, C3H/HeJ, compared to B6 mice (Rosen et al.

1997), we also evaluated serum IGF-I levels in these mice and found that the serum IGF-I level between B6 and congenic mice was not significantly different.

Table 5. Serum levels of IGF-I and alkaline phosphatase in congenic and B6 mice

Strain (n)	IGF-I (ng/ml)	Alkaline phosphatase (mU/ml)*
B6.CAST-1T (4)	295.5±17.4	71.3±4.5
B6 (7)	298.7±18.3	97.6±5.8

*P=0.013; values are mean ± SD**.** N= no. of observations

In conclusion, the phenotypic characterization of congenic sublines of mice that carry CAST chromosomal regions that cover the initial BMD QTL in chr 1 confirmed the effect of the chr 1 QTL on BMD variations. Furthermore, microarray data provided evidence that the BMD variation between B6 and CAST mice is due to high bone turn-over in the low BMD B6 mice compared to the high BMD CAST mice. This overall conclusion is supported by our serum assay data.

2) The BMD QTL in chr 1 was identified in other inbred strains cross

The progenitor strains of MRL/MPJ (MRL) and SJL/J (SJL) obtained from The Jackson laboratory (Bar harbor, ME) were crossed with each others to generate MRL.SJL-F1 population of mice. MRL have low vBMD mice (600 mg/cm^3) while SJL mice have high vBMD mice (790 mg/cm^3). Then, the F1 mice were crossed to get F2 population. Mice were then sacrificed and bones were collected and stored in PBS for pQCT measurements.

Linkage analyses using MAP QTL (4.0) program (CPRO-DLO, Wageningen, The Netherlands) were performed after genotyping the female F2 mice (data published in Calcif Tissue Int, Masinde et al., 2002). **Figure 5**. shows the QTLs identified by pQCT in the MRL X SJL-F2 population, six significant QTLs were identified in six different chromosomes, but the highest LOD scores were exhibited by the BMD QTLs in chr 1 and chr 17 (5.9 and 5.8, respectively). Furthermore, the BMD QTL in chr 1 identified in this cross MRL X SJL overlaps with the QTL found previously identified in the B6 X CAST cross which shows the importance of this QTL on BMD variation.

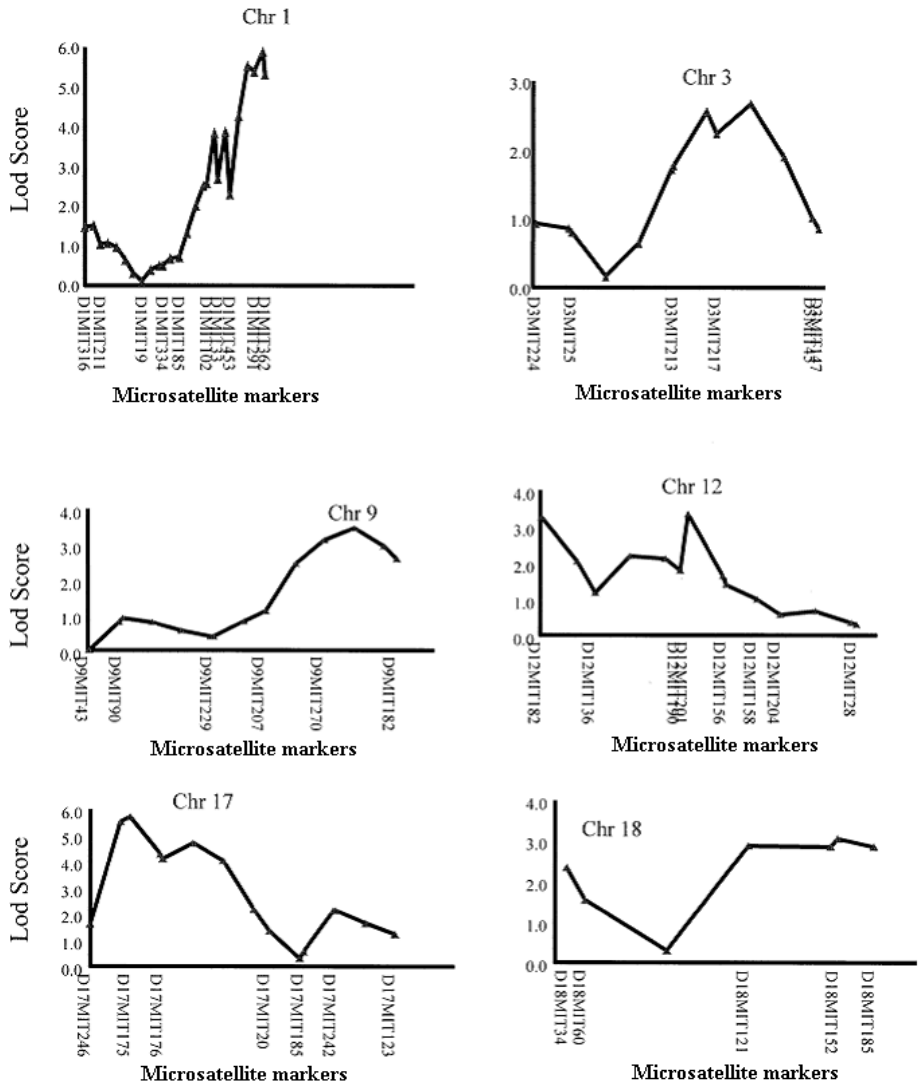

Figure 5. Graphs of bone mineral density (BMD) QTLs identified in the MRL x SJL-F2 population of female mice (Masinde et al., 2002).

3) Relationship between BMD and bone strength

Bone breaking strength is an ultimate measurement of resistance to fracture; it is mainly determined by bone mineral density (BMD), bone size, and bone quality. Since BMD contributes substantially to bone strength and can be practically measured with marked sensitivity and precision, the evaluation of BMD is the most commonly used method for predicting fracture risk in humans.

BMD is known to be a complex phenotype strongly influenced by genetic factors (Arden et al. 1996; Harris et al., 1998) and fracture liability has also been shown to be heritable (Deng et al., 2000; Michaelsson et al., 2005). Thus, to determine the genetic relationship between BMD and bone breaking strength; we measured femur-breaking strength (FBS) by three-point bending using an Instron DynaMight Low-Force Testing System, the wholegenome scan was carried out using 119 polymorphic markers in the 633 (MRL X SJL) F2 female mice. The interval mapping was performed to detect significant association between femur BMD or FBS and marker loci in F2 progeny using MapQTL software (Version 4.0; Wageningen, The Netherlands).

Six significant quantitative trait loci (QTL) affecting bone breaking strength were found on chromosomes 1, 2, 8, 9, 10, and 17, which together explained 23% of F2 variance. Of those, the QTL on chromosomes 2, 8, and 10 seem to be unique to bone breaking strength, whereas the remaining three QTL (chr 1, 9 and 17) are concordant with femur BMD QTL. Genetic analysis suggests that, of these six FBS QTL, three influence BMD, two influence bone quality, and one influences bone size (data published in Genomics, Li et al., 2002). Based on the data that chr 1 contains a QTL that regulates bone strength besides BMD illustrate the importance of this QTL.

4) Construct a BAC clone contig that covers the QTL region of chromosome 1 in the subcongenic lines.

a. Identify probes, design primers, and amplify probes that can be used for BAC contig construction. We used probes mainly collected/chosen from three sources: publications (Eddleston et al., 1999; Underhill et al., 1999); the mouse genome database for molecular markers and probes (www.rodentia.com/wmc/index.html); and currently available mouse genome sequences for new probes (www.ncbi.nlm.nih.gov/genome/seq/MmHome.html). A total of 45 STS, including genes, ESTs, and microsatellite markers, were used in our screening. Probes were amplified by PCR or RT-PCR. The amplified products then were used as templates for ^{32}P labeling and were used in the hybridization described below.

b. Hybridize the high-density filters of the BAC library with pooled probes. We have used the RPCI-23 mouse BAC library from Roswell Park Cancer Institute (RPCI) for our contig construction. It was made from the kidney and brain genomic DNA of a female B6 mouse. We first screened the high-density filters with pooled probes. We then constructed secondary filters with positive clones and conducted secondary screening with individual probes. Clones finally were connected to each other with the hybridization information.

For hybridization of high-density filters of the BAC library using pooled probes, we followed the procedure provided by RPCI (www.chori.org/bacpac). The purified PCR products then were labeled with ^{32}P. Pooled probes between 10 and 20 were used to hybridize one set of high-density filters at 65^{o}C overnight. Filters were exposed for one to five days to ensure the optional background. In case too many clones were positive, positive clones were divided into strong, medium, and weakly positive groups. Seven hundred positive clones were identified from the total library in the initial screening using pooled probes, which were subsequently grown to make secondary filters

c. Construct new filters of positive clones from high-density filters. Selected positive clones from first hybridization were then used to make secondary filters. Clones were picked up from the library and grown on LB medium overnight. A 384-well pin tool was used to transfer the selected clones onto new Nylon membrane filters. Two new filters were made from seven hundred clones.

d. Hybridize the new filters with individual probes. The new filters were hybridized using individual probes. These BAC clones were subjected to amplification with the original STS markers. Finally, the positive clones for each probe were identified.

e. Identify overlapped clones among positive clones to construct the contig. Clones that contained more than one marker were used to construct the contig. If two clones contained at least one identical marker/probe as well as other different markers/probes, they were considered to be neighboring clones with overlapping sequences. Eventually, a contig was constructed with the overlapping markers/probes among all the neighboring clones.

f. Sequenced genomic sequences of 8 BAC cones in the BAC contig.

In collaboration with the Advanced Center for Genome Technology at the University of Oklahoma, we have sequenced the genomic sequences of eight BAC clones within the BAC contig of the QTL locus. These eight clones are a19-191, p9-22, h6-395, m12-116, j4-157, i20-137, e19-140, a8-85.

In conclusion BAC clones analyses and sequencing allowed us to map the chromosomal region 169-176 Mb (data published in Genetica; Gu et al., 2002), but since phenotypic characterization of B6.CAST-1 congenic sublines of mice provided evidence for the presence of more than one BMD loci (see below) we planned to use congenic sublines of mice and use the Celera database which became available to us as well as the NCBI database to screen for the BMD candidate genes in chr 1.

5) Production of more congenic sublines of mice to narrow down the size of the BMD QTLs in chr 1.

a. Generate more congenic sublines of mice

C100-193 and C168-185 have been used to prepare additional congenic sublines. For all congenic sublines, we have used a "C" letter referring to the cast allele, followed by the position (in megabases) of the two markers flanking the donated CAST segment. These congenic lines carried the CAST chromosomal regions which covered approximately 93 Mb of chromosome 1, the equivalent to 100-193 Mb in chr 1 according to the NCBI database. Additional crosses between the congenics and the B6 progenitor produced new recombinations carrying smaller overlapping segments that were fixed in the nine congenic sublines reported herein (**Figure 6**). Each subline was genotyped using 38 polymorphic markers that encompass the initial BMD QTL. Databases used to identify the polymorphic markers included the Mouse Genome Informatic database (http://www.informatics.jax.org/) and the NCBI database (www.ncbi.nlm.nih.gov). Twenty-nine markers were found in the Jackson mouse database, while two markers were identified by screening CT-repeated sequences within the QTL region through the NCBI database. Then, the primers flanking the dinucleotide repeat sequences were designed and used for PCR analyses. Polymorphism was determined by checking the size differences of the repeated sequences between the B6 and CAST mice.

Primers newly designed in this study:

Mg4718-F: 5'-GCA TTT TGA TCC CTT ATA ATA CA-3'
Mg4718-R: 5'-GTG GAA GAC CCT TGA ATG G-3'
Mg4723-F: 5'-GCA TAG CCA ACA AAA GAA ATC TAA TG-3'
Mg4723-R: 5'-GCA GTG TAG CTC AGT GGT AGA TCA C-3'

After each cross, the progenies were genotyped as described above. We have also used fluorescently end-labeled primers to amplify genomic regions of interest. Using labeled primers, the sizes of the fluorescently-labeled PCR products were directly determined by the ABI PRISM 377 GeneScan Analyzer. PCR products from B6, CAST and their F1 hybrids were used as standards to identify the mouse genotypes.

Fig. 6 shows the size of the cast chromosomal segment carried by each congenic subline as well as the polymorphic markers used for genotyping. The nine new congenic sublines as well as the subline identified previously are presented in **Fig. 6**.

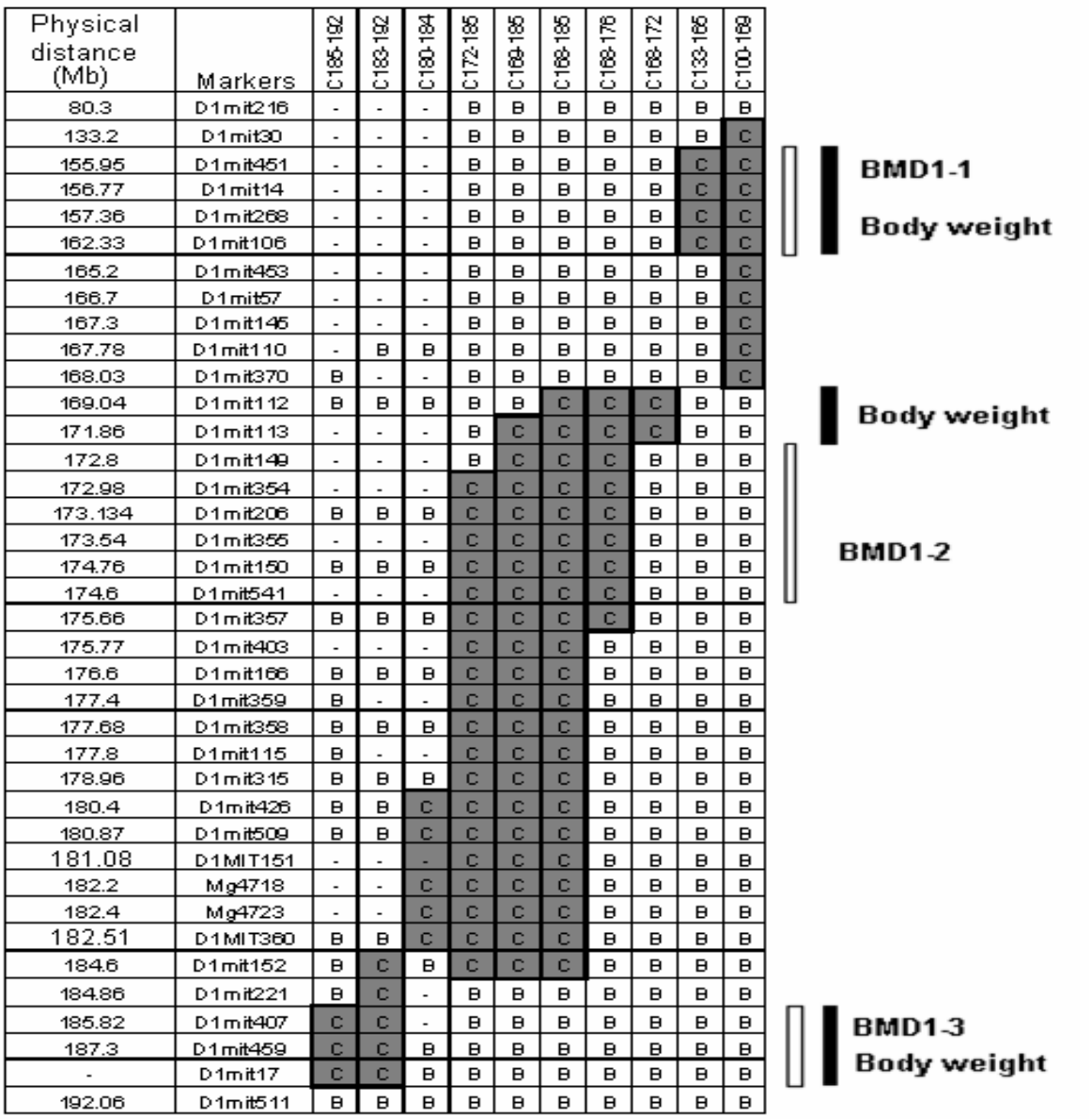

Figure.6. The regions of CAST Chr 1 transferred from CAST mice onto B6 background, for the ten congenic sublines. The genotyping data for every marker are represented with "B" referring to homozygous b6/b6, "C" referring to cast/cast and "-" for data not available. The names of the subcongenic lines are at the top. We used a letter "C" followed by the proximal and distal limits of cast alleles carried by the congenic sublines in megabases. The grey squares denote the CAST chromosomal regions carried by each congenic subline. The open bars indicate the potential BMD QTLs and the solid bars present the QTL related with body weight and bone size traits. The polymorphic markers with their physical positions along Chr 1 are presented at the left. BMD loci are designated as BMD1-1, BMD1-2 for the second locus and BMD1-3 for the third locus.

b. Phenotypic characterization of the new congenic sublines of mice

We analyzed 8-13 female mice from the B6 line and from each congenic subline at 16 weeks of age. Body weights were recorded at necropsy. Bones collected were stored in 1 x PBS

buffer supplemented with 0.05% sodium azide. Then, isolated femurs were assessed using the peripheral quantitative computed tomography (pQCT) system from Stratec XCT-RESEARCH (Norland Medical System, Fort Atkinson, WI, USA), operating at a resolution of 0.07 mm. The bone scans were analyzed with an outer threshold of 630 mg/cm3 to determine bone area/total volume. This threshold was selected to yield values for total bone areas that are consistent with bone histomorphometric derived values. A second analysis was carried out with a threshold set at 230 mg/cm^3 to determine mineral content. Isolated femurs were scanned at nine locations symmetrically located around the midpoint, 11% of the femur length apart and covering the entire length. The vBMD was calculated by dividing total mineral content by the associated total volume. Femur vBMD as well as periosteal circumference, endosteal circumference, and cortical thickness were evaluated at the mid-diaphysis region of the femurs (average of slices 4 and 5). Analyses of the scans were performed using manufacturer-supplied software program (Stratec Medizintechnik GMBH Bone Density Software, version 5.40C). The sublines of mice that were genetically homozygous cast/cast at chromosome 1 segments were homozygous for B6 at more than 99% of the remaining genome (Shultz et al., 2003). Therefore, femoral vBMD variations observed within congenic sublines generated in this study were attributed to a CAST donated segment.

Femur vBMD and other related bone parameters were evaluated at the mid-diaphysis region of the femur using pQCT for the nine congenic sublines newly generated as well as for the parental C168-185, along with age- and gender-matched B6. Figure 6 shows the relative change in various phenotypes introduced by CAST donated regions compared with B6 control mice. All the sublines, which carried overlapping CAST segments from the region 100-185 Mb of the centromere, exhibited a significantly greater vBMD compared to the B6 mice, except sublines C168-172 and C180-184 (**Fig. 7A**). The vBMD change for various subcongenic lines were +12.0% for C100-169, +5.0% for C133-165, +7.6% for C168-176, +9.0% for C168-185, +8.6% for C169-185, +10.6% for C172-185. When these data are superimposed on the genetic map shown in **Fig. 6**, there is evidence for the presence of two separates genetic loci that regulate vBMD positively; one located within 133-165 Mb (BMD1-1), the second located within 172-176 Mb (BMD1-2). Furthermore, sublines C183-192 and C185-192, which carried overlapping CAST chromosomal regions at the distal region of Chr 1, showed a significant decrease of femoral vBMD compared to B6 mice (-6.0%), indicating the presence of a third locus with a negative effect on femur vBMD (BMD1-3).

We evaluated the body weights of these congenic sublines to determine if a body weight phenotype co-segregates with mid-diaphyseal vBMD. **Fig. 7B** shows that sublines carrying cast alleles from the BMD1-1 and BMD1-3 loci exhibited significantly smaller body weight compared to B6 (5-8%), while sublines which covered the BMD1-2 locus exhibited significantly greater body weight compared to B6 mice (6-8%). The overall correlation (**Table 6**) between body weight and vBMD among the 10 sublines was positive (r=+0.5; p=0.12), but did not reach statistical significance. Moreover, the adjustment for body weight or femur length did not affect the significance of femoral vBMD change (data not shown). This provided evidence that body weight is not responsible for the vBMD variation introduced by CAST donated segments. **Fig. 7B** shows that there were no significant changes in femur length among the ten sublines except for C168-172 mice which exhibited reduced body weight (-9.7%) and smaller femur length (-3%) compared to B6 control mice.

Other bone parameters such as endosteal circumference (EC), periosteal circumference (PC), and cortical thickness (CT), were analyzed to determine if other phenotypes co-segregated

with the vBMD phenotype or could account for the changes in femoral vBMD. Sublines which carried cast alleles underlying BMD1-1 and BMD1-2 loci showed significantly smaller EC compared to B6 control mice; EC from C100-169, C168-176 and C172-185 were 7%, 3.3 and 4% smaller than B6 mice, respectively. In contrast, the two sublines (C183-192 and C185-192) that covered the distal BMD locus (BMD1-3) showed a slight (2-4%) but significant increase in EC compared to the B6 control mice (**Fig. 7C**). No significant difference in EC was found in sublines C168-185, and C169-185. Among the ten subcongenic lines there was a significant negative correlation between the changes of vBMD and EC (r=-0.67, p=0.024).

With respect to PC, the sublines C168-185, and C169-185 showed significantly greater PC (3-4%, **Fig. 7C**). However, after adjustment for body weight and femur length, they lost the significant difference with B6 control mice. While subline C168-172 showed significantly smaller PC and EC compared to B6 control mice, the significance was lost after adjustment for body weight and femur length, which suggests the presence of a genetic locus associated with body weight and bone size at 168-172 Mb from the centromere.

A change in vBMD can be explained on the basis of change in CT and/or material BMD. In our study, sublines showing a higher vBMD exhibited significantly greater CT compared to the B6 mice (4-9%) (**Fig. 7C**) and, when tested for correlation, a strong correlation was found between vBMD change and CT among all the sublines (r=0.97; p=0.0001) (**Table 6**). Thus, a change in cortical thickness, rather than cortical material density properties, appears to mainly drive the QTL changes in vBMD observed in our congenic sublines.

Fig. 7A

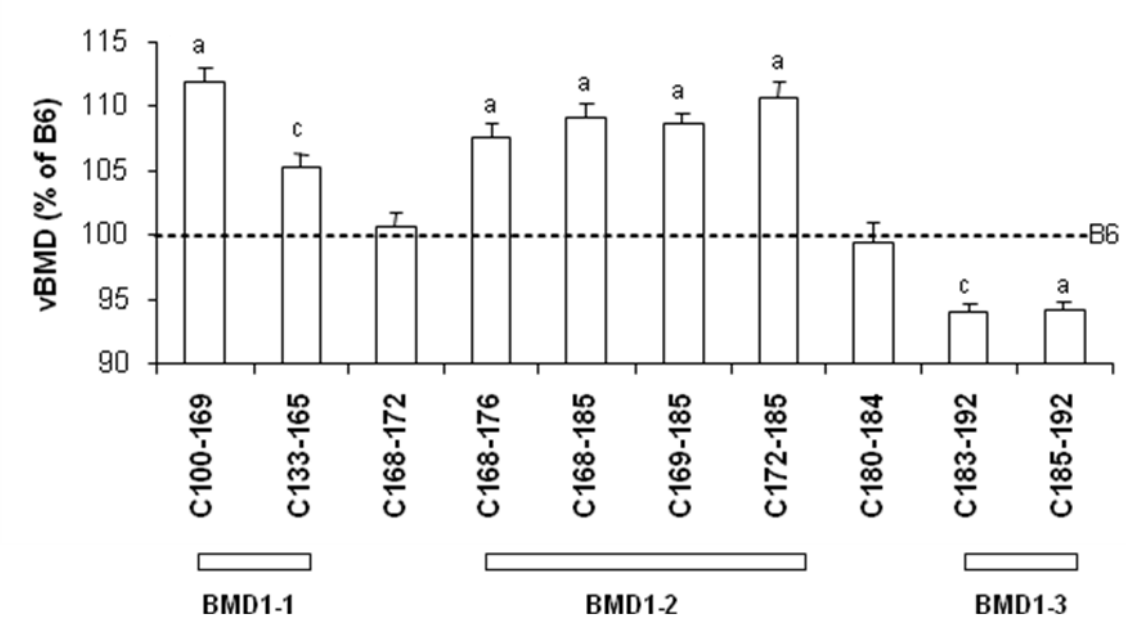

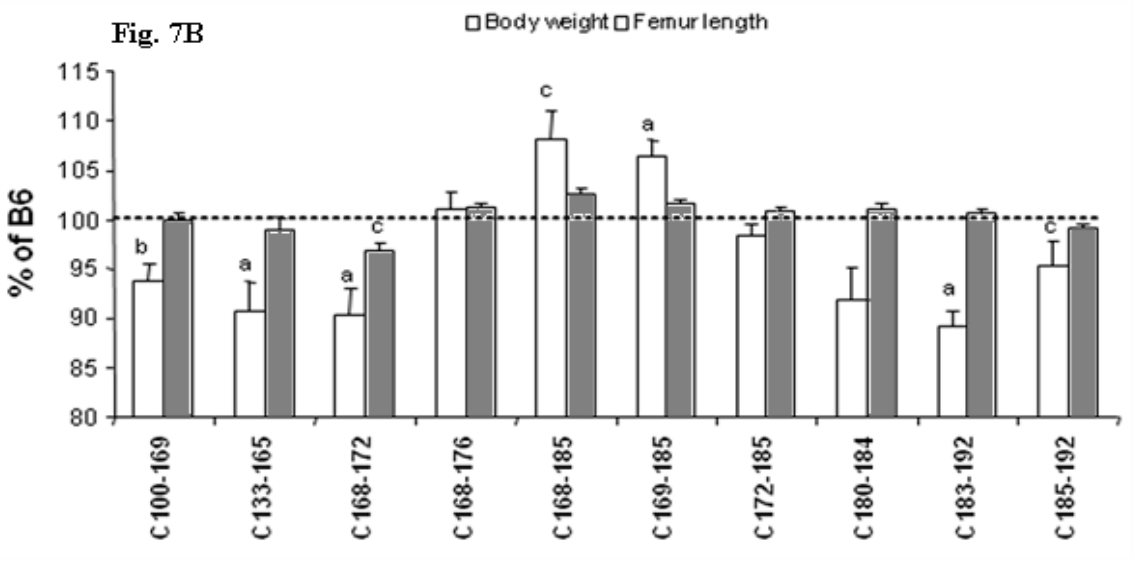

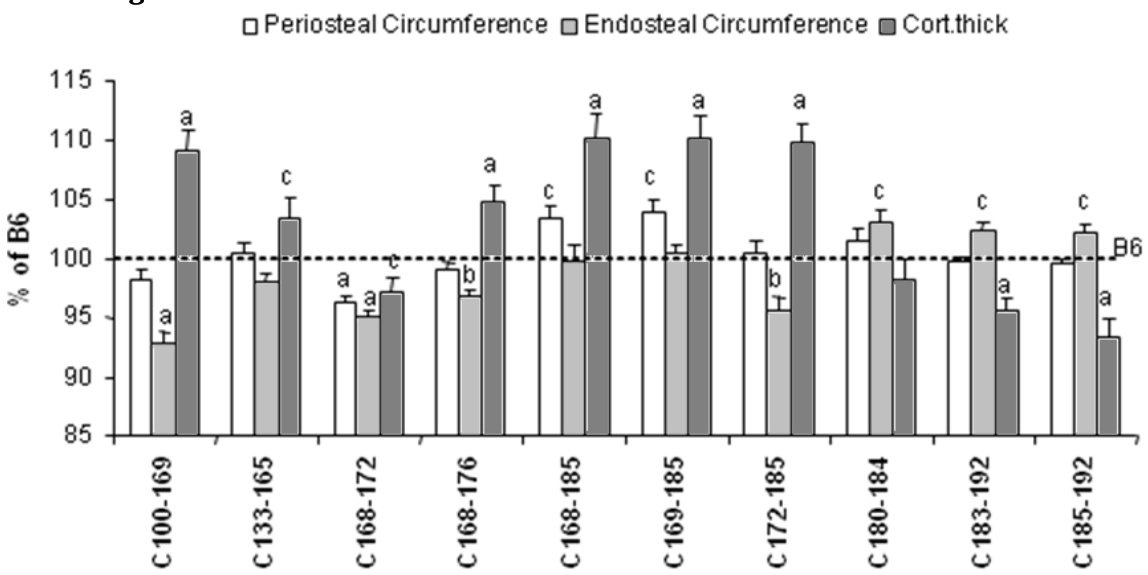

Figure 7. Femoral and body weight data from the ten different subcongenic strains of mice. Data are expressed as a percentage change from B6 and are mean + SEM, n=8-19. The X axis represents the sublines characterized in this study. The identified BMD loci are indicated by solid bars underneath the names of the sublines that carry each locus. **Figure 7A**. Mid-diaphysis femur vBMD. **Figure 7B**. Body weight and femur length. **Figure 7C.** Mid-diaphysis femur periosteal circumference and endosteal circumference and cortical thickness. In each panel, significant differences between B6 control mice and congenic sublines are indicated by lowercase letters. $^{a}P<0.005$, $^{b}P=0.01$, $^{c}0.01<P<0.05$ using t-test. Comparison of the effect size between subcongenic lines was tested by ANOVA and Neuman-keuls post-hoc test. If the conservative Bonferroni correction for multiple t-test comparisons is applied, those effects identified with "a" are still statistically significant. This includes all the vBMD effects and 8 of 9 cortical thickness effects.

Table 6. Correlation among various phenotypes from the ten congenic sublines tested.

	Crt.Thickness	Perios.C	Endos.C	Weight	Femur length
vBMD	**0.97**	0.26	**-0.80**	0.50	0.09
Crt.Thickness	1.00	0.43	**-0.67**	0.62	0.23
Perios.C	0.43	1.00	0.37	**0.77**	0.54
Endos.C	**-0.67**	0.37	1.00	-0.03	0.28
Weight	**0.62**	**0.77**	-0.03	1.00	0.45
Femur length	0.23	0.54	0.28	0.45	1.00

Significant correlations are shown in bold ($p<0.05$, N=10). Values for all phenotypes were expressed as a percentage difference compared with B6 mice. Crt.Thickness, refers to cortical thickness. Perio.C, refers to periosteal circumference. Endo.C, refers to endosteal circumference.

In conclusion, the majors findings from the current studies are: (1) comprehensive and systematic congenic coverage revealed multiple vBMD loci in the distal portion of Chr 1, each locus is able to affect femoral vBMD independently in a B6 background; (2) skeletal phenotype analyses of these congenic sublines showed that these genetic loci in B6 background have not only a positive effect, but also a negative effect on vBMD phenotype; (3) The three loci affect vBMD phenotype by influencing mainly endocortical bone formation and/or bone resorption; (4) interactions between BMD loci in Chr 1 contribute in part to femoral vBMD variation; and (5) body weight/bone size QTL maybe present at the central region of the major BMD QTL in Chr 1. (Data published in Journal of Bone and Mineral Research; Edderkaoui et al., 2006).

6) Fine Mapping of chr 1 BMD QTL

In order to narrow down the size of the BMD QTL in chr 1 and to determine if more than one gene in chr 1 are involved in the BMD variation observed between the high BMD CAST and the low BMD B6 mice, we have decide to fine map the initial BMD QTL using a large number markers and of B6-CAST-F2 mice. Therefore, spleens from 656 B6.CAST-F2 female mice were received from Wes Beamer (TJL) to be used for genotyping. Extractions of genomic DNA from the spleens were performed following the Gentra PurGene protocol (PUREGENE Tissue kit, Part#D-7000A). In order to fine map the BMD QTL in Chr 1, we used 33 polymorphic markers located within the BMD QTL region that covers 29.73 cM in mouse Chr 1, between D1mit106 and D1mit511 as described by Edderkaoui et al., (2006), instead of the 7 markers which were previously used to identify the major BMD QTL in this region (Beamer et al., 1999). The number of markers was increased in order to detect and evaluate the effect of more potential recombinations within the major QTL region.

Genotyping data from the F2 population were analyzed using MapQTL (4.0) software (CPRO-DLO, Wageningen, The Netherlands) and Mapmaker software was used to test the reproducibility of MapQTL data. MapQTL interval mapping was used for quantitative trait loci mapping, and the LOD score significant thresholds were calculated using MapQTL permutation tests at a confidence level of 99%.

Phenotypic characterization of the ten congenic sublines of mice led to the identification of three BMD loci at Chr 1 by superimposing the CAST chromosomal regions carried by each congenic subline. The BMD1-1 locus was located between D1mit133-D1mit453 (133.2-165.2 Mb), BMD1-2 locus was located between D1mit113-D1mit150 (171.86-174.76 Mb) and a BMD1-3 which regulates BMD negatively was located between D1mit221-D1mit511 (184.86-192.06 Mb). We have then further fine mapped the Chr 1 QTL region by genotyping 565 B6.CAST-F2 female mice with a large number of polymorphic markers within this region. Interval mapping using MapQTL 4.0 to identify the linkage between polymorphic markers and femur total volumetric BMD (vBMD) within the F2 female mice showed three peaks/QTL; peak 1 at marker D1mit453 (BMD1-1, at 165.2 Mb), peak 2 at marker D1mit354 (BMD1-2, at 172.98 Mb) and peak 3 at marker D1mit359 (designated as BMD1-4 at 177.4 Mb) (**Fig. 8**), that were significantly associated with femoral vBMD of B6.CAST-F2 female mice. MapMaker software also identified three significant linkages at the same positions (**Table** 7), which explained 9.3%, 10.7% and 9% of the BMD variation within the B6.CAST F2 population, respectively. Thus, Chr 1 contains at least four BMD loci three of which regulate BMD positively and one negatively.

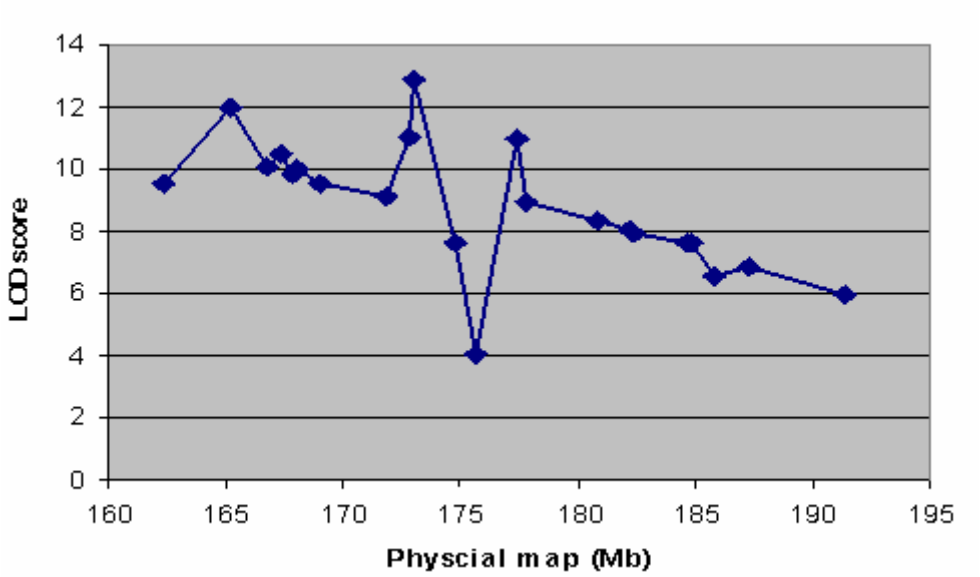

Figure 8. Fine mapping of BMD QTL in chromosome 1 using 33 polymorphic markers. Linkage analyses showed three peaks suggesting at least three BMD QTLs within Chr 1. The X axis represents the physical distance beginning with the centromeric side and extending toward the telomeric side of Chr 1, starting from marker D1mit106 at 162.33 Mb according to National Center for Biotechnology Information database (http://www.ncbi.nlm.nih.gov/). Y axis represents the likelihood values for the presence of a segregating QTL at each marker (LOD score).

Table 7. Identification of BMD QTL intervals in chromosome 1 using MapMaker software.

Total vBMD	MapMaker QTL intervals (Mb)	LOD score
BMD1-1	164.6-166.7	10.3
BMD1-2	171.6-174.76	11.2
BMD1-4	177.46-184.6	11.1

We have performed a classical "two-point"/pairwise linkage analysis of our data using 12 markers along the initial BMD QTL in Chr 1. The software determines the markers that are linked with each others and calculates the likelihood (LOD score) of the presence of a QTL between each pair of markers.

In conclusion, fine mapping using a large number of markers that cover the initial BMD QTL in chr 1 confirmed the presence of the BMD1-1 and BMD1-2 loci identified previously using congenic mice and provided evidence for the presence of a BMD1-4 locus between at 177.5-180 Mb of chr 1 which needs to be confirmed by generating more congenic sublines of mice.

7) Identification of BMD1-2 candidate gene

Since the BMD1-2 QTL showed the highest LOD score, we chose to screen BMD candidate genes within this locus. The congenic subline C168-176 exhibited a significantly greater vBMD compared to the B6 mice (9.8%, P=0.01), while C168-172 did not show any differences compared to the B6 controls. Using this data, we could safely eliminate the genes located at the 168-172 Mb chromosomal region from further analyses which narrowed down the size of the BMD1-2 locus to 172-176 Mb from the centromere in Chr 1.

a. Gene expression profiling

In order to screen for potential BMD candidate genes in the 172-176 Mb region, we compared the expression levels of all known genes and ESTs located in this region between the bones of the B6 control mice and the two congenic sublines described above. We chose gene expression change to identify candidate genes, since it is known that SNPs at both the regulatory regions (promoter, 3'-UTR) and coding regions (*via* feed back loop) could affect the expression of the gene (Schadt et al., 2003, and Chesler et al., 2005). In addition, this strategy has been successfully used in a recent study by Klein et al. (2004) to identify a QTL gene that negatively regulates peak bone density. Since C168-172 does not show a BMD phenotype, it was used as a negative control, so only genes that showed a difference in the expression between C168-176 and B6, but not between C168-172 and B6, were further analyzed. Among all genes analyzed, only the *DARC* gene, located at 173.26 Mb, showed a 6-fold increase of the expression in the C168-176 congenic subline when compared to the control progenitors (published data in Genome Research; Edderkaoui et al., 2007), while no difference was found in expression between the C168-172 and B6 control mice. Since none of the other genes exhibited more than 2-fold difference that is significant, we focused on *DARC* as a candidate gene.

b. Skeletal phenotype of DARC-KO mice

If the increase of DARC gene expression in B6.CAST-1 congenic mice is responsible for the greater femur BMD exhibited by the C168-176 mice, we would expect DARC-KO mice to show a lower femur BMD compared to control mice. To test this hypothesis, we compared the phenotype of DARC-KO mice generated in a B6 background with that of age-gender matched wild type B6 progenitors. Body weight as well as femur length were similar for the two strains (**Fig. 9**), while total femur vBMD was increased in the DARC-KO mice compared to the wild type control mice. The trabecular volume was 13% smaller in the DARC-KO mice compared to the wild type mice ($p<0.01$), the endosteal circumference was 3.8% decreased and there was no change in periosteal circumference, which resembles the phenotype of the C168-176 subline and confirms the involvement of the DARC gene in BMD variation. Based on these data we consider an alternate possibility that the high expression of DARC is due to a loss of the protein function

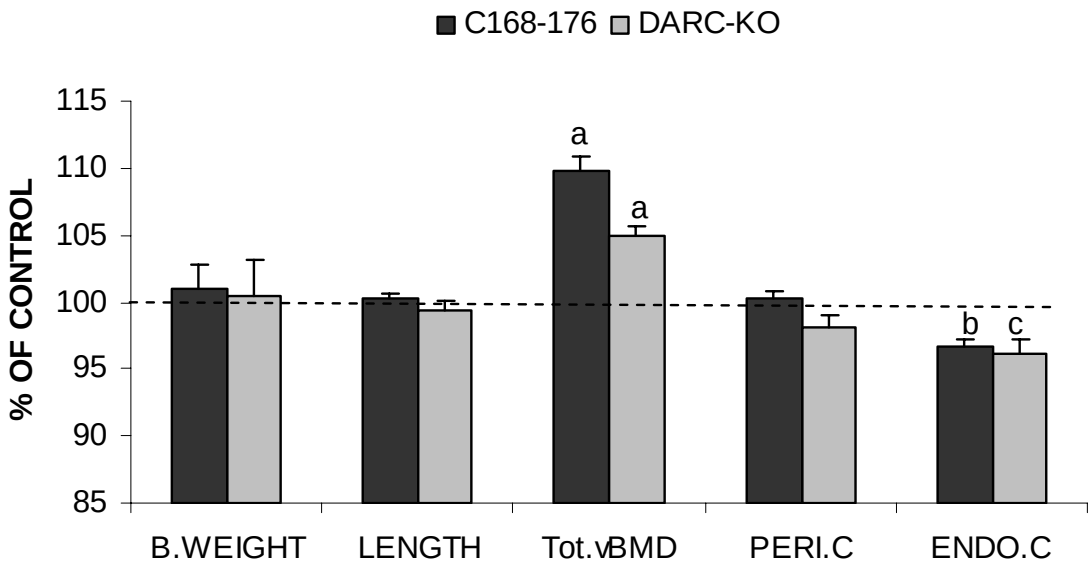

Figure 9. Femoral and body weight data from the C168-176 subline of mice and *DARC*-KO mice. Data are expressed as a percentage of B6 controls and are means ± SEM. [a]P<0.01, [b]P=0.01, [c]P=0.05 as calculated by *Student's t-test*, with n=10-14. B.Weight, represents body weight, Length is the femur length, Tot.vBMD, refers to total femur volumetric BMD, PERI.C; represents the periosteal circumference and ENDO.C represents the endosteal circumference. Femurs were assessed using the peripheral quantitative computed tomography (pQCT) system from Stratec XCT-RESEARCH (Norland Medical System, Fort Atkinson, WI, USA) as previously described (Edderkaoui *et al*., 2006).

c. SNPs analyses

We next sequenced the *DARC* gene to determine the SNPs that might be the cause of the difference in the expression between the B6 mice and the high BMD congenic subline of mice. Using the NCBI database and in-house sequencing, we have identified 28 polymorphisms that distinguish the *DARC* gene in the B6 from the CAST strain (**Table 8**), with three SNPs located at the promoter region, 15 polymorphism sequences located at the intervening sequence, and 10 polymorphisms at the coding region. Among the polymorphisms in the coding region, only six led to amino acid changes (Table 8). None of the polymorphisms discovered in the promoter region covered the consensus sequences that potentially regulate the transcription process, so it is

likely that the difference in the expression of the *DARC* gene is due to the SNPs in the coding region. In order to determine if the SNPs in the *DARC* gene could be responsible for BMD variation, we compared the *DARC* gene sequence of the B6 and CAST with another high BMD strain, namely C3H/HeJ (C3H). We found that the six informative SNPs in the coding region were conserved in both the CAST and C3H, suggesting that one or more of these SNPs could contribute to the high BMD phenotype exhibited by CAST and C3H mice (Table 8).

Table.8. SNPs found in Duffy gene.

SNPs Position (bp)	Nucleotide change (CAST/B6)	Intron/Exon	Amino-acid change	Amino acid position
129	A/T	Intron		
131-132	GT/-	Intron		
147	C/T	Intron		
163	C/T	Intron		
184	G/A	Intron		
201	T/C	Intron		
285	C/T	Intron		
308	T/C	Intron		
310	A/T	Intron		
372	A/G	Intron		
382	G/T	Intron		
405	A/T	Intron		
454	T/C	Intron		
467	C/T	Intron		
493	C/A	Exon2	T/N	10
631	A/G	Exon2	D/G	56
644	G/T	Exon2		
830	T/C	Exon2		
920	T/C	Exon2		
1044	A/G	Exon2	T/A	194
1084-1085	CT/TG	Exon2	T/M	207
1126	T/C	Exon2		
1267	C/T	Exon2	T/I	268
1286	T/C	Exon2		

"SNP" means single nucleotide polymorphism. "aa" means amino acid. The positions of the SNPs in the promoter regions were taken according to the sequence reported by Luo et al. (2000), while the polymorphism sequences located within the gene from the start codong till the stop codon were taken according to CAST sequence AB039077. The gene was sequenced from -580bp till the stop codon.

d. Reduced bone resorption in the femur mid-diaphysis of *DARC*-KO mice

To determine if the increase of femur vBMD in *DARC*-KO mice is due to an increase in bone formation or due to a reduction in resorption, we have performed histomorphometry measurements in the femurs isolated from *DARC*-KO mice and from control *DARC*+/+ mice as described by Edderkaoui *et al*. (2007). We found TRAP positive bone resorbing surface was significantly reduced both at the endosteum (47%, p=0.002) and at the periosteum (8%, p=0.02) of femurs isolated from the *DARC*-KO mice compared to control mice (**Fig.10**). In contrast, bone

formation rate was not significantly different in the femurs of *DARK*-KO mice compared to control mice (**Fig.10**). We are in the process of generating the congenic subline of mice carrying *BMD1-2* locus for the purpose of performing histomorphometry studies in order to confirm the increased BMD in the congenic mice is also due to reduced bone resorption.

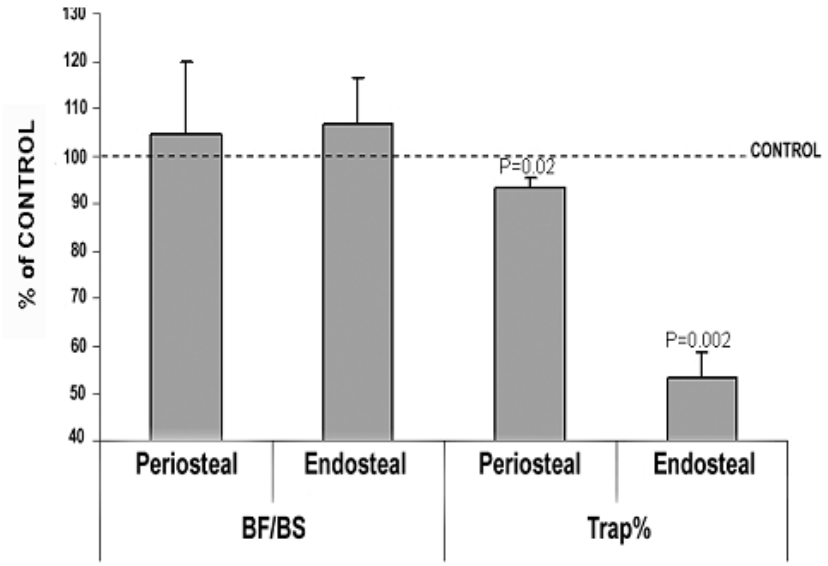

Figure 10. Bone formation and bone resorption in femur from *DARC*-KO mice. Bone formation is calculated as bone surface (BF) divided by total bone surface (BS). Bone resorption (trap%) is calculated as (the resorbing surface/bone surface)*100 and it is expressed as the percentage of wild type.

e. *DARC* binds to chemokines

We next determined if amino acid changes in *DARC* could have contributed to the loss of function in the congenic mice. Among the six SNPs found in the coding region, the aspartic acid at position 56 seems to be significant due to its location close to the cysteine at position 49, which is required to form the disulfide bridge between the transmembrane helices 1 and 7 in the chemokine binding pocket (Tournamille et al., 1997) as shown in **Fig. 11**. The change of a small and neutral amino acid glycine with a negatively charged aspartic acid could change the conformation of the protein as well as the chemical environment of the binding sites, which consequently may affect the binding of the *DARC* protein to the chemokines and/or the stability of *DARC* protein. Accordingly, we predict that the *DARC* protein in CAST to bind to chemokines much less efficiently compared to the *DARC* protein from B6 mice. To test this hypothesis, we analyzed the binding of chemokines to MDBM cells derived from *DARC*-KO and congenic mice. We chose MCP-1, RANTES and IL-8 as ligands for the binding studies based on previous findings that these chemokines bound to the *DARC* protein and all the three chemokines have been shown to regulate osteoclast formation. By using ^{125}I-labelled MCP-1, IL-8 and RANTES for the binding studies, we found that the specific binding of the three chemokines was significantly reduced in the MDBM cells derived from both C168-176 subline and *DARC*-KO

mice compared to the B6 mice (**Fig.12**) which suggests that the SNPs in the binding pocket of *DARC* are responsible of the chemokine binding alteration.

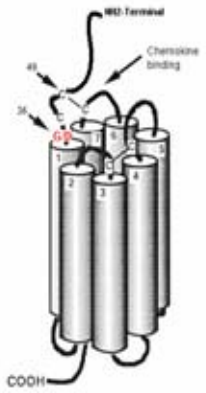

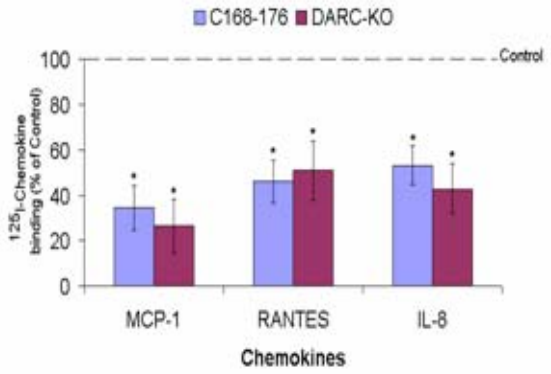

Figure 11. Schematic presentation of the predicted model **of *DARC* protein, based on analogy with the IL8 type A receptor (modified fromTournamille et al., 1997).**
The three cysteine residues that form the chemokine binding site are brought into close proximity by a disulfide bridge between t he first and the fourth extracellular domains of DARC protein. The cysteine residue at the N -terminal that forms the bridge is at position 49 in mouse *DARC* sequence. The position of the SNP G56D is indicated.

Figure 12 Binding of threechemokinesto MDBM cells.
Isolation and culture conditions for MDBM cells were as described previously (Edderkaoui et al., 2007). MDBM cells were incubated at 37°C/RT in the presence of either only ^{125}I-chemkine or in the presence of both labeled and unlabelled chemokine . The specific binding was expressed as the CPM value in the absence of cold chemokine subtracted from the CPM value in the presence of cold chemokine , *P<0.05 as measured by Student 's *t-fest*, n=8-10.

f. Reduced osteoclast differentiation in MDBM cells derived from DARC-KO and Chr 1 congenic mice

Since *DARC* protein binds to a number of chemokines which regulate osteoclastogenesis, we next determined if reduced binding of chemokines to *DARC* in congenic mice is associated with corresponding changes in osteoclast formation. We, therefore, determined the effects of RANKL and MCSF, two major cytokines that are critical for osteoclast generation (Quinn et al., 1998 and Takahashi et al., 1999) using MDBM cells-derived from *DARC*-KO and corresponding control mice. The *DARC*-KO showed a 50% decrease in the number of TRAP-positive MNCs compared to the wild type mice (**Fig. 13**). Furthermore, despite the increase of *DARC* gene expression in the C168-176, this subline showed a 70% decreased formation of TRAP-positive MNCs compared to B6 control mice (**Fig. 13**).

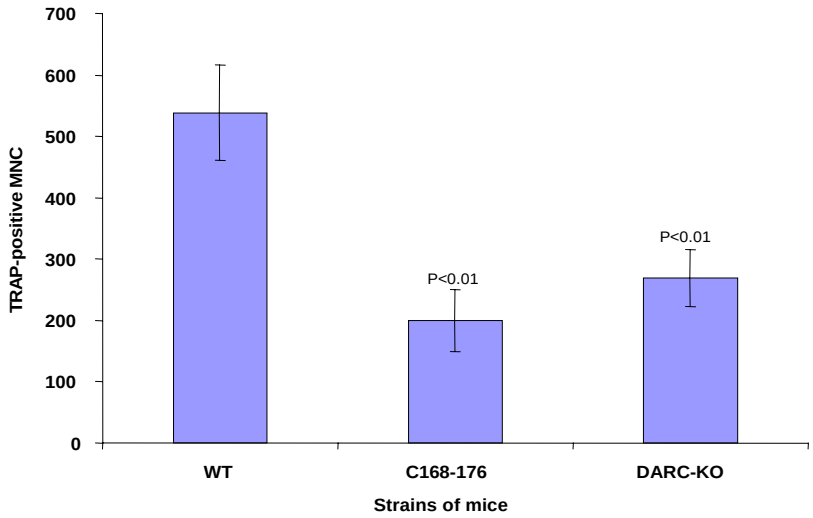

Figure 13.*In vitro* analysis of MDBM cells derived from B6 control mice, C168-176 subline, and *DARC*-KO mice in response to RANKL (100 ng/ml) and M-CSF (100 ng/ml). After 10 days in culture, cells were stained for TRAP activity. Only cells with more than 2 nuclei (MNC: multinucleated cells) w ere counted. Data are expressed as a percentage of wild type mice and are mea n ± SEM, n= 6-8 mice.

Consistent with the *in vivo* data that *DARC* is involved in regulating formation of multinucleated cells and thereby bone resorption, our *in vitro* studies have shown that treatment of MDBM cells with *DARC*-Antibody (*DARC*-Ab) in the presence of RANKL and M-CSF resulted in a significant reduction in the number of TRAP-positive multinucleated cells (**Fig. 14**). Furthermore, RANKL induced osteoclast differentiation was also decreased in murine monocytic RAW264.7 cells in the presence of *DARC*-ab (data not shown). Our hypothesis predicts that *DARC* regulation of chemokine action is involved in regulating trafficking and fusion of osteoclast precursors. We, therefore, counted the number of nuclei in RANKL/MCSF-induced TRAP-positive MNCs in the presence of *DARC*-ab or control IgG. We found that there was a significant decrease in the number of nuclei per osteoclast in response to treatment with *DARC*-ab in differentiating cultures of MDBM as well as RAW264.7 cells (**Fig. 14C**). These data together are consistent with the proposed model that *DARC* regulates osteoclast formation and that reduction in *DARC* function as in the case of B6.CAST-1 congenic mice results in reduced bone resorption and accordingly increased BMD.

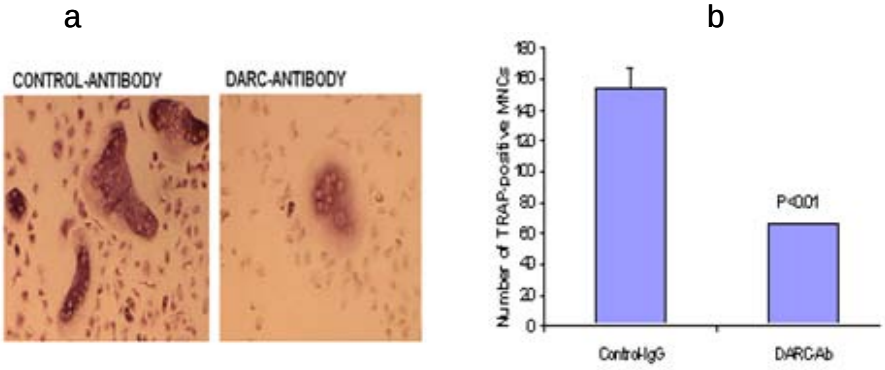

Figure 14. TRAP-stained cells from wild type B6 mice. After six days treatment of MDBM cells derived from wild type mice with goat polyclonal *DARC*-Ab in the presence of RANKL and M-CSF (right panel). (a) TRAP-stained MNCs (b) The graph represents the number of TRAP-positive MNCs.

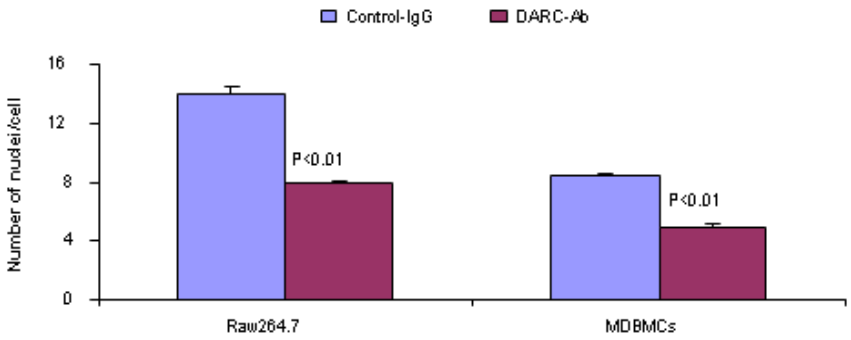

Figure 14C. Effect of *DARC* neutralization with specific antibody on the number of nuclei per TRAP-positive cells. The number of nuclei per TRAP-positive cells were calculated from the counts of cells and nuclei shown in Fig.14B and the RAW264.7 cells treated with 25 ng/ml RANKL for 6 days in presence or absence of *DARC*-Ab, 3 mice and 3 wells per animal were used for MDBMCs. 3 replictaes for each condition were used for RAW264.7 cells. The data are shown as mean $\pm$ SEM. P vs control-IgG.

g. Evidence that DARC is involved in regulating migration of osteoclast precursors

To investigate the mechanism by which DARC could regulate osteoclast differentiation, we considered the possibility of the involvement of DARC in osteoclast fusion based on the finding that DARC protein is involved in the pro-migratory activities of chemokines on the endothelium-blood interface (Pruenster et al., 2006). Furthermore, MCP-1 and RANTES, ligands for DARC protein, have been shown to be involved in the recruitment of osteoclast monocyte precursors and facilitate RANKL-induced osteoclastogenesis and, in particular, enhanced fusion (Li et al., 2007). To test for a role for DARC in regulating chemotaxis in osteoclast precursors, we used mouse monocyte cell line RAW264.7 as a model since it has been reported that RANKL increased the production of chemokines that bind to DARC in both RAW264.7 and bone marrow cells (Okamatsu et al., 2004; Cappellen et al., 2002). To evaluate the prediction that DARC is involved in regulating mobility of osteoclast precursors towards chemokines, we determined the consequence of neutralizing DARC action on the migration of RAW264.7 cells towards chemokines. Briefly, RAW264.7 cells (2 X 10^5 cells/insert) were placed in the upper chamber of cell culture inserts of 8 µm pore size. 2 hours later, the cells were treated with DARC-specific antibody or control IgG. The lower chambers contained media supplemented with fetal bovine serum and RANTES or MIP-1 gamma. 24 hours thereafter, the cells that migrate to the bottom wells were counted. As shown in **figure 15**, the number of cells that migrated to bottom wells containing RANTES or MIP-1 gamma was significantly greater than the BSA control. Treatment of cells with *DARC*-ab led to a significant reduction in the number of cells that migrated towards the bottom well containing the chemokines. These data demonstrate that RAW264.7 cells migrate towards chemokines in the absence of RANKL and that chemotaxis of RAW264.7 cells towards chemokines is dependent on functional DARC. Studies proposed in this grant application will confirm this preliminary data using MDBM cells.

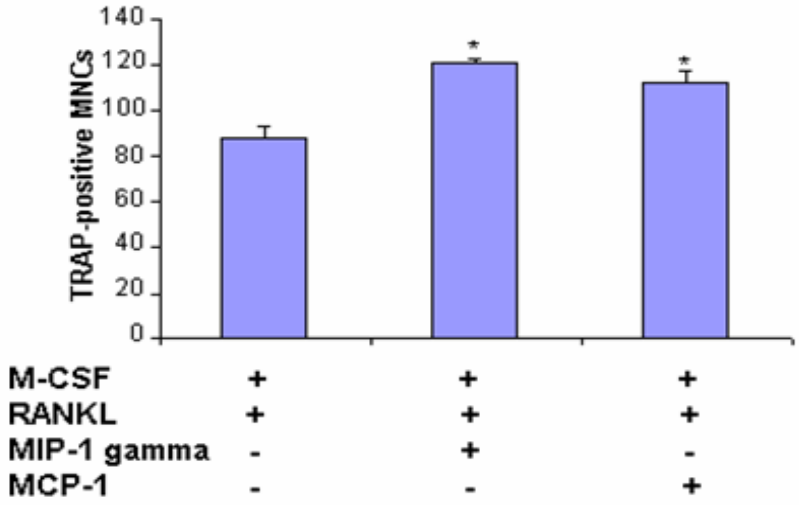

Figure 15. Significant increase in the formation of TRAP-positive MNC in response to MIP-1 gamma and MCP-1. Raw264.7 cells were treated with 10 ng/ml M-CSF and 1 ng/ml RANKL in presence or in absence of 10ng/ml MIP1 gamma or 100 ng/ml MCP-1. The cells were TRAP-stained and the TRAP-positive cells with more than 2 nuclei were counted after 4 days treatment. *P<0.05*vs* cells treated with M-CSF and RANKL only. n = 4-6

h. Chemokines amplify the effect of RANKL on the formation of TRAP-positive multinucleated osteolcasts.

Our model predicts that chemokine signaling interacts with RANKL signaling to amplify formation of osteoclasts. To evaluate this possibility, we examined the effect of MCP-1 and MIP-1 gamma on formation of multinucleated TRAP-positive cells in the presence of sub optimal concentrations of RANKL (1 ng/ml) using RAW264.7 cells. It was found that the addition of MCP-1 or MIP-1 gamma to cultures of RAW264.7 cells led to a significant increase in the formation of TRAP-positive multinucleated osteoclasts (**Fig. 16**). Our data showing significant stimulatory effect of chemokines on RAKL-induced formation of multinucleated osteoclasts in RAW cells is consistent with what has been reported on the positive effects of chemokines on osteoclast formation in human peripheral blood mononuclear cells (Yang et al., 2006; Kim et al., 2005). Our proposed experiments will examine the effect of various chemokines that bind to DARC on the formation of osteoclasts using MDBM cells to evaluate the extent to which chemokines regulate osetoclast formation and how much of this effect is independent of RANKL. We will examine the role of DARC in mediating the chemokine effects on the formation of osteoclasts in the presence or absence of RANKL.

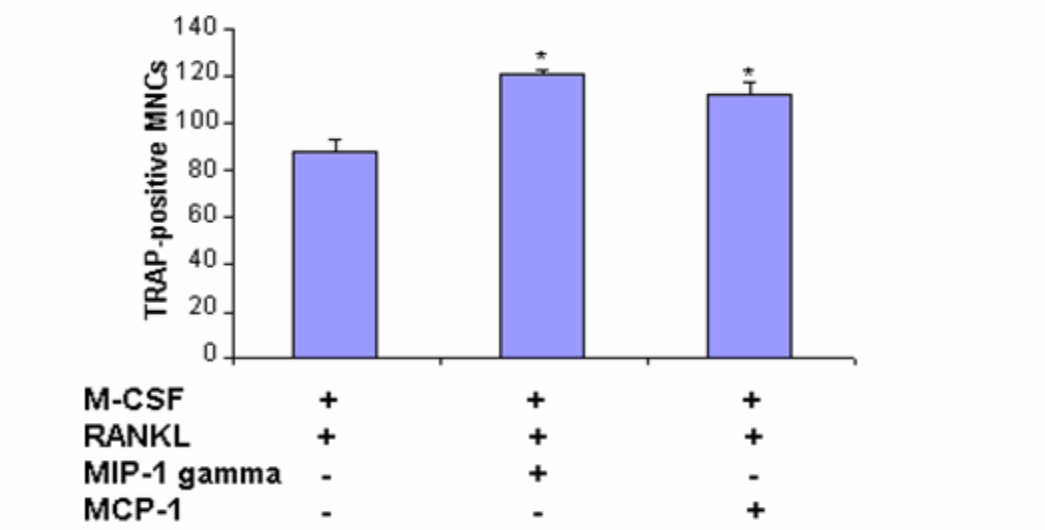

Figure 16. Significant increase in the formation of TRAP-positive MNC in response to MIP-1 gamma and MCP-1. Raw264.7 cells were treated with 10ng/ml M-CSF and 1 ng/ml RANKL in presence or in absence of 10ng/ml MIP1 gamma or 100 ng/ml MCP-1. The cells were TRAP-stained and the TRAP-positive cells with more than 2 nuclei were counted after 4 days treatment. *P<0.05*vs* cells treated with M-CSF and RANKL only. n = 4-6

i. Blockade of DARC activation reduced expression of osteoclast fusion markers

Since osteoclast migration and differentiation were found to be altered by DARC-antibody, we have analyzed the effect of DARC-antibody on the expression of cell fusion and differentiation markers such as the dendritic cell-specific transmembrane protein (DC-Stamp) and CD47 which have been reported to play key role in fusion of osteoclast precursors (Kukita et al., 2004; Yagi et al., 2005; Yagi et al., 2006). To this end, RAW264.7 cells were treated with control IgG or DARC antibody in the presence of RANKL for 24 hours. Thereafter, RNA was extracted and used for real time RT-PCR for measurement of expression levels of DC-STAMP and CD47. **Fig. 17** shows that treatment of RAW264.7 cells with RANKL led to a significant increase in the expression of CD47 and DC-Stamp, as expected. However, neutralization of DARC protein with its specific antibody led to a significant reduction in the expression levels of markers of osteoclast fusion (CD47 and DC-Stamp). Our proposed studies will confirm this preliminary data using MDBM cells derived from DARC-KO and control mice.

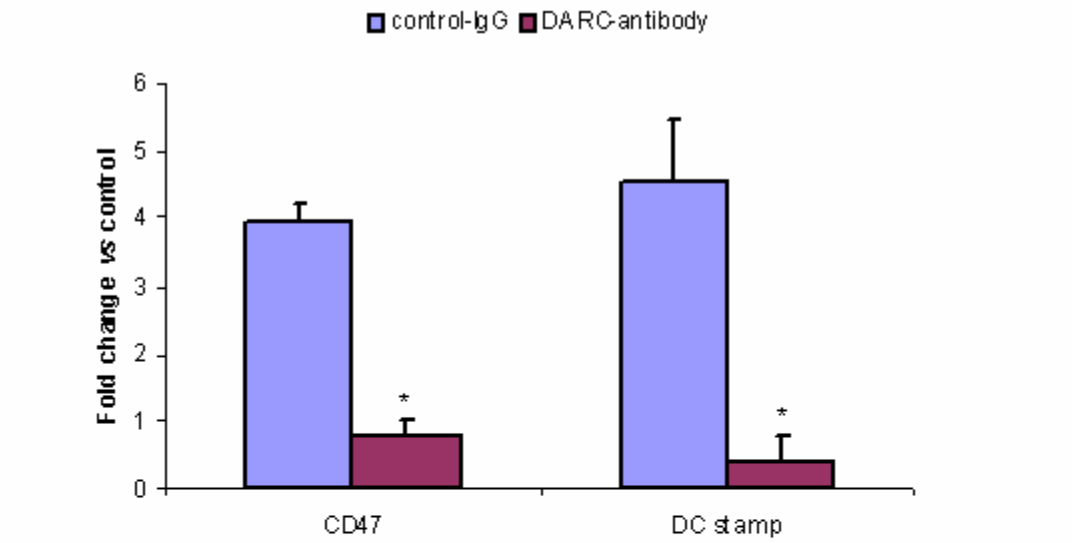

Figure 17. Response of Raw264.7 cells to RANKL in the presence or absence of *DARC* specific antibody. The cells were seeded at 2. 10^5 cells/well in 24-well plates and treated with 25 ng/ml RANKL and control IgG or *DARC*-antibody. The quantification of mRNAs was performed by real time RT-PCR after one day of treatment. The relative differences in expression between the groups were determined using cycle time (Ct) values as follows: The Ct values of the genes of interest were first normalized with 18S of the same sample; then the relative differences between the control cells and the cells treated with the RANKL in presence or absence of *DARC* antibody were calculated and expressed as relative increases or decreases (fold change). Values are Mean ± SEM of 3 replicate samples.*$P<0.05$ *vs* cells treated with control IgG.

j. Inhibition of RANKL-induced ERK phosphorylation by DARC-Ab

The importance of MAPK pathway in the fusion of osteoclast precursors is evident from the studies of Kim et al. (Kim et al., 2006) which have shown that treatment with MAPK inhibitors blocked fusion of human peripheral mononuclear cells to form multinucleated TRAP positive cells. We, therefore, tested if neutralization of DARC action influenced ERK pathway during fusion of osteoclast precursors. To this end, we first tested if components of MAPK pathway are activated in RAW264.7 cells that were stimulated with RANKL. We found that 15 minutes treatment with RANKL induced ERK1/2 phosphorylation. Interestingly, the activation of RANKL-induced ERK1/2 is reduced up on pre-treatment of RAW264.7 cells with DARC-ab (**Fig. 18**). Our proposed studies will examine if DARC is involved in chemokine-induced increase in ERK phosphorylation and the role of ERK

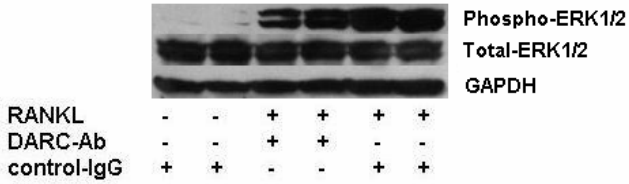

Figure 18. ERK activation after treatment with RANKL. Raw264.7 cells were treated with polyclonal goat *DARC*-Ab or control IgG for 10 minutes. Then, 25 ng/ml RANKL was added to the cells. 15 minutes thereafter, the cells were harvested, and immunoblot analysis was performed using 30 µg whole cell extract and antibodies specific for phosphorylated ERK1/2, total ERK and GAPDH.

pathway in the chemotaxis and fusion of osteoclast precursors.

In conclusion, using fine mapping and congenic sublines of mice we have narrowed down the size of the BMD1-2 locus to 4 Mb. Then, gene expression and SNPs analyses led to the identification of DARC and BMD1-2 candidate gene. In vitro studies as well as the characterization of DARC-KO mice provided evidence that DARC regulate BMD negatively by enhancing osteoclast differentiation (data published in Genome Research; Edderkaoui et al., 2007).

8) Gender specificity in chr 1

In our previous studies (above), using only female mice of B6.CAST-1 congenic sublines

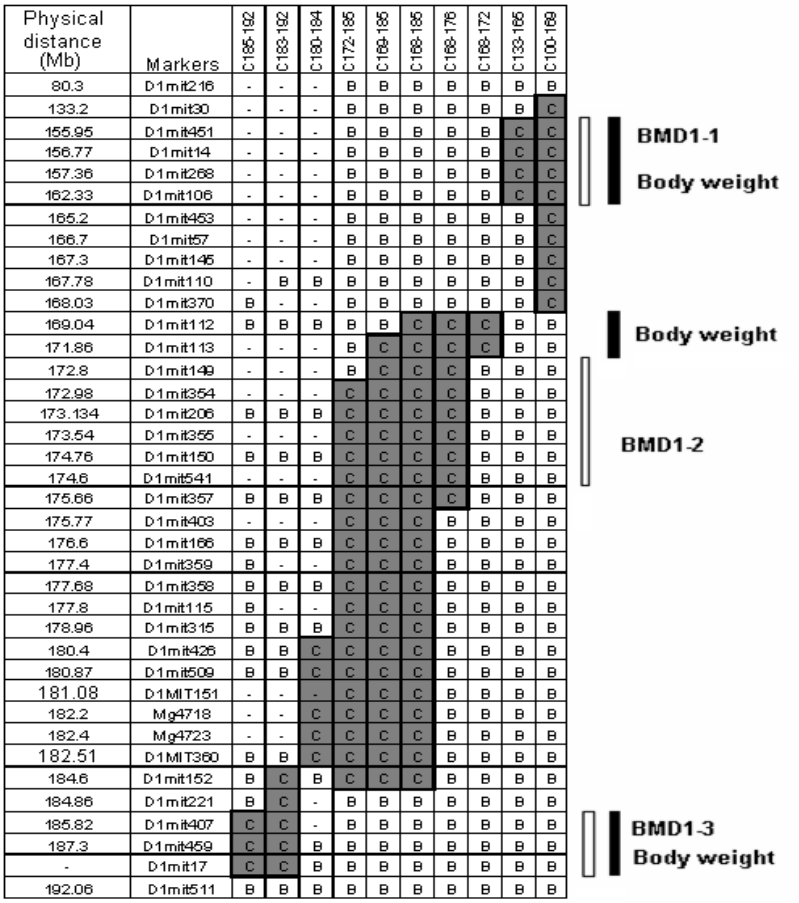

Physical distance (Mb)	Markers	C185-192	C183-192	C180-184	C172-185	C169-185	C168-185	C168-176	C168-172	C133-165	C100-169
80.3	D1mit216	-	-	-	B	B	B	B	B	B	B
133.2	D1mit30	-	-	-	B	B	B	B	B	B	C
155.95	D1mit451	-	-	-	B	B	B	B	B	C	C
156.77	D1mit14	-	-	-	B	B	B	B	B	C	C
157.36	D1mit268	-	-	-	B	B	B	B	B	C	C
162.33	D1mit106	-	-	-	B	B	B	B	B	C	C
165.2	D1mit453	-	-	-	B	B	B	B	B	B	C
166.7	D1mit57	-	-	-	B	B	B	B	B	B	C
167.3	D1mit145	-	-	-	B	B	B	B	B	B	C
167.78	D1mit110	-	B	B	B	B	B	B	B	B	C
168.03	D1mit370	B	-	-	B	B	B	B	B	B	C
169.04	D1mit112	B	B	B	B	B	C	C	C	B	B
171.86	D1mit113	-	-	-	B	C	C	C	C	B	B
172.8	D1mit149	-	-	-	B	C	C	C	B	B	B
172.98	D1mit354	-	-	-	C	C	C	C	B	B	B
173.134	D1mit206	B	B	B	C	C	C	C	B	B	B
173.54	D1mit355	-	-	-	C	C	C	C	B	B	B
174.76	D1mit150	B	B	B	C	C	C	C	B	B	B
174.6	D1mit541	-	-	-	C	C	C	C	B	B	B
175.66	D1mit357	B	B	B	C	C	C	C	B	B	B
175.77	D1mit403	-	-	-	C	C	C	B	B	B	B
176.6	D1mit166	B	B	B	C	C	C	B	B	B	B
177.4	D1mit359	B	-	-	C	C	C	B	B	B	B
177.68	D1mit358	B	B	B	C	C	C	B	B	B	B
177.8	D1mit115	B	-	-	C	C	C	B	B	B	B
178.96	D1mit315	B	B	B	C	C	C	B	B	B	B
180.4	D1mit426	B	B	C	C	C	C	B	B	B	B
180.87	D1mit509	B	B	C	C	C	C	B	B	B	B
181.08	D1MIT151	-	-	-	C	C	C	B	B	B	B
182.2	Mg4718	-	-	C	C	C	C	B	B	B	B
182.4	Mg4723	-	-	C	C	C	C	B	B	B	B
182.51	D1MIT360	B	B	C	C	C	C	B	B	B	B
184.6	D1mit152	B	C	B	C	C	C	B	B	B	B
184.86	D1mit221	B	C	-	B	B	B	B	B	B	B
185.82	D1mit407	C	C	-	B	B	B	B	B	B	B
187.3	D1mit459	C	C	B	B	B	B	B	B	B	B
-	D1mit17	C	C	B	B	B	B	B	B	B	B
192.06	D1mit511	B	B	B	B	B	B	B	B	B	B

BMD1-1
Body weight
Body weight
BMD1-2
BMD1-3
Body weight

Figure 19. The regions of CAST Chr 1 transferred from CAST mice onto B6 background, for the ten congenic sublines. The genotyping data for every marker are represented with "B" referring to homozygous b6/b6, "C" referring to cast/cast and "-" for data not available. The names of the subcongenic lines are at the top. We used a letter "C" followed by the proximal and distal limits of cast alleles carried by the congenic sublines in megabases. The yellow squares denote the CAST chromosomal regions carried by each congenic subline. The solid bars indicate the potential BMD QTLs and the open bar presents the QTL related with body weight and bone size traits. The polymorphic markers with their physical positions along Chr 1 are presented at the left. Open squares represent the BMD loci (BMD1-1, BMD1-2 and BMD1-3) and the black squares represent the body weight loci.

of mice, we have identified three genetic loci within the BMD QTL in Chr 1 that affect femur vBMD either positively (BMD1-1, BMD1-2) or negatively (BMD1-3). Furthermore, linkage analyses using B6.CAST-F2 female mice suggested the presence of an additional BMD locus in Chr 1 (BMD1-4). In order to further narrow down the size of the BMD loci in Chr 1 and allow for a successful screening of BMD candidate genes that exert gender specific effects, we have generated new congenic sublines of mice by backcrossing the C168-185 subline of mice (previously described in [above]) with B6 progenitors. The congenic sublines of mice used in this study are described in **figure 19.** To investigate the sex specificity of the vBMD, we analyzed the skeletal phenotypes of both males and females of the five congenic sublines of mice described in **figure 19**. Both the site specific mid-shaft (Mid-BMD) and the total femur BMD have been analyzed.

Among the female mice, the four congenic sublines of mice; C100-169, C168-176, C175-185 and C178-185 exhibited a significantly higher tot-BMD compared to B6 female mice. However, the C168-172 female mice did not show any significant difference in femur vBMD when compared with B6 female mice (**Fig.20 and 21**). The C100-169 subline which carries CAST alleles at the BMD1-1 locus exhibited a 4.2% increase of tot-BMD compared to B6 female mice ($P = 0.01$, **Fig. 20**) and C168-176 subline which underlies the BMD1-2 locus showed an 8.0% increase of tot-BMD ($P < 0.001$, **Fig. 20**). The C175-185 and C178-185 congenic sublines of female mice showed 5% ($P = 0.01$) and 4.3% ($P = 0.02$) increase of total BMD, respectively (**Fig. 20**). Thus, each of the congenics except C168-172 covers a chromosomal region containing a BMD locus.

To examine the sex specificity in Chr 1, the femur BMD of the male congenic sublines was analyzed. Similar to the females, C100-169 and C168-176 male mice showed significantly greater tot-BMD (3.5% and 5.2%, respectively) compared to B6 male mice (**Fig. 20**). In contrast, tot-BMD of femurs isolated from C175-185 and C178-185 male mice was not significantly different compared to the B6 male mice (**Fig. 20**). The effect of sex on tot-BMD for C175-185 and C178-185 congenic sublines of mice was confirmed by two-way-ANOVA ($P < 0.05$, **table 9**).

The analyses of mid-BMD showed that in addition to gender specific differences, there were also site specific differences among different congenic sublines of mice. C100-169 and C168-176 female mice showed 10.0% and 6.8% increase of mid-BMD compared to B6 female mice, respectively ($P < 0.001$, **Fig. 21**). However, C100-169 male mice showed only 4% increase of mid-BMD compared to B6 male mice ($P = 0.048$), and C168-176 male mice did not show any significant difference with B6 male mice ($P = 1.0$).

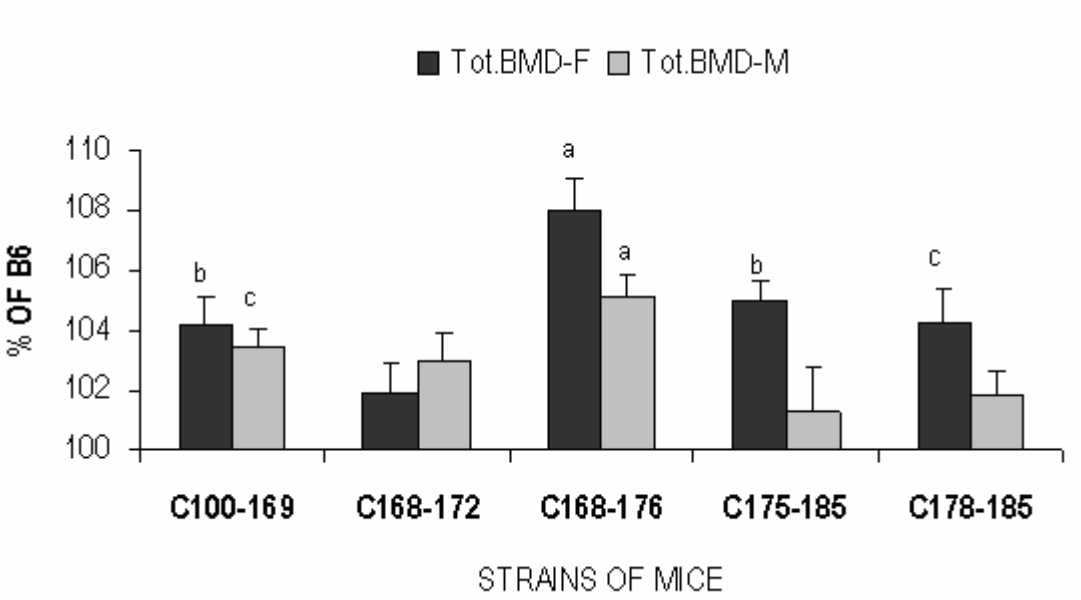

Figure 20. Total Femoral vBMD of the five congenic sublines compared to gender-matched B6 mice from both male and female mice. The data are expressed as a percentage of the gender-matched B6 mice. Two-way ANOVA was performed to determine the significant differences between each congenic subline and the gender-matched B6 mice. $^{a}P < 0.01$, $^{b}P = 0.01$, $0.01 < {}^{c}P < 0.05$ after correction with post-hoc Bonferroni test. Tot.BMD-F; refers to total femur vBMD in female mice, Tot. BMD-M; refers to total femur vBMD in male mice.

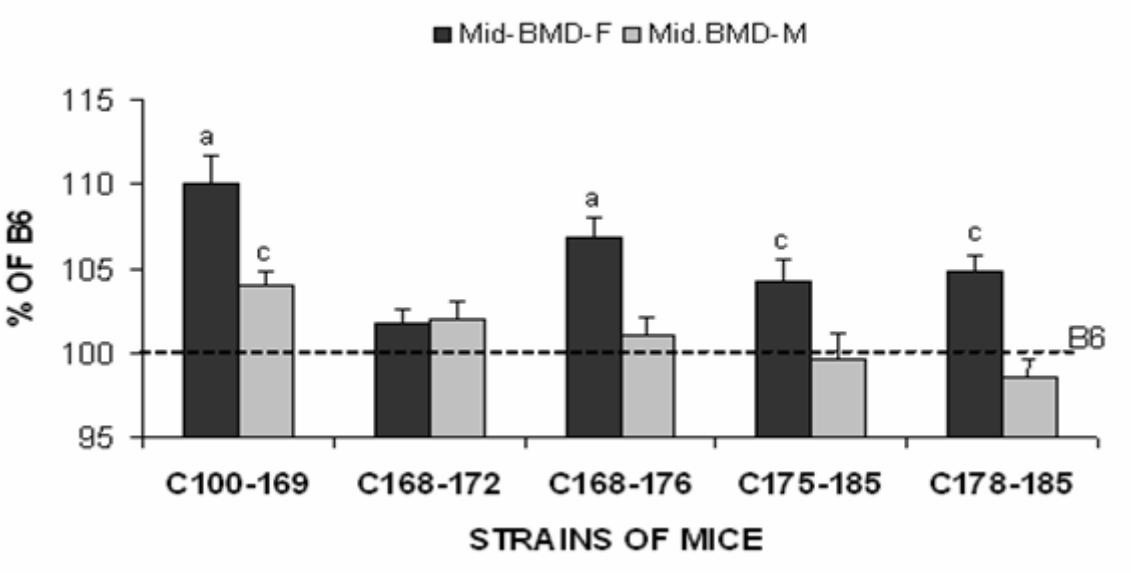

Figure 21. Femur mid-diaphyseal vBMD of the five congenic subline of mice compared to gender-matched B6 control mice. The data are expressed as a percentage of the gender-matched B6 mice. Two-way ANOVA was performed to determine the significant differences between each congenic subline and the gender-matched B6 mice. $^{a}P < 0.01$, $^{b}P = 0.01$, $0.01 < {}^{c}P < 0.05$ after correction with post-hoc Bonferroni test.mid.BMD-F; refers to femur mid-diaphysis vBMD in female mice, and mid.BMD-M refers to femur mid-diaphysis vBMD in male mice.

The two-way ANOVA (**table 9**) confirmed the sex-specificity of femur mid-BMD phenotype for congenic sublines C100-169 (P = 0.0005) and C168-176 (P = 0.0002). Furthermore, female mice of both C175-185 and C178-185 sublines showed significantly greater mid-BMD compared to B6 female mice (4.2% and 4.8%, respectively), while males from C175-185 and C178-185 sublines of mice did not show any significant difference in mid-BMD when compared with B6 male mice.

We have also evaluated the body weight and femur length of these congenic sublines to determine if these two parameters co-segregate with femur BMD and to test for sex specificity (**Fig. 22**). Among all congenic sublines of female mice C100-169 showed 5% smaller body weight compared to B6 female mice (P = 0.045) and C168-172 subline exhibited a 7.5% reduced body weight compared to female B6 control mice (P = 0.03), and a slight (3%) but not significant decrease of femur length compared to gender-matched B6 mice. Body weight and femur length in the other sublines of female mice were similar to B6 female mice. However, among male mice C100-169, C168-172 and C168-176 sublines showed a significant decrease of body weight compared to age and gender-matched B6 control mice (9%, 6.2% and 6%, respectively). Femur length was slightly reduced in C100-169 and C168-172 male mice compared with B6 male mice. 2-way ANOVA test confirmed the sex specificity of body weight showed by C168-176 (F = 12.8, P = 0.0007) but not C168-172 (P = 0.6) or C100-169 (P = 0.5) sublines of mice.

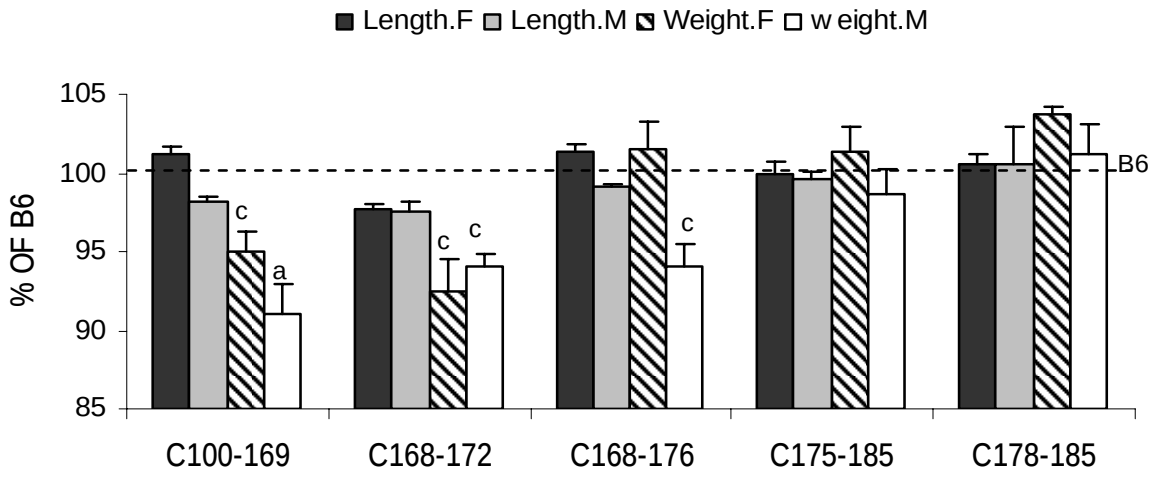

Figure 22. Femur length and body weight from the five congenic sublines and compared to gender-matched B6 mice. Length-F is femur length of female mice and Length-M: refers to femur length of male mice. Weight-F: is body weight of female mice Weight-M: refers to body weight of male mice. Body weight and femur length are expressed as a percentage of gender-matched B6 mice. $^{a}P < 0.01$, $0.01 < {}^{c}P < 0.05$ after correction with post-hoc Bonferroni test.

Table 9. Univariate tests of significance for the sex effect on femur vBMD.

Strains	Tot-BMD		Mid-BMD	
	F	*P* value	F	*P* value
C100-169 (*BMD1-1*)	0.00	0.87	**13.45**	**0.0005**
C168-172	1.60	0.21	0.00	0.84
C168-176 (*BMD1-2*)	2.67	0.11	**16.49**	**0.0002**
C175-185 (*BMD1-4*)	**12.4**	**0.0009**	**6.82**	**0.011**
C178-185 (*BMD1-4*)	**4.00**	**0.046**	**27.4**	**0.000003**

Two-way ANOVA was performed for each congenic subline of mice after normalization by mean values from B6 control mice, sex and strains were taken as independent factors. F and P values are given for the interaction term. Significant differences between sexes for a given strain are marked in bold characters. The name the BMD locus carried by each congenic subline is marked between parentheses.

In conclusion, body weight and the skeletal phenotype of five B6-CAST congenic sublines of mice provided evidence for the presence of the BMD1-4 locus at 178-180 Mb in chromosome 1. The BMD1-4 locus imparts a gender-specific effect on both femur mid-shaft and tot-BMD. However, femur mid-BMD but not tot-BMD was significantly affected by the gender on C1681-76 subline which carried BMD1-2 locus. Moreover, a body weight genetic locus was found at 168-172 Mb from the centromere of Chr 1, the interaction of this locus with other genes in Chr 1 seems to be sex dependent.

9) A BMD QTL in Chromosome 17 with Pleiotropic Effects on Multiple Phenotypes

a) Bone size and body weight QTL in chr 17

In addition of chr 1 BMD QTLs, we have identified BMD QTL in chr 17 with a high LOD score (7.5) in the cross MRL x SJL (**Fig 5**), this QTL designated as Fbs17P6.6L8.4 also affects femur breaking strength (FBS). Fbs17P6.6L8.4 is one of the largest QTL for FBS and has not been previously reported to have association with bone related phenotypes. MQM mapping revealed that this QTL also influenced other bone-related phenotypes and body weight. In addition to having a strong linkage with FBS at a lod score of 8.5, the QTL has a significant association with femur BMD and body weight (**Fig. 23**), and a suggestive association with femur length. Variation contributed by this QTL varies from 8.5% to 2.5% with an average of 5.6%. These data predict that the gene underlying this QTL may have a general regulatory role on multiple bone metabolism pathways. In this regard, one candidate gene localized right under the peak of the QTL (6.5 cM), encoding mitogen activated protein kinase-4 (*MAP3K4*), was brought to our attention. The mitogen activated protein kinases (MAPKs) represent one of the important signaling mechanisms in response to environmental stimuli (Chan-Hui et al., 1998). MAPKs are phosphorylated and activated by MAPK kinases (MAPKKs), which in turn are phosphorylated and activated by MAPKK kinases. Thus, it is biologically possible for MAP3K4 to affect several bone metabolic pathways through signaling signal transduction pathways.

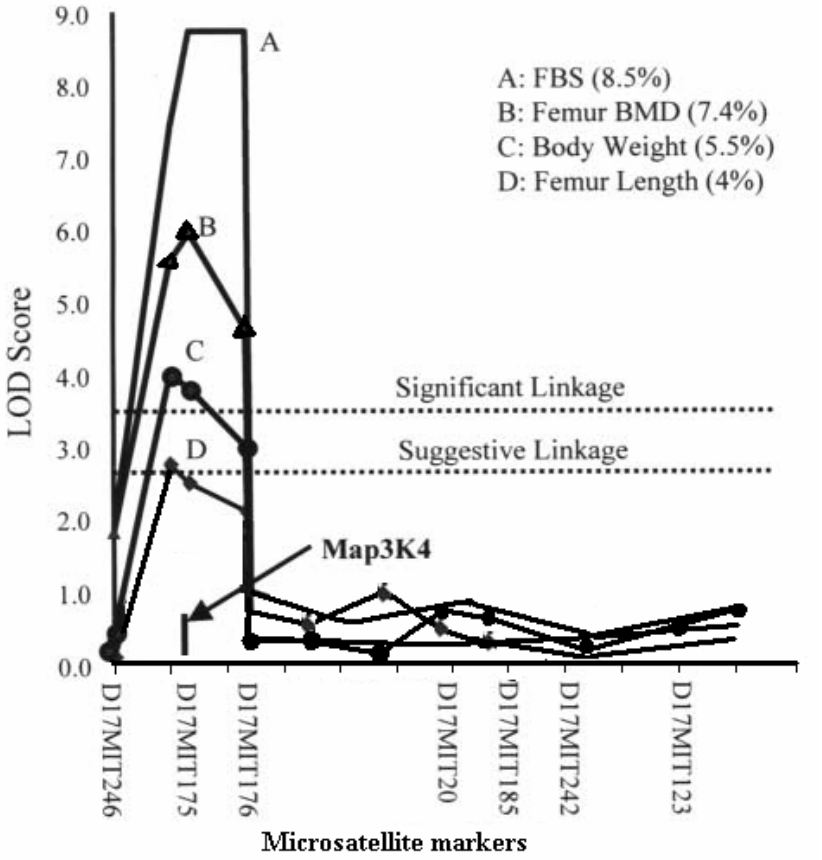

Figure. 23. A novel QTL, Fbs17P6.6L8.4, has pleiotropic effects on multiple bone related phenotypes and body weight. Dashed horizontal lines represent significant and suggestive lod thresholds determined by permutation test. Numbers in parentheses represent the percentage of F2 variance explained by this QTL. The position of a candidate gene is marked (Map2K4).

b) Fine mapping chr 17 BMD QTL

Our previous QTL study of the MRL/MpJ and SJL/J cross was done with only female mice (Masinde et al., 2002). The first objective of the current study was to verify that the same QTL on chromosome 17 existed in the male mice of the MRL/Map X SJL/J cross. The second objective was to fine-map this QTL using the male F2 mice. The current study is only the first stage towards the identification of chromosome 17 BMD genes. The second stage is to breed additional female F2 mice in MRL/MpJ X SJL/J so that we can perform phenotype and genotype analysis in an approximate total of 2000 MRL X SJL F2 mice. Hopefully, all these steps will significantly narrow down the QTL region on chromosome 17, so that a reduced number of candidate genes can be examined to determined which candidate gene is responsible for the femur and total body BMD QTL on chromosome 17.

The 633 female F2 mice of MRL X SJL were used earlier (Li et al., 2002, Masinde et al., 2002). For this study, four weeks old mice of inbred strains: MRL/MpJ (MRL), and SJL/J (SJL) were obtained from the Jackson Laboratory (Bar Harbor, Maine). Additional 474 F2 male mice of MRL and SJL were generated at the Animal Research Facility, J.L. Pettis Vaterans Administration Memorial Medical Center. A PIXIMUS densitometer (LUNAR Corporation, Madison, WI) was used for the measurement of the whole body BMD on the 7 weeks old live animals. At the same time, body weight was recorded for each animal. Then the F2 male mice were killed. Liver was isolated for DNA extraction. Femurs were isolated from both legs. Femur BMD and other femur parameters were determined from the mid-shaft portion of a single femur (usually right femur) using pQCT (Stratec XCT 960 M, Norland Medical System, Ft. Atkinson, WI).

Table 10. **Markers used in fine-mapping the BMD QTL in chromosome 17**

Number	Name	Distance (Mb)	Distance (cM)
1	D17Mit268	3.619	2.7
2	D17Mit246	7.868	0
3	D17Mit113	11.388	2.2
4	D17Mit61	29.238	6.6
5	D17Mit81	29.510	5.5
6	D17Mit175	30.443	6.6
7	D17Mit214	32.835	9.8
8	D17Mit83	33.453	8.7
9	D17Mit64	37.027	10.9
10	D17Mit176	40.888	12
11	D17Mit269	42.697	26.7
12	D17Mit35	43.700	14.2
13	D17Mit250	45.625	19.7
14	D17Mit68	45.735	19.7
15	D17Mit115	45.740	18.6
16	D17Mit177	46.733	19.7
17	D17Mit270	48.700	32.2
18	D17Mit139	50.841	25.1
19	D17Mit20	55.558	29.5
20	D17Mit152	63.696	32.8
21	D17Mit185	66.877	35

The genotyping methods were described previously (Li et al. 2002; Masinde et al., 2002). Twenty one chromosome 17 genetic markers were genotyped for the F2 male mice of MRL X SJL (Table 10). The average distance between markers was 3.16 Mb or 1.74 cM. This covers the 3.62-66.88 Mb QTL region out of 92 Mb for the entire chromosome 17. Genotype data was analyzed using MapQTL (5.0) (Van Ooijien, 2004). MapQTL's interval mapping option was used.

Permutation test of MapQTL was used to obtain the LOD scores for the significant thresholds at 0.05 and 0.01 probability levels. For the whole body parameters such as body BMD and body bone area obtained from PIXIMUS, the size of the animal was an influencing factor. Therefore, these parameters were adjusted by body weight. Simple linear regression analysis

was carried out using STATISTICA (Release 7, StatSoft, Inc. Tulsa, OK). The adjusted parameters were the residuals of the linear regression.

Although the male F2 mice of MRL X SJL were much bigger (average weight of 32.11g at 7 weeks of age compared to 24.26g for the females), the interval mapping results show that the same chromosome 17 QTL also existed in the male mice. The LOD score was 4.03 ($P < 0.01$) at the position of 45.70 Mb for femur BMD (**Figure 24**. **Table 11**). Because the number of male mice in the current study was much smaller (only 474 compared to 633 female mice), this LOD score is comparable to the 5.8 LOD score obtained earlier from the female mice (Masinde et al., 2002). At its peak, this QTL explained about 3.9% of the F2 femur BMD variance. Much high LOD score was obtained for the whole body BMD. The LOD score was 5.66 ($P < 0.01$) (**Figure 24**, **Table 11**). It explained about 6.1% of the body BMD's F2 variance. It is noticed that there is also a body weight QTL at roughly the same position (47.74 MB) (**Figure 24**, **Table 11**). The LOD score was 5.08 ($P < 0.01$). Because there is a body weight QTL, and because the whole body BMD is influenced by the size of the animal, we have used the adjusted whole body BMD in the QTL analysis, which had taken body weight out of consideration. Therefore, we can conclude that the body BMD QTL on chromosome 17 is independent of the body weight QTL at the same location. In fact, the LOD scores before and after the body weight adjustment were very similar, again to confirm the finding that the BMD QTL was independent of the body size QTL.

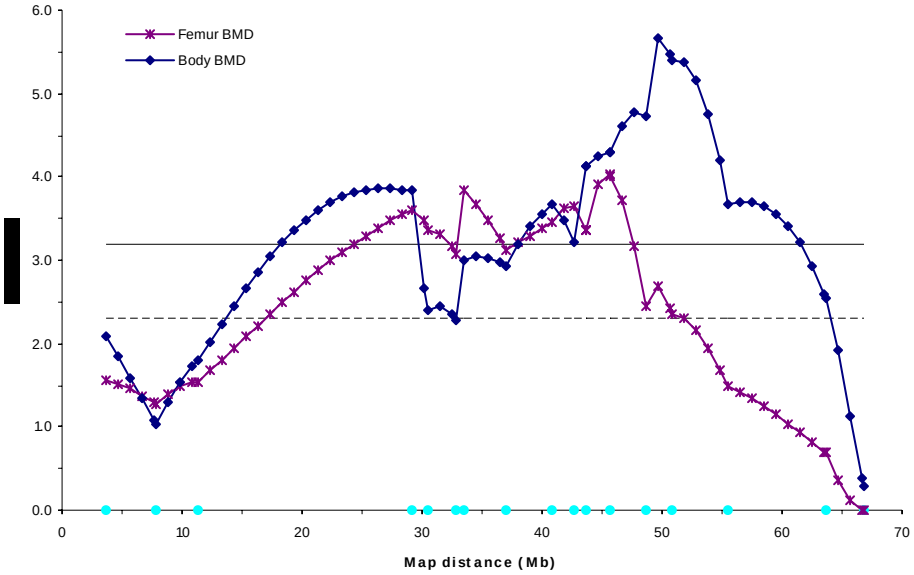

Figure 24. LOD scores of the chromosome 17 QTL for whole body and femur BMD. The whole body BMD was adjusted for body weight using the residuals of the simple linear regression analysis. The filled circles on the X-axis indicate genotyped marker positions.

Table 11. **Chromosome 17 QTL for body weight and different bone phenotypes in MRL X SJL F2 male mice**

Trait	Peak position (Mb)	Nearest marker	LOD score	Significance level	Variance explained (%)	One LOD interval (Mb)
Body weight	47.74	D17Mit270	5.08	0.01	5.3	8.01
Adjusted body BMD	49.70	D17Mit20	5.66	0.01	6.1	8.10
Adjusted body bone area	40.89	D17Mit176	2.82	0.05	2.7	6.66
Femur BMD	45.70	D17Mit115	4.03	0.01	3.9	26.31
Femur length	44.70	D17Mit35	2.84	0.05	2.9	18.39
Femur PC	45.74	D17M115	2.50	0.05	1.6	17.81

Besides bone density, there were also QTLs for bone size on chromosome 17. The LOD scores of the adjusted body bone area obtained from PIXIMUS, femur length and femur periosteal circumference obtained from pQCT were all significant at $p < 0.05$ level (2.82, 2.84 and 2.50, respectively) (**Table 11**). The peak positions were all around 41 to 46 Mb, very similar to the 46 to 50 Mb positions for femur and body BMD QTL.

In conclusion, we have narrowed down the size of the BMD QTL in chr 17 from 63 Mb to 26 Mb. This QTL was shown to be extreme pleiotropic on bone and body size phenotypes in both male and female mice (**Li et al., 2002; Yu et al., 2008**)

10) Additional genetic loci that affect bone parameters

In order to identify the chromosome regions that may harbor wound healing genes, we have generated and used the cross MRL X CAST. We took advantage of the availability of the F2 mice of this cross, and carried out QTL mapping of bone density. The rationale of using this cross is that most previous studies to identify loci involved in bone mineral density (BMD) regulation have used inbred strains with high and low BMD in generating F2 mice. However, differences in BMD may not be a requirement in selecting parental strains for BMD QTL studies. In this study, we intended to identify novel QTL using a cross of two strains, MRL and CAST, both of which exhibit relatively high BMD when compared to previously used strains. In addition, CAST was genetically distinct and useful in identifying QTL genes. As mentioned before, for this cross we generated 328 MRL X CAST F2 mice of both sexes. Then we measured femur BMD and periosteal circumference (PC) using peripheral quantitative computed tomography (pQCT). Whole-genome genotyping was performed with 86 microsatellite markers. We have published the results of this study in Calcified Tissue International Journal (Yu, Mohan et al. 2007). Briefly, a new BMD QTL on chromosome 10 and another suggestive one on chromosome 15 were identified from the cross between the two high bone density inbred strains of mice MRL x CAST (**Figure 25**). A significant femur periosteal circumference QTL identified on chromosome 9 and a suggestive one on chromosome 2 were similar to those detected in MRL X SJL. QTLs were also identified for other femur and forearm bone density and bone size phenotypes, some of which were co-localized within the same chromosomal positions as those for femur BMD and femur PC. This study demonstrates the utility of crosses involving inbred strains of mice which exhibit a similar phenotype in QTL identification (Yu et al., 2007).

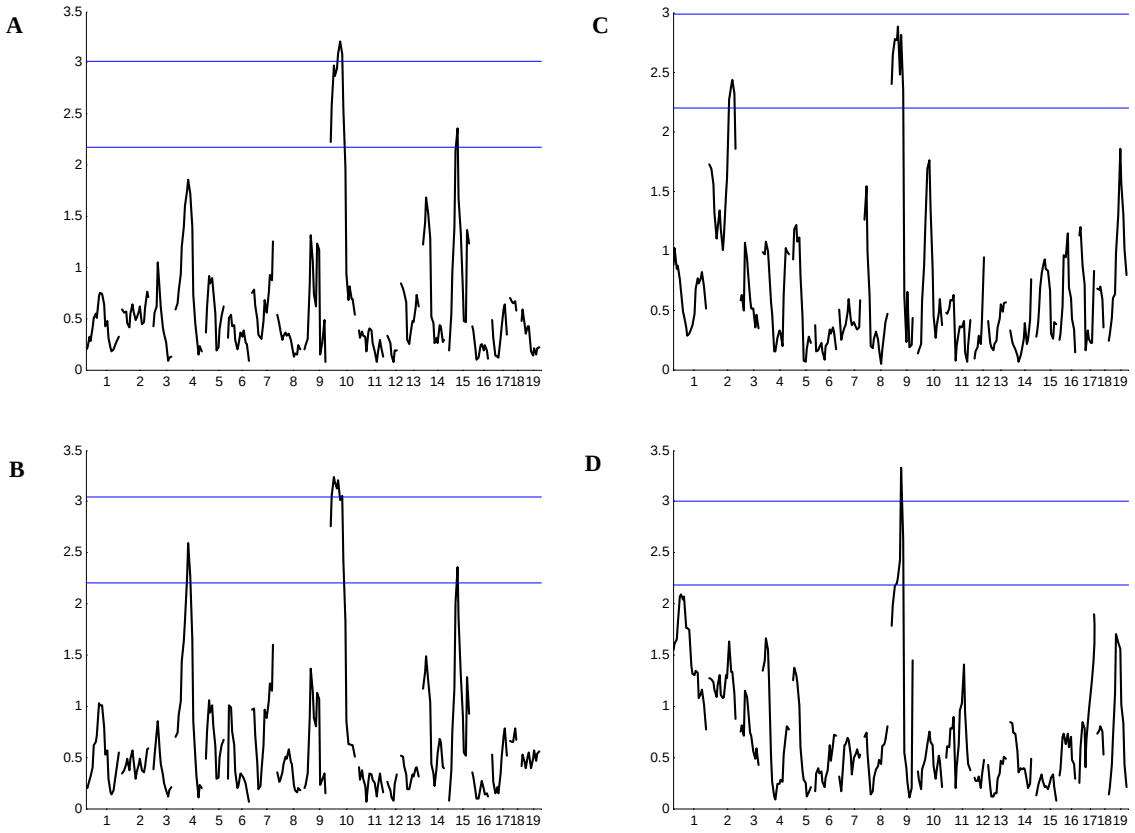

Figure 25. LOD score graphs of the genome wide scans for femur BMD and femur PC obtained from MRL X CAST F2 using Pseudomarker (MAINSCAN function). The x axis of the graphs shows the map position in chromosome numbers. The y axis shows the LOD score. The upper and lower horizontal lines indicate the LOD thresholds for significant and suggestive significance at $P < 0.05$ and 0.33, respectively. **A)** Femur BMD analyzed without covariates. **B)** Femur BMD analyzed with body weight as an additive covariate. **C)** Femur PC analyzed without covariates. **D)** Femur PC analyzed with body weight as an additive covariate.

3) KEY RESEARCH ACCOMPLISHMENTS

- We have confirmed the effect of the chr 1 QTL on femur bone mineral density
- Our in-house microarray data provided evidence that the difference in BMD between B6 and CAST mice is mostly due to high bone turn-over in the low BMD B6 mice compared to the high BMD CAST mice.
- We have generated new B6.CAST subcongenic mice and measured their skeletal phenotype, which provided evidence for the presence of four BMD loci within the initial BMD QTL in chromosome 1.
- We have narrowed down the size of the BMD1-2 QTL to 4 Mb
- We have identified DARC as a BMD1-2 QTL gene which regulates BMD negatively
- We demonstrated the effect of Duffy gene on osteoclastogenesis.
- We have identified gender specific BMD in chr 1
- We have narrowed down the size of the gender specific BMD1-4 to 2 Mb
- We have narrowed down the size of the pleiotropic QTL in chr 17 from 63 Mb to 26 Mb.

- We have identified new genetic loci that regulate bone mineral density

4) REPORTABLE OUTCOMES

a) Publications:

1- Li X, Mohan S, Gu W, Wergedal J, Baylink DJ. Quantitative assessment of forearm muscle size, forelimb grip strength, forearm bone mineral density and forearm bone size in determining humerus breaking strength in ten inbred strains of mice. Calcified Tissue Int 68:365-369, 2001.
2- Masinde GL, Li X, Gu W, Wergedal J, Mohan S, Baylink DJ. Quantitative trait loci for bone density in mice: The genes determining total skeletal density and femur density show little overlap in F2 mice. Calcified Tissue Int 71:421-428, 2002.
3- Li X, Masinde G, Gu W, Wergedal J, Mohan S, Baylink DJ. Genetic dissection of femur breaking strength in a large population (MRL/MpJ X SJL/J) of F2 mice: Single QTL Effects, Epitasis, and Pleiotrophy. Genomics 79:734-740, 2002.
4- Li X, Masinde G, Gu W, Davidson H, Mohan S, Baylink DJ. Chromosomal regions harboring genes for the work to femur failure in mice. Functional and Integrative Genomics 1:367-374, 2002.
5- Gu WK, Li XM, Edderkaoui B, Strong DD, Lau KH, Beamer WG, Donahue LR, Mohan S, Baylink DJ., Construction of a BAC contig for a 3 cM biologically significant region of mouse chromosome 1. Genetica;114(1):1-9 (2002).
6- Gu W, Li X, Lau KH, Edderkaoui B, Donahae LR, Rosen CJ, Beamer WG, Shultz KL, Srivastava A, Mohan S, Baylink DJ. Gene expression between a congenic strain that contains a quantitative trait locus of high bone density from CAST/EiJ and its wild-type strain C57BL/6J. Funct Integr Genomics; 6:375-86 (2002).
7- Masinde, GL, Wergedal, J, Davidson, H., Li, X, Mohan, S, Baylink, DJ. Quantitative trait loci for periosteal circumference (PC): Identification of single loci and epistatic effects in F2 MRL/SJL mice. Bone 32:554-60, 2003.
8- W.K. Gu, X.M. Li, B.A. Roe, K.H.W. Lau, B. Edderkaoui, S. Mohan, and D.J. Baylink. Application of Genomic Resources and Gene Expression Profiles to Identify Genes That Regulate Bone Density. Current Genomics 4(1), 63-74 (2003).
9- Bouchra Edderkaoui, David J. Baylink, Wesley G. Beamer, Jon E. Wergedal, Nancy R. Dunn, Kathryn L. Shultz and Subburaman Mohan. Multiple Genetic Loci from CAST/EiJ Chromosome 1 Affect vBMD Either Positively or Negatively in a C57BL/6J Background. J. Bone Miner. Research, 21(1): 97-104. (2006)
10- Masinde GL, Li R, Nguyen B, Yu H, Srivastava AK, Edderkaoui B, Wergedal JE, Baylink DJ, Mohan S. New quantitative trait loci (QTL) that regulate wound healing in an intercross progeny from DBA/1J and 129X1/SvJ inbred strains of mice. Funct Integr Genomics 6: 157–163 (2006)
11- Yu H, Mohan S, Edderkaoui B, Masinde GL, Davidson HM, Wergedal JE, Beamer WG, Baylink DJ. Detecting Novel Bone Density and Bone Size Quantitative Trait Loci Using a Cross of MRL/MpJ and CAST/EiJ Inbred Mice. Calcif Tissue Int. 80(2):103-10. (2007)
12- Edderkaoui B, Baylink DJ, Beamer WG, Wergedal JE, Porte R, Chaudhuri A, and Mohan S. Identification of mouse Duffy Antigen Receptor for Chemokines (Darc) as a BMD QTL gene. Genome Res.17(5):577-85 (2007)

13- Edderkaoui B, Baylink DJ, Beamer WG, Wergedal JE, and Mohan S. Genetic regulation of femur bone mineral density: Complexity of Sex effect in chromosome 1 revealed by subcongenic line of mice. Bone. 41(3):340-5 (2007)

14- Yu H, Edderkaoui B, Cortez A, Davidson HM, Wergedal JE, Baylink DJ, Mohan S.Mapping of the chromosome 17 BMD QTL in the F(2) male mice of MRL/MpJ x SJL/J.Genetica. 2008 Mar 11

b) Presentations in Scientific Meetings:

1. Gu, W-K, M Hellan, XM Li, MH-C Sheng, WG Beamer, JE Wergedal, K-HW Lau, S Mohan and DJ Baylink. Evaluation of the effect of a quantitative trait locus (QTL) on peak bone mineral density (BMD) using congenic mice. International Conference on Progress in Bone and Mineral Research, Vienna, Austria. (November 30 – December 2, 2000).
2. W-K. Gu, B. Edderkaoui W.G. Beamer, X. Li, M.H-C. Sheng, J. E. Wergedal, M. Hellan, K-H.W. Lau, L.R. Donahue K. L. Shultz, C.J. Rosen, S. Mohan, and D.J. Baylink. The *cast* allele of mouse Chr 1 QTL acts in a gender-dependent, differential activating manner to increase BMD. Fourth Annual Research Symposium at LLU. 2001.
3. Gu, X. Li, K. H. W. Lau, B. Edderkaoui, L. R. Donahue, C. J. Rosen, W. G. Beamer, K. L. Shultz, A. K. Srivastava, S. Mohan, D. J. Baylink. Differential Gene Expression between a congenic strain that contains quantitative trait loci (QTL) of high bone density from CAST/EiJ and its wild type strain C57BL/6J. Plenary Poster at the 23rd Annual meeting of the American Society for Bone and Mineral Research. Phoenix, Arizona, USA. (October 12-16, 2001). (Suppl 1): 16 F109.
4. Bouchra Edderkaoui, Mohan Subburaman, Wergedal Jon, Nancy Dunn, Wesley G. Beamer, Leah R. Donahue, and David J. Baylink. Three closely mapped genetic loci in chromosome 1 acting via different mechanisms contribute to BMD phenotype. Oral presentation at the 26th Annual Meeting of the American Society for Bone and Mineral Research, Seattle, Washington, USA. (October 1-5, 2004).
5. H. Yu, S. Mohan, B. Edderkaoui, G. Masinde, J. E. Wergedal, W. Beamer, D. J. Baylink. Detecting BMD and Bone Size QTL Using a Cross of MRL and CAST Inbred Strains of Mice Both of Which Exhibit High BMD. Poster at the 27th Annual Meeting of the American Society for Bone and Mineral Research at Nashville, Tennessee, USA. (Sep.23-27, 2005).
6. B. Edderkaoui, D. J. Baylink, W. G. Beamer, K. L. Shultz, N. R. Dunn, J. E. Wergedal, and S. Mohan. CAST chromosome 1 QTL is complex and contains three BMD loci and one bone size locus: Evidence from subcongenic lines. Plenary Poster at the 27th Annual Meeting of the American Society for Bone and Mineral Research at Nashville, Tennessee, USA. (Sep.23-27, 2005).
7. H Yu, S Mohan, B Edderkaoui, GL Masinde, H Davidson, JE Wergedal, WG Beamer, DJ Baylink. Detecting BMD and bone size QTL using a cross of MRL and CAST inbred strains of mice both of which exhibit high BMD. Poster at the 27th Annual Meeting of the American Society for Bone and Mineral Research at Nashville, Tennessee, USA. (Sep.23-27, 2005).
8. H Yu, DJ Baylink, HM Davidson, GL Masinde, B Edderkaoui, JE Wergedal, S Mohan. Chromosome 9 MRL-SJL congenic mice reveal sex-biased regulation of bone size. Poster presentation at the 28th Annual meeting of the American Society for Bone and Mineral Research, Philadelphia, USA, Sep. 15-19, 2006.
9. Edderkaoui B, Baylink DJ, Beamer WG, Shultz KL, Wergedal JE, and Mohan S. Congenic Mice Reveal Gender Specificity of Femoral BMD in Chromosome 1. Accepted for Poster

presentation at the 28th Annual meeting of the American Society for Bone and Mineral Research, Philadelphia, USA, Sep. 15-19, 2006.

10. Edderkaoui B, Baylink DJ, Beamer WG, Wergedal JE, Porte R, Chaudhuri A, and Mohan S. Identification of Duffy blood group antigen as a BMD QTL gene, accepted for Oral presentation at the 28th Annual meeting of the American Society for Bone and Mineral Research, Philadelphia, USA, Sep. 15-19, 2006.

5) CONCLUSIONS

a) The initial BMD QTL in chr 1 is the result of four BMD loci.
b) Duffy knockout mice exhibits, in vivo and in vitro, a phenotype similar to that of B6-CAST subcongenic mice that carries DARC from CAST, which confirmed the effect of Duffy gene on BMD variation and osteoclastogenesis
c) The initial BMD QTL in chromosome 1 carries gender specific BMD loci.
d) In addition of BMD loci, chromosome 1 carries at least two body weight QTLs
e) BMD loci can regulate both bone mineral density and bone breaking strength
f) In addition of its effect on BMD, the QTL in chromosome 17 also regulates bone size and body weight.
g) Our data demonstrate for the first time that genetic variations in DARC gene regulate peak BMD by influencing osteoclast bone resorption.

6) REFERENCES

- Simonelli C. (2007) Medicare Cuts DXA to the Bone. Minn Med. 90(6):34-5.

- Shen H, Recker RR, Deng HW. (2003) Molecular and genetic mechanisms of osteoporosis: implication for treatment. Curr Mol Med. 3:737–757.

- Ioannidis JP, Ng MY, Sham PC, Zintzaras E, Lewis CM, Deng HW, Econs MJ, Karasik D, Devoto M, Kammerer CM, Spector T, Andrew T, Cupples LA, Duncan EL, Foroud T, Kiel DP, Koller D, Langdahl B, Mitchell BD, Peacock M, Recker R, Shen H, Sol-Church K, Spotila LD, Uitterlinden AG, Wilson SG, Kung AW, Ralston SH. (2007) Meta-analysis of genome-wide scans provides evidence for sex- and site-specific regulation of bone mass. J Bone Miner Res. 22:173–183.

- Kaye M, Kusy RP (1995) Genetic lineage, bone mass, and physical activity in mice. Bone 17:131–135

- Jamsa T, Jalovaara P, Peng Z, Vaananen HK, Tuukkanen J (1998) Comparison of three-point bending test and peripheral quantitative computed tomography analysis in the evaluation of the strength of mouse femur and tibia. Bone 23:155–161

- Beamer WG, Shultz KL, Churchill GA, Frankel WN, Baylink DJ, Rosen CJ, Donahue LR (1999) Quantitative trait loci for bone density in C57BL/6J and CAST/EiJ inbred mice. Mamm Genome **10**:1043-1049.

- Beamer WG, Shultz KL, Donahue LR, Churchill GA, Sen S, Wergedal JR, Baylink DJ, Rosen CJ (2001) Quantitative trait loci for femoral and lumbar vertebral bone mineral density in C57BL/6J and C3H/HeJ inbred strains of mice. J Bone Miner Res **16**:1195-1206.

- Devoto M, Shimoya K, Caminis J, Ott J, Tenenhouse A, Whyte MP, Sereda L, Hall S, Considine E, Williams CJ, Tromp G, Kuivaniemi H, Ala-Kokko L, Prockop DJ, Spotila LD (1998) First-stage autosomal genome screen in extended pedigrees suggests genes predisposing to low bone mineral density on chromosomes 1p, 2p and 4q. Eur J Hum Genet **6**:151-7.

- Niu T, Chen C, Cordell H, Yang J, Wang B, Wang Z, Fang Z, Schork NJ, Rosen CJ, Xu X (1999) A genome-wide scan for loci linked to forearm bone mineral density. Hum Genet **104**:226-233.

- Shen H, Zhang YY, Long JR, Xu FH, Liu YZ, Xiao P, Zhao LJ, Xiong DH, Liu YJ, Dvornyk V, Rocha-Sanchez S, Liu PY, Li JL, Conway T, Davies KM, Recker RR, Deng HW (2004) A genome-wide linkage scan for bone mineral density in an extended sample: evidence for linkage on 11q23 and Xq27. J Med Genet **41**:743-51.

- Klein RF, Mitchell SR, Phillips TJ, Belknap JK, Orwoll ES (1998) Quantitative trait loci affecting peak bone mineral density in mice. J Bone Miner Res **13**:1648-1656.

- Bouxsein ML, Uchiyama T, Rosen CJ, Shultz KL, Donahue LR, Turner CH, Sen S, Churchill GA, Muller R, Beamer WG (2004) Mapping quantitative trait loci for vertebral trabecular bone volume fraction and microarchitecture in mice. J Bone Miner Res **19**:587-599.

- Klein RF, Carlos AS, Vartanian KA, Chambers VK, Turner EJ, Phillips TJ, Belknap JK, Orwoll ES (2001) Confirmation and fine mapping of chromosomal regions influencing peak bone mass in mice. J Bone Miner Res **16**:1953-61.

- Masinde GL, Li X, Gu W, Wergedal J, Mohan S, Baylink DJ 2002 Quantitative trait loci for bone density in mice: the genes determining total skeletal density and femur density show little overlap in F2 mice. Calcif Tissue Int **71**:421-428.

- Arden NK, Baker J, Hogg C, Baan K, Spector TD (1996) The heritability of bone mineral density, ultrasound of the calcaneus and hip axis length: A study of postmenopausal twins. J Bone Miner Res 11:530–534.

- Harris M, Nguyen TV, Howard GM, Kelly PJ, Eisman JA (1998) Genetic and environmental correlations between bone formation and bone mineral density: A twin study. Bone 22:141–145.

- Deng HW, Chen WM, Recker S, Stegman MR, Li JL, Davies KM, Zhou Y, Deng H, Heaney R, Recker RR (2000) Genetic determination of Colles' fracture and differential bone mass in women with and without Colles' fracture. J Bone Miner Res 15:1243–1252.

- Li X, Masinde G, Gu W, Wergedal J, Mohan S, and Baylink DJ (2002) Genetic dissection of femur breaking strength in a large Population (MRL/MpJ x SJL/J) of F2 mice: single QTL effects, epistasis, and pleiotropy. Genomics 79(5): 734-740.

- Michaelsson K, Melhus H, Ferm H, Ahlbom A, Pedersen NL (2005) Genetic liability to fractures in the elderly. Arch Intern Med 165:1825–1830.

- Koller DL, Econs MJ, Morin PA, Christian JC, Hui SL, Parry P, Curran ME, Rodriguez LA, Conneally PM, Joslyn G, Peacock M, Johnston CC, Foroud T. (2000) Genome screen for QTLs contributing to normal variation in bone mineral density and osteoporosis. *J Clin Endocrinol Metab*. Sep;85(9):3116-20.

- Ralston SH. (2002) Genetic control of susceptibility to osteoporosis. J Clin Endocrinol Metab. Jun;87(6):2460-6. Review.

- Masinde GL, Li X, Gu W, Wergedal J, Mohan S, Baylink DJ. (2002) Quantitative trait loci for bone density in mice: the genes determining total skeletal density and femur density show little overlap in F2 mice. Calcif Tissue Int. 71:421-8

- Eddleston J, Murdoch JN, Copp AJ, Stanier P. (1999) Physical and transcriptional map of a 3-Mb region of mouse chromosome 1 containing the gene for the neural tube defect mutant loop-tail (Lp). Genomics; 56(2):149-59.

- Underhill DA, Canfield VA, Dahl JP, Gros P, Levenson R. (1999) The Na,K-ATPase alpha4 gene (Atp1a4) encodes a ouabain-resistant alpha subunit and is tightly linked to the alpha2 gene (Atp1a2) on mouse chromosome 1. Biochemistry;38(45):14746-51.

- Gu WK, Li XM, Edderkaoui B, Strong DD, Lau KH, Beamer WG, Donahue LR, Mohan S, Baylink DJ. (2002) Construction of a BAC contig for a 3 cM biologically significant region of mouse chromosome 1. *Genetica*;114(1):1-9.

- Gu W, Li X, Lau KH, Edderkaoui B, Donahae LR, Rosen CJ, Beamer WG, Shultz KL, Srivastava A, Mohan S, Baylink DJ. (2002) Gene expression between a congenic strain that contains a quantitative trait locus of high bone density from CAST/EiJ and its wild-type strain C57BL/6J. Funct Integr Genomics; 6:375-86.

- Worley J, Bechtol K, Penn S, Roach D, Hanzel D, Trounstine M, Baker D (2000) A systems approach to fabricating and analyzing DNA microarrays. In: Schena M (ed) Microarray biochip technology. Eaton, Natick, Mass. pp 65–85.

- Asensio AC, Rodriguez-Ferrer CR, Oaknin S, Rotllan P. Human diadenosine triphosphate hydrolase: preliminary characterisation and comparison with the Fhit protein, a human tumour suppressor. Acta Biochim Pol 2000;47(2):435-41

- Adam M, Robert F, Larochelle M, Gaudreau L. (2001) H2A.Z is required for global chromatin integrity and for recruitment of RNA polymerase II under specific conditions.Mol Cell Biol; 21(18):6270-9

- Drage LA, Davis MD, De Castro F, Van Keulen V, Weiss EA, Gleich GJ, Leiferman KM. (2002) Evidence for pathogenic involvementof eosinophils and neutrophilsin Churg-Strauss syndrome. J Am Acad Dermatol;47(2):209-16.

- Rosen CJ, Dimai HP, Vereault D, Donahue LR, Beamer WG, Farley J, Linkhart S, Linkhart T, Mohan S, Baylink DJ (1997) Circulating and skeletal insulin-like growth factor-I (IGF-I) concentrations in two inbred strains of mice with different bone mineral densities. Bone 21:217–223.

- Shultz KL, Donahue LR, Bouxsein ML, Baylink DJ, Rosen CJ, Beamer WG (2003) Congenic strains of mice for verification and genetic decomposition of quantitative trait loci for femoral bone mineral density. J Bone Miner Res 18:175-85.

- Edderkaoui B, Baylink DJ, Beamer WG, Wergedal JE, Dunn NR, Shultz KL and Mohan S. (2006) Multiple Genetic Loci from CAST/EiJ Chromosome 1 Affect vBMD Either Positively or Negatively in a C57BL/6J Background. J. Bone Miner. Research, 21(1): 97-104.

- Schadt EE, Monks SA, Drake TA, Lusis AJ, Che N, Colinayo V, Ruff TG, Milligan SB, Lamb JR, Cavet G, Linsley PS, Mao M, Stoughton RB, Friend SH. (2003) Genetics of gene expression surveyed in maize, mouse and man. Nature;422(6929):297-302.

- Chesler EJ, Lu L, Shou S, Qu Y, Gu J, Wang J, Hsu HC, Mountz JD, Baldwin NE, Langston MA, Threadgill DW, Manly KF, Williams RW. (2005) Complex trait analysis of gene expression uncovers polygenic and pleiotropic networks that modulate nervous system function. Nat Genet.; 37(3):233-42.

- Klein RF, Allard J., Avnur Z., Nikolcheva T., Rotstein D., Carlos AS., Shea M., Waters RV., Belknap JK., Peltz G., Orwoll ES. (2004) Regulation of bone mass in mice by the lipoxygenase gene Alox15. Science; 30: 229-232.

- Edderkaoui B, Baylink DJ, Beamer WG, Wergedal JE, Porte R, Chaudhuri A, and Mohan S. (2007) Identification of mouse Duffy Antigen Receptor for Chemokines (Darc) as a BMD QTL gene. Genome Res.17(5):577-85.

- Luo H, Chaudhuri A, Zbrzezna V, He Y, Pogo AO. (2000) Deletion of the murine Duffy gene (*DARC*) reveals that the Duffy receptor is functionally redundant. Mol Cell Biol **20**(9):3097-101. Erratum in: Mol Cell Biol. **23**(8):3030 (2003).

- Tournamille C, Le Van Kim C, Gane P, Blanchard D, Proudfoot AE, Cartron JP, Colin Y. (1997) Close association of the first and fourth extracellular domains of the Duffy antigen/receptor for chemokines by a disulfide bond is required for ligand binding. J Biol Chem. **272**(26):16274-80.

- Quinn JM, Elliott J, Gillespie MT, Martin TJ. (1998) A combination of osteoclast differentiation factor and macrophage-colony stimulating factor is sufficient for both human and mouse osteoclast formation in vitro. Endocrinology 139(10):4424-7.

- Takahashi, N, Udagawa, N., and Suda, T. (1999) A new member of tumor necrosis factor ligand family, ODF/OPGL/TRANCE/RANKL, regulates osteoclast differentiation and function. Biochem Biophys Res Commun 256(3):449-55.

- Pruenster M, Rot A. (2006) Throwing light on DARC. Biochem Soc Trans. 34(Pt 6):1005-8. Review.

- Li X, Qin L, Bergenstock M, Bevelock LM, Novack DV, Partridge NC. (2007) Parathyroid hormone stimulates osteoblastic expression of MCP-1 to recruit and increase the fusion of pre/osteoclasts. J Biol Chem 282(45):33098-106.

- Okamatsu Y, Kim D, Battaglino R, Sasaki H, Späte U, Stashenko P. (2004) MIP-1 gamma promotes receptor-activator-of-NF-kappa-B-ligand-induced osteoclast formation and survival. J Immunol. 173(3):2084-90.

- Cappellen, D., Luong-Nguyen, N. H., Bongiovanni, S., Grenet, O., Wanke, C., and Susa, M. (2002) Transcriptional program of mouse osteoclast differentiation governed by the macrophage colony-stimulating factor and the ligand for the receptor activator of NFkappa B. J. Biol. Chem 277:21971-21982.

- Yang M, Mailhot G, MacKay CA, Mason-Savas A, Aubin J, Odgren PR. (2006) Chemokine and chemokine receptor expression during colony stimulating factor-1-induced osteoclast differentiation in the toothless osteopetrotic rat: a key role for CCL9 (MIP-1gamma) in osteoclastogenesis in vivo and in vitro. Blood 107(6):2262-70.

- Kim, M.S., Day, C.J., and Morrison, N.A. (2005) MCP-1 is induced by receptor activator of nuclear factor-{kappa}B ligand, promotes human osteoclast fusion, and rescues granulocyte macrophage colony-stimulating factor suppression of osteoclast formation. J Biol Chem. 280(16):16163-9.

- Kukita T, Wada N, Kukita A, Kakimoto T, Sandra F, Toh K, Nagata K, Iijima T, Horiuchi M, Matsusaki H, Hieshima K, Yoshie O, Nomiyama H. (2004) RANKL-induced DC-STAMP is essential for osteoclastogenesis. J Exp Med. 200(7):941-6.

- Yagi M, Miyamoto T, Sawatani Y, Iwamoto K, Hosogane N, Fujita N, Morita K, Ninomiya K, Suzuki T, Miyamoto K, Oike Y, Takeya M, Toyama Y, Suda T. (2005) DC-STAMP is essential for cell-cell fusion in osteoclasts and foreign body giant cells. J Exp Med. 202(3):345-51.

- Yagi M, Miyamoto T, Toyama Y, Suda T. (2006) Role of DC-STAMP in cellular fusion of osteoclasts and macrophage giant cells. J Bone Miner Metab. 24(5):355-8.

- Kim MS, Day CJ, Selinger CI, Magno CL, Stephens SR, Morrison NA. (2006) MCP-1-induced human osteoclast-like cells are tartrate-resistant acid phosphatase, NFATc1, and calcitonin receptor-positive but require receptor activator of NFkappaB ligand for bone resorption. J Biol Chem 281(2):1274-85.

- Masinde GL, Li X, Gu W, Wergedal J, Mohan S, Baylink DJ. (2002) Quantitative trait loci for bone density in mice: the genes determining total skeletal density and femur density show little overlap in F2 mice. Calcif Tissue Int; 71(5):421-8.

- Van Ooijen, JW. MapQTL® 5 (2004) Software fore the mapping of quantitative trait loci in experimental populations. Kyazma B.B., Wageningen, Netherlands.

- Chan-Hui, P. Y., and Weaver, R. (1998) Human mitogen-activated protein kinase mediates the stress-induced activation of mitogen activated protein kinase cascades. Biochem. J. 15: 599–609.

B. TECHNICAL OBJECTIVE 2: TO IDENTIFY THE KEY GENES THAT ARE INVOLVED IN THE SOFT-TISSUE REPAIR/REGENERATION IN MRL/MPJ AND SJL/J MICE.

1. INTRODUCTION

Biological response to injury in higher organisms falls into two categories: wound repair and regeneration. Wound repair often involves formation of scar tissue without normal architecture and restoration of full function. Regeneration, on the other hand, involves gross replacement and restoration of adult tissue mass with normal architecture and function, and in extreme cases, full organs. Regeneration is a fundamental property for an individual's survival and well-being. Invertebrates and some vertebrate species have developed the strong ability to heal and regenerate through evolution (Odelberg 2004). The most dramatic example is the replacement of a snail's head after its removal (Dinsmore 1991). Past regeneration research has been primarily focused on the amphibians, particularly urodeles (commonly known as salamanders), since they can re-grow numerous adult organs including jaws, limbs, spinal cord, tail and even parts of the heart (Brockes 1997; Tanaka 2003). Because of amenability to genetic manipulation, zebrafish has been increasingly used in regeneration studies. Zebrafish can also regenerate adult structures such as spinal cord, scales, fins and heart (Johnson and Weston 1995; Poss, Nechiporuk et al. 2002; Raya, Consiglio et al. 2004).

Although possessing an innate regenerative capability that could be activated (Han, Yang et al. 2005), higher organisms show very limited ability to regenerate (Lambert 1994). In mammals, it is considered a lost phenotype (Heber-Katz, Leferovich et al. 2004). However, there are a few noted exceptions of regeneration in mammals, and these include re-growth of deer's antlers (Goss 1970), growth of mouse digits and human fingertips (King 1979; Borgens 1982), and closure of rabbit ear holes (Goss and Grimes 1975). Humans are also capable of liver regeneration (Schaffner 1991). Another exception was serendipitously discovered. Experiments show that the MRL inbred mouse can heal and close 2-mm ear punch holes completely within 30 days (Clark, Clark et al. 1998; Singer and Clark 1999). Normal cartilage and skin with replaced hair follicles appear in the place of the ear punch without showing any sign of scar formation (Heber-Katz, Leferovich et al. 2004). Like MRL, its presumed progenitor LG/J (LG), also shows better healing than other strains of inbred mice (Kench, Russell et al. 1999), which can heal to various degrees, but cannot close the ear holes.

Besides of ear hole healing, recent evidence shows that the MRL mouse possesses other unique healing abilities. For example, the MRL mouse healed digit tips more quickly and regenerated nails to a greater degree in comparison to two other strains of mice, C57BL/6 (B6) and DBA/1J (DBA) (Chadwick, Bu et al. 2007). It also displayed faster and more complete healing of corneas after alkali-burning injury in the eyes (Ueno, Lyons et al. 2005). It has been reported in some studies that MRL is also capable of cardiac muscle regeneration (Leferovich, Bedelbaeva et al. 2001; Heber-Katz, Leferovich et al. 2004; Haris Naseem, Meeson et al. 2007). Therefore, the MRL mouse generally has the ability of faster wound healing and greater regenerativity in various tissues, although the extent of this ability is still yet to be fully determined and is not expected to be unlimited. But the ear healing itself is a very complex

process, and involves not only the skin but also other tissues, such as cartilage and muscle, which composes most of the ear.

Injury is a major health problem. Developing effective clinical strategies to treat injuries requires a thorough understanding of the genes and the molecular mechanisms involved in the wound healing process. Since the inbred MRL mouse can fast heal and close ear holes that are punched in the ears rapidly, completely and without scar formation, it can serve as a model for mammalian fast wound healing. Identification of the genes involved in this fast wound healing process is the focus of this project. The rationale is that genes regulating fast wound healing in mice may also be important for rapid wound healing in humans, and identifying these genes could lead to new gene therapy targets for the treatment of injuries.

We have proposed different specific objectives in different periods of the project. In the earlier period, we adopted a broad approach with emphasis on both chromosomes of 1 and 9, and genes in the QTL regions of the two chromosomes. The specific objectives of the earlier period called for mapping the QTLs, developing congenic lines, evaluating the phenotype of the congenic lines, identifying genes in the QTL regions, conducting expression, sequencing and knockout analyses and in vivo testing on the identified genes. In the later period, we had narrowed our focus with the emphasis just on chromosome 9, and furthermore, on the narrowed region of the chromosome 9 QTL. To do so, we set up specific objectives to first fine map the QTL region and develop sub congenic lines. Then, we obtain candidate genes from the narrowed region, and conduct sequencing, develop new techniques in vitro, and test the candidate genes in vitro. However, all these different specific objectives of the project have been designed with the following goals in mind:

1) To identify an appropriate pair of inbred mouse strains that exhibits extreme difference of wound healing ability.
2) To identify major genetic loci that contribute to variation in wound healing among the inbred strains in mice through a combination of genetic crosses and QTL analysis.
3) To confirm the validity of the identified genetic loci by performing additional crosses using same or new pairs of mouse strains.
4) To utilize various molecular genetic approaches such as fine mapping, congenic development, expression profiling, sequence analysis and functional assays to identify potential candidate genes that contribute to the improved wound healing.

During different funding periods of the project, we have successfully accomplished all the proposed specific objectives. For the sake of continuity and clarity, we have organized this progress report in the following sections:

1) Evaluation of the inheritance of wound healing/soft tissue regeneration in mice.
2) Development of congenic and sub congenic lines to narrow QTL regions with the emphasis on chromosome 9.
3) Fine mapping of the chromosome 9 QTL regions to identify the candidate genes.
4) Expression analysis of the identified candidate genes.
5) Detection of mutations in the coding regions of the candidate genes.
6) Development of in vitro technique to test the functions of the candidate genes.
7) Development of in vivo technique to test the functions of the candidate genes.

2. BODY

1) Evaluation of the inheritance of wound healing/soft tissue regeneration in mice. We began our studies of wound healing/soft tissue regeneration by surveying 20 different inbred strains of mice. The results of our study have been published in a paper (**Li, Gu et al. 2001**). To summarize these results, we have found that major differences existed among the surveyed inbred strains (**Figure 1**). MRL and its presumed progenitor strain LG showed the fastest healing, and healed four times faster than the worst healing strains. They could close the ear hole completely within 30 days after it was punched, while poor healing strains such as C57BL/6J (B6) failed to do so (**Figure 2**). Better healing healers also included DBA/1J (DBA). Among poor healing strains, Balb/c and SJL showed the slowest healing rates. Compared to MRL, CAST/EiJ (CAST) is also a poor healer. Except MRL and LG, inbred mice were never able to close the ear holes. That is why punching an ear hole has been used as a standard technique to label mice. With regard to the time required for the healing process, the most important period is days 6 to 20, when healing is the fastest, and the greatest differences are manifested among inbred strains (**Figure 1**). The healing rate is also highly inheritable, with the heritability of 86%. Therefore, these data provide experimental evidence that the MRL mouse exhibits a unique ability to heal certain types of soft tissue wounds, and can be used as an experimental model to identify the molecular basis for mammalian wound healing.

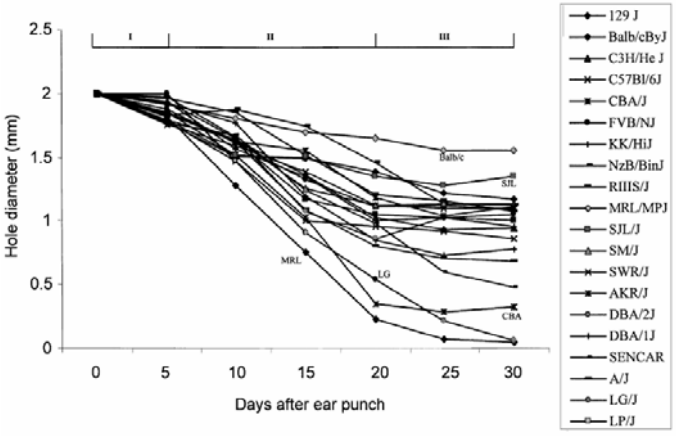

Figure 1. Rates of healing of a 2-mm ear hole in 20 inbred strains of mice. The healing process can be divided into three phases on the basis of the rate of healing: initiation phase (I), rapid-healing phase (II), and slow-healing phase.

In order to identify the genes involved in wound healing/soft tissue regeneration, we have conducted genome-wide scans using F2 populations of inbred mouse strains. We used super healer MRL and poor healing strains such as SJL and CAST in generating crosses. To support the results from the MRL crosses, we have also examined a cross involving a better healer DBA and a poor healer 129X1/SvJ (129). Therefore, during the project we have generated a total of 1,453 F2 mice in three different crosses, which were MRL X SJL (633 females), MRL X CAST (171 females and 157 males) and DBA X 129 (304 females and 188 males). We have published the results of these studies in three papers (**Masinde, Li et al. 2001; Yu, Mohan et al. 2005; Masinde, Li et al. 2006**). To briefly summarize the results of these studies, our genome-wide scan results indicated that QTLs exist on at least 10 Chrs: 1, 3, 4, 6, 7, 9, 12, 13, 17 and 18. Among these 10 QTLs that have been identified, the chromosome 9 QTL is the No. 1 QTL in terms of the likelihood for the presence of wound healing genes. This QTL consisted of multiple peaks based on our data from the cross of MRL X SJL (Masinde, Li et al. 2001). One of the two peaks, the distal Sth9, was shown to have a LOD score of 16.1. That is the highest LOD score in MRL X SJL and in any other crosses

that have been made for mouse ear hole wound healing/regeneration either by us or by others. This QTL was also present in another cross of ours involving MRL: MRL X CAST (Yu, Mohan et al. 2005).

Other chromosomes that harbor important QTLs include chromosomes 1 and 4, although chromosome 4 is not covered in any specific objectives. The chromosome 1 QTL had a LOD score of 7, and explained about 7% of the F2 phenotypic variance. The reasons why the chromosome 4 is also important are multi-folds. First, like the chromosome 9, chromosome 4 harbors two QTLs: Sth3 at 21.9 cM and Sth4 at 50.3 cM (Masinde, Li et al. 2001). With LOD scores of above 6, they each explained about 6% of the phenotypic variance in the F2 of MRL X SJL. They can be considered the third largest set of QTLs after those of chromosomes 9 and 1. Secondly, one of the chromosome 4 QTLs, Sth4, is present in multiple crosses. We believe that it is the same as the heal8 QTL associated with markers D4Mit13 and D4Mit148 in the MRL X B6 cross, identified by another group of researchers (Blankenhorn, Troutman et al. 2003; Heber-Katz, Chen et al. 2004). It was also found as Earheal2 associated with D4Mit170 in our DBA X 129 cross, where a better healing allele was contributed by DBA (Masinde, Li et al. 2006). Our analysis with the cross of MRL X CAST showed that two other markers D4Mit203 and D4Mit170 were also associated with the peaks of significant LOD scores of chromosome 4 (Yu, Mohan et al. 2005).

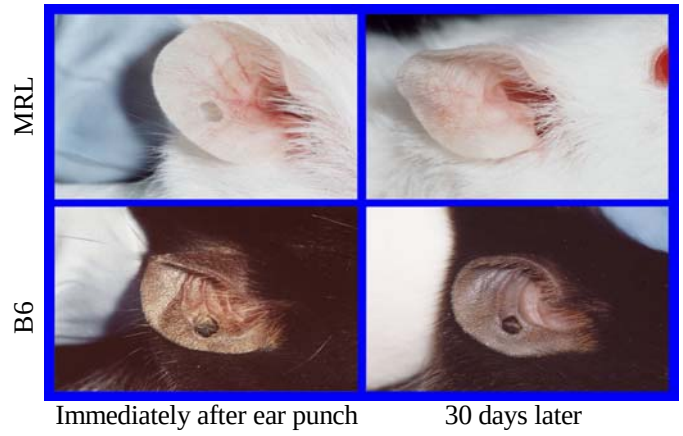

Figure 2. Comparison of ear-healing rate and quality in MRL and B6 strains of mice. At 30 days after ear punch, MRL completely healed the 2 mm hole with normal tissue, while B6 healed 45% of the hole with scar tissue.

2) Development of congenic and sub congenic lines to narrow QTL regions with the emphasis on chromosome 9. As mentioned above, our studies of the super healing MRL mouse crossed with poor healing mouse strains identified a total of 10 significant QTLs for wound healing/soft tissue healing. The largest of these is present on chromosome 9. The LOD score for this QTL was 16.11 for the healing phenotype on day 25 after ear punch injury in the MRL X SJL cross. It explained 13.3% of the variance in the F2 mice. Accordingly, these results suggest that this QTL region contains one or more genes that make important contributions to the super healing phenotype of the MRL mouse. For these reasons, the chromosome 9 QTL has been the main focus of our studies.

To develop congenics, we first crossed MRL females to SJL males. By crossing F1 females back to SJL males (recurrent parent), we obtained N1 mice. N1 mice were genotyped using markers specific for the QTL region on chromosome 9. N1 heterozygous females that carried the MRL genotype in the QTL regions were crossed back to SJL males to produce N2 congenics, which were again genotyped using the same markers. This process was repeated for more than 8 generations (N8) in the production of congenic strains for the chromosome 9 QTL. The overall proportion of contribution of genome by the non-recurrent parent can be estimated by the formulae of $(1/2)^{8-1}$. Thus, the MRL genome present in N8 congenics was only 0.78%. In other words, the genomic composition of the N8 congenic is almost identical to the recurrent SJL parent, with the exception of the MRL contribution of the selected QTL region. For phenotypic evaluation of the congenic lines in wound healing, ear punch was done on the three and half week's old animals. Ear punch closure measurement was made at days 3, 7, 15, 21, and 25 after the punch was made. Fifteen male and fifteen female mice from each homozygous congenic line plus the MRL and SJL parental lines were used in the phenotype analysis.

Table 1. Genotypes of congenic mice for chromosome 9 markers[a]

Map Pos (cM)	2	8	23	24	32	34	40	42	44	47	49	54	56	60	63	70
Map Pos (Mb)	10	32	50	50	61	66	76	76	90	99	99	101	103	111	117	121
Marker (D9Mit-)	43	90	229	71	207	336	263	270	157	35	355	182	347	350	201	151
SJL.MRL9-1	S	S	S	S	M	M	M	M	M	M	M	M	M	M	M	M
SJL.MRL9-2	S	S	S	S	M	M	M	M	S	S	S	S	S	S	S	S

[a] M = homozygous for MRL; S = homozygous for SJL.

The results of congenic analysis of the chromosome 9 QTL are published in our recent paper (**Yu, Baylink et al. 2007**). To briefly summarize these results, we have obtained one homozygous congenic strain named SJL.MRL9-1 at N8 generation **(Table 1**). This congenic contains a fragment from MRL between 60 Mb (38 cM) and distal end of chromosome 9 in the otherwise SJL genetic background. Majority of the congenic mouse's genome ($1 - (1/2)^{(8-1)}$ = 99.22%) was homozygous for SJL. The transferred chromosomal fragment from MRL encompassed the whole chromosome 9 QTL region. Evaluation of this congenic strain has indicated that the male congenic mice showed significant better healing than male SJL progenitor mice (**Figure 3**). Their average ear hole size of the congenics was 12% smaller than that of poor healing SJL at 25 days post injury. The female congenic mice also healed better than female SJL mice at day 25 and later dates, but the difference was not significant, probably due to small sample sizes. Therefore, the chromosome 9 QTL contributes significant amount of

the healing difference between MRL and SJL, and has more pronounced healing effect in male mice.

The sex difference in the ear healing of the congenic mice serves to reflect the fact that the ear healing is a sexual dimorphic phenotype, and the effect of the chromosome 9 QTL genes is more pronounced in poor healing males. As in a previous study by another group (Blankenhorn, Troutman et al. 2003), we also observed this sexual dimorphism. A separate study (**Figure 4)** shows a typical response of male and female MRL mice to the ear punch injury.

The SJL.MRL9-1 line contains the entire region of the chromosome 9 QTL. In terms of sub congenics, we have obtained one sub congenic line at N10 generation, SJL.MRL9-2 (**Table 1**). This sub congenic strain only covers part of the chromosome 9 QTL region, i.e. 9.8 cM (15.7 Mb) long on the proximal end of the QTL. We have also evaluated this sub congenic line for healing response. There is a significant difference between the congenic male mice and the SJL male mice. The average ear hole size of the congenic line based on 16 mice was 13.70% smaller than the corresponding SJL mice. No significant difference exists between the congenic female mice and the SJL female mice due to sexual dimorphism. These results are similar to what we obtained from the SJL.MRL9-1 full congenic line.

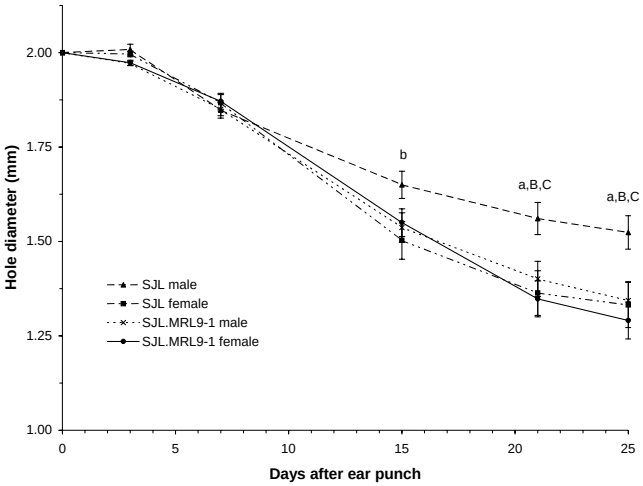

Figure 3. Healing rates of the 2 mm ear punch holes in the SJL.MRL9-1 mice vs. the SJL mice. N=21, 27, 26, 27 for SJL males, SJL.MRL9-1 males, SJL females, SJL.MRL9-1 females, respectively. Values are shown as Mean ± SEM. a = P< 0.05 vs. SJL.MRL9-1 male; b = P< 0.05 vs. SJL female; B = P<0.01 vs. SJL female; C = P<0.01 vs. SJL.MRL9-1 female.

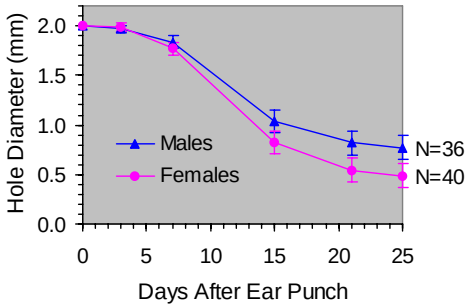

Figure 4. Sexual dimorphism in the ear healing of MRL mice. Values are shown as means ± standard error of 40 females and 36 males. t-Test $P < 0.05$ at day 21 and day 25. Therefore, females healed significantly better than males beginning at day 21 after ear punch.

Although the SJL.MRL9-2 line only contains part of the chromosome 9 QTL, the phenotypic effect of the congenic line on healing rate in the male mice, is the same as that of the longer congenic line. There are two possibilities to explain this observation. First, the genes that contributes to the chromosome 9 QTL resides within the SJL.MRL9-2 region. In this sense, we have narrowed the whole chromosome 9 QTL region from 38.2 cM to 9.8 cM. We can next identify the genes that are located between 38.2 cM (60.7 Mb) and 41.5 cM (76.45 Mb) of chromosome 9, where the

SJL.MRL9-2 line covers. We can now screen these genes to identify candidate genes for wound healing/soft tissue regeneration. Secondly, the numbers of mice used in these experiments are not sufficiently large to make the assumption that congenic lines SJL.MRL9-1 and SJL.MRL9-2 have similar amount of phenotypic effect on ear healing. Much large numbers of mice are needed to make this determination.

Table 2. Genotypes of congenic mice for chromosome 1 markers[a]

Map Pos (cM)	0	3.3	8.7	36.1	37.2	49.2	59	75.4	104	110
Marker (D1MIT-)	64	316	231	33	19	216	185	102	291	17
Congenic (N6)	H	H	H	H	H	H	H	H	H	H

[a] H = heterozygous between MRL and SJL.

Table 3. Genotypes of congenic mice for chromosome 4 markers[a]

Map Pos (cM)	5.2	12.1	17.9	35.5	51.3	60	61.9	69.9	81
Marker (D4Mit-)	18	196	214	178	31	203	204	170	42
Congenic #1 (N12)	H	H	H	H	H	H	H	H	H
Congenic #2 (N12)	H	H	H	H	H	H	H	S	S

[a] H = heterozgyous between MRL and SJL; S: homozygouse for SJL.

In terms of the congenic development for the chromosome 1 QTL, we have advanced the crossing to the N6 generation, and obtained five congenic mice heterozygous for most of chromosome 1 markers (**Table 2**). The congenic fragment from the MRL parent in the SJL background is from 0 to 110 cM on chromosome 1, which covers the QTL peak at 49.2 cM. For the chromosome 4 congenics, we have advanced the crossing to the N12 generation. The congenic fragment from the MRL parent in congenic line #1 is from 5.2 cM to 81 cM (**Table 3**). This chromosomal fragment covers both QTLs *Sth3* at 21.9 cM and *Sth4* at 50.3 cM. **Table 3** also shows that we have a sub congenic line named congenic #2, with a shorter chromosomal fragment. Preliminary analysis of four heterozygous mice of the sub congenic #2 at N10 generation showed very promising results. Based on two measurements for each ear hole on both left and right ears of each mouse, wound healing rates were significantly different between the congenic mice and the poor healing SJL mice 15 days after ear punch (**Figure 5**). Thus, the congenic mice showed much smaller hole size than the SJL mice even in the heterozygous state. These data and the QTL data showing the presence of chromosome 4 QTL in multiple crosses provide definitive evidence that chromosome 4 contains key genes for wound healing/soft tissue regeneration.

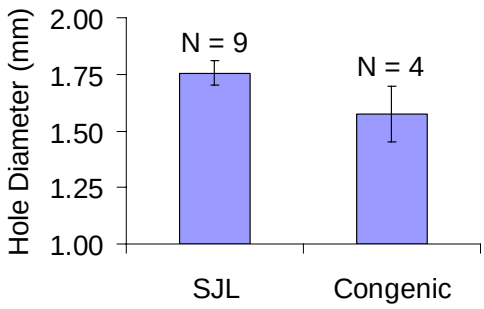

Figure 5. Comparison of wound healing rates between heterozygous congenic #2 mice and homozygous SJL mice 15 days after ear punch. Student's t-Test $P = 0.037$, indicating a significant difference.

3) Fine mapping of the chromosome 9 QTL regions to identify the candidate genes. Our congenic analysis is important and helpful in the confirmation of the QTL effect. However, based on our results on chromosome 9, we would need a rather large number of congenic lines, a large number of congenic mice in each line, and a quite a long term to narrow down the QTL region. Therefore, other approaches are such as fine mapping coupled with sophisticated genetic analyses might be more useful. Fine mapping is a major approach used to narrow down a QTL region for consideration of candidate genes. In order to fine map the chromosome 9 QTL in MRL X SJL, we have bred new additional F2 mice for this cross (474 males and 473 females) since our first QTL study (Masinde, Li et al. 2001). Adding them to the 633 female mice in the original study, we have a total of 1,580 F2 mice of MRL X SJL. We have genotyped a total of 23 microsatellite markers within the QTL region with an average distance of 3.1 cM or 5.1 Mb. Interval mapping was carried out using the MapQTL program. The length of a QTL peak was defined by the 2-LOD interval. The 2-LOD interval is a genome region delimited by positions on both sides of the QTL peak where LOD scores fall 2 from the highest point. The 2-LOD interval is equivalent to the 95% confidence interval for a QTL peak. We also analyzed these data using a Bayesian shrinkage estimation (**Wang, Zhang et al. 2005**). This Shrinkage estimation is a novel method in QTL mapping that was developed recently by a research team at the University of California at Riverside using the data generated from this project and in collaboration with our group. This method allows marker intervals that contain no QTL to have estimated effects close to zero, whereas intervals containing noticeable QTL to have estimates subject to virtually no shrinkage. The purpose of this analysis was to place the QTL peaks in narrow regions of the chromosome.

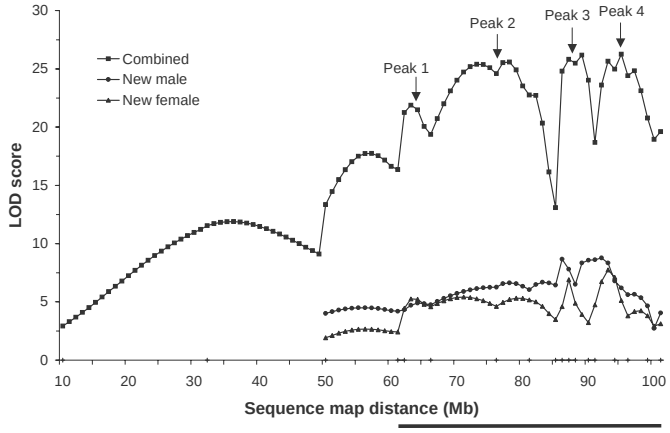

Figure 6. LOD scores of the chromosome 9 QTL in the F2 mice of MRL X SJL. N = 1,564, 465, 466 for the combined population, the new males and new females, respectively. The combined population includes 633 female mice from the original study. Arrows identify positions of four peaks defined by the 2-LOD intervals. Dark bar underneath indicates the chromosomal region covered by the congenic SJL.MRL9-1 line.

Table 4. The chromosome 9 QTL peaks determined from the MapQTL analysis.

Peak	Position (Mb)	LOD Score	2-LOD interval (Mb)[a]	Interval length (Mb)
1	63.49	21.9	60.8 - 65.8	5
2	78.45	25.6	68.8 - 84.5	15.7
3	89.38	26.2	85.5 - 89.8	4.2
4	95.20	26.3	94.2 - 97.5	3.3

[a] Positions where LOD scores were 2 less than that of the peak position.

We have presented the fine mapping results in a recent paper for congenic analysis we listed earlier (Yu, Baylink et al. 2007). Significant LOD scores were obtained for the new F2 mice in both males and females, indicating that there was no gender effect for the chromosome 9 QTL (**Figure 6**). These LOD scores were similar to those in the original study (Masinde, Li et al. 2001). In the interval mapping analysis of the combined data of the new male and female mice plus the original female mice, we have identified four major peaks, labeled 1–4, within the QTL region (**Figure 6**). They had LOD scores varying from 21.9 to 26.3, with peaks 3 and 4 higher than 1 and 2 (**Table 4**). Peaks 3 and 4 each explained about 8% of the F2 phenotypic variance. The total summarized length of the 2-LOD intervals for all four peaks was only 28 Mb.

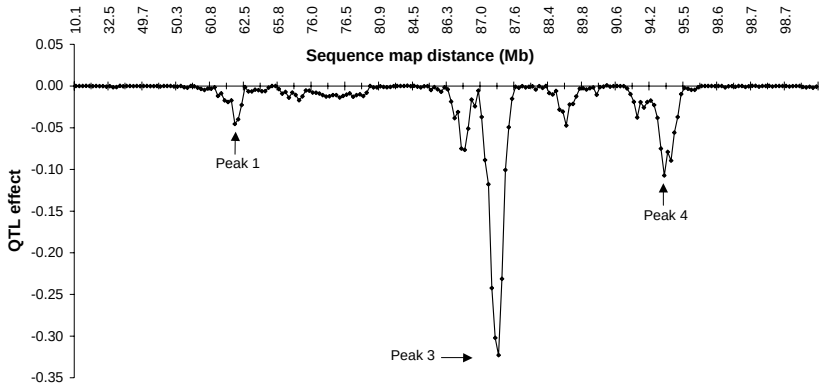

Figure 7. Additive effect of the chromosome 9 QTL obtained from the Bayesian shrinkage estimation. Numbers above indicate the marker positions in Megabase (Mb). Arrows denote position of three identified peaks.

Table 5. The chromosome 9 QTL peaks determined from the Shrinkage analysis.

Peak	Position (Mb)	Peak effect	Variance (%) [b]	Peak interval (Mb)	Interval length (Mb)
1	61.98	-0.05	0.7	60.8 - 62.5	1.7
3	87.31	-0.32	35.8	86.3 - 87.6	1.3
4	94.73	-0.11	4	94.2 - 95.5	1.3

[a] Peak numbers correspond to those in **Table 4**.

[b] $=1/2*(a^2/V_p)$ where a is the effect, and V_p is the phenotypic variance.

In the Bayesian shrinkage analysis of the same combined data, three peaks were identified, corresponding to three of the four identified by MapQTL, with peak 2 missing (**Figure 7**). Peak 3 was the major peak, explaining about 36% of the F2 variance, followed by peak 4 with 4% of the variance (**Table 5**). Peak 1 explained only 0.7% in comparison. Summarizing both MapQTL and Shrinkage analysis results, we show that there are at least three peaks within the chromosome 9 QTL influencing the wound healing/soft tissue regeneration phenotype. A major peak, peak 3, with the largest phenotypic effect was located in a region of just 1.3 Mb indicated by the Shrinkage analysis, and no more than 4.2 Mb by MapQTL. Therefore, we used this 4.2 Mb 2-LOD region to identify genes that are located within peak 3. Data mining of mouse genome (Build 36.1) showed that this is a candidate genes rich region, and there are 41 known genes (**Table 6**). We believe that one or more of these genes are responsible for the wound healing/soft tissue regeneration QTL on chromosome 9, and play a key role in the superior healing ability of the MRL mouse.

Table 6. Candidate genes located under peak 3 of the Chr 9 QTLs.

Pos (Mb)	Symbol	Description	Function
85.48	Ibtk	inhibitor of Bruton agammaglobulinemia tyrosine kinase	protein kinase binding
85.58	LOC434426	similar to 60S ribosomal protein L7a (Surfeit locus protein 3)	
85.62	9330154J02Rik	RIKEN cDNA 9330154J02 gene	
85.64	Tpbg	trophoblast glycoprotein	extracellular matrix
86.10	2610018I03Rik	RIKEN cDNA 2610018I03 gene	carboxypeptidase activity
86.35	Pgm3	phosphoglucomutase 3	carbohydrate metabolism
86.37	Rwdd2	RWD domain containing 2	
86.38	Mod1	malic enzyme, supernatant	malate metabolism
86.49	A330041J22Rik	RIKEN cDNA A330041J22 gene	
86.54	Prss35	protease, serine, 35	proteolysis and peptidolysis
86.56	Snap91	synaptosomal-associated protein 91	phospholipid binding
86.81	C030002E08Rik	RIKEN cDNA C030002E08 gene	
86.82	Cyb5r4	cytochrome b5 reductase 4	heme metabolism
86.92	LOC666777	hypothetical protein LOC666777	
86.93	LOC244958	similar to Protein C6orf117	
86.99	4922501C03Rik	RIKEN cDNA 4922501C03 gene	tight junction barrier function
87.19	LOC384961	similar to budding uninhibited by benzimidazoles 3 homolog	
87.50	Tbx18	T-box18	anterior/posterior specification
87.94	LOC384962	similar to High mobility group protein 1 (HMG-1) (HMG-B1)	
88.08	LOC272633	similar to mitochondrial carrier family protein	
88.13	Nt5e	5' nucleotidase, ecto	nucleotide catabolism
88.17	Snx14	sorting nexin 14	intracellular protein transport
88.25	Syncrip	synaptotagmin binding, cytoplasmic RNA interacting protein	mRNA processing
88.32	2810026P18Rik	RIKEN cDNA 2810026P18 gene	
88.35	4930422I07Rik	RIKEN cDNA 4930422I07 gene	krueppel associated box
88.38	LOC547109	similar to tripartite motif-containing 43	RYanodine receptor
88.52	Bcl2a1d	B-cell leukemia/lymphoma 2 related protein A1d	
88.64	LOC666731	similar to tripartite motif protein 17	RYanodine receptor
88.75	Bcl2a1a	B-cell leukemia/lymphoma 2 related protein A1a	apoptosis
88.88	LOC666747	similar to tripartite motif protein 17	RYanodine receptor
88.91	4930579C12Rik	RIKEN cDNA 4930579C12 gene	
89.00	Bcl2a1b	B-cell leukemia/lymphoma 2 related protein A1b	apoptosis
89.01	Mthfs	5, 10-methenyltetrahydrofolate synthetase	metabolism
89.39	AF529169	cDNA sequence AF529169	integral to membrane
89.50	Tmed3	transmembrane emp24 domain containing 3	protein transport
89.53	B230218L05Rik	RIKEN cDNA B230218L05 gene	protein-protein interactions
89.71	Rasgrf1	RAS protein-specific guanine nucleotide-releasing factor 1	intracellular signaling cascade
89.85	Ctsh	cathepsin H	proteolysis and peptidolysis
89.89	Morf4l1	mortality factor 4 like 1	regulation of cell growth
89.92	LOC621414	transmembrane protein 41B pseudogene	
89.96	Adamts7	a disintegrin-like and metallopeptidase type 1 motif 7	proteolysis and peptidolysis

4) Expression analysis of the identified candidate genes. Over the years, we have employed different strategies in expression analysis to identify genes that are important in wound healing/soft tissue regeneration. Initially, we conducted protein expression analysis. For this analysis, we employed the surface-enhanced laser desertion and ionization (SELDI) ProteinChip technology. After that, we switched to cDNA using microarray. We also conducted cDNA based restrictive fragment differential display-PCR (RFDD-PCR). Lately, we use the whole genome oligonucleotide microarray. In terms of mouse strains, we initially used MRL and B6, since MRL is the super healer, while B6 is a poor healer and the mostly commonly used strain in animal studies. Recently, we have switched to SJL for the poor healing strain. SJL is one of the worst healers. We have also used SJL in QTL mapping and congenic analysis.

For the expression analysis at protein level, the temporal protein profiles of the ear-punched tissues of regeneration strain MRL and non-regeneration strain B6 were analyzed using the SELDI ProteinChip technology. The results have been published in a paper (**Li, Mohan et al. 2000**). To briefly summarize these results, five candidate proteins were identified in which responses of MRL to the ear punch were 2-4-fold different compared to that of B6. Their corresponding genes were predicted using an antigen-antibody assay validated mass-based approach. Most of the predicted genes are known to play a role, or are likely to play a role in the wound healing/tissue regeneration. Of the five candidate proteins, the amount of the 23,560 Da protein in the ear-punched tissue was significantly correlated with the rate of ear healing in six representative strains of mice, making it a good candidate. We speculate that the increased concentration of the 23,560 Da protein in the wound tissue could stimulate the expression of various growth-promoting proteins, and consequently speed up the wound healing/regeneration processes. In addition, there were calgranulin A and Ras-related protein RAB-8. Thus, this study has shown that examination of protein expression profiles using SELDI technology coupled with database search is an alternative approach to search for candidate genes for wound repair/soft tissue regeneration.

In order to identify and analyze the genes that are expressed at the inflammatory stage of repair (i.e., 24 h after injury), we conducted a cDNA microarray, and examined the expression of 8,734 sequence-verified genes in response to ear punch in MRL and B6 mice. We have published the results in a paper (**Li, Mohan et al. 2001**). To briefly summarize these results, we have identified a number of differentially expressed genes. Most of these were up-regulated genes with a few of down-regulated genes. The up-regulated genes were either specific to the ear punch injury regardless of strains, or unique to super healer MRL. These included genes for hemoglobin alpha, lipocalin 2, glycoprotein 49B, laminin gamma 2, keratin complex 2-6A, small proline-rich protein 1A and 2A and formin-binding protein. It is noted that all these proteins are either involved in inflammation or in base membrane or extracellular matrix formation. Thus, many differentially expressed genes in the microarray can be readily assigned to wound-repairing pathways. In addition, there are many others that belong to pathways not previously associated with wound repair. For example, many genes of unknown function (ESTs) exhibited a more than two fold increase in MRL or B6 mice, suggesting that current understanding of the molecular events at the inflammatory stage of repair is still limited.

In addition to the cDNA based microarray, we have also carried out pathway focused oligonucleotide array. For this analysis, we used extracts from healing tissues from MRL and

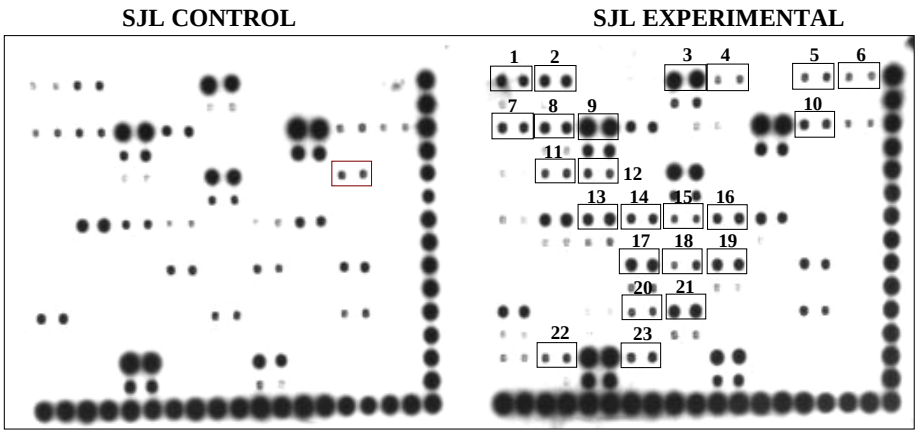

Figure 8. Increased activation of proinflammatory transcription factors in SJL mice. The activity of different proinflammatory transcription factor was measured in control and healing SJL mice. The results presented here show increased activity of several transcription factors in healing SJL mice

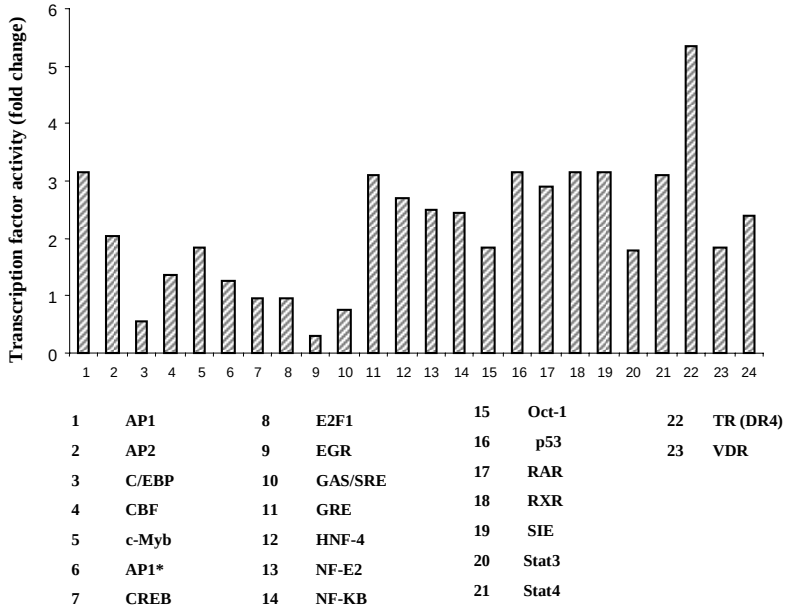

Figure 9. Fold increase in the activity of different proinflammatory transcription factors in healing tissue of SJL mice. Quantification of the array data showed 2-4 fold increase in the activity of indicated transcription factors in healing tissue of SJL mice compared to control tissue. AP-1: Activator protein-1; AP-2: Activator protein-2; C/EBP: CCAAT/enhancer binding protein; CBF: C-repeat binding factor; CREB: cAMP-response element-binding protein; EGR: early growth response; GRE: glucocorticoid-responsive element; HNF-4: hepatocyte nuclear factor-4; SIE: sis inducible element; NF-κB: nuclear factor-kappa B; RAR: retinoic acid receptor; TR: thyroid hormone receptor; VDR: vitamin D receptor.

SJL mice to identify potential end points that could be used in our functional evaluation of candidate genes. Scarless wound healing in MRL mice probably involves the expression of a wide variety of genes. Since the gene expression in response to extracellular signals is regulated through the activation of various signal transduction pathways and transcription factors, we investigated the difference in the activation of various transcription factors and signaling pathways in healing tissues of MRL and SJL mice. For these experiments, around 1 mm healing tissues around the ear punch hole were collected from MRL and SJL mice. These tissues were processed for the isolation of nuclear and cytoplasmic extracts using protocols previously described (Kumar, Chaudhry et al. 2002; Kumar and Boriek 2003; Kumar, Lnu et al. 2003). Nuclear extracts were used to study the activation of various transcription factors. In

brief, nuclear extracts from the control and healing tissues were incubated with set of oligonucleotides consisting of consensus sequences for the different pro-inflammatory transcription factors. Transcription factor-bound oligonucleotides were separated from the unbound oligonucleotides by passing them through a spin column. Transcription factor bound oligonucleotides were then denatured to make them single stranded and used to hybridize with a membrane that contains array of oligonucleotides for these transcription factors. The signal was developed using the reagents and protocols provided by the manufacturer. The results of the transcription factor array are presented in **Figure 8**. The representative data presented shows a drastic increase in the activity of many transcription factors in healing SJL tissue compared to control tissues.

The transcription factor data was analyzed for the fold change in the activity of various transcription factors. A significant increase in the activity of inflammation-associated transcription factors such as AP-1, AP-2, c-Myb, GRE, HNF-4, NF-E2, NF-κB, p53, Stat4 and thyroid hormone receptor (TR) was observed in regenerating SJL mice (**Figure 9**). The activity of many of these pro-inflammatory transcription factors increased to a much smaller extent in the healing tissue of MRL mice compared to SJL mice (data not shown).

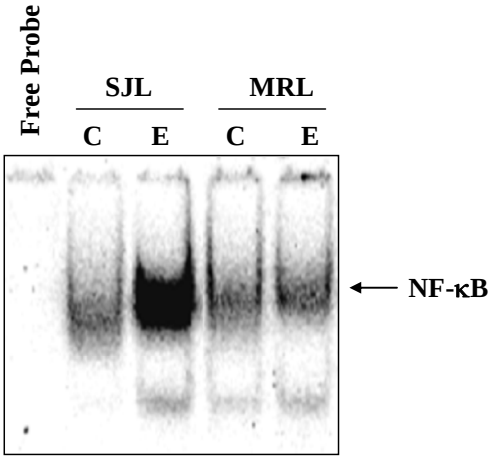

Figure 10. Higher activation of NF-κB transcription factor in SJL mice compared to MRL mice. DNA binding activity of NF-κB transcription factor in healing tissue measured using EMSA shows higher activity in SJL mice compared to MRL mice.

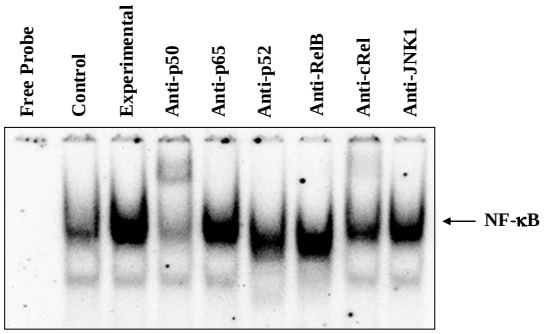

Figure 11. Activated NF-κB complex consists of P50 and C-Rel subunits in healing SJL tissues. Super-shift analysis of NF-κB/DNA complex suggests that activated NF-κB contains p50 and c-Rel subunits in healing tissue of SJL mice.

Among many transcription factors involved in mediating the immune and inflammatory response, NF-κB is prominent. Since there was higher activation of NF-κB in healing tissue of SJL mice, we compared the activation of NF-κB in MRL and SJL mice using Electrophoretic mobility shift assay (EMSA). For these experiments, the nuclear extracts from control and healing tissues of MRL and SJL mice were prepared by using low salt and high salt buffers. Concentration of proteins was measured using BioRad protein assay reagent. Equal amount of nuclear proteins from different samples was incubated with ^{32}P-labeled oligonucleotides consisting NF-κB consensus sequences. NF-κB/DNA complex was then separated on a 7.5% native polyacrylamide gel electrophoresis. The gels were dried and the DNA-binding activity of

NF-κB was quantified using ImageQuant software. Interestingly, we found that the activation of NF-κB was significantly higher in SJL mice compared to MRL mice (**Figure 10**) suggesting increased inflammatory response in SJL mice compared to the MRL mice.

Different combinations of Rel/NF-κB proteins can constitute an active NF-κB heterodimer that binds to specific sequences in DNA (Karin and Delhase 2000; Karin and Lin 2002). To know the constituents of NF-κB complex visualized by EMSA in regenerating SJL tissues, we performed super-shift analysis by a method described previously (Kumar and Boriek 2003; Kumar, Lnu et al. 2003). Nuclear extracts were incubated with antibody to p50, p65, p52, RelB, or c-Rel and then conducted EMSA. Antibody to either p50 or c-Rel subunits of NF-κB shifted the band to a higher molecular weight (**Figure 11**), suggesting that the activated NF-κB complex consisted mainly of p50 and p65 proteins. Irrelevant antibodies such as anti-JNK1 had no effect on the mobility of NF-κB.

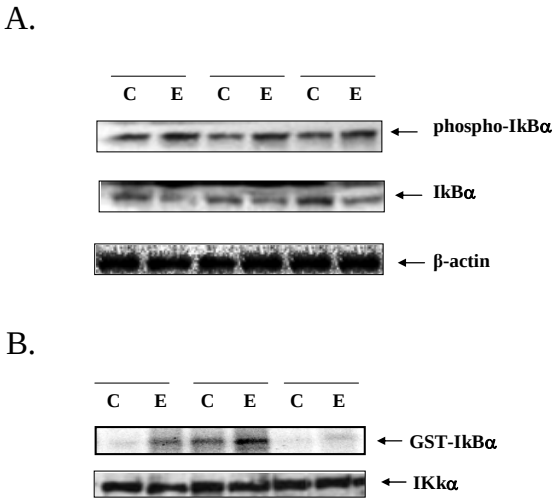

Figure 12. Activation of NF-κB involves phosphorylation and degradation of IKBα protein. **A)** The tissue lysates form healing mice were subjected to Western blot analysis using phosphor-specific or total IκBα antibody. The data show higher levels of phosphorylated IκBα protein in healing ear tissue compared to control. Total cellular levels of IκBα protein was decreased in healing tissue compared to controls. **B)** Higher enzymatic activity of IKK was observed in healing tissue compared to controls. C: control; E: experimental.

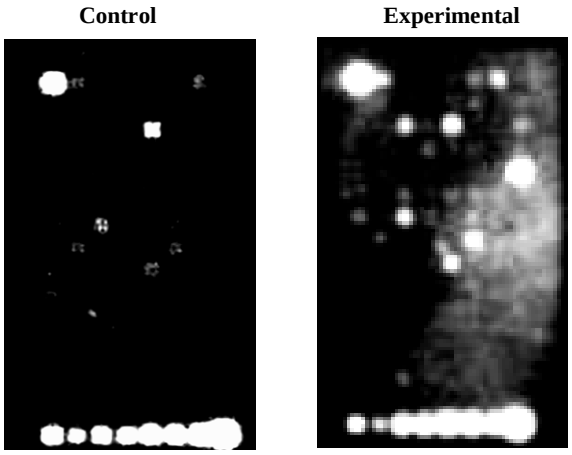

Figure 13. Increased expression of NF-κB pathway related genes in healing tissue. NF-κB pathway specific array analysis revealed increased expression of genes involved in the activation of NF-κB transcription factors.

The activation of NF-κB by inflammatory cytokines such as TNF-α is achieved through the phosphorylation of IκBκ at ser-32 and ser-36 residue followed by its polyubiquitination and degradation (Kumar, Takada et al. 2004). The degradation of IκBα leads to the nuclear translocation of NF-κB. We studied whether the activation of NF-κB in regenerating soft tissue in SJL mice was associated with the phosphorylation and degradation of IκBα. The cytoplasmic extracts from control and regenerating SJL tissues were subjected to Western blot analysis, using antibodies that detect phosphorylated IκBα or total IκBα protein. The data presented in **Figure 12A** show that the phosphorylation level of IκBα protein is

increased in regenerating soft tissue from the SJL mice. The increased phosphorylation of IκBα was associated with the degradation of IκBα protein (**Figure 12A**).

The degradation of IκBα is preceded by its phosphorylation by IκB kinase (IKK) at ser-32 and ser-36 residue (Kumar, Takada et al. 2004). We investigated the activation of IKK in healing ear tissue in SJL mice. The cytoplasmic extracts prepared from regenerating tissue of SJL mice were immunoprecipitated with IKKγ antibody and the kinase activity was determined using GST-IκBα (1-54) as a substrate. A significant increase in the IKK activity was observed in regenerating soft tissue in SJL mice (**Figure 12B**).

We also studied the expression of the genes involved in the activation of NF-κB transcription factor in SJL mice. For these experiments, the RNA was isolated from control and SJL mice 2 days post-injury. The RNA was converted into cDNA and was used to hybridize with the pathway specific NF-κB array. The data presented here suggest that the expression of several genes involved in the activation of NF-κB signaling pathway were increased in regenerating SJL mice (**Figure 13**). We have thus clearly established that the activation of pro-inflammatory transcription factor NF-κB is prominent in SJL mice and can be a useful functional assay for studying soft tissue regeneration.

For transcript level expression analysis, we have also used restriction fragment differential display-PCR (RFDD-PCR) to isolate genes differentially expressed in the MRL (good healer) mouse and the B6 (poor healer) mouse at different stages of wound healing. We chose the RFDD-PCR technology for several reasons. First, this recently developed, innovative technology overcomes the limitations of standard differential display (i.e., preferential amplification of 3'-ends of the transcripts and a high number of false positives), and has the capacity to not only identify differentially expressed genes, but to also identify the sequence polymorphism within the gene. Second, this technology does not require previously constructed cDNA libraries or sequence databases, thus presenting immense advantages when screening for novel therapeutic gene targets. Third, the availability of the entire mouse genome sequence from the public database and available fast-wound healing QTLs further enhance the power of this technology to identify fast-wound healing genes.

We have published the results of this study in a paper (**Masinde, Li et al. 2005**). To briefly summarize these results, we identified 36 genes that were differentially expressed in the regenerating tissues of good and poor healer strains, of which several genes are also genetically linked to wound healing and thus are potential candidate genes for scarless wound healing. These genes belong to different ontologies that may be involved in wound healing/regeneration. We have also identified several genes that are within the wound healing QTL regions. Most of the identified are structural genes encoding proteins for membrane and extracellular matrix. The proteins included vimentin, elongation factor 1-alpha 1, and keratin complex 1. The identification of genes that are differentially expressed and also genetically linked to wound healing provides a framework for future identification of wound healing genes.

Lately, we have also conducted expression analysis using an oligonucleotide based microarray to identify candidate genes. The microarray we used was the Oligator "MEEBO" Mouse Genome Set (illumina, San Diego, CA), which contained 27,784 unique genes. We have

conducted two experiments: one using MRL and one using the congenics. The MRL experiment was carried out with 5 female MRL mice and 5 female SJL mice. The congenic experiment was carried out with 8 male congenic SJL.MRL9-1 mice and 9 male SJL mice. Three weeks and half old mice were ear-punched. The punched-out tissue served as the control of each mouse. At day 4 after the ear punch, about 2 mm wide tissues surrounding the ear punch was cut as the injury treatment. RNA was isolated from both the control and treatment tissues.

Data analysis was carried out using GeneSpring software (Agilent Technologies, Palo Alto, CA). Fold change was the main measure of differential expression between the treatment and the control. Based on our experience, this measure tends to underestimate the difference in gene expression. For example, 1.5 fold change could actually reflect more than 2 fold of difference, the usually cutoff in microarray studies. We tried to use the spike-ins controls to correct this discrepancy in data analysis. The spike-ins were RNA samples with known ratios between C3 and C5, the two dye channels that are used to label the treatment and the control. The median fold change for each of the seven spike-in controls was calculated. Then, these fold change values were made linear to percentage changes with positive and negative numbers to represent up or down regulation, respectively. Linear regression was then carried out using the input RNA ratio as the dependent variable and the linear percentage change as independent variable. Finally, the obtained regression formulae were used to predict input ratios for the genes on the chip from their linear percentage change calculated from fold change.

For the MRL experiment, we have identified 1,745 genes that were significantly different between the day 4 ear-punch treatment and the day 0 control in either MRL alone, SJL alone or both strains (**Table 7**). In MRL, 811 genes were significant, with 11 genes greater than 1.5 fold up regulation and 9 greater than 1.5 fold down regulation. In SJL, there were 882 significant genes, 40 and 25 genes in 1.5 fold down and up regulations, respectively. Forty-two genes were up or down regulated at the same time in MRL and SJL, and 10 genes showed mixed pattern of regulation.

Table 7. Numbers of genes that are significant in the MRL microarray analysis.

	Fold Change[a]				Total
Regulated	<= 0.67	0.67 - 1.0	1.0 - 1.5	>= 1.5	
MRL only	10	404	386	11	811
SJL only	40	422	395	25	882
Both up or down	6	14	14	8	42
One up one down					10
Total					1745

[a] While "<= *0.67*" and "*0.67 - 1.0*" represent >= 1.5 fold down-regulation and < 1.5 fold down-regulation, respectively, "*1.0 - 1.5*" and ">= *1.5*" represent < 1.5 fold up-regulation and >= 1.5 fold up-regulation.

Genes with more than 1.5 fold of change are listed in **Table 8**. There were mainly three types of genes that were differentially expressed genes between the treatment and the control, i.e

genes induced by soft tissue injury. The first category was genes of small proline-rich proteins. The second category was cell structure-related genes. These included genes for actins, keratins, myosins, procollagens, and tubulins. The third category was genes for the proteases and their inhibitors.

Table 8. Known genes that are significant, and 1.5 fold up or down-regulated in the MRL vs SJL microarray experiment

Gene Name	Chr	MRL Fold	MRL Adj	SJL Fold	SJL Adj	Gene Description
In both MRL & SJL						
AK084926	1	6.042	15.078	2.396	5.216	RIKEN cDNA C030045D06 gene
BC046809	17	4.061	9.438	3.525	8.519	Bromodomain containing 2
Unc5a	13	3.531	7.929	2.810	6.427	Unc-5 homolog A (C. elegans)
Nfasc	1	2.898	6.126	1.590	2.859	Neurofascin
5430432M24Rik	2	1.956	3.444	1.688	3.145	Mus musculus RIKEN cDNA 5430432M24 gene (5430432M24Rik), transcript variant 2
Fgfr2	7	0.602	-1.160	0.594	-0.867	Mus musculus fibroblast growth factor receptor 2 (Fgfr2), transcript variant 2
Fkbp1a	2	0.260	-7.381	0.367	-3.913	FK506 binding protein 1a
In MRL only						
Mmp16	4	3.688	8.376			Mus musculus matrix metalloproteinase 16
Gabpb1	2	2.256	4.299			Mus musculus GA repeat binding protein, beta 1 (Gabpb1), transcript variant 1
Tnfsf14	17	2.040	3.684			Tumor necrosis factor (ligand) superfamily, member 14
Pira4	7	1.901	3.288			Paired-Ig-like receptor A4
Slc6a2	8	1.875	3.214			Solute carrier family 6 (neurotransmitter transporter, noradrenalin), member 2
AI428936	7	1.563	2.325			Expressed sequence AI428936
D630023O14Rik	1	0.668	-0.693			RIKEN cDNA D630023O14 gene
D030041I09Rik	1	0.661	-0.738			Nicotinamide nucleotide adenylyltransferase 2
Pla2g4a	1	0.652	-0.797			Mus musculus phospholipase A2, group IVA (cytosolic, calcium-dependent)
AW555464	12	0.635	-0.914			Mus musculus expressed sequence AW555464 (AW555464)
Hsd17b12	2	0.620	-1.023			Hydroxysteroid (17-beta) dehydrogenase 12
Rpl23	11	0.620	-1.023			Ribosomal protein L23
Eef2	10	0.610	-1.098			Mus musculus eukaryotic translation elongation factor 2
Dia1	15	0.606	-1.129			Diaphorase 1 (NADH)
AW742319	9	0.509	-2.024			Protein tyrosine phosphatase-like A domain containing 1
Hnrpab	11	0.436	-2.961			Heterogeneous nuclear ribonucleoprotein A/B
In SJL Only						
Postn	3			3570.000	10441.172	Periostin, osteoblast specific factor
Sprr2d	3			3.616	8.785	Small proline-rich protein 2D
Stfa1	16			3.603	8.747	Stefin A1
Stfa3	16			3.025	7.056	Stefin A3
Fa2h	8			2.598	5.807	Fatty acid 2-hydroxylase
AK039445	1			2.597	5.804	Protein phosphatase 1, regulatory (inhibitor) subunit 12B
Aqp4	18			2.311	4.968	Aquaporin 4
IGKV13-73-1	6			2.169	4.552	Mus musculus IgVk go33r pseudogene.
TRGV1	13			2.103	4.359	Mouse T-cell receptor germline gamma chain gene V-region (V108B).
MoV3sS4gp1	8			2.101	4.353	Mammalian orthoreovirus 3 segment S4, complete sequence.
Krt2-6b	15			1.951	3.915	Keratin complex 2, basic, gene 6b
1810007M14Rik	16			1.680	3.122	RIKEN cDNA 1810007M14 gene
D630010B17Rik	15			1.545	2.727	RIKEN cDNA D630010B17 gene
Barx1	13			1.521	2.657	BarH-like homeobox 1
Ctla2a	13			1.516	2.642	Cytotoxic T lymphocyte-associated protein 2 alpha
Baiap1	6			1.506	2.613	Membrane associated guanylate kinase, WW and PDZ domain containing 1
AF191028	5			0.663	-0.354	Cysteine endopeptidase, papain-type (XCP2)
Tnnt1	7			0.646	-0.470	Mus musculus troponin T1, skeletal, slow
Myom2	8			0.640	-0.513	Myomesin 2
Ank	15			0.631	-0.578	Mus musculus progressive ankylosis
Pgam2	11			0.614	-0.706	Phosphoglycerate mutase 2

Mylpf	7	0.608	-0.753	Mus musculus myosin light chain, phosphorylatable, fast skeletal muscle
Krt2-17	15	0.607	-0.761	Keratin complex 2, basic, gene 17
Btc	5	0.602	-0.801	Betacellulin, epidermal growth factor family member
Actn2	13	0.592	-0.883	Actinin alpha 2
Cidea	18	0.583	-0.960	Cell death-inducing DNA fragmentation factor, alpha subunit-like effector A
Tnni2	7	0.577	-1.012	Troponin I, skeletal, fast 2
Casp6	3	0.573	-1.047	Mus musculus caspase 6
Eln	5	0.570	-1.074	Elastin
Hrc	7	0.570	-1.074	Histidine rich calcium binding protein
1110020C03Rik	4	0.551	-1.251	RIKEN cDNA 1110020C03 gene
Tcap	11	0.549	-1.270	Titin-cap
3110040M04Rik	1	0.538	-1.379	RIKEN cDNA 3110040M04 gene
BC057690	1	0.534	-1.420	Signal transducer and activator of transcription 1
Tnnc2	2	0.508	-1.700	Troponin C2, fast
Elovl5	9	0.503	-1.758	ELOVL family member 5, elongation of long chain fatty acids (yeast)
3110079O15Rik	1	0.480	-2.036	Mus musculus RIKEN cDNA 3110079O15 gene
Hbb-b1	7	0.480	-2.036	Hemoglobin, beta adult major chain
Scd1	19	0.452	-2.414	Stearoyl-Coenzyme A desaturase 1
Col8a1	16	0.431	-2.729	Procollagen, type VIII, alpha 1
Fhl1	x	0.409	-3.094	Four and a half LIM domains 1
Atp2a1	7	0.375	-3.743	ATPase, Ca++ transporting, cardiac muscle, fast twitch 1
Wif1	10	0.374	-3.763	Wnt inhibitory factor 1

As for the chromosome 9 QTL genes, there are 791 known genes between 55 Mb and 124 Mb on chromosome 9 as of June 2006 based on the mouse genome build 36.1 from NCBI. Among these, 491 were on the chip, with 7 genes per Mb. The other 300 genes were not included in the microarray, and could still be involved in wound healing/soft tissue regeneration. Out of the 491 genes, 28 were significant (**Table 9**). Two of these genes showed greater than 1.5 fold down regulation (**Table 10**). In terms of expression profiles that fit the criteria of the candidate genes for the chromosome 9 QTL, they should be uniquely differentially expressed in either super MRL or poor healers such as SJL. This differential expression can be in the form of either down or up regulation. These two genes all fit these criteria.

Table 9. Numbers of genes in the QTL region of chromosome 9 that are significant.

	Fold Change[a]				Total
Regulation	<= 0.67	0.67 - 1.0	1.0 - 1.5	>= 1.5	
MRL only	1	8	6	0	15
SJL only	1	4	8	0	13
Both up or down	0	0	0	0	0
Total					28

[a] While "<= *0.67*" and "*0.67 - 1.0*" represent >= 1.5 fold down-regulation and < 1.5 fold down-regulation, respectively, "*1.0 - 1.5*" and ">= *1.5*" represent < 1.5 fold up-regulation and >= 1.5 fold up-regulation.

In conclusion, most differentially expressed genes, either in MRL or SJL alone, or in both strains, were related to small-proline proteins, cell structural proteins, and matrix

metalloproteinases and their inhibitors. Finally, based on expression patterns in MRL or SJL alone, we have identified two candidate genes in the chromosome 9 QTL region for further examination.

Table 10. Candidate genes in the Chr 9 QTL region that showed differential expression patterns in two microarray experiments.

Gene Name	Position (Mb)	QTL Peak	Experiments	Strain	Regulation	Description
AW742319	64.784989	1	MRL vs. SJL	MRL	1.5 fold down	Protein tyrosine phosphatase-like A domain containing 1
Elovl5	77.703052	2	MRL vs. SJL	SJL	1.5 fold down	ELOVL family member 5, elongation of long chain fatty acids (yeast)

Table 11. Genes that are tested in real time PCR in the chromosome 9 QTL region.

Gene	Start Pos (bp)	Stop Pos (bp)	QTL Peak	Gene Description
Itga11	62475867	62581966	1	integrin, alpha 11
Map2k5	62961776	63175858	1	mitogen activated protein kinase kinase 5
Smad3	63444773	63556000	1	MAD homolog 3 (Drosophila)
Smad6	63751143	63819327	1	MAD homolog 6 (Drosophila)
Map2k1	63983794	64051338	1	mitogen activated protein kinase kinase 1
Rab11a	64514239	64535762	1	RAB11a, member RAS oncogene family
Parp16	65012727	65037224	1	poly (ADP-ribose) polymerase family, member 16
Pdcd7	65144074	65157649	1	programmed cell death protein 7
Rasl12	65196544	65210704	1	RAS-like, family 12
Oaz2	65474596	65488303	1	ornithine decarboxylase antizyme 2
Csnk1g1	65707016	65843020	1	casein kinase 1, gamma 1
Usp3	66315887	66390986	1	ubiquitin specific peptidase 3
Tln2	67017280	67338759	1	talin 2
Foxb1	69556916	69559991	2	forkhead box B1
Ccnb2	70206853	70220718	2	cyclin B2
Aqp9	70909221	70961849	2	aquaporin 9
Ccpg1	72782710	72813123	2	cell cycle progression 1
Gnb5	75097304	75131580	2	guanine nucleotide binding protein, beta 5
Tpbg	85639128	85642507	3	trophoblast glycoprotein
Pgm3	86349194	86368545	3	phosphoglucomutase 3
Rwdd2	86368771	86371614	3	RWD domain containing 2
Mod1	86378094	86492941	3	malic enzyme, supernatant
Prss35	86539561	86554745	3	protease, serine, 35
Snap91	86562350	86678320	3	synaptosomal-associated protein 91
Tbx18	87502145	87529206	3	T-box18
Nt5e	88125533	88169982	3	5' nucleotidase, ecto
Snx14	88174668	88236822	3	sorting nexin 14
Syncrip	88250166	88280101	3	synaptotagmin binding, cytoplasmic RNA interacting protein
Rasgrf1	89707668	89827694	3	RAS protein-specific guanine nucleotide-releasing factor 1
Ctsh	89852402	89873982	3	cathepsin H
Morf4l1	89889562	89912655	3	mortality factor 4 like 1
Adamts7	89961138	89997904	3	a disintegrin-like and metallopeptidase (reprolysin type) with thrombospondin type 1 motif, 7
Atp1b3	96142025	96173651	4	ATPase, Na+/K+ transporting, beta 3 polypeptide
Rnf7	96280289	96327074	4	ring finger protein 7
Rasa2	96351797	96440845	4	RAS p21 protein activator 2
Spsb4	96752834	96827707	4	splA/ryanodine receptor domain and SOCS box containing 4 (alias: SSB4)

As we know, no microarray can possibly include all genes of a specific genome. Accordingly, our microarray analysis only covered about half of the candidate genes in the chromosome 9 QTL region. Even if some genes were in the microarray, we still needed to confirm the microarray results through alternative means. For this purpose, we conducted real time PCR. We chose 36 candidate genes in the QTL region (**Table 11**). These genes are located within QTL peaks 1 (13 genes), 2 (5 genes), 3 (14 genes) and 4 (4 genes). Some of these genes such as Oaz2 were also included in the microarray. Again, same as microarray, we used both super healer MRL and poor healer SJL in real time PCR. For each of the three weeks old mice we used in the experiment, the ear tissues at day 0 were used as the control, and the day 4 tissues after the ear punch were used as the treatment. We used three mice as three biological replicates for each gene. We carried out three PCR reactions for each mouse RNA sample pair. In other words, we had three technical replicates for each biological replicate. Therefore, we had a total of nine replicates for each treatment/control.

The real time PCR experiments are still ongoing. **Table 12** shows some genes for which we have finished all nine replicates and obtained significant results in real time PCR. They showed greater than 2 fold up regulation after the ear punch injury. Most interesting of these were Usp3 at 66.32 Mb under QTL peak 1 and Ccpg1 at 72.78 Mb under QTL peak 2. Usp3 was up regulated 5.87 fold in the MRL injured ear tissues. However, it was up regulated only modestly 1.75 fold in SJL. Similarly, CCpg1 was up regulated 4.90 fold in MRL and stayed almost the same with 1.13 fold change in SJL. The differential expression patterns of these two genes might explain part of the phenotypic difference between MRL and SJL in ear punch healing, i.e. the part caused by the chromosome 9 QTLs. In other words, the chromosome 9 QTLs were caused by the up regulation of these two genes in super healer MRL and almost unchanged regulation in poor healer SJL.

Table 12. Candidate genes of the Chr 9 QTLs that showed significant injury-induced regulation in the ear tissues.

Gene	MRL Cont DCt	MRL Exp DCt	MRL DDCt	MRL Fold Change	SJL Cont DCt	SJL Exp DCt	SJL DDCt	SJL Fold Change
Map2k5	13.08	8.78	-4.29	19.8	12.43	9.74	-2.79	8.83
Usp3	8.33	5.78	-2.55	5.87	6.26	5.45	-0.8	1.75
Tln2	10.47	8.57	-1.9	3.74	9.69	7.84	-1.84	3.59
Ccnb2	11.34	7.05	-4.29	19.52	9.65	7.09	-2.56	5.9
Ccpg1	8.27	5.98	-2.29	4.9	6.45	6.28	-0.17	1.13

Note: 'Dct' refers the difference in threshold cycles between target (amplified gene) and reference (internal control gene). We used the GAPDH-1 as the reference. 'DDct' refers the difference between Dct of the day 4 experiment (Exp) and that of the day 0 control (Cont) in each mouse strain.

The MRL micorarray and the follow-up real time RT-PCR is helpful in identifying candidate genes. But, there are many phonotypical differences between the two strains. For example, the animal sizes are different, and MRL mice are bigger than SJL mice. The bone densities are different, and MRL mice have higher bone density. Accordingly, the identified genes by the expression analysis using either micorarray or real time RT-PCR may not indicate directly that they are responsible for the fast wound healing phenotype. Results of the expression analyses can be only used as supporting evidence. Since the congenic mice only contain the QTL region of the chromosome 9 QTL, the expression analysis using the congenic mice might be more helpful in identifying the candidate genes. This is why we have conducted a second microarray analysis using the congenic and SJL mice.

For the chromosome 9 QTL, there were 41 genes within the peak 3 region, and 28 of the 41 genes were present in the microarray. In the micorarray analysis using the congenic and SJL mice, seven of these 28 genes showed significantly different expressions between the day 4 and day 0 samples in either SJL.MRL9-1 mice or SJL mice (**Table 13**). In other words, the injury treatment induced expression changes in these genes during the 4 day period. While one gene (Mod1) was down-regulated, the rest were all up-regulated. Especially notable were three Bcl2 genes. The maximum change among the three genes was 22.4% for Bcl2a1b in SJL.MRL9-1 mice. The small expression changes in these genes probably reflected the small overall changes for all genes on the chips, and thus could due to technical reasons. It is also possible that changes may have been larger at other time points or for certain cell populations. In conclusion, microarray analysis identified seven significant genes from the 41 candidate genes for the chrosome 9 QTL.

Table 13. Candidate genes within peak 3 of the chromosome 9 QTL that are significant in the gene expression studies using microarray.

Position	Gene	Annotated	SJL.MRL9-1		SJL	
(Mb)	name	function	Fold Change[a]	*p* value[b]	Fold change[a]	*p* value[b]
86.4	Mod1	Malate metabolism	0.755	**0.0003**	0.759	**0.0001**
86.5	Prss35	Proteolysis	1.265	**0.0007**	1.362	**0.0000**
88.3	4930422I07Rik	Unknown	1.044	0.5640	1.159	**0.0224**
88.5	Bcl2a1d	Apoptosis	1.138	**0.0412**	1.059	0.2460
88.8	Bcl2a1a	Apoptosis	1.087	**0.0129**	1.006	0.9260
89.0	Bcl2a1b	Apoptosis	1.224	**0.0112**	1.191	**0.0073**
89.9	Ctsh	Proteolysis	1.270	**0.0015**	1.111	**0.0458**

[a] Fold change refers to the day 4 samples (treatment) vs. day 0 samples (control).

[b] Bold font indicates significance at $p < 0.05$.

In conclusion, our expression analyses using different platforms and using MRL and two poor healing strains are useful in identifying various genes as the candidate genes for wound healing/regeneration. These genes can be used in the next step in identification of the wound healing genes. This next step would be the functional testing using various in vitro and in vivo techniques, coupled with sequencing of these genes in order to identifying the polymorphism that may be responsible for the QTL. The shortcoming of these expression analyses is that the results are not consistent in identifying the same candidate genes. This could be due to the different platforms we used for these expression analyses. Based on this experience, we believe that decisions regarding the choice of candidate genes have to be made based on both the expression analyses and other information, which includes among others, gene functions, the biological processes the genes are involved in, and the importance of the gene functions and the biological processes to wound healing. In this sense, the three Bcl2 anti-apoptotic genes and the anti-apoptotic processes need to be further examined as the possible candidate genes for the chromosome 9 QTL.

5) Detection of mutations in the coding regions of the candidate genes. In all above sections, whether on congenic analysis or on fine mapping or expression analysis, the ultimate objective is to identify candidate genes of wound healing/regeneration. We have used three approaches, fine mapping, congenic analysis and expression analysis, either individually or combined to achieve this goal. Over the entire project period, we have identified many candidate genes that are not only located on the major QTL regions of chromosomes 1 and 9, but also on other chromosome regions. However, we need to further confirm them as candidate genes. One way to confirm is through sequencing. We have employed the approach of direct sequencing to identify mutations or polymorphisms between super healer MRL and poor healer SJL that may explain the difference between the two in the healing phenotype. The complete list of genes that have been sequenced during the project period is shown in **Table 14**. The table also lists the chromosomal locations and their major functions. As can be seen, these genes are involved in signaling, DNA binding, cell cycle control, cell migration, cell proliferation, and skeletal development, which are all important processes in wound healing/tissue regeneration. Among these genes, ATP1B3 (ATPase, Na+/K+ transporting, beta 3 polypeptide), CXCR4, RBP1 (Retinol binding protein 1, cellular, also called CRBP), and TTK (Ttk protein kinase) are also located in either the chromosome 1 or chromosome 9 QTL regions.

Table 14. Candidate genes that are sequenced for mutations between MRL and SJL mice.

Gene Symbol	Full Name	Chromosomal Location	Major Function
ARNT2	Aryl hydrocarbon receptor nuclear translocator 2	7:71385510-71547885	Regulation of transcription
ATP1B3	ATPase, Na+/K+ transporting, beta 3 polypeptide	9:96176577-96208203	Integral to membrane
CTGF	Connective tissue growth factor	10:24357683-24359991	Skeletal development
CXCR4	Chemokine (C-X-C motif) receptor 4	1:128425227-128429292	Cell migration
E2F1	E2F transcription factor 1	2:154622987-154633201	Apoptosis
FOXM1	Forkhead box M1	6:129017917-129030792	Cell proliferation
GJA1 (Connexin43)	Nucleophosmin 1	10:56418919-56432102	Cell-cell signaling
MSX1	Homeo box, msh-like 1	5:36303825-36307788	DNA binding
RBP1 (CRBP)	Retinol binding protein 1, cellular	9:98262249-98285839	Lipid metabolism
RUNX2 (CBFA1)	runt related transcription factor 2	17:42965353-42970028	Skeletal development
TTK	Ttk protein kinase	9:84264841-84301923	Peptidyl-serine phosphorylation

In order to sequence these genes, genomic DNA was isolated from the ears of MRL and SJL mice at two months of age. Ear tissues of five or six animals from each strain were pooled together and used in DNA isolation. A series of PCR primers that amplify the overlapping fragments of the coding regions of the plus strand of the candidate genes were designed. Mutations, if any found, were also confirmed by sequencing the minus strand using another set of PCR primers. For each gene, the DNA accession that was used to design primers was a reference sequence (i.e. manually annotated mRNA sequence in GenBank). PCR products were run on and isolated from agarose gels, and purified using a Qiagen PCR purification kit. Sequencing was performed on the ABI 3700 sequencer. Sequence fragments were assembled together using the Vector NTI software. Assembled Sequences were aligned using the ClustalW software (http://www.ebi.ac.uk/clustalw/index.html).

We have sequenced some or all parts of the mRNA for the genes listed in **Table 14**. We have identified several mutations between MRL and SJL. Two genes that had mutations worth mentioning are the CXCR4 and APT1B3, which are located in the chromosome 1 and 9 QTL

regions, respectively. The mutation in CXCR4 occurring at position 914 of the nucleotides changed G to A in the SJL mouse (**Figure 14, Table 15**). This resulted in a change of amino acid from glycine to glutamic acid at position 265 of the protein. Similarly, two synonymous mutations were found in the ATP1B3 gene of the MRL mouse (**Figure 15, Table 15**). G->A and C->T at positions of 829 and 970, respectively, did not result in any change in the amino acid composition. Although there may not be enough evidence to suggest that these mutations or polymorphisms were actually responsible for the observed phenotype difference between MRL and SJL in ear healing, they certainly provide a basis for further studies of these genes.

```
NM_009911       AGGGGGACATCAGTCAGGGGGATGACAGGTACATCTGTGACCGCCTTTACCCCGATAGCC 720
MRL             ------------------------------------------------------------C
SJL             ------------------------------------------------------------C
                                                                             *
NM_009911       TGTGGATGGTGGTGTTTCAATTCCAGCATATAATGGTGGGTCTCATCCTGCCCGGCATCG 780
MRL             TGTGGATGGTGGTGTTTCAATTCCAGCATATAATGGTGGGTCTCATCCTGCCCGGCATCG
SJL             TGTGGATGGTGGTGTTTCAATTCCAGCATATAATGGTGGGTCTCATCCTGCCCGGCATCG
                ************************************************************
NM_009911       TCATCCTCTCCTGTTACTGCATCATCATCTCTAAGCTGTCACACTCCAAGGGCCACCAGA 840
MRL             TCATCCTCTCCTGTTACTGCATCATCATCTCTAAGCTGTCACACTCCAAGGGCCACCAGA
SJL             TCATCCTCTCCTGTTACTGCATCATCATCTCTAAGCTGTCACACTCCAAGGGCCACCAGA
                ************************************************************
NM_009911       AGCGCAAGGCCCTCAAGACGACAGTCATCCTCATCCTAGCTTTCTTTGCCTGCTGGCTGC 900
MRL             AGCGCAAGGCCCTCAAGACGACAGTCATCCTCATCCTAGCTTTCTTTGCCTGCTGGCTGC
SJL             AGCGCAAGGCCCTCAAGACGACAGTCATCCTCATCCTAGCTTTCTTTGCCTGCTGGCTGC
                ************************************************************
NM_009911       CATATTATGTGGGGATCAGCATCGACTCCTTCATCCTTTTGGGAGTCATCAAGCAAGGAT 960
MRL             CATATTATGTGGGGATCAGCATCGACTCCTTCATCCTTTTGGGAGTCATCAAGCAAGGAT
SJL             CATATTATGTGGGAATCAGCATCGACTCCTTCATCCTTTTGGGAGTCATCAAGCAAGGAT
                ************* ******************************************
NM_009911       GTGACTTCGAGAGCATTGTGCACAAGTGGATCTCCATCACAGAGGCCCTCGCCTTCTTCC 1020
MRL             GTGACTTCGAGAGCAT----------------------------------------
SJL             GTGACTTCGAGAGCAT----------------------------------------
                ****************
```

Figure 14. Alignment of mRNA sequences from mouse strains MRL and SJL and accession NM_009911 for the CXCR4 gene. NM_009911 sequence was the same as that of mouse strain FVB/N. Nucleotide positions on NM_009911 are shown on the right. Mutation is indicated by the absence of a star at position 914.

Table 15. Mutations that are identified by direct sequencing.

Gene	DNA Acc.	Start Codon Pos.	DNA Change	Protein Acc.	Protein Change	Mutant Strain
CXCR4	NM_009911	120	G914A	NP_034041	Gly265Glu	SJL
ATP1B3	NM_007502	149	G829A	NP_031528	Gln227Gln	MRL
ATP1B3	NM_007502	149	C970T	NP_031528	Val274Val	MRL

```
NM_007502       AAAGTATTTTCCATATTATGGGAAAAAACGGCATGTTGGATATCGACAGCCCCTAGTTGC 840
SJL             ---------------------------------GTTGGATATCGACAGCCCCTAGTTGC
MRL             ---------------------------------GTTGGATATCGACAACCCCTAGTTGC
                                                  ************ **********
NM_007502       CGTACAGGTCAAATTTGACTCTGGTCTTAACAAGAAAGAAGTAACAGTTGAGTGCCATAT 900
SJL             CGTACAGGTCAAATTTGACTCTGGTCTTAACAAGAAAGAAGTAACAGTTGAGTGCCATAT
MRL             CGTACAGGTCAAATTTGACTCTGGTCTTAACAAGAAAGAAGTAACAGTTGAGTGCCATAT
                ************************************************************
NM_007502       TGCTGGAACCAGGAACCTAAAAAACAAGAATGAGCGTGACAAGTTCTTGGGACGTGTTTC 960
SJL             TGCTGGAACCAGGAACCTAAAAAACAAGAATGAGCGTGACAAGTTCTTGGGACGTGTTTC
MRL             TGCTGGAACCAGGAACCTAAAAAACAAGAATGAGCGTGACAAGTTCTTGGGACGTGTTTC
                ************************************************************
NM_007502       GTTCAAAGTCACAGCACGAGCCTAGGAATAGGATGTCTCCACAGAATTCATGTTGTGTTG 1020
SJL             GTTCAAAGTCACAGCACGAGCCTAGGAATAGGATGTCTCCACAGAATTCATGTTGTGTTG
MRL             GTTCAAAGTTACAGCACGAGCCTAGGAATAGGATGTCTCCACAGAATTCATGTTGTGTTG
                ********* ************************************************
```

Figure 15. Alignment of mRNA sequences from mouse strains MRL and SJL and accession NM_007502 for the ATP1B3 gene. NM_007502 was obtained from mouse strain BALB/C. Nucleotide positions on NM_007502 are shown on the right. Mutations are indicated by the absence of stars at positions 829 and 970.

6) Development of in vitro technique to test the functions of the candidate genes. For in vitro testing, we need to establish a cell culture system, where MRL produces more cells than poor healing strains. In order to determine whether there is a difference in cell accumulation between super healer MRL and poor healing strains, and whether cell culture can be used for in vitro testing, we have successfully developed methods of establishing cell cultures from ear biopsy tissues of individual mice so that accumulation rates can be statistically calculated for different strains (**Figure 16**). In addition, we were also able to determine accumulation rates using Alamar Blue assay of the passage 3 cultured cells. Results showed that there was a significant, more than 30% difference between the two mouse strains (**Figure 17**). In addition, two lines of evidence suggested that this difference was innate. First, the assay was conducted after cells were cultured for at least two weeks, indicating this difference was not a simple carry-over effect from the tissues. Secondly, cells obtained from the initial punch tissues and cells from the surrounding tissues a week later had the same accumulation rates for each mouse strain. In other words, the cell accumulation potential was not either stimulated due to the punch injury or lost during in vitro culture. Therefore, the difference of cell accumulation rates between MRL and SJL can explain the healing response of the two strains. The super healing ability of the MLR mouse is due to the faster accumulation rates of the ear cells of MRL mice. Cell culture can be used as in vitro system to study gene expressions and to test gene functions.

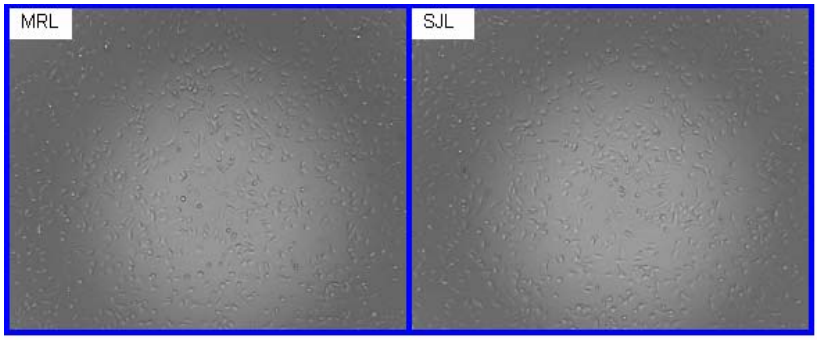

Figure 16. Cell cultures at 50-60% confluency established from the explant ear tissues of the super healer MRL and poor healer SJL mice. The images are under 4X magnification.

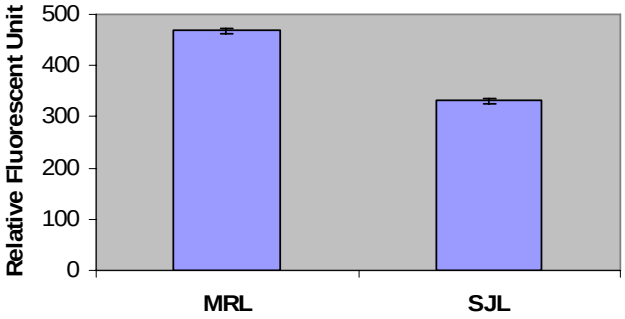

Figure 17. Differential accumulation rates in vitro for the ear cells of MRL and SJL mice. There was a significant difference between MRL and SJL at $p < 0.01$. The data were from the 192 wells of cells in two 96 well plates for each mouse strain.

To limit the inclusion of unwounded tissues and to maximize the inclusion of newly healing tissue in the in vitro system, a ring or donut of newly formed tissue of less than 0.5 mm thickness was carefully dissected from the wound site and used for cell culture work. Considerable care was given to ensure that the amount of extraneous (non-healing) tissue was kept to a minimum in these biopsies. We have conducted an experiment to determine the validity of the in vitro system. In this experiment, we removed biopsies from unwounded (day 0) and regenerating tissues (days 2, 4, 7 and 14 after ear punch) from MRL mice and evaluated expression levels of adipocyte, chondroblast, smooth muscle and fibroblast cell markers. These new data shown in **Table 16** demonstrate that expression levels of adipocyte, chondroblast, smooth muscle and fibroblast markers were reduced by 18,

17, 10 and 2-fold, respectively in biopsies obtained 2 days after ear punch compared to day 0 (unwounded tissue). However, at later time points (day 7 and 14), expression levels of specific markers of some but not other cell types increased compared to day 2. Our results have identified at least two distinct phases in cell-specific responses to ear punch injury in MRL mice: 1) Significant decreases in a majority of cell specific markers between 0 and 2 days, which may reflect a strong dedifferentiation response to injury; 2) A dramatic increase in cell specific markers with later time points, which may likely reflect growth and regeneration of ear punch wounds. Based on these data, we are confident that the biopsies used in cell culture were mostly formed tissues with minimal contamination from unwounded tissue for our in vitro functional system.

Table 16. Relative expression levels of cell-specific markers in the MRL ear punch biopsies.

Cell Type	Marker Gene	Fold Change[a]			
		D0 - D2	D2 - D4	D4 - D7	D7 - D14
keratinocyte	Krtl-14	-1.16	1.29	1.11	1.52
fibroblast	P4hb	-1.84	1.26	1.12	1.77
chondrocyte	Col2a1	-16.8**	3.84**	-1.27	11.31**
adipocyte	Adipoq	-18.13**	4.14**	-1.75	3.36**
smooth muscle	Myh11	-9.58**	4.99**	-1.41	3.71**

[a] D0, D2, D4, D7 and D14 represent tissues collected at different days post ear punch (D0: unwounded tissue). Values are mean fold changes (N = 3-6) between two different time points. **: $P < 0.05$.

To determine the feasibility of lentiviral system in silencing the wound healing candidate genes, we purchased the eGFP short hairpin RNA (shRNA) lentiviral virus from Sigma-Aldrich (St. Louis, MO; Product #: SHC005V) and used it in the in vitro trial assay. First, we obtained a cell line, M1GFP, expressing the eGFP (enhanced green fluorescence protein) gene from Dr. Shin-Tai Chen at the vector core lab of the Musculoskeletal Disease Center (MDC). M1GFP was generated by transducing MC3T3 mouse osteoblasts cells with an MLV-based vector containing the eGFP gene. The expression of eGFP or its inhibition by shRNA-derived siRNA in the M1GFP cells was measured by the intensity of green fluorescence using a Multi-Detection Microplate Reader (BioTek Instruments; Winooski, VT). We carried out the experiment in a 96 well plate with 1,000 cells/well + 10 lentiviral particles/cell (MOI = 10). Our results showed that there was a significant effect of inhibition by the lentivirial shRNA. The eGFP expression as expressed by the fluorescence reading was reduced over 90% (**Figure 18**). Therefore, lentiviral system based shRNA is effective in vitro in inhibiting gene expression, and we have established a procedure for in vitro siRNA assays. A similar procedure can be applied on the wound healing genes in mouse ear cells.

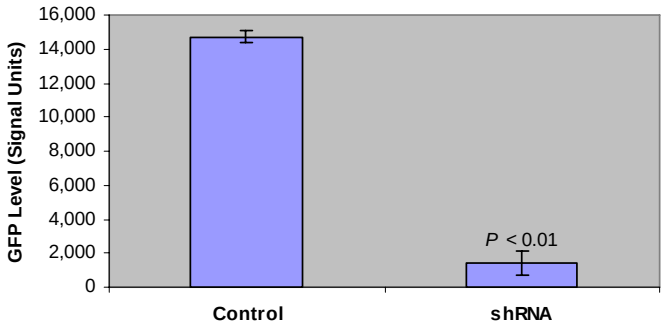

Figure 18. Effect of lentivirial system based shRNA on eGFP expression in the M1GFP mouse osteoblast cells as measured with a micro-plate reader.

7) Development of in vivo technique to test the functions of the candidate genes. In our case, an in vivo technique refers a method that is used to determine the effect on ear healing. Because most of the mouse ear is so thin that local injection of any treatment substance cannot be made. Therefore, we have been using topical application as the method of testing substances. However, topical application has not generated promising results. This could be due to the difficulty for the substance to penetrate the epidermis of the mouse ear. Recently, we have developed a new method of local delivery. In this method, we punch an ear hole as close to the ear canal as possible. A subcutaneous injection can then be made from the body side and in the adjacent thicker area of the ear. There are two advantages for this method. First, there is disparity in terms of healing rates in different areas of the ear. The area near the ear canal for the injection heals the fastest. This has been shown in an experiment that was carried out using MRL mice where we punched three holes on the ear (**Figure 19**). One hole was close to the ear canal ("inner" hole). A second hole was placed just above the edge of the ear ("edge" hole). A third hole was punched at 2 mm from the farthest edge ("outer" hole). The three holes all healed differently from each other (**Figure 20**). The inner hole healed the fastest. Most of the mice closed the inner hole within two weeks. The outer hole ranked second. The edge hole was the slowest to heal; there was hardly any healing by day 25. Therefore, the farther from the ear canal, the slower the healing, and the closer to the ear canal, the better the healing. Secondly, unlike the topical application, this method is effective because we have observed a blister-like bulge on the ear after the injection, indicating the entire amount of the injected drug is retained. Therefore, the fast healing coupled with the effective drug delivery makes the ear punch an ideal model to determine wound healing.

Figure 19. Ear punch experiment showing location affecting the ear healing in the MRL mouse. **Left:** illustration of locations of the punch holes in the ear. **Middle**: picture showing the ear immediately after ear punch. **Right:** picture showing the ear 25 days after ear punch.

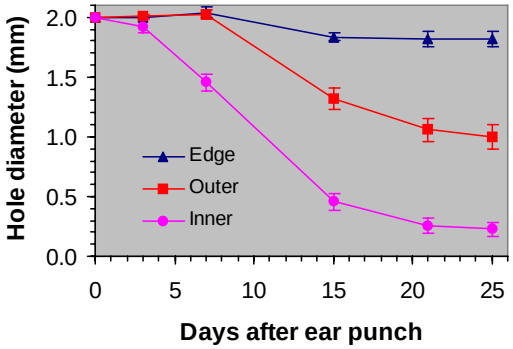

Figure 20. Differential healing rates for ear holes that were punched in different regions of the ears of MRL mice as expressed in the hole diameters (mm).

For the actual in vivo trial assay, we used a green mouse. The green mouse is a transgenic mouse that carries a green protein gene responsible for the green bioluminescence of the jellyfish Aequorea victoria. The green mouse we used was obtained from Dr. Sue Hall at MDC. It contains the eGFP gene in the genetic background of B6, which makes all tissues green under the excitation UV light. Currently, we have tried to use the subcutaneous injection method to deliver the eGFP-shRNA containing lentiviral virus in a few mice. For each experiment, we first collected ear tissues with a 2-mm biopsy punch from both ears of

each mouse as described above. Then, we carried out the viral injection on the right ear also described above. At day 5, we collected ear tissues again with a 3-mm biopsy punch from the same sites of both ears. We used the day 0 tissues as the baseline for adjustment of the day 5 tissues and the left ear as the control for adjustment for the right ear. All tissues were placed in a 96-well plate, and their green color intensity was read in a Multi-Detection Microplate Reader. The tissues were then grinded for protein isolation. The isolated proteins were also used to measure eGFP intensity. In a preliminary experiment with two mice, we found the green color in the right ears treated with the virus was much less than the expected value calculated in consideration of the day 0 baseline and the color change of the left ear control. We achieved over 70% reduction in green color for both mice. However, we are still in the process of improving this method. But unlike topical application, we are confident that this approach will work for in vivo testing. In addition, in vivo knockdown using anti-sense oligodeoxynucleotide has been used successfully in other studies (Nakano, Oyamada et al. 2008).

The ultimate in vivo functional testing is to knockout genes and to use the knockout mice. We have used the knockout mice to test the CXCR4 gene and to determine its role in wound healing/soft tissue regeneration. As we have discussed earlier, one of the major QTLs for wound healing/sot tissue regeneration is located on chromosome 1 at 36.9–81.6 cM. At 67.4 cM within this QTL region is the chemokine receptor gene CXCR4. We believe that CXCR4 is a strong candidate gene of the chromosome 1 QTL. This is based on the following reasons. First, our in vitro study of ear cells indicates that differences in healing response between the super healer MRL and poor healers such as SJL may be in part explained by the differences in cell accumulation rate. Previous studies show that CXCR4 and the SDF-1 axis, which CXCR4 belongs to, regulate the proliferation of many cells types including stem cells. Secondly, our ear punch experiment presented above suggests that location on the ear affects the rate of wound healing, and the closer to the ear canal, the better healing. Thus, wound healing factors may originate in the blood. One of such factors could be CXCR4 positive cells. CXCR4, a chemokine receptor on cell's surface, regulates the trafficking of various types of CXCR4+ cells, especially CXCR4+ stem cells along the gradient of its chemotactic ligand SDF-1. Trafficking of CXCR4+ stem cells to the wound site leads to local cell proliferation and wound healing. Thirdly, in our array analysis, expression of CXCR4 was significantly up-regulated during wound healing and between good and poor healer mice (data not presented). Finally, beside cell migration and proliferation, other processes such as inflammation, cell adhesion, cell-cell and cell-matrix interactions are also involved in regulating wound healing. It is known that CXCR4 and the SDF-1 axis are involved in all these processes.

In view of these roles of CXCR4 in wound healing, mice deficient for CXCR4 would thus be expected to show a deficiency in their healing response. To examine this, we obtained CXCR4 knockout and their corresponding controls from The Jackson Laboratory (Bar Harbor, Maine). As shown in **Figure 21**, an analysis of healing rates of ear punch injuries in the CXCR4 knockout, wild type control from the same colony and progenitor C57BL/6 strain (6 females each) demonstrated that mice deficient in CXCR4 exhibited an increased rate of healing from day 15 post injury onwards. No differences were seen between the wild control from the same colony and the progenitor strain. These results are somewhat surprising. However, the explanation for this observation may lay in the possibility that stem cell trafficking to the wound site may also be mediated by alternative means other than CXCR4, such as CXCR7, another

receptor for SDF-1. Regardless of theoretical basis, these experimental data DO demonstrate in vivo testing using the knocokout mice can be used to identify candidate genes for wound healing/soft tissue regeneration.

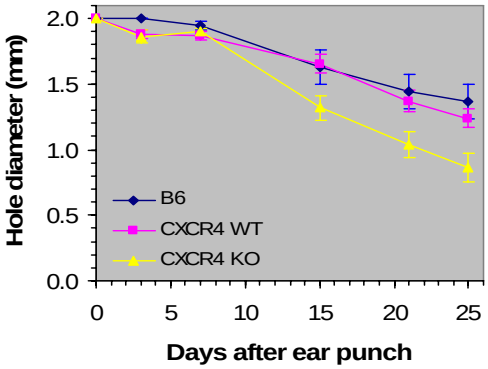

Figure 21. Differential ear healing rates of the CXCR4 knockout mice as compared to the wild type control mice from the same colony and the progenitor C57BL/6 mice.

3. KEY RESEARCH ACCOMPLISHMENTS

1) We have evaluated the ear wound healing of 20 different inbred strains of mice. We have found major differences among the surveyed inbred strains. We have also found a strong heritability for the ear wound healing phenotype.

2) We have generated three crosses, MRL X SJL, MRL X CAST and DBA X 129, and produced a total of 1,453 F2 mice. Through the linkage analyses of these crosses we have identified a number of QTLs on different chromosomes, among which the chromosome 9 QTL is the most important one and harbors presumably key genes for wound healing/regeneration.

3) We have obtained one congenic and one sub congenic homozygous strain for the chromosome 9 QTL and several heterozygous congenic strains for the chromosome 1 and 4 QTLs. We have evaluated these congenic and sub congenic strains for their phenotypic performance in wound healing/regeneration. We have obtained significant differences between the congenic strains and the poor healing progenitor strain.

4) We have bred 947 additional mice for MRL X SJL, making a total of 1,580 F2 mice for this cross. We have used these mice for fine mapping of the chromosome 9 and 4 QTL regions. Fine mapping of the chromosome 9 QTL region has enabled us to identify the major effect region to just a few megabases and a few dozens of candidate genes.

5) We have conducted several expression analyses including a protein expression analysis, a cDNA microrray analysis, a cDNA based restriction fragment differential display-PCR analysis and an oligonucleotide based pathway and whole genome microarray analyses. In each analysis, we have identified a number of significant genes that can be considered the candidate genes for wound healing/regeneration. These genes are involved in various pathways such as those for small-prolines, inflammation, cell structures, extracellular matrix formation, and apoptosis, to name a few.

6) Over the entire project period, we have sequenced the coding region for a total of 11 candidate genes that are not only located on the QTL regions of chromosome 9 and other chromosomes but also in the non-QTL regions of the mouse chromosomes. We have identified some mutations, for example in the CXCR4 gene of the chromosome 1 QTL and the APT1B3 gene of the chromosome 9 QTL.

7) We have established a cell culture system for in vitro testing. We have found that the cell accumulation rate of super healer MRL was much faster than poor healer SJL, thus confirming the utility of such a system. In addition, we have also tested a lentiviral shRNA system for in vitro knocking down of gene expression.

8) We have developed a new method of local delivery for in vivo testing. In this method, we punch an ear hole close to the ear canal. A subcutaneous injection can then be made from the body side and in the adjacent thicker area of the ear.

4. ADDITIONAL PROGRESS

The funding through this grant has supported not only the proposed work on wound healing/soft tissue regeneration but also other related work. In the following section, Reportable Outcomes, we have listed all publications that have stemmed out of the work either wholly or partially supported by this grant. Some of the related work is on methodologies for the proposed work, such as QTL and microarray analyses. Other however is on bone density and bone size -- parameters that are related to bone fracture and fracture repair. We believe that the process of fracture repair is relevant to that of wound healing. Both probably are under the controls of common genes and common mechanisms. Due to limit of space, we cannot present all of our work. We only present one piece of related work on bone-regeneration as an example.

Genetic variation in bone-regenerative capacity has not been studied in any animal model system. We developed a "drill-hole" model in the tail vertebra of inbred strains of mice that allows us to reproducibly introduce an injury with a defined boundary and quantify the rate of bone healing using the combination of high-resolution Faxitron X-ray imaging and the ChemiImager 4000 Low Light Imaging System. We have published the results in a publication (**Li, Gu et al. 2001**). To briefly summarize the results of this study, we demonstrate using this model that bone-regenerative capacity is a genetically controlled trait with an estimated heritability of 72%, and that it differs significantly among inbred strains of mice. Of the 12 inbred strains tested, Sencar/PtJ was identified as the most suitable model for the study of hard-tissue regeneration. This strain regained 73% of bone loss 30 days after injury, in contrast to the slow healer, CBA/J, which recovered only 25% of the bone loss during the same period. Bone-regenerative capacity was not correlated with soft-tissue-regenerative capacity, suggesting that different sets of genes may regulate soft- and hard-tissue regeneration. It was, however, significantly correlated with total bone mineral density ($R = 0.49$, $p < 0.01$), indicating that high bone density is associated not only with prevention of bone fracture, but also with promotion of bone regeneration

5. REPORTABLE OUTCOMES

1) Li X, Mohan S, Gu W, Miyakoshi N, Baylink DJ. Differential protein profile in the ear-punched tissue of regeneration and non-regeneration strains of mice: a novel approach to explore the candidate genes for soft tissue regeneration. Biochem Biophys Acta 1524:102-109, 2000.

2) Li X, Gu W, Masinde G, Hamilton-Ulland M, Rundle CH, Mohan S, Baylink DJ. Genetic variation in bone-regenerative capacity among inbred strains of mice. Bone 29:134-140, 2001.

3) Li X, Gu W, Masinde G, Hamilton-Ulland M, Xu S, Mohan S, Baylink DJ. Genetic control of rate of wound healing in mice. Heredity 86:1-7, 2001.

4) Li XL, Mohan S, Gu W, Baylink DJ. Analysis of gene expression in the wound repair/regeneration process. Mammalian Genome 12:52-59, 2001.

5) Masinde G, Li X, Gu W, Davidson H, Mohan S, Baylink DJ. Identification of would healing/regeneration QTLs at multiple time points that explain seventy percent of variance in (MRL/MpJ and SJL/J) F2 population. Genomics Res 11:2027-2033, 2001.

6) Li X, Gu W, Mohan S, Baylink DJ. DNA microarrays: their use and misuse. Microcirculation 9:13-22, 2002.

7) Masinde GL, Li X, Gu W, Davidson H, Hamilton-Ulland M, Mohan S and Baylink DJ. Quantitative trait loci (QTL) for lean body mass and body length in MRL/MPJ and SJL/J F2 mice. Functional and Integrative Genomics 2:98-104, 2002.

8) Masinde GL, Li X, Gu W, Hamilton UM, Mohan S, Baylink DJ. Quantitative trait loci that harbor genes regulating muscle size in (MRL/MPJ X SJL) F2 mice. Functional and Integrative Genomics 2:120-125, 2002.

9) Mohan S, Masinde G, Li X, Baylink DJ. Mapping Quantitative Trait Loci That Influence Serum IGF Binding Protein-5 levels in F2 Mice (MRL/MPJ X SJL/J). Endocrinology 144:3491-6, 2003.

10) Wang H, ZhangYM, Li X, Masinde G, Mohan S, Baylink DJ, Xu S. Bayesian Shrinkage Estimation of Quantitative Trait Loci Parameters. Genetics 170:465-480, 2005

11) Yu H, Mohan S, Masinde G, and Baylink DJ. Mapping the Dominant Wound Healing and Soft Tissue Regeneration QTL in MRL X CAST. Mammalian Genome 16:918-924, 2005.

12) Li X, Quigg R, Zhou J, Xu S, Masinde G, Mohan S, Baylink DJ. A Critical Evaluation of the Effect of Population Size and Phenotypic Measurement on QTL Detection and Localization using a Large F2 Murine Mapping Population. Genetics and Molecular Biology 29:166-173, 2006.

13) Masinde G, Li R, Nguyen B, Yu H, Srivastava A, Edderkaoui B, Wergedal J, Baylink DJ and Mohan S. New Quantitative Trait Loci (QTL) That Regulate Wound Healing in an intercross progeny from DBA/1J and 129x1/SvJ inbred strains of mice. Funct Int Genomics 6:157-163, 2006.

14) Yu H, Baylink DJ, Masinde GL, Li R, Nguyen B, Davidson HM, Xu S, Mohan S. Mouse Chromosome 9 Quantitative Trait Loci for Soft Tissue Regeneration: Congenic Analysis and Fine Mapping. Wound Repair Regen 15:922-7, 2007.

6. CONCLUSIONS

1) Evaluation of 20 different inbred strains of mice indicated that major differences existed among mouse strains in the ear hole healing. MRL and its presumed progenitor strain LG showed the fastest healing, and healed four times faster than the worst healing strains. With a heritability of 86%, the ear wound healing phenotype is strongly genetically determined and a polygenic quantitative trait whose genes can be identified.

2) Based on the data of F2 mice from either super healer MRL or good healer DBA in crossing with poor healers, we have identified QTLs on at least 10 chromosomes, which are 1, 3, 4, 6, 7, 9, 12, 13, 17 and 18. The magnitude of these QTLs as measured by the LOD score and the amount of variance explained indicate that those on chromosomes 9, 1 and 4 are most important and contain key genes for the ear healing phenotype.

3) Chromosome 9 and 4 congenic analyses have indicated that mice containing the QTL regions of MRL chromosomes showed better healing than the poor healing SJL mice. This is especially true with male mice where the chromosome 9 congenic showed significant 12% better healing than SJL.

4) Fine mapping using 1,580 F2 mice of the MRL X SJL cross indicated the presence of at least three effect peaks within the chromosome 9 QTL region. Peak 3, within just a few megabases on the chromosome, explained 36% of the F2 phenotypic variance based on the Bayesian shrinkage estimation, and was the major peak. Therefore, peak 3 is the most likely region harboring the chromosome 9 QTL genes. There were only 41 candidate genes in this region.

5) Expression analysis indicated that this analysis can be used to identify candidate genes of polygenic quantitative traits. In each of several expression analyses that have been done, we identified a number of significant genes that may be responsible for wound healing/regeneration. Most of these are involved in the biological processes or pathways related to wound healing/tissue regeneration. The examples of the identified genes include keratin complex 2-6A, small proline-rich protein 1A and 2A and formin-binding protein, which are all involved in base membrane or extracellular matrix formation. Notable among other identified genes are anti-apoptotic Bcl2a1a, Bcl2a1b and Bcl2a1d.

6) Sequencing the coding regions of the candidate genes in the QTL or non-QTL regions of the chromosomes can be used to identify mutations or polymorphisms that may be responsible for the wound healing/regeneration phenotype. We have identified several mutations in the CXCR4 gene of the chromosome 1 QTL and the APT1B3 gene of the chromosome 9 QTL. However, their relationships to the wound healing phenotype are yet to be determined.

7) The accumulation rate of ear cells from super healer MRL in vitro was much faster than those from poor healer SJL. This indicates that the super healing phenotype of the MRL mouse is probably due to the faster cell accumulation, and that cell culture is a valid system for in vitro testing for effect on wound healing. Our data also show that a lentiviral shRNA can be used in vitro to knock down gene expression.

8) In vivo testing for effect on wound healing can be done by local injection on the ear. An ear hole is first punched next to the ear canal. Then, a subcutaneous injection of a testing substance can be made from the body side and in the adjacent thicker area of the ear. Gene knockout mice can also used in evaluation of candidate genes in wound healing.

9) In summary, we have made achievements in several fronts in the genetics of wound healing/tissue regeneration. These achievements have added significant knowledge to the regenerative medicine, and also laid a foundation for the identification of the wound healing/soft tissue regeneration genes.

10) Our results from this project strongly suggest that anti-apoptosis and one or more of anti-apoptotic genes Bcl2a1a, Bcl2a1b and Bcl2a1d are the biological process and the genes, respectively, that are responsible for the chromosome 9 QTL. For the chromosome 1, CXCR4 is a strong candidate of the QTL genes. CXCR4 and the SDF-1 axis may be involved in wound healing/soft tissue regeneration by mediating the mobilization and trafficking of CXCR4+ stem cells to the wound site, leading to local cell proliferation.

11) In conclusion, we have made several significant advances in our effort to identify genes and their pathways that contribute to fast wound healing.

7. REFERENCES

Blankenhorn, E. P., S. Troutman, et al. (2003). "Sexually dimorphic genes regulate healing and regeneration in MRL mice." Mamm Genome **14**(4): 250-60.

Borgens, R. B. (1982). "Mice regrow the tips of their foretoes." Science **217**(4561): 747-50.

Brockes, J. P. (1997). "Amphibian limb regeneration: rebuilding a complex structure." Science **276**(5309): 81-7.

Chadwick, R. B., L. Bu, et al. (2007). "Digit tip regrowth and differential gene expression in MRL/Mpj, DBA/2, and C57BL/6 mice." Wound Repair Regen **15**(2): 275-84.

Clark, L. D., R. K. Clark, et al. (1998). "A new murine model for mammalian wound repair and regeneration." Clin Immunol Immunopathol **88**(1): 35-45.

Dinsmore, C. (1991). A History of Regeneration: Milestones in the Evolution of a Science. New York, Cambridge University Press.

Goss, R. J. (1970). "Problems of antlerogesis." Clin Orthop Relat Res **69**: 227-38.

Goss, R. J. and L. N. Grimes (1975). "Epidermal downgrowths in regenerating rabbit ear holes." J Morphol **146**(4): 533-42.

Han, M., X. Yang, et al. (2005). "Limb regeneration in higher vertebrates: developing a roadmap." Anat Rec B New Anat **287**(1): 14-24.

Haris Naseem, R., A. P. Meeson, et al. (2007). "Reparative myocardial mechanisms in adult C57BL/6 and MRL mice following injury." Physiol Genomics **30**(1): 44-52.

Heber-Katz, E., P. Chen, et al. (2004). "Regeneration in MRL mice: further genetic loci controlling the ear hole closure trait using MRL and M.m. Castaneus mice." Wound Repair Regen **12**(3): 384-92.

Heber-Katz, E., J. Leferovich, et al. (2004). "The scarless heart and the MRL mouse." Philos Trans R Soc Lond B Biol Sci **359**(1445): 785-93.

Heber-Katz, E., J. M. Leferovich, et al. (2004). "Spallanzani's mouse: a model of restoration and regeneration." Curr Top Microbiol Immunol **280**: 165-89.

Johnson, S. L. and J. A. Weston (1995). "Temperature-sensitive mutations that cause stage-specific defects in Zebrafish fin regeneration." Genetics **141**(4): 1583-95.

Karin, M. and M. Delhase (2000). "The I kappa B kinase (IKK) and NF-kappa B: key elements of proinflammatory signalling." Semin Immunol **12**(1): 85-98.

Karin, M. and A. Lin (2002). "NF-kappaB at the crossroads of life and death." Nat Immunol **3**(3): 221-7.

Kench, J. A., D. M. Russell, et al. (1999). "Aberrant wound healing and TGF-beta production in the autoimmune-prone MRL/+ mouse." Clin Immunol **92**(3): 300-10.

King, P. A. (1979). "Trapped finger injury." Med J Aust **2**(11): 580-2.

Kumar, A. and A. M. Boriek (2003). "Mechanical stress activates the nuclear factor-kappaB pathway in skeletal muscle fibers: a possible role in Duchenne muscular dystrophy." Faseb J **17**(3): 386-96.

Kumar, A., I. Chaudhry, et al. (2002). "Distinct signaling pathways are activated in response to mechanical stress applied axially and transversely to skeletal muscle fibers." J Biol Chem **277**(48): 46493-503.

Kumar, A., S. Lnu, et al. (2003). "Mechanical stretch activates nuclear factor-kappaB, activator protein-1, and mitogen-activated protein kinases in lung parenchyma: implications in asthma." Faseb J **17**(13): 1800-11.

Kumar, A., Y. Takada, et al. (2004). "Nuclear factor-kappaB: its role in health and disease." J Mol Med **82**(7): 434-48.

Lambert, P. R. (1994). "Inner ear hair cell regeneration in a mammal: identification of a triggering factor." Laryngoscope **104**(6 Pt 1): 701-18.

Leferovich, J. M., K. Bedelbaeva, et al. (2001). "Heart regeneration in adult MRL mice." Proc Natl Acad Sci U S A **98**(17): 9830-5.

Li, X., W. Gu, et al. (2001). "Genetic variation in bone-regenerative capacity among inbred strains of mice." Bone **29**(2): 134-40.

Li, X., W. Gu, et al. (2001). "Genetic control of the rate of wound healing in mice." Heredity **86**(Pt 6): 668-74.

Li, X., S. Mohan, et al. (2001). "Analysis of gene expression in the wound repair/regeneration process." Mamm Genome **12**(1): 52-9.

Li, X., S. Mohan, et al. (2000). "Differential protein profile in the ear-punched tissue of regeneration and non-regeneration strains of mice: a novel approach to explore the candidate genes for soft-tissue regeneration." Biochim Biophys Acta **1524**(2-3): 102-9.

Masinde, G., X. Li, et al. (2005). "Isolation of wound healing/regeneration genes using restrictive fragment differential display-PCR in MRL/MPJ and C57BL/6 mice." Biochem Biophys Res Commun **330**(1): 117-22.

Masinde, G. L., R. Li, et al. (2006). "New quantitative trait loci that regulate wound healing in an intercross progeny from DBA/1J and 129 x 1/SvJ inbred strains of mice." Funct Integr Genomics **6**(2): 157-63.

Masinde, G. L., X. Li, et al. (2001). "Identification of wound healing/regeneration quantitative trait loci (QTL) at multiple time points that explain seventy percent of variance in (MRL/MpJ and SJL/J) mice F2 population." Genome Res **11**(12): 2027-33.

Nakano, Y., M. Oyamada, et al. (2008). "Connexin43 knockdown accelerates wound healing but inhibits mesenchymal transition after corneal endothelial injury in vivo." Invest Ophthalmol Vis Sci **49**(1): 93-104.

Odelberg, S. J. (2004). "Unraveling the molecular basis for regenerative cellular plasticity." PLoS Biol **2**(8): E232.

Poss, K. D., A. Nechiporuk, et al. (2002). "Mps1 defines a proximal blastemal proliferative compartment essential for zebrafish fin regeneration." Development **129**(22): 5141-9.

Raya, A., A. Consiglio, et al. (2004). "The zebrafish as a model of heart regeneration." Cloning Stem Cells **6**(4): 345-51.

Schaffner, F. (1991). "Structural and functional aspects of regeneration of human liver." Dig Dis Sci **36**(9): 1282-6.

Singer, A. J. and R. A. Clark (1999). "Cutaneous wound healing." N Engl J Med **341**(10): 738-46.

Tanaka, E. M. (2003). "Cell differentiation and cell fate during urodele tail and limb regeneration." Curr Opin Genet Dev **13**(5): 497-501.

Ueno, M., B. L. Lyons, et al. (2005). "Accelerated wound healing of alkali-burned corneas in MRL mice is associated with a reduced inflammatory signature." Invest Ophthalmol Vis Sci **46**(11): 4097-106.

Wang, H., Y. M. Zhang, et al. (2005). "Bayesian shrinkage estimation of quantitative trait loci parameters." Genetics **170**(1): 465-80.

Yu, H., D. J. Baylink, et al. (2007). "Mouse Chromosome 9 QTL for Soft Tissue Regeneration: Congenic Analysis and Fine Mapping." Wound Repair Regen **15**(6): 922-7.

Yu, H., S. Mohan, et al. (2005). "Mapping the dominant wound healing and soft tissue regeneration QTL in MRL x CAST." Mamm Genome **16**(12): 918-24.

PROGRESS REPORT 1999-2008, TECHNICAL OBJECTIVE-3

3.1 INTRODUCTION

Osteoporosis is a systemic skeletal disease characterized by low bone mass and micro architectural deterioration of bone tissue. The low bone mass in osteoporotic patients is a result of low amount of bone accrued during the early life, a high rate of bone loss in later life, or a combination of both factors. The factors known to influence bone mass accumulation during growth include heredity, gender, diet, endocrine effectors, and mechanical forces. Quantitatively, the most important determinants appear to be hereditary, which is exemplified in the genetic epidemiological analyses related to recurrence risk and twin studies on bone mineral density (BMD) and bone turnover. Although the precise value of genetic contribution to BMD is subject to discussion, several studies have estimated the heritability for BMD to be as high as 80%, suggesting that the majority of variance in peak BMD values can be explained by genetic factors. This suggests that there are "bone density" genes, variants of which could result in BMD levels that vary from one individual to another. These differences can be seen during attainment of peak BMD early in life or in the rate of bone loss later in life. BMD is a polygenetic trait with multiple genes believed to be involved in regulating bone density. Genome-wide linkage screens for genes underlying BMD variability, conducted in humans and mice, have identified important regions on several chromosomes (described as quantitative trait loci, QTLs) that regulate BMD and other traits. So far, these studies have confirmed the influence of some major genes on BMD and related traits; however, the identification of gene(s) has not yet been accomplished. Therefore, application of chemical mutagenesis screen to identify genes that regulate skeletal tissues was considered as an effective complementary approach to discover gene function. The chemical mutagen N-ethyl-N-nitrosourea (ENU) was proven to be most effective in generating mutations in mice, with a frequency of one mutation per gene every 175-655 gametes, providing a highly efficient screen of mutagenized mice of phenotypes of interest. The ENU approach has produced variants in several disease models that mimic phenotypes commonly seen in humans in the clinical setting. The successful application of ENU in several phenotype driven screens in various centers was encouraging factor in our strategy to apply ENU for discovering musculoskeletal phenotypes, which was not employed elsewhere. An added advantage of this approach was that any locus identified in the ENU study would presumably represent one gene in contrast to QTLs identified by linkage studies, which is likely to represent multiple genes at each locus. Thus, positional cloning of the gene identified by the ENU mutagenesis approach was considered potentially easier.

The goal of the Technical Objective-3 was to identify and characterize novel genes or to elucidate the function for known genes that play key role in the metabolism of bone and soft tissue using a phenotype driven ENU mutagenesis approach. The major advantage of this systematic ENU screening is that one begins with a phenotype of interest and is therefore assured of finding a gene whose function is relevant to the organ system of interest. The typical whole genome mutagenesis screen involved treating the male mice with ENU and breeding them to wild type females. The offspring are screened through a series of tests to identify the individual phenotypic deviant (a term used for extreme-scoring) mice, which is most likely to bear a large effect Mendelian mutation. The phenotypic deviant mouse, which is often defined as 2-3 SD units from non-mutagenized control mean, are backcrossed with wild type mice to determine whether the abnormality segregates bimodally in their offspring. Once we have identified mutant strains with phenotype of interest and

established that mutation is stable and inheritable then next step was to identify the mutant gene. Mapping of the mutant gene was initiated by identifying the chromosomal location of the mutation by standard QTL mapping approach. The mutant locus was then fine mapped to narrow the locus to a few genes and then by applying microarray and sequencing techniques, we believed we can identify the mutant gene. In future studies we would determine the consequences of mutation on gene product and its functions. In addition, we will determine if there are polymorphisms in human homologs and evaluate the significance of such polymorphisms in epidemiological studies. The ultimate goal was to provide a fundamental molecular foundation for future therapies and diagnostic risk assessments for the musculoskeletal system in battlefield injuries.

To accomplish the goal of identifying genes that regulates determinants of bone strength using ENU mutagenesis approach, we proposed several Specific Objectives during the grant period 1999-2008 with the following broad goals in mind.

1) Optimize ENU dose, injection schedule, time of recovery after ENU injections, breeding procedures for ENU injected males, and, screening strategy to identify ENU induced phenotypic deviants.
2) Generate mutations by ENU treatment of male mice, and screen by one-generation dominant and two-generation recessive mutations.
3) Confirm interesting phenotypic deviants by backcrossing them with wild type mice and perform phenotypic characterization of mutant mice that appear to be inheritable in backcross.
4) Map the chromosomal location of the mutants by interval mapping approach.
5) Apply microarray technique to identify genes and potential pathways that are differentially expressed in mutant mice.
6) Identify candidate gene in the chromosomal locus of selected mutant mouse.

We have successfully completed all of the proposed objectives. For the sake of clarity and continuity, we have organized the progress report using the specific goals described above.

3.2 BODY OF PROGRESS REPORT

3.2 GOAL 1. Optimize ENU dose, injection schedule, time of recovery after ENU injections, breeding procedures for ENU injected males, and screening strategy to identify ENU induced phenotypic deviants.

3.2.1 Determination of optimal N-ethyl-N-nitrosourea (ENU) dose and breeding procedures

I. We initially selected C3H/HeJ (C3H) mice in our ENU mutagenesis program, which we earlier identified to possess the highest bone mineral density (BMD) among 13 inbred strains. Since ENU mutagenesis most likely leads to generation of hypomorphs, it was predicted that use of a strain with high BMD mice is ideal for identifying genes that regulate higher bone density in C3H mice. In addition, it was reported that C3H mice was one of the few strains that can tolerate ENU very well and is one of the most fertile strains after a initial recovery period. Consequently, large number of mutants could be generated with similar amount of effort, as compared to other strains of mice that are relatively less fertile after ENU injections. An added advantage with C3H strain is that spermatogonia from this strain can be frozen successfully for subsequent recovery of mutants. This is an essential feature for the success of our ENU program.

II. Injection of ENU in C3H male mice: Seven batches of 8-10 week old C3H/HeJ (C3H) males were weighed individually and then injected with 85-350 mg/kg dose of ENU by intra peritoneal injections (for details of dose for each group see **Table 1**). All C3H male mice were purchased from The Jackson Lab (Bar Harbor, ME) and acclimatized for 2 weeks before ENU injections. ENU was purchased from Sigma Chemical Co. (St Loius, MO) in a 100mL serum bottle (ISOPAC, Cat # N3385, containing 1 g powder, and stored in -20°C in its original shipping container). To make ENU solution, 5mL of 100% ethanol was injected in the ISOPAC ENU bottle and suspension was warmed in a 60^{o}C water bath, and subsequently diluted to 10 mg/mL using sterilized citrate/phosphate buffer. ENU concentration was finally determined by measuring the absorbance at 395nm, where 0.7 OD was considered equivalent to 1.0 mg/mL.

III. Each mouse was individually weighed, and ENU was administered by intra-peritoneal injections. After ENU injections, all mice were placed in the disposable animal cages (four mice per cage) and maintained for 48 hours in the fume hood, where ENU is administered. Two days after the ENU injections, all mice were placed in a room with 12-hour day/night cycle and fed standard rodent diet for 10-12 weeks in groups of 2-4 mice/cage. ENU was handled with extreme care since it is a powerful mutagen.

IV. Our optimization studies with various doses of ENU indicated that a fractionated dose of 300 mg/kg (3X100 mg/kg) was well tolerated by C3H mice. About 40% of male founders produced live pups with a cumulative dose of 300 mg/kg of ENU. Based on these findings, we decided to inject C3H mice with an ENU dose of 3X100 mg/kg. In the subsequent years of grant, we injected two batches of 8-10 week old 20 C3H male mice, four batches of 20 B6 mice, and three batches of MRL mice with 3x100 mg/kg of ENU. These ENU injected males were used for generating F1 (for dominant screening) and F3 (for recessive screening) progeny. The B6 and MRL strains of mice were also injected with a dose of 3X100 mg/kg of ENU because we observed that both MRL and B6 mice can tolerate similar dose and regain fertility within 12-20 week post ENU injection (**Table-2**). We timed the ENU injection schedule with an interval of 3-month period, which allowed us a continuous supply of ENU mutagenized C3H, B6, and MRL males for breeding with wild type females.

V. Breeding of ENU injected Males: Since ENU is mutagenic or cytotoxic to all stages of spermatogenic cells, causing cessation of cell division and cell death, successfully mutagenized mice are rendered temporarily sterile after existing post-meiotic cells have completed spermatogenesis to become mature spermatozoa, which takes about 4 weeks after ENU injection. In a typical case, new rounds of spermatogenesis will cease for 10-12 weeks following injection, during this period surviving mutagenized stem cell spermatogonia repopulate the testis. In case of C3H mice, we observed that C3H males regained fertility 12-14 weeks period after the final ENU injection. Mortality and fertility was monitored and recorded at this stage. To insure enough progeny are produced in the life span of a male, each ENU-treated C3H males was mated with two 8-10 week old C3H females. The females, once become pregnant are moved to isolator cages for delivery of off springs. A new female is added to ENU male to replace the pregnant female. After 8-10 week period, the males are rotated back to the original group of females to start the cycle over again. Female mice were replaced with younger mice (10 weeks) after 6

months and the males were replaced with new ENU treated mice after three months (**Figure-1**).

VI. To insure that repeat mutations are not scored from one ENU injected male, a maximum of 50 progeny was generated and screened for each male.

3.2.2 Identification of phenotypes that will be screened in ENU induced mutants.

In any forward genetic screen, the yield would depend on type of the phenotypic screen and the sensitivity and reproducibility of measurements. Since the phenotypic screen for ENU studies involves a large number of animals, it was imperative that we must be able to perform them in a quick manner.

Our focus was on musculoskeletal phenotypes. Therefore, we developed a systematic and detailed screening procedure for identifying phenotypes related to bone mass, bone turnover, bone structural properties etc and addressed issues related to reliability of screening procedures. Bone mineral density (BMD) measurement is the most common phenotypic trait used in studies evaluating heritability or polymorphic gene markers of osteoporosis because osteoporosis is defined in individual patients by low bone density. However, several other factors also contribute to bone strength and determine fracture risk, including: bone size, shape, architecture, tissue quality, age, body weight, and muscle strength. In addition, we focused of total body phenotypes such as total body bone density, total body bone size etc. because our priority was to identify mutations that have global affect of phenotype. In summary, we have used multiple skeletal and extra skeletal traits to assess the skeletal status of ENU mutagenized progeny. Our phenotypic screens were divided into four categories as shown below.

a) Markers of bone turnover
   - i) C-telopeptide
   - ii) Osteocalcin
   - iii) Skeletal alkaline phosphatase

b) Growth screens
   - i) Body weight
   - ii) IGF-I
   - iii) Total mass by PIXImus

c) Bone phenotype screens
   - i) Total body bone mineral density, bone size, bone mineral content by PIXImus
   - ii) X-ray images by Faxitron

d) Soft tissue regeneration screen in ear punch healing

3.2.3 Optimization of phenotypic screening method to allow for maximal reproducibility and sensitivity.

We used population based reference values to identify mice with abnormal phenotype or a phenotypic deviant. However, the utility of these conventional population-based values remains unknown unless the data on biological variation are available and the factors affecting biological variations are minimized in our screening. In the mouse model, data on biological variation in biochemical markers was scarce and published data on biological

variations indicated differences in circadian variation in different strains. As a result, optimization of all screening procedures to maximize sensitivity and discriminatory power was essential for efficient ENU screen. One of the important parameter for biochemical measurements is to establish the appropriate sampling time for optimal use of biochemical markers to reflect bone turnover changes. To establish the optimal sampling time, we evaluated three main components of biological variation in C3H/Hej mice, the strain used in the ENU mutagenesis: 1) the circadian changes; 2) within-subject (longitudinal) variation; and between-subject (population) variation. *Our data on biological variation in biochemical marker assays was published by Srivastava et al (Bone, 2001)*.

Circadian variation

The biological variation studies were performed for three mouse bone turnover assays, namely osteocalcin, C-telopeptide (Type-I collagen alpha-1 chain), and skeletal alkaline phosphatase. The diurnal variation was studied over a 24-hour period covering 12-hour light/dark cycle. To determine whether the circadian rhythm is intrinsically regulated or influenced by restricted food intake, circadian rhythm was also studied in male and female C3H mice by collecting blood after a 12-hour fasting period.

Longitudinal variation

Longitudinal variation was studied over a 7-day period. Two studies were performed: 1) blood samples were collected in the morning on day 1, day 3, and day 7; 2) blood samples were collected as described in study one but in the afternoon. The longitudinal variation expressed as coefficient of variance (CV) in osteocalcin, C-telopeptide, and sALP concentrations were 17%, 14%, and 16%, respectively. The longitudinal variations were not significantly influenced by the time of blood collection in sALP and osteocalcin levels, whereas C-telopeptide levels showed significantly higher within-subject day-to-day variation in morning samples.

Population Variation

Between-subject variations were calculated from samples collected on three different days, and mean value of population CV (from three days) are shown in the manuscript by Srivastava et al (Bone 2003). The average between-subject (n=12) CV for C-telopeptide was 60% higher for morning blood collection as compared to afternoon samples ($p<0.05$) (**Table-3**).

Strategy for biochemical screening and evaluation: The above results highlighted the importance of the timing of sample collection for appropriate interpretation of the bone marker data. Based on our data, we have formulated the following strategy for biochemical and other phenotype screening in our ENU study:

i) All blood samples were collected between 1500 – 1600 hours. We chose this time because we observed comparatively lower between-subject variation in C-telopeptide and sALP levels. To avoid the effect of circadian variation all blood samples will be invariably collected between same time periods.

ii) The blood samples will be collected by retro-orbital sinus puncture under the anesthesia. Once anesthesia is administered, animals are sedated for >30 minutes. During this period, DEXA measurement was performed using PIXImus. This avoided repeated administration of anesthesia and reduced the risk of fatality.

iii) Since there are age and sex related differences in biochemical markers levels, separate reference range were obtained and utilized to identify abnormal value. A separate reference range was generated and utilized for repeat measurements

performed at 16 weeks of age. In addition to normal reference range, comparisons with littermates were also used to define abnormal bone phenotype.

iv) Abnormal values were defined as 2-3 SD (standard deviation) lower or higher than the age and sex matched normal reference range.

Identification of Size Sensitive Phenotypic Deviants: The densitometric size parameters, such as BMC, bone area, femur BMD, measured by PIXImus and total and cortical BMC, total bone area, endosteal and periosteal circumference, and cortical thickness measured by pQCT techniques, are size-dependent. Hence, it is necessary to normalize the bone mass and bone size data in F1 and F3 progeny with body weight. To derive the body-weight-adjusted bone size traits data, we regressed each of the size traits with body weight using male (n=60) and female (n=60) non-mutagenized control mice that are 10-week and 16-week old. We analysed this correlation with regression analysis. Since, the regression line showed significant and positive intercept for all size sensitive traits, indicating that the ratio of size parameters and body weight changes over a range of values; we used the estimating regression equation derived from the normal mice population to normalize size traits in the F1 and F3 progeny. For example, the following formula was used for adjusting size sensitive traits in female 10-week C3H mice determined by PXIXImus: [Adjusted Size Trait = Non-Adjusted Size Trait/(Slope $\times$ Body Weight + Intercept) where Intercept and Slope are from regression analysis of this Size Trait in 10-week old normal female population (n=60)]. The observed weight-adjusted values for size parameters showed statistically non-significant and negligible correlation with body weight (**Figure-2 & Table-4**). The body weight adjusted size phenotypes had 10-50% lower variation (population CV) as compared to un-adjusted phenotypes (**Table-4**). Since the calculated value was a ratio of observed over body weight normalized non-mutagenized value, this manipulation allowed us to compare all parameters on one scale including male and female data.

Strategy for Screening Skeletal Phenotype

Our aim was to optimize a screening procedure in which we can reproducibly detect phenotypic differences of 5-10% magnitude. In this regard, the pQCT technology offers high precision, and has been successfully applied and validated for bone density measurements in a mouse model. However, pQCT measurements are time consuming, a crucial limitation in a large-scale screening, and published data shows that highest precision is achieved in excised bone as compared to *in-vivo* measurements. An alternative to the pQCT is the DEXA, which also has an acceptable precision of 2-4%CV for bone density and body composition parameters. An advantage of the DEXA is that it measures the total body skeletal BMD. We are interested in total body BMD because we are interested in genes that affect the entire skeleton. While it is known that some genes have specific effects on a given skeletal site, our first priority would be to identify genes that affect the entire skeleton. Therefore, we chose to use DEXA, rather than pQCT, for the screening of live animals where speed, cost effectiveness, and whole body BMD were important issues.

The major shortcoming of DEXA measurements was that the BMD is a projected areal density rather than true volumetric density. We observed a significant correlation between BMD and body weight **(Table-4)**, indicating the DEXA BMD is size sensitive. Thus, areal density could result in potential errors in classification particularly if comparison is made between bones of different sizes. Differences in size could arise due to differences in body weight, which could be due to litter size and nursing ability of the mother. Therefore, we compared mutagenized progeny by using unadjusted DEXA BMD data as well as BMD data normalized by body weight. This manipulation provided a BMD independent of bone size (data not shown) as well as reduced population variance. Use of pQCT in secondary screen

overcomes the major deficiency in DEXA measurements in the primary screen and provided details on structural abnormalities in bone, particularly differences in size, which are hard to confirm by DEXA measurements alone. We selected the tibia for pQCT measurements because placement of landmarks was more precise in the tibia as compared to femur or other bones. The high *in-vivo* precision achieved by this procedure is evident in a very low population CV of 1.9 – 2.7% in the bone density measurement in the tibia.

3.2.4 Adapt each phenotypic screen to be applied to large populations of mice.

Ideally, one would like to identify the skeletal phenotypes in an early age group to increase the number of mice screened per unit time. However, rapid changes takes place in the skeleton in young mice, and therefore, variation is larger in young mice. This is illustrated in **Figure-3**, which shows CVs of three selected parameters (BMD, BMC, and Bone Area) obtained by DEXA in 6-week, 10-week, and 16-week old mice. The high variance, seen in 6-week old mice would lead to classification error and the possibility of a higher rate of false positive or negative outliers. Although, the 16 weeks appears as an ideal age for screening skeletal phenotypes, the age was a critical factor for housing cost of mice, as it will affect the maximum number mice that are housed at given time. Therefore, we selected the 10-week time point for screening; this minimizes the housing cost with a minimal loss of precision, as compared to the 16-week mice. Our screening strategy is described below.

i) On days 1-21: To systematically screen for anomalies identifiable at birth and during weaning, cages will be inspected daily for litters. Following observations will be recorded: a) litter size; b) deaths between birth and weaning; and c) obvious visible anomalies. A hole was punched (2-mm) in each ear for monitoring regeneration (size of hole).

ii) On day 31: Size of the ear hole is measured to monitor STR.

iii) On day 42: Size of the ear hole is measured to monitor STR.

iv) On day 70: Weights were recorded on electronic balance with measurement errors <0.01% at 25 g. Between 1500-1600 hours, animals were sedated by injectable anesthesia and 200-250 ul blood collected by retro orbital sinus puncture. All biochemical measurements were performed in blood collected between 1500-1600 hours. Blood was transferred to small tubes (1.0-ml capacity) with clot activating gel and stored at 4^{o}C until serum separated. Serum was aliquoted in 2-3 aliquots and stored at -70^{o}C for biochemical analysis. Serum samples were assayed in duplicate in single run to avoid the effect of between-run variation. BMD and muscle mass measurements were performed during this period using PIXImus. Animals were kept warm and frequently recover in 30-60 minutes.

v) On day 112: In order to confirm a bone phenotype, blood is collected when animals are 112 ± 2 days old. Bloods is collected as described above and bone density measurements repeated at this time using PIXImus. Biochemical tests were performed on the serum and compared with age and sex matched normal range, and with littermates, to confirm the phenotype.

vi) Aging phenotypes: Mice with abnormal bone turnover will be kept for extended periods (12-18 months), during which period bone density measurements will be repeated several times to detect long-term effects altered bone turnover on changes in BMD or BMC.

Using the above strategy, we generated normal range data from 6-16 week old male and female mice. All skeletal phenotype described above were measured in identical ways as ENU-induced mutants were screened. We continuously obtained normal data from B6

(n=60-100), C3H (n=10-40), and MRL (n=20-30) mice and updated our previously generated normal ranges. More than three seasonal groups of mice were obtained from The Jackson Laboratory to overcome seasonal variation in skeletal phenotypes. In addition to musculoskeletal phenotypes, we also obtained normative data on bone marker phenotype, blood chemistry phenotypes and hematology phenotypes. Representative data from one strain is shown in **Table 5-6**, similar data were obtained from B6, C3H, and MRL strains of mice (details not shown). These data were critical for deciding whether a given offspring from ENU treated male is mutant or normal.

Identification of Mutants: An abnormality is recognized if a phenotype differs by 2-3 standard deviations (±2-3 SD) as compared to baseline values obtained earlier using age- and sex-matched wild type control mice. In addition, visible phenotypes were recorded at the time of weaning and at six weeks of age. Measurements that are found to be abnormal are repeated at ten weeks and at sixteen weeks to confirm the phenotype. For this purpose, we have obtained additional baseline values for age- and sex-matched C3H mice for ten weeks and sixteen weeks of age.

3.3 GOAL 2. Screening of phenotypic deviants from one-generation dominant and two-generation recessive screens.

To make the most cost effective use the ENU mutagenesis program, the screening strategy should seek to identify many diverse phenotypes. In this regard, our screen was designed to include a wide-rang of phenotypes such as bone density, bone size, morphological defects, biochemical, and growth related traits. Since ENU mutations are point mutations, we expected mutations generated in this study to be monogenic with phenotypic differences of approximately 5-15% from the normal non-mutagenized controls, and therefore, the other major requirement of our ENU program was an ability to detect deviations of modest magnitude. The high resolution of DEXA and pQCT measurement and a moderate population variation allow us to detect a change of 6-18% in bone density and size phenotypes with 99% confidence limits.

*The generation and screenings of mice were performed as described in **Figure-1**. Representative data on dominant and recessive screen progeny was described by Srivastava et al (Bone, 2003)*. Mice outside the 2-3 SD ranges were identified as phenotypic deviants. Data from size sensitive traits were analyzed as such and after adjustment with body weight as described above. Mouse classified as phenotypic deviants at 10-week screen were retested at 16-weeks. Those mice confirmed as outliers based on 16-week normative data were then considered for backcross with wild type mice to confirm inheritance.

Numbers of mice generated during the entire grant period were described in **Table-7**, which also show data from three different strains of mice and number of phenotypic deviants produced. During the entire grant period we screened more than 2800 mice for dominant and recessive mutations. Although we screened >1400 C3H/HeJ mice, we observed only a few phenotypic deviants in this strain of mice. This could be due to the fact that the C3H mice include >500 mice that are produced during the optimization of ENU doses; thus, a large number of mutants were produced with suboptimal dose. On the contrary, we identified unusually large number of phenotypic deviants from MRL/MpJ mice, we believed that this could be attributed to two reasons: 1) there were multiple mutations that caused large magnitude of change in F1 and F3 progeny but when these mice were backcrossed with wild type mice there was gradual loss of phenotype and we did not recover many

mutants; 2) multiple mutations also resulted in several phenotypic deviants showing poor performance in breeding, which could not be sustained.

Our data also showed that lesser number outliers were with abnormal levels of biochemical markers and none of them were confirmed in backcross. We believe that several of these phenotypic deviants had multiple mutations, such as the phenotypic deviant mouse with increased levels of sALP was also associated with a hyperactive circling behavioral phenotype that affected the nursing ability and could not be backcrossed. In addition, despite our significant effort to minimize the variability of the biochemical marker measurement the high inter-individual variability limited the utility of markers to identify outliers. The high variability meant that 50% or higher differences were required to be classified as a phenotypic deviant. Since markers are systemic indicators of bone metabolism, it may be possible that genes causing changes in a specific skeletal site will not result in a greater than 50% change in systemic markers. The bone marker phenotypic deviant mice identified in our screen probably represented multiple mutations which either could not be bred or the phenotype was gradually reduced when the mutations were diluted in backcrosses.

The phenotypic deviants that were confirmed in our repeat testing are described in **Tables 8-11**. The quantitative phenotypic deviants included phenotypes such as, bone density, bone size, bone marker, and blood chemistry. The detailed description of these phenotypic deviants and phenotype characterization of these phenotypic deviants is described in next section. Because of the significant efforts involved in progeny testing, we focused on those phenotypic deviants that had highest differences in phenotypes.

3.4 GOAL 3. Confirm interesting phenotypic deviants by backcrossing them with wild type mice and perform phenotypic characterization of mutant mice that appear to be inheritable in backcross.

The phenotypic deviant mice were bred with wild type females to determine whether the abnormality segregates bimodally in their offspring with the expected 1:1 or 1:3 Mendelian ratios. Selected phenotypic deviants that pass this test are subsequently used for mapping the chromosomal location of the mutation. Because it is anticipated that each F1 progeny will have 20-40 mutations, backcross was carried out in at least two-generation of mice by isolating those mice with the phenotype of interest and then selectively breeding them to eliminate about 50% of undesirable mutations in each generation. Therefore, after 2-3 generations, each affected mouse will have 5-10 mutations with minimal chances that multiple mutations affecting the same phenotype.

A technical difficulty in the quantitative phenotype-driven mutagenesis is characterizing mice generated from backcross. The animals are not genotyped at this stage to differentiate mutant from non-mutant genotypes; thus, phenotype distribution is the only means for separating the mutants from their unaffected littermates. Even after selecting a 3SD unit difference criterion to classify mutants, we still noticed an overlap of mutant and non-mutant phenotype. Thus, there is possibility that classification errors in distinguishing outliers could lead to potential breeding of an un-affected progeny mistakenly identified as a phenotypic deviant. To overcome this possibility, we bred only extreme scoring mice for generating affected progeny and excluded the mice that are on the borderline of 3SD criteria.

We observed that several of the outliers identified in the 10-week screen had phenotype values between 1SD - 3SD units when repeat tested at 16-week. However, due

to the significant efforts involved in progeny testing, we only pursued outliers (after 16-week screening) with the highest differences, which was independent of body weight (and body size). We backcrossed >30 phenotypic deviants mice (including C3H, B6, and MRL mice) with wild type mice (**Tables 9-10**). Each phenotypic deviant was mated with 1-2 wild type male or female mice. Once the mating is successful, pregnant mice is separated and placed separately to give birth to B2 littermates. If F1 affected mouse is a female, it is reintroduced for mating to produce 3-5 litters totaling about 20-25 F2 pups. If the affected mouse is male, 3-5 female mice were mated simultaneously. The inheritance testing (IT) F2 offspring were screened at 10-week and 16-weeks of age. A mutation is considered inheritable if the phenotype is recovered in the backcrossed progeny.

We confirmed several phenotypic deviants as inheritable including mutants with binary phenotypes such as syndactyly, hip displasia, and line 2.8.6 (binary phenotype of greasy agouti fur and low BMD). Several of the phenotypic deviants did not produce sufficient litters to sustain successful F3 breeding. Some phenotypic deviant mice did not produce the required number of F3 mice and hence could be confirmed as mutant strain. Furthermore, the magnitude of phenotype was reduced as we bred these phenotypic deviants for more than one generation. Consequently, none of these phenotypic deviants were further evaluated or maintained.

We confirmed four quantitative phenotypic deviants that include 917M (low bone area), line 12184 (high total body bone density), line 12137 (high total body bone density), Of these three mice, the 917M, 12184, 12137 mice were bred extensively to produce >5 generations of mice (**Table-11**). Thus, these mutants were confirmed in more than two generations of inheritance-test crosses with wild type B6 females. The ratio of affected and non-affected mice corresponds to 40-50% for dominant phenotypic deviants and 20-25% for recessive mutation, which was close to expected ration for dominant (50% affected) or recessive mutation (25% affected). We maintained the live colonies of all the dominant mutants until we archived these mutant strains by cryopreservation. We performed sperm cryopreservation of two affected males from Lines 917M, 12184, and 12137 to archive the mutant strain. In future, live colony may not be maintained and if required live pups will be revived by in-vitro fertilization.

The abnormal mice identified in our ENU screen can be classified under two categories: 1) mice with binary/visible abnormalities; and 2) mice with quantitative anomalies. A brief description of selected phenotypic deviants is provided below.

i) Dominant Spotting: Dominant Spotting mutation is characterized by the presence of white patches of hypopigmented skin and hair (**Figure-4**). Heterozygotes produced by mating ENU male mice with wild-type female mice have some white spotting with or without slightly diluted pigmentation. The F1 affected mouse, a female, is fertile and bred for inheritance testing. Published data indicates that dominant spotting is usually associated with slight anemia and some mutations are homozygous lethal. We have not tested if the heterozygotes are anemic or the mutant homozygotes are lethal. Several dominant spotting mutants have been mapped to c-kit oncogene and phenotypically resembles human piebald trait, which is a defect in melanocyte development that causes patches of hypopigmented skin and hair.

ii) Syndactyly: Syndactyly is characterized by fusion of two or more digits in both fore paws and hind paws. In heterozygotes, the hind feet show soft-tissue syndactylism and shortening of nails and terminal phalanges (**Figure-4**). The original F1 with syndactyly was a male with both hind paws and fore paws affected. We

backcrossed the syndactyly mutants with wild-type mice. About 25% of the mice, both male and female, were found to be affected by syndactyly.

iii) Kinky Tail: The kinky-tail phenotype is characterized by a sharp bend in an otherwise normal-size tail. There was no other skeletal or growth related abnormality observed in this mouse. An x-ray image of the tail of the affected mouse shows that kinky-tail could be due to some degree of spina bifida resulting in a curly or kinky tail. The penetrance of this mutation has been shown to be very low.

iv) Phenotypic Deviant with Agouti Coat Color and Low Bone Density: We identified an agouti coat color mouse in recessive screening of the C3H/HeJ (C3H) strain of mice. The mutant mice showed 8-10% lower total body bone density and bone mineral content. To generate additional F3 mice, we bred the affected male and female phenotypic deviants, which could be easily identified by agouti coat color, which has a greasy appearance, as shown in **Figure-5**. About 25% of IT progeny were classified as affected. The in-vivo DEXA scan of total body bones and tibia shows that bone density was significantly lower in mutant mice as compared to WT control.

v) Dysplasia: We observed three phenotypic deviants with hip dysplasia in B6 dominant screen, X-ray images from two of these phenotypic deviants are shown in **Figure-6a & b**. These mice have normal gate indicating that dysplasia does not hinder in movement. However, only one of the dysplasia phenotypic deviant (12.6.4) showed inheritance where progeny from backcross with wild type mice showed some form of dysplasia.

Quantitative Phenotypic Deviants: We screened >1900 progeny for all phenotypes listed in Section 3.2.2. We observed >100 quantitative phenotypic deviants in our primary screening performed at 10-weeks and confirmed >30 quantitative phenotypic deviants in 16-week repeat testing. The selected phenotypic deviants are listed in **Tables 12-14**, which includes those that were not confirmed in backcross with wild type mice. Characteristics of a few phenotypic deviants confirmed in the repeat testing are separately discussed below. Detailed phenotypic characterization of important phenotypic deviants is described below.

i) **Mutant Line 917M** - *In-vivo Bone Area Phenotype Characterization:* In our previous ENU mutagenesis screen for dominant musculoskeletal phenotypes using a C57BL/6J (B6) strain of mice, a phenotypic deviants was discovered which exhibited a highly significant decrease in bone size attended by an increase in fat mass. Three main parameters that assess bone size such as, bone area, bone mineral content (BMC), and periosteal circumference were all significantly lower in affected mice even after adjustment for decreased body weight as shown in the **Table-8**. Interestingly, the total body bone area phenotype was consistently expressed in males (92% affected), whereas, only 6% of females exhibited partial phenotype (**Figure-7**) (**Tables 12-14**).

a) *Sex-Specific Differences in Bone Size*: Sex differences in long bone morphology emerge after the pubertal period as seen in both human and animal studies. At both central and peripheral sites, young adult women had a bone cross-sectional area that is 20-25% less and a bone mass that is 20% less than young adult males. As observed in humans, skeletal size shows a similar sexual dimorphism in the B6 strain of mice. As compared to WT B6 (n=20-100) females, the total bone area in WT B6 males (n=20-100) at 6-, 10-, and 16-weeks is 12.9%, 11.5% and 8.5% higher ($p<0.0001$), respectively. In contrast, the total body bone area at 10-weeks and 16-weeks was 0.3% and 4.9% lower, respectively, in 917M male mice as compared to

female 917M littermates (**Figures 8-10**). In addition, if we compare 917M mice and their female littermates with WT mice, the female mice were within ±2% of the bone area of age matched WT mice. Whereas the bone area in 917M mice was 8-10% lower between the 6-16 week age range (**Figure-11**). These data clearly suggest that mutation is affecting a sex-related disparity in bone size. In 917M mice the postpubertal growth in bone size is severely impaired whereas bones in female grow normally. Based on these data, we hypothesize that the 917M gene is involved in the gender-specific increase in bone size during puberty.

b) *Ex-vivo Bone Area Phenotype Characterization*: In addition to the in-vivo measurements of bone size, we also measured bone size in excised bone from the mutant and compared them with wild type. The periosteal circumference and total bone area covering the entire length of femur and tibia are shown in **Figure-12**, which indicates that the bone area and periosteal circumference was significantly lower in tibia as well as femur from mutant mice (n=5) as compared to that of age matched WT control mice (n=5).

c) Determination of Bone Area Phenotype by Histological Measurements: To determine the differences in bone formation rate that may contribute to decreased bone area in mutant mice, bones were dual labeled at 10-day interval using tetracycline and animals sacrificed at 16 week age. The tibia and femurs were excised and midshaft region examined by histochemical analysis. The results are shown in **Table-12**, which indicate that bone size was significantly reduced in mutant mice as compared to WT mice. Although, there was a 23% reduction in bone formation rate, in mutant male mice, this reduction in bone formation rate was not statistically significant due to large variation and small sample size. In conclusion, the histological data confirms our earlier observations of reduced bone size phenotype and indicates that phenotype could be caused by a decreased bone formation rate by osteoblasts in mutant mice.

d) Bone area measurements in 3-16 week old mice (**Figure-13**) indicates that lower bone area in mutant mice appears after 3-week age and continues to decrease upto 16-week age. However, the testosterone levels measured in 917M and wild type controls indicate that low bone area appears to be unrelated to testosterone levels (**Figure-14**) during puberty. We continued to breed this line and maintained a small colony.

e) *In vitro Phenotypic Characterization of 917M Osteoblast***:** The possible mechanism by which the radial bone size or periosteal circumference could be lower in mutant mice involves; 1) impaired bone formation activity by periosteal osteoblasts; and 2) increased bone resorption as compared to formation with the net result being decreased periosteal circumference. To explore the cellular mechanisms, we evaluated if periosteal cells from 917M and WT mice exhibit intrinsic differences in terms of proliferation and apoptosis potential. The methodology of these assays had been described by Srivastava et al (JBMR, 2005).

f) *Decreased Cell Proliferation of Periosteal Osteoblasts from 917M Mice*: The basal proliferation potential of 917M osteoblasts showed a 25% decrease, as compared to WT controls (**Figure-15)**. The 2-way ANOVA revealed that osteoblasts from affected 917M mice had significantly reduced proliferation (p-value <0.001 for interaction), whereas the proliferation rate was not altered in cells from female littermates (**Figure-15**) of 917M mice. No significant differences in the specific activity of alkaline phosphatase were observed between cells from WT (6.6 ± 0.9 mU/mg protein) and 917M mice (6.8 ± 0.8 mU/mg protein), indicating 917M and wild-type osteoblasts had the same differentiation potential.

g) *Increased Apoptosis of Periosteal Osteoblasts from 917M Mice*: Caspase activity in periosteal osteoblasts from 917M affected male mice was 23% higher as compared to WT mice, whereas, cells from female 917M littermates did not show significant differences in the Caspase activity as compared to those from WT (2-way ANOVA with a sex-phenotype interaction p-value of 0.0431) (**Figure-16**). This suggests a Caspase-dependent increase in apoptosis of osteoblast cells from 917M. FACS of periosteal osteoblasts from 917M mice indicated a significantly higher (18.7%) number of apoptotic cells from 917M male mice as compared to those from WT (13.3%). There was no significant difference in total apoptosis in cells isolated from female littermates of 917M mice by FACS analysis (**Figure-16**).

h) *Reduced Mechanosensitivity of periosteal osteoblast from 917M mice*: Long bone cross-sectional growth is strongly driven by mechanical load, which is a known environmental factor that modulates bone adaptive response by activating periosteal bone formation with increasing usage (69). Morphological differences in bone size may impair this bone adaptive response to mechanical loading because a smaller cross-sectional area would lead to higher stress under similar loading conditions, leading to deficiency in an important positive feedback mechanism that influences bone size with increasing usage. There is evidence that gender secondarily affects the ability of bone cells to respond to biomechanical signals. For instance, the aging skeleton responds to declines in endosteal bone mass by increasing femoral periosteal circumference: the increases in postmenopausal women are less than in aging men. In mice lacking estrogen receptor-α, increases in cortical bone due to loading are reduced. Indeed, studies in both humans and animals have shown that exercise combined with estrogen replacement produced increases in bone mineral density greater than either treatment alone (e.g.). Thus, there is ample evidence for the influence of loading on the periosteal circumference and the ability of the sex hormones to modulate a skeletal response to biomechanical load. To test the hypothesis that mutation in the gene that regulates bone size may also influence the response to mechanical stress, we used a well-established *in-vitro* shear stress model. Application of a 30-min steady flow shear stress at 20 dynes/cm^2 on WT osteoblasts consistently caused a 60-80% (p<0.01) increase in the [^{3}H]-thymidine incorporation compared to the control cells not subjected to shear stress (**Figure-17**). In contrast, the shear stress-stimulated increase in proliferation was only 5% (of control) in cells from the 917M mice (**Figure-17**). The 2-way ANOVA reveals that in control mice, sex had no significant difference in response to stress (p-value 0.3345), whereas

in 917M littermates, the affected 917M mice had a significantly reduced response to shear stress (p-value <0.0001 for interaction). Based on these data, we predict that the 917M gene is mechanosensitive and the mutation in 917M gene reduces the proliferative response of periosteal cells in the 917M mice. This unique feature will be used as criteria in our strategy to test function of a candidate gene in the 917M locus.

i) *Reduced Bone Formation Rate in 917M Mice*: To determine if a decrease in the bone formation rate that may contribute to decreased bone area in mutant mice, bones were dual labeled at a 10-day interval using calcein and animals were sacrificed at 14-16 weeks of age. The midshaft region of femur examined by histomorphometric analysis showed >20% reduction in the bone formation rate (per cross section) in 917M mice (**Figure-18**) as compared to WT or non-affected littermate. Although this reduction in bone formation rate was not statistically significant due to small sample size, the dynamic histomorphometric analysis indicate a definite trend towards decreased bone formation rate in 917M mice as compared to WT or non-affected 917M male mice.

j) *Evidence that single gene mutation contributes to observed bone size phenotype*

Based on the following rationale we believe that the bone size phenotype in 917M mice is caused by a single gene mutation. 1. The ENU treatment of male mice would typically produce 50-100 random mutations covering the whole genome. By assuming that there may be 50-100 genes that regulate bone size in the whole genome, the likelihood of a single gene ENU mutant carrying multiple gene mutations for bone size phenotype is rather low. 2. After six generations of breeding, the bone size did not change. Typically, the ENU mutations are diluted by a factor of 50% after each generation of breeding with WT mice. If multiple mutations contributed to reduction in bone size, the magnitude of bone size get reduced in successive generations as the number of mutations gets diluted because of the recombination. However, this was not observed in 917M mice. 3. Our genome-wide search for loci affecting bone size revealed only one locus that was contributed by 917M mice.

In conclusion, our preliminary data on the bone area and cellular characterization of the osteoblasts cells from mutant 917M indicates that the decreased bone area in mutants may in part be due to decreased osteoblast cell numbers.

ii) **Mutant Line 12184**- Line 12.18.4 was generated in a dominant screening of C57BL/6J (B6) strain of mice. The phenotypic deviant had 10-14% high total body bone density (body weight adjusted) and 7-14% high bone mineral content (**Figure-19**). The aBMD (values in mg/cm^2) for 12184 progenitor mice at 16-week age was 0.056 (male) as compared to WT male mice 0.049±0.002 (Mean±SD, n=69). The BMC Z-scores at 10-week for 12184 progenitor mice was 2.8. At 16-week age, BMC Z-score was 2.4 for 12184 progenitor mice. The body weights of 16-week old 12184 progenitor mice were 14% higher, as compared to WT mice. We bred the phenotypic deviants with B6 females and generated about >300 progeny during this grant period. About 50% of the backcrossed progeny were classified as affected. We used these mice from to perform the following characterization: 1) *ex-vivo* pQCT

analysis of the excised tibia and femur; 2) histological examination of bone formation rate and bone resorption rate after dual labeling with tetracycline; 3) bone strength; and 4) response to mechanical loading. Of these experiments, we completed *ex-vivo* examination of tibia and femur using pQCT. The pQCT scan of tibia and femur shows there is higher total bone density and an increase in periosteal bone perimeter. At the same time, the endosteal perimeter is not increased. These data suggested that the phenotype could be due to increase periosteal bone formation as well as reduced endocortical bone resorption. *Phenotype characterization of this mutant has been published by Mohan et al (Bone, 2007)* (**Figures 19-20**).

a) Measurement of Bone Density Phenotype in 12184 Mice: We evaluated bone density in 6-week old mice and also in female mice that are 1-year old. At 3-week age, the aBMD was not significantly different in 12184 mutant mice as compared to WT control (**Figure-20**). At 6, 10, and 16 week of age the mean aBMD was 5-8% ($p<0.01$), 15-16% ($p<0.01$) and 13-14% ($p<0.001$), respectively, higher in female 12184 mutant mice (**Figure-20**). The male mice showed a higher aBMD (17% higher) at 6-week age as compared to female mice. The data on 3-16 week old 12184 mice indicates that mutation results in higher bone density at early age and higher bone density is maintained over a period of 1-year (1-year data not shown).

b) *Characterization of Osteoblast Cell Function in Mutant 12184*: To investigate if 12184 mutation could influence osteoblast cell function, we isolated the periosteal osteoblasts from femur and tibiae of normal and 12184 mutant mice and propagated them in culture for *in vitro* phenotypic characterization. In brief, the mice were euthanized with CO_2 and decapitated. Soft tissue was removed from femur and tibia without scraping off the bones so that periosteal cells were not lost at this point. Femur and tibia were placed separately in 50 ml falcon tubes containing sterile PBS, and subsequently in culture dish containing 10 ml of DMEM/antibiotics and the left over muscles were removed from the bones. The periosteal cells were extracted from bone by collagenase digestion for 90 minutes at 37^oC. Cells were counted and plated at a density of 10^6 cells per dish and grown with 10% FBS/DMEM/antibiotics. Periosteal osteoblasts at passage 2-3 were used to study cell proliferation, differentiation, and apoptosis. These characteristics of cells from mutant mice were compared with cells isolated in identical manner from age-and sex-matched wild type mice. Cell proliferation was studied using (3H)-thymidine incorporation and results were confirmed by uptake of Almar Blue dye. Cell differentiation was measured by observing changes in the alkaline phosphatase activities using PNPP as substrate. For apoptosis studies, the Homogeneous Caspases Assay from Roche Biochemicals was used which is a fluorimetric assay for the quantitative *in vitro* determination of caspases activity in microplates. Periosteal cells were incubated with DEVD-Rhodamine 110 for 2 h. Upon cleavage of the substrate by activated caspases, fluorescence of the released Rhodamine 110 was measured. Apoptosis results were further confirmed using FACS analysis of isolated cells in presence/absence of 10%FCS.

- Apoptosis (caspase activity): **Figure-21A** shows the rate of apoptosis, as measured by the caspase activities in periosteal osteoblasts isolated from 10-week old B6 normal and ENU mutant mice. No significant changes were observed in the caspase activities in the

cells of mutant mice as compared to those from normal mice (**Figure-21A**).

- Cell Differentiation: The specific activity of alkaline phosphatase (a marker of osteoblasts differentiation) was estimated in periosteal cells derived from normal and ENU mutant mice (**Figure-21B**). No significant changes were observed in ALP activities of cells from mutant mice as compared to those from wild type mice.
- Cell Proliferation: **Figure-21C** shows the basal proliferation rates of periosteal osteoblasts isolated from femur and tibiae of 10-week-old normal and ENU mutant B6 female mice. No significant changes were observed in the basal rate of cell proliferation in cells from mutant mice as compared to the normal WT mice (**Figure-21C**).
- Histomorphometric Assessment of Bone Formation and Bone Resorption in Mutant Mice: Dynamic changes in bone formation at the midshaft femur (right) of mutant and control mice (included WT as well as non-affected littermates) are shown in **Figure-22A**. The endosteal bone formation rate (BFR) was not different in 12184 mice. Differences in BFR at periosteum in 12184 mice were not statistically significant. The average tartrate resistant acid phosphatase (TRACP) labeled surface, which indicates static histomorphometric measure of osteoclast number, was 23% (p=0.156) reduced at endosteum in 12184 bones (**Figure-22B**).

iii) **Mutant Line 12137**- Line 12.13.7 was also generated in a dominant screening of C57BL/6J (B6) strain of mice. We bred the phenotypic deviants with B6 females and generated >300 progeny during this grant period. The mutant have 10% high body weight, 10-14% high body weight adjusted total body bone density, and 10-25% high body weight adjusted bone mineral content as compared to wild type control mice. We completed ex-vivo examination of tibia and femur using pQCT. The pQCT scan of tibia and femur shows that total bone density was higher in mutant mice as compared to WT control. We did not see any significant differences in periosteal or endosteal circumference, which suggested that changes in bone size cannot account for increased bone density. We continued to explore the cellular mechanisms that cause increase in bone density using histological analysis. *Phenotype characterization of this mutant has been published by Mohan et al (Bone, 2007)* (**Figure-19**).

a) *Measurement of Bone Density Phenotype in 12137 Mice at 6-Week and 1-Year Time Points:* We evaluated bone density at 6-week old mice and also in female mice that are 1-year old. These data are shown in **Figure-23**, and indicates that mutation results in higher bone density at an early age, and higher bone density is maintained over a period of 1-year.

b) *Characterization of Osteoblast Cell Function of Mutant12137*: To study the cellular mechanism of increased bone density in the 12137 mutant, we isolated the periosteal osteoblasts from femur and tibiae of normal and 12137 mutant mice as described above for 12184 mutant mice and propagated them in culture for *in-vitro* phenotypic characterization. The following characteristics were examined:

c) Cell Proliferation: **Figure-24A** shows the basal proliferation rates and proliferation rate when stimulated with calf serum and IGF-I of periosteal osteoblasts isolated from femur and tibiae of 10-week-old normal and ENU

mutant B6 female mice. Our preliminary results indicate that the basal proliferation rate appears to be higher in osteoblasts isolated from 12137 mice. In addition, a significantly higher rate of proliferation was observed in osteoblast cells isolated from 12137 mice in the presence of calf serum but not IGF-I (**Figure-24A**). Increased basal proliferation rates in 12137 osteoblast cells were confirmed by alamarBlue dye uptake as shown in **Figure-24B**.

d) Apoptosis (Caspase activity): **Figure-24C** shows the rate of apoptosis, as measured by the caspase activities in periosteal osteoblasts isolated from 10-week old B6 normal and ENU mutant mice. No significant changes were observed the caspase activities in the cells from mutant mice as compared to those from normal mice (**Figure-24C**).

e) Histomorphometric measurements to determine cellular mechanism of high bone density phenotype in 12137 mutant mice: We performed histological examination of bone formation rate and bone resorption rate after dual labeling with tetracycline at 14-week and 16-week time points. After second tetracycline injection, femur and tibia were isolated and cleared of surrounding tissues. To measure bone formation and resorption, a location 1 mm proximal to the midshaft was marked on the femur with a pencil. A 5 mm segment of the femur midshaft was cut from the bone starting at the mark and going distally. The samples were fixed in 10% formalin for 4 hours, rinsed in PBS, and then partially decalcified (6 hours) in 10% EDTA in the cold. The samples were infiltrated in glycol methacrylate and embedded vertically with the midshaft end down. The samples were sectioned with a Jung microtome and the first 1 mm of material discarded until the mid point of the shaft was reached. Sections were prepared for analysis by staining for ALP and tartrate resistant acid phosphatase (TRAP). Total ALP and TRAP covered surfaces were measured using the Osteomeasure system equiped with a digitizing tablet (Osteometrics, Atlanta, GA and color camera (Sony, Japan).

Results of dynamic histological examination of femur midshaft region are shown in **Figure 22**. Bone area at the femur midshaft in 16-week old mutant mice (A) was significantly higher as compared to WT control mice examined in previous grant periods. In addition, endocortical bone formation rate (B & C) at the femur midshaft measured by tetracycline labeling is shown (periosteal bone formation rate was significantly affected). These data suggest that high BMD phenotype in mutant mice appears to be due to increased endocortical bone formation and/or reduced bone resorption.

iv) **Phenotypic deviants with high bone density Line 10145** – Line 10145 was generated in recessive screening of the C3H/HeJ (C3H) strain of mice. The mutant mice showed 23% high total body bone density and about 17% lower bone area and no changes in bone mineral content. We bred the phenotypic deviants with C3H females in a three-generation breeding protocol similar to that described in **Figure-1** and generated about 30 progeny in this grant period. The *in-vivo* DEXA and pQCT scan of total body bones and tibia shows that bone density was higher in the mutant mice as compared to WT control. However, we observed a shift in total body bone density and volumetric bone density in WT male and female mice, such that the total body BMD in WT mice was similar to those in mutant mice. To confirm this upward shift in BMD, we obtained new male (n=5) and female (n=5) mice from The Jackson Lab in the current reporting period and obtained total body BMD at 10- and 16-weeks

of age. We compared this data with data obtained in 2001 and data collected in 2005 was significantly higher (**Figure-25**). Due to this increased BMD in WT mice, which we routinely obtain from The Jackson Laboratory for propagating the 10145 line, we decided not to pursue this line any further because of this discrepancy.

v) **Phenotypic deviants with high bone density B2.4**: The phenotypic deviants (Line 2.4) was identified as a 15-20% high total body bone density and bone mineral content whereas the bone area was largely unaffected. The body weight was about 5-8% higher in the phenotypic deviant mice, however, the body weight adjusted BMD was 10-12% higher. We generated 118 mice in this grant period for characterization of high bone density phenotype (**Figure-26**).

a) *Measurement of Bone Density Phenotype in Line 2.4 Mice*: We evaluated bone density in 10-week and 16-week old mice and the results are shown in **Figure-26**.

b) *Measurement of Ex-vivo pQCT Bone Density*: Total bone density (mg/cm^3) and cortical bone density were measured by pQCT in femur and tibia from 16-week old male and female progeny from backcross. Nine slices covering the entire length of the bone were scanned, and slices 1 & 9 were excluded from analysis due to large variation. Total bone density of affected 2.4 mice was consistently higher ($p<0.05$) over the entire length of femur. The increase in bone density appears to be associated with increased bone area due to increased periosteal perimeter.

c) *Histomorphometric measurements to determine cellular mechanisms of high bone density phenotype in Line 2.4 mutant mice*: We performed histological examination of bone formation rate and bone resorption rate after dual labeling with tetracycline at 14-week and 16-week time points. Bones were processed as described above for mutant 12137.

d) Results of dynamic histological examination of femur midshaft region are shown in **Figure-27**. Bone area at femur midshaft in 16-week old mutant mice (A) was significantly higher as compared to WT control mice. In addition, bone formation rate measured by dual labeling was increased at both periosteal and endosteal surfaces (**Figure-27**) at femur midshaft. These data suggest that that high BMD phenotype in mutant mice is due to increased bone formation.

e) *Genotyping of Line 2.4 Mutant*: Since the phenotype was interesting and we have bred this mutant extensively, we selected this phenotypic deviants for genotyping to identify chromosomal location of the mutation. In order to identify mutant locus, we bred 2.4 mutant with C3H/HeJ mice to produce approximately 28 F1 mice, which were then bred F1 male with F1 females to produce about 98 female F2 mice. We completed the phenotype analysis of these F2 mice and currently genotyping the F2 mice for QTL analysis.

i) **Phenotypic deviants with high volumetric bone density Line20:** The phenotypic deviants (Line 20) was identified as a high bone density measured by PIXI. The total body bone density was 10-17% higher in male or female mice as compared to WT mice (**Figure-28**). The high bone density appears to be associated with 9-25% higher bone mineral content as compared to WT control mice, whereas bone area was within only 1-4% different from WT control mice. The body weights of the phenotypic deviants mice were 6-10% higher, however, the body weight adjusted BMD was also 8-10% higher.

ii) **Phenotypic deviants with blood chemistry phenotypes:** We bred two phenotypic deviants (line 19.4 and Line 3.2) with abnormal lipid levels (total cholesterol, high density cholesterol, and triglycerides) and one phenotypic deviant (Line 7.2E) with high blood urea nitrogen levels (described in **Tables 8-10**). Some of the F3 progeny appears to be affected with high blood lipid levels; however, these levels were measured in non-fasting blood and could be influenced by food consumption. We are currently collecting additional fasting samples to confirm these lines.

iii) **Phenotypic deviants with Low Alkaline Phosphatase Levels & High Bone Density:** We observed one phenotypic deviants (Line 29.2) where low alkaline phosphatase values (30-40%) in serum were accompanied by higher bone density (+1.8SD units). We bred this phenotypic deviants and produced >40 mice in this line. Preliminary data on alkaline phosphatase levels is shown in **Figure-29**, which indicates that alkaline phosphatase levels in some mice were>80% lower as compared to littermates. The bone density in these mice was also higher, which would suggest that mutation affects gene(s) that control bone turnover. We are currently generating additional mice to confirm these findings.

iv) **Phenotypic deviants with High Total Body & Volumetric BMD:** We bred two phenotypic deviants, Line 5.4 and Line 5.3, with high total body bone density measured by DEXA. Both phenotypic deviants were identified in recessive screen in B6 background. The high total body bone density correlated with volumetric bone density and cortical thickness. The cortical thickness was > 3SD units different from the wild type control mice. We generated 50 mice from Line 5.4 and about 100 mice from Line 5.3 during this reporting period. Approximately 25% of the F3 mice showed a high BMD phenotype. The bone density data from Line 5.4 was shown in **Figure-30A**. The correlation with volumetric BMD and cortical thickness is shown in **Figure-30B & C**. We performed e*x-vivo* bone density and bone size measurements in femur and tibia from high bone density mutant Line 5.4. The increased bone density was associated with higher bone area, which appears to be due to lower endosteal circumference in affected 5.4 female mice. These data suggest that the phenotype can be explained by decreased bone resorption and/or increased bone formation at endocortical bone surface.

The total body BMD data from Line 5.3 was shown in **Figure 31A**. The total body bone density also showed significant correlation with volumetric BMD and cortical thickness (**Figure 31 B & C**). Additional characterization of *ex-vivo* bone density and bone size measurements in femur and tibia by pQCT were performed. The increased bone density was associated with higher bone area. The phenotype characteristic of Line 5.3 appears to be similar to Line 5.4 and, thus, suggesting similar gene mutation in these two lines.

v) **Phenotypic deviants with Slow Soft-Tissue Healing (M1.2d):** Phenotypic deviants with reduced soft-tissue regeneration (STR) capacity: As expected, we observed several phenotypic deviants with reduced soft-tissue regeneration capacity. In wild type MRL mice, a 2 mm ear punch is 80-90% healed in 3-weeks after making the hole, thus, the 99% confidence limits for slow healing after 3-weeks is 1.2 mm. Several mice showed only 10-30% healing. However, our data also showed a large variation in STR rate in F1 progeny and it was possible that some of the slow healing mice were false positive. Consequently, we are only focusing on those phenotypic deviants that showed no healing. We bred a few soft tissue regeneration phenotypic

deviants with wild type MRL female mice to test heritability. A prominent phenotypic deviant M1.2d expressed slow or no healing of a 2 mm ear punch hole in MRL strain of mice. We generated >100 mice during this reporting period and soft-tissue healing data is shown in **Figure 32**. Since the mutation affects tissue healing rate in an MRL background, we explored differential gene expression using microarray in this line, which is described in Specific Objective 3.

vi) **Phenotypic deviants with abnormal hematological parameters**: In the dominant screen, during 2004-2006 screens we also included whole blood hematology measurements using Hemavet 950 (Veterinary Multi-species Hematology System with 5 part differential capability from Drew Scientific & Escalon Medical Corp., Wayne, PA), which is designed for mouse hematology measurements. Peripheral blood was drawn (80-100 microliters) by retro-orbital puncture using a Pasteur pipette. Blood was collected in Microtainer brand tubes containing K_2EDTA (Becton Dickinson, Franklin Lakes, NJ) and samples analyzed using a Cell-Dyn 3500R automated veterinary hematology analyzer according to the manufacturer's instructions. The hematological parameters measured included hematocrit, platelet counts, hemoglobin, WBC, RBC, lymphocytes, neutrophils, mean cell volume etc. We observed several phenotypic deviants in our primary screen with platelet count, mean cell volume, hematocrit, hemoglobin, monocyte etc. Four phenotypic deviants were confirmed in the 16-week retesting and two of the phenotypic deviants survived and were backcrossed. However, none of the backcrossed progeny showed the abnormal phenotype.

3.5.1 GOAL 4. Map the chromosomal location of the mutants by interval mapping approach.

We selected three main mutant lines of mice for genotyping based on phenotype characterization discussed above and magnitude of change obtained in the phenotypic deviants after backcross. All three phenotypic deviants were from dominant screen, 917M, 12184, and 12137 strains. In all these mutant strains of mice, phenotype was observed at two different ages (10-week and 16-week) and inheritance was confirmed in sufficient number of backcrossed progeny. In addition, these mice also showed phenotype in at least one different background strain of mice than that was used for backcross. These data revealed that the mutant gene would show expected phenotype in a different genetic background during genotyping.

General procedures for mapping mutation: Since mutations represent quantitative phenotypes, we employed linkage analysis to map the chromosomal location of the mutants. When a different strain of mice is used for interval mapping of a mutant strain, the mapping will reveal several quantitative traits loci (QTL) associated with the background strains, which is irrespective of mutation. Thus, our mapping is inherently confounded by presence of background QTLs. However, we anticipated that our mapping data would disclose one major linkage mapped to a single chromosome, especially in small number of F2 mice (50-100) because small effect background QTL detection will be obscured by larger variance in small F2 population (normally 300-800 F2s are required to reveal background QTLs between inbred strains). This assumption was based on the observation that effect size of the mutant mice was larger than all published linkages (QTLs) reported for different skeletal phenotypes in wild type strains. Therefore, the linkage obtained from mutant mice will represent a much larger effect segregated through the F2 population. To ensure that our mapping represents mutant locus, we also studied background QTLs occurring in F2

population generated from same strains of mice that is used for mutant mutant mice with similar power to detect QTLs.

To map mutations in B6 background, we selected C3H/HeJ wild type strain to perform three intercrosses. To generate F1 mice, the mutant male is mated with 3-4 normal wild type female mice. Each F1 female is then bred with each F1 male to produce at least one litter, with minimum of 4 pups. To generate F1 mice from wild type, the male wild type mice from same strain, as in case of mutant male, is mated with 3-4 normal wild type female mice of different strain. Therefore, the breeding pattern is identical in mutant and wild type intercross. The tail clips were collected from F2 mice from different intercrosses and genomic DNA was extracted for genotyping. Genomic DNA was isolated from tail clips using DNAeasy kits (Qiagen) for mouse tissue. DNA samples were quantified and quality determined by measuring their absorbance at 260 nm and 280 nm. If a DNA sample was not satisfactory, we extracted genomic DNA from back-up tissue (ear punch) for genotyping.

A genome-wide genotyping scan was undertaken in F2 mice using microsatellite polymorphic markers. Between 50 and 60 fluorescently labeled [labeled with FAM (blue), VIC (green), and NED (yellow)] informative markers were PCR amplified from F2 DNA. Markers were spaced at either end of each chromosome, and in some cases in the middle (for larger chromosomes). We performed >24,000 PCR reactions to achieve genotyping in these two intercrosses. PCR reactions and running conditions allowed from 4 to 6 microsatellite markers to be multiplexed in a single electrophoretic lane. All 6 reactions were run in a single capillary on the ABI 3100 DNA analyzer. Following electrophoresis on the ABI 3100 DNA Analyzer, Genotyper software macros were used to semi-automatically score the allele calls for all the multiplex pools of every single F2 mice. The pooled products were analyzed for fragment size on ABI Model 3100 DNA Analyzer and Genescan software was used to size alleles (Applied Biosystems). After initial scoring by these macros, allele calls were visually checked and edited if necessary. Allele calls and edits were done using Genotyper software (Applied Biosystems) and exported as tab-delimited tables. A table of the calls was generated and the allele sizes converted into respective allele bins for entering into interval mapping software programs.

Phenotype data and genotype data were imported into the software in text file format; mice with missing phenotypic and genotypic data were coded as phenotype unknown. The interval mapping was performed by the Pseudomarker MAINSCAN program written for the MATLAB (Mathworks Inc., Natick, MA, USA) programming environment as described in previous reports. We calculated posterior probability densities for individual chromosome to define the 95% confidence interval (CI) for selected locus. Posterior probability density is a likelihood statistic that gives rise to the 95% confidence intervals. Linkage analyses were also performed using MapQTL 5.0 (DLO Center for Plant Breeding and Reproduction Research, Wageningen, The Netherlands) as described for F2 intercrosses. Both Pseudomarker and MapQTL 5.0 analyses yielded similar results. Percent variance explained by each locus was calculated for peak interval by MapQTL software. The genome wide cut-off value for significant LOD scores was determined by 1000 permutation test.

i) ***<u>Mapping Chromosomal Location of the Phenotypic Deviant 917M</u>***

To map 917M, we bred 917M F1 hybrids (C3H/B6) to produce a total of 142 917M F2 mice. A total of 142 C3HB6 F2 mice were generated from three 917M male mice. Male and female mice were mapped separately. The bone area of male F1 and F2 mice is shown in **Figure-33**. The mean bone area in 917M C3HB6F1 male mice

(**Figure-33**) was 8-12% lower ($p<0.01$ by ANOVA) as compared to WT C3HB6F1 male mice, which shows that the low bone area phenotype was expressed in C3H background. Similarly, the bone area in 917M C3HB6F2 male mice significantly lower as compared to WT C3HB6F2 male mice The body weight adjusted bone area of F2 males (n=69) generated from both 917M and wild type B6 mice was normally distributed. The results from whole-genome linkage analysis using total bone area showed evidence for linkage at loci on Chr 1 (LOD score 4.9 at 45 cM) and Chr 4 (LOD score 7.9 at 10.5 cM) (**Figures 34-35**). The LOD scores for Chr 1 and Chr 4 QTLs were 3.4 ($p>0.05$) and 6.8 ($p<0.01$), respectively, when body weight was used as a covariant (data analyzed using Pseudomarker program). The LOD scores for Chr 4 QTL for femur bone area, periosteal circumference, and endosteal circumference when body weight was used as covariant were, 6.2 ($p<0.01$), 9.1 ($p<0.01$), 5.6 ($p<0.01$), respectively. Genome wide linkage analysis of C3HB6 F2 females (n=60) generated from 917M B6 male did not show any significant QTL (data not shown).

Interval mapping using eight additional marker (total of 11 markers) for Chr 4 and bone size traits revealed peak interval on proximal Chrs 4 at 10.5 cM with a LOD scores 4.0-8.2 (genome-wide error rate of $p < 0.05$) as shown in **Figure-35**. However, the peak interval for periosteal circumference was shifted to 50 cM with LOD score of 6.6 (genome-wide error rate of $p< 0.01$). Bone size QTLs on Chr 4 explained 38-42% of the phenotypic variance in bone area of F2 male mice. Alleles in the Chr 4 interval that are inherited from the B6 parental strain contribute to a significantly lower bone area than do alleles inherited from C3H (**Figure-36**). . Alleles of Chr 1 interval that contribute to low bone area are for genotype C3H /C3H.

QTL-QTL Interactions for total body bone area trait in 917M mutant strain

Two loci show interactions when the genotype at one locus influences the effect of the other locus. **Table-15** shows genome-wide significant interactions observed in B6C3H F2 mice for total body bone area. The interaction involving Chr 1 and Chr 4 was noteworthy because Chr 1 locus was the only other locus that was associated with any significant QTL observed for bone size. The combined variance explained by the two interactive QTL on Chr 1 and Chr 4 was 60% of the F2 population (calculated separately by Pseudomarker Fit QTL algorithm). Other significant interactions were noticed between 10cM and 80 cM region of the Chr 4. Both Chr 1 and Chr 4 harbor loci known to regulate bone density and bone biomechanical properties phenotypes. A significant interaction between these loci would suggest a complex interaction between genes that regulate skeletal phenotypes or suggest the presence of modifying loci influencing bone area trait.

ii) **Linkage Analyses for Bone Size in Wild Type C3HB6 F2 mice**

To identify background QTLs between B6 and C3H strains of mice, we bred wild type B6 males with wild type C3H females to generate F1 hybrids (C3H/B6). We subsequently intercrossed F1 hybrid males and females to produce a total of 186 F2 mice. Male and female mice were mapped separately. A whole-genome linkage search for loci affecting the body size traits (total body bone area and total bone area and periosteal circumference at midshaft tibia) in WT C3HB6 F2 male (n=92) and female (n=85) did not reveal any suggestive or significant QTLs (**Figure-34**). A suggestive QTL for total bone area was observed on Chr 14 (LOD score 4.7 at 5 cM) when body weight was used as a covariate (data not shown).

iii) **Mapping Chromosomal Location of the Phenotypic Deviants 12137 and 12184**

The intercross of 12137 and 12184 mutants with C3H generated 164 and 137 F2 mice, respectively, for linkage analysis (**Figures 37- 40**). The aBMD for F2 male was 5% ($p<0.001$) higher as compared to the F2 female mice but body weight adjusted aBMD were not significantly different (p=NS). Therefore, body weight adjusted aBMD was combined for interval mapping to increase the power to detect linkage. The frequency distribution of body weight adjusted aBMD of F2 mice showed normal distribution with Shapiro-Wilk w=0.9847 (p=0.1314) for 12184 and w=0.9864 (p=0.1332) for 12137 mutant F2 mice. The results of interval mapping of the body weight adjusted aBMD are shown in **Tables 16 & 17** and **Figure-38**. Similar results were obtained when aBMD phenotype (unadjusted) was used for interval mapping; since male and female F2 mice have significant differences in aBMD these results are shown separately in **Tables 16 & 17**. The LOD scores for aBMD determined using body weight as a covariate were higher for 12137 male and 12184 female mice (**Table-17**). Our mapping data showed only one significant or suggestive QTL on Chr 4 (**Figure-39**).

To fine map the chromosome 4 locus affecting bone density, we used 11 markers on chromosome 4. We then mapped all F2 mice with additional polymorphic microsatellite markers covering the entire length of chromosome 4 as shown in **Figure-40**. The fine mapping indicated that QTL peak was located between 65 cM and 75 cM region. In addition to data combined from male and female, we performed interval mapping of BMD and BMC traits separately for male and females. The results indicated that only one peak at chromosome 4 influenced bone density. The analysis of 95% confidence interval using 4-11 microsatellite markers is shown in **Figure-40**. The Chr 4 locus explained approximately 24-33% of the phenotypic variance in aBMD of F2 mice from 12137 and 12184 mutants. The phenotypic effect for the high aBMD allele calculated for Chr 4 peak marker best fit a dominant mode of inheritance for 12137 mice and as additive mode of inheritance for 12184 mice (based on ANOVA, $p<0.05$).

We also calculated linkage for body weight phenotype for 12137 and 12184 F2 mice. A significant linkage was observed on Chr 16 (5.0 cM, LOD score 3.3, p=0.000528) for female 12137 F2 mice. Similarly, a significant linkage was observed for male 12184 mutant mice on Chr 13 (30 cM, LOD 3.8, p=0.000173). No significant (cut-off was LOD 3.2 at $p<0.05$) or suggestive linkage (cut-off was LOD 2.9 at $p<0.10$) was observed for body weight phenotype in male 12137 or female 12184 mice. These data suggest that body weight phenotype was regulated by independent QTLs as compared to QTLs regulating aBMD phenotype in these mutant mice.

iv) **Linkage Analyses for Total Body Bone Density in Wild Type C3HB6 F2 mice**

To identify background QTLs that regulate total body bone density between B6 and C3H strains of mice, we performed linkage analysis in F2 mice from wild type B6 and C3H as described above. A whole-genome linkage search for loci affecting the total body bone density in WT C3HB6 F2 male (n=92) and female (n=85) did not reveal any suggestive or significant QTLs (**Figure-39**).

v) **Linkage Analyses for Total Body Bone Density in Line B2.4**

We generated 28 C3HB6 F1 mice by breeding 2.4 male mice with WT C3H mice. We generated a total of 98 F2 female by breeding 28 F1 mice for QTL mapping. We

have screened 92 F2 female progeny for bone density and size phenotypes at 10-week and at 16-week age as described in our dominant and recessive screen protocol. Genome wide main QTL(s) associated with total body bone mineral density (BMD) (measured by DEXA) in 10-week old intercrossed B6C3H F2 female mice (n=97) generated from mutant mice B2.4 was shown in **Figure-41**. The linkage analysis did not disclose and significant or suggestive linkages. Because the mutation was inherited in a recessive mode and we only mapped a limited number of F2 mice, it could be possible that we have very few mutant mice in the F2 population. Thus, our interval mapping strategy has limited power to detect linkage to a recessive mutation. This was in contrast to dominant ENU mutations where we were able to determine QTLs with only 69 F2 mice.

iv) **Fine Mapping of 917 Locus**

Since we completed the proposed objective of mapping mutant strain at low resolution within the grant period, we focused on fine mapping one of the most promising mutants. This was above and beyond the specific objectives proposed for the grant. We selected 917M because of interesting phenotype and also because the mutation was originally mapped to a novel locus.

Our strategies to identify mutant gene(s) from within the <1 cM region of 917 locus involves first identifying all functional positional candidate genes present in the 917 locus based on function and expression in skeletal tissues. The current understanding suggests that there are 30,000 genes in the mouse genome; thus, we anticipate that total number of predicted genes to be 20-40 in the 917M locus (<1 cM). Based on the rationale that approximately 20% of the 30,000 genes have been well characterized, we believe we have to study 4-8 genes even if all of them are involved in regulating skeletal tissues. We can subsequently sequence coding and/or regulatory region of these selected functional positional candidates.

b) **Fine Mapping of 917 Locus Using Higher Marker Density**

To fine map the chromosome 4 locus affecting bone density, we used 22 markers on chromosome 4 (**Table-18**). We first established the 95% confidence interval of 917 locus by calculating posterior probability density plot (**Figure-42**) using the Pseudomarker algorithm, which shows peak was located between 2 cM and 20 cM region. Next we identified all microsatellite markers available between C3H/HeJ and C57BL/6J strains of mice for the chromosome 4 between the 95% confidence interval of 917 locus. We then re-genotyped the F2 male mice (n=69) with these additional polymorphic microsatellite markers. Our results indicate that when additional markers were added the proximal peak was resolved into three major peaks, each showing significant LOD scores ($p<0.05$) (**Figure-43**). The posterior probability density plot showed that probability of middle peak, located at 10-12 cM, harboring the mutant gene was higher. Since the analysis was performed on small number of F2 mice, the multiple peaks could be result of artifact and the results needs to be validated using large number of F2 mice so that there are sufficient recombination to allow 1-2 cM resolution. Consequently, additional F2s were generated to further increase the resolution of 917M locus.

c) **Fine Mapping of 917 Locus Using Additional F2 mice**

d) Generation of F1 and F2 Mice for Fine Mapping of Line 917M: The key factors in high resolution mapping strategies are number of recombination events, the marker density and the effect size of the QTL. Mapping to a resolution of 10 cM usually requires analysis of >300 F2 mice. We believe that our strategy to generate about 100-150 additional F2 males combined with a >10% effect size, and 22 microsatellite markers could lead to a higher resolution of 917M locus. By employing a denser map by identifying 10-30 additional markers in the 5 cM region, we will be able to narrow the 917M locus to <1 cM. Based on the above rationale, we initiated an intercross of 917 with C3H/HeJ strain of mice to generate approximately 300 additional F2 mice.

We intercrossed three different 917M males with several C3H female mice to generate more than 45 F1 mice. The F1 mice were then bred to produce approximately 300 F2 mice, among them were 143 male F2 mice that were phenotyped and genotyped using microsatellite markers as described previously (**Figures 44 & 45**). We used 22 microsatellite markers in the 0-45.5 cM region of chromosome 4, where the 917M locus was assigned (**Table-18**). The microsatellite sequences and locations were obtained from Mouse Genome Informatics (http://www.informatics.jax.org). To perform interval mapping, we combined our new F2 data from 143 mice with the previously published F2 data from 69 male mice using a newly suggested approach of combined-cross analysis. This approach of combined analysis of data from multiple crosses have been suggested as means to increase resolution of the shared QTLs, the underlying reasons are increased marker density and the impact of combining the F2 data is equivalent to that of adding more recombination events in the QTL region by using additional mice in a cross. The combined data included 14 microsatellite markers in the 0-45 cM region. Linkage analysis was performed as described in previous sections using combined F2 genotype data and combined body weight adjusted total body bone area at 16-week from two crosses. Result of the interval mapping showed (**Figure-46A**) a peak between the D4Mit171 (3.2 cM) and D4Mit6 (20.8 cM) markers with the highest LOD score at D4Mit196 (12.1 cM). The 95% confidence intervals (CI) derived from posterior probability plot as described previously were 8-19 cM. The confidence interval defined as LOD-1 was 6-19 cM. Thus our fine mapping data confirmed our previous findings and localized the mutation to a narrower 8-19 cM region of the Chr 4. We did not achieve much higher resolution because we only produced about 143 of the 300 F2 required for optimum resolution.

Comparative Genome Analysis to narrow the 917M Locus: To further narrow the 917M locus, we explored for orthologous region in rat (Chr 5) and human (Chr 6, 8, & 9) genome database where linkage have been identified for bone size phenotype. Unfortunately, no orthologous linkages in rat or human have been published in the 917M support interval. A recent study by Lang et al (33) indicated the presence of loci on proximal Chr 4 that regulate total femur size (a measurement derived from periosteal circumference or cross-section area) in B6xBDA F2 mice and a BXD recombinant strain (generated from B6 & DBA strains of mice). The 95% CI of this locus overlapped with 917M support interval but the peak of these loci were outside the 95% CI of 917M locus (**Figure-46B**).

3.6.1 GOAL 5. Apply microarray technique to identify genes and potential pathways that are differentially expressed in mutant mice.

Our next goal was to identify the candidate gene in the chromosomal locus established for the selected mouse mutants. Our strategy to determine mutant gene included use of microarray technique to identify those genes that are differentially expressed between mutant mice and control mice in skeletal tissues. There were several reasons that we believed that microarray experiments will lead to identification of mutant gene. First, we can determine if any of the differentially expressed genes are located in the same chromosomal region earlier identified by linkage analysis. There is possibility that the causative gene may directly show an expression difference if the mutation is in the transcriptional regulatory region. Alternatively, loss of protein function due to coding sequence mutation may influence expression via diminished negative feed back regulation. Direct sequencing of the promoter elements or individual expression of genes by qRT-PCR of large number of candidates would be daunting. Expression data would help to prioritize those genes in the support interval that are most likely to harbor mutation in promoter or regulatory region. Importantly, the expression data would aid in identifying any mutation that ultimately leads to reduced steady state levels of message of mutant gene. Any mutation that affects a splice-junction, or creates a stop codon, is likely to undergo nonsense mediated decay and this could result in a reduced level of message on the array.

i) Selection of Mutant Strains for Microarray: We selected four mutant strains, 917M, 12184, 12137, and a soft tissue regeneration mutant line M1.2d to study gene expression. We selected the 917M, 12184, and 12137 lines because these mutants were mapped to a precise chromosomal location. In addition, we selected a new mutant line M1.2d because this strain offered us unique model to look into MRL strain of mice with very low healing capacity. We have already identified several important and precise QTLs for MRL strain that regulate ear punch healing capacity.

ii) General Procedure for Extraction of RNA from Various Tissues: For extraction of total RNA from bone and marrow tissues, the tissue homogenate were prepared in appropriate amount or lysis solution/beta-mecaptoethanaol mixture (20ul/mg) and cells manually lysed with a mortar and pestle. The cellular debris is removed by centrifuging up to 600ul of homogenate through the mini prefiltration column, for 3 minutes at 13000 rpm, and collecting the filtrate. Equal volume of 70% ethanol added to the filtrate, placed on ice for at least 5 minutes, and further purified using spin columns from RNeasy Total RNA Isolation Kit (Qiagen, Chatsworth, CA, USA) according to the manufacturer's instructions. Using the above protocol, we have obtained very high quality RNA from small amounts of tissue (50 milligrams and less). Before microarray analysis, each sample was evaluated for quality of the RNA by spectrophotometric analysis using Agilent 2100 Bioanalyzer. Concentration of the RNA yield was determined by spectrophotometric analysis using the convention that 1 OD at 260 nm equals 40 ug per ml. The absorbance was checked at 260 and 280 nm for determination of sample concentration and purity. Only samples with A260/A280 ratio close to 2.0 were selected for microarray analysis for pure RNA.

iii) Microarray Procedure: To perform in-house microarray, the pooled RNA was reverse transcribed into cDNA, labeled, and hybridized on our in-house microarray, which was created using Corning UltraGaps II glass slides and includes 16000 mouse genes or uncharacterized expressed sequence tag (EST) clone. To make slides the PCR products were spotted using a Genetix Q-Array2 robotic arrayer. The arrays

are also spotted with Amersham Lucidea Universal Scorecard controls to insure correct gene expression values were obtained from each array. The Lucidea Universal ScoreCard is a set of 23 unique microarray controls that can be used with samples from most species and with any microarray platform. The controls are artificial genes that generate pre-determined signal intensities that do not change across samples or experiments. Thus, the microarray analysis is not dependent on relative quantification. The controls generate a calibration curve for determining limits of detection, linear range, and data saturation, and they can be used as universal references for validating and normalizing microarray data. Controls are spotted in duplicate in the first and last PCR plates to insure proper data tracking.

The microarray slides were scanned using a GSI Lumonics ScanArray 4000 scanner. The arrays are scanned at a resolution of 10 microns which corresponds to ~15 pixels in diameter of each of the ~30,000 spots and a spacing of ~5 microns between the spots. The signal intensity of all microarray images is determined using Imagene 5.1 software. This software uses a patented image processing technology to provide quantification of microarray images of high density. Quality control measures include automated flagging of good, marginal and absent spots so that these can be filtered in the expression analysis.

iv) Analysis of Microarray Data: Significance of differentially expressed genes was calculated by TTEST analysis, with $p<0.05$ as significantly altered gene expression. An average-fold change for the four comparisons of the selected genes was then calculated. We looked at fold change for all differentially expressed genes with $p<0.05$. Further understanding the role of the differentially expressed genes in the pathways is critical in microarray studies. For this purpose, we use Gene Ontology to classify genes, to identify the pathways involved in each microarray study. Gene Ontologies are structured, controlled vocabularies that describe gene products in terms of their associated biological processes, cellular components and molecular functions in a species-independent manner. To determine if differentially expressed genes represent a pathway that is controlled by an upstream regulatory gene located in the chromosomal region for mutant gene, we have looked into all differentially expressed genes that could be likely candidate gene.

v) **Microarray Analysis of Skeletal Tissues from 917M mutant Mice:** To collect RNA from mutant mice, we have to rely on phenotype distribution because the genotype is not available currently. Consequently, we screened several male progeny from 917M at 6-weeks and 10-weeks of age and selected those mice that exhibited Z-score of <-2.5 at both time points. We used three replicates from three affected 917M mice. The ends of the tibia and femur were cut to flush out bone marrow, which was collected separately. The bones were then flushed with phosphate buffer saline solution. The bone and marrow were then stored at $-70^{o}C$ in RNALater (Ambion) according to manufacturer's protocol until extracted by pulverizing the bone in liquid nitrogen. Since we proposed to use bones from wild type mice as control, we collected additional tibia and femur from wild type female mice (n=3) exactly as described for mutant mice.

Significance of differentially expressed genes was calculated by TTEST analysis, with $p<0.05$ as significantly altered gene expression. An average-fold change for the four comparisons of the selected genes was then calculated. We looked at fold change for all differentially expressed genes with $p<0.05$. Using these selection criteria, approximately 50 genes were differentially regulated in the bone

from mutant mice compared with control mice. Those genes that are differentially regulated for 917M mutant and are located on Chr 1 or 4 are shown in **Table-19**. Some interesting candidates were described in **Table-20**.

vi) **Microarray Analysis of Osteoblasts from 917M mutant Mice:** In addition to skeletal tissues from 917M mice we also used osteoblasts cells from 917M mutant mice and WT mice to identify genes that are differentially expressed between mutant and wild type cells. The rationale for using the osteoblast from male 917M mice was based on two previous findings: 1) osteoblast cell proliferation was defective (**Section 3.4**); and 2) the 917 mutation affects the bone size in male mice only indicating a role of androgen in mediating the influence of mutant gene. The periosteal cells were isolated as described in previous sections of this report.

To identify candidate gene that are differentially expressed in osteoblasts from 917 mice as compared to osteoblasts from WT mice, we isolated the periosteal osteoblasts from femur and tibiae of 917 mutant and WT mice and propagated them in culture. In brief, the mice were euthanized with CO_2 and decapitated. Soft tissue was removed from femur and tibia without scraping off the bones so that periosteal cells were not lost at this point. Femur and tibia were placed separately in 50 ml falcon tubes containing sterile PBS, and subsequently in culture dish containing 10 ml of DMEM/antibiotics and the left over muscles were removed from the bones. The periosteal cells were extracted from bone by collagenase digestion for 90 minutes at 37^oC. Cells were counted and plated at a density of 10^6 cells per dish and grown with 10% FBS/DMEM/antibiotics. Periosteal osteoblasts at passage 2-3 were used to study differential display. We performed two experiments: 1) we compared the expression of the genes in the osteoblasts from 917 and WT mice (basal level differences); and 2) we treated osteoblasts from 917 and WT mice with dihydrotestosterone (5α-DHT). Osteoblast cultures were maintained overnight in an Alpha-MEM medium containing 10% steroid stripped fetal calf serum. Then culture medium was replaced with a medium containing 5α-DHT at a concentration of 10^{-8} to 10^{-10} M or vehicle for 48-hours. After 48-hours cells were isolated and RNA extracted as described above.

For extraction of total RNA from bone and marrow tissues, the cells were manually lysed with a mortar and pestle. The cellular debris was removed by centrifuging up to 600ul of homogenate through the mini prefiltration column, for 3 minutes at 13000 rpm, and collecting the filtrate. Equal volume of 70% ethanol added to the filtrate, placed on ice for at least 5 minutes, and further purified using spin columns from RNeasy Total RNA Isolation Kit (Qiagen, Chatsworth, CA, USA) according to the manufacturer's instructions. Using the above protocol, we have obtained very high quality RNA from small amounts of tissue (50 milligrams and less). Before microarray analysis, each sample was evaluated for quality of the RNA by spectrophotometric analysis using Agilent 2100 Bioanalyzer. Only samples with A260/A280 ratio close to 2.0 were selected for microarray analysis.

Results of microarray analysis revealed 164 genes that were differentially expressed in osteoblasts from 917 mice as compared to WT mice (basal level differences in gene expression). Similarly, when osteoblasts were treated with 5α-DHT, approximately 179 genes were significantly different in osteoblasts from 917 as compared to WT mice. To identify what pathways were specifically affected at basal

level and what pathways were altered when osteoblasts were treated with 5α-DHT, we performed pathway analysis of differentially expressed genes at both basal and stimulated conditions.

Interestingly, the microarray analysis from bone and osteoblasts identified one common gene, *Cbfa2t1h*, runt-related transcription factor 1, translocated to, 1 (cyclin D-related) (new symbol *Runx1t1*, other synonyms ETO, MTG8), was significantly (p=0.000407) higher in osteoblasts from 917M as compared to those from wild type mice when osteoblasts were treated with 5α-DHT. The *Runx1t1* is also located within the mutant locus on chromosome 4. The normalized expression of a potential candidate, was approximately six folds higher in skeletal tissues of mutant mice as compared to WT control (**Figure-47**). We validated the microarray based expression differences by quantitative qRT-PCR, which confirmed that expression of *Runx1t1* was about 2-folds higher in mRNA from skeletal tissues and osteoblasts from 10-week old mutant mice as compared to WT controls (**Figure-47**). We rigorously pursued this gene to identify its role in osteoblasts and skeletal tissues.

i) **Differentially Expressed Genes for 12317 and 12184 Mutant Mice**. To collect RNA from mutant mice, we have to rely on phenotype distribution. Consequently, we screened several female progeny from 12137 for total body bone density at 6- and 10-weeks of age and selected those mice that exhibited Z-score of 2.5 or more at both time points. We used three affected 12137 and three affected 12184 mice. To collect RNA sample, we sacrificed 12137 and 12184 mice, tibia and femurs were quickly isolated from any attached tissue. The ends of the tibia and femur were cut to flush out bone marrow, which was collected separately. The bones were then flushed with phosphate buffer saline solution. The bone and marrow were then stored at –70^{o}C in RNALater (Ambion) according to manufacturer's protocol until extracted by pulverizing the bone in liquid nitrogen. Since we proposed to use bones from wild type mice as control, we RNA collected from tibia and femur from wild type female mice (n=3) exactly as described for 917M mutant mice.

Analysis of the microarray data showed that more than 250 genes are significantly up or down regulated for 12137 mutant. There were approximately 194 genes upregulated and approximately 68 genes were down regulated. Analyses of the microarray data of 10-week old female 12184 mice (n=4) showed that expression of 262 genes (among them 150 were EST clones or splice variants) were significantly altered, of which 194 genes were up regulated and 68 genes were down regulated. **Table-21** shows genes that are differentially regulated and known to be involved in regulation of skeletal tissues. Since point mutations caused by ENU may not produce differences in expression levels of genes, these genes could reflect changes in affected pathways.

vii) **Differentially Expressed Genes for M1.2D Mutant Mice** For line M1.2d, we punched a 2 mm hole in each ear of the mutant progeny (shown in **Figure-32**) when mice were 3-weeks old. Four days after the 2 mm ear punch, we collected approximately 0.5 mm of the tissue lining the 2 mm hole from one ear; the other ear was left untouched to monitor rate of healing at 21-days post ear punch. If the untouched ear hole healed after 21-days, the other ear tissue sample collected at 4-day was categorized as unaffected and if healing was significantly reduced (hole size 1.0-2.0) the tissue sample was categorized mutant. Tissue samples from 2-3 mice

were pooled to make one replicate. We collected 4 affected and 4 control replicates and then stored at –70^{o}C in RNALater (Ambion) according to manufacturer's protocol until extracted by pulverizing the tissue in liquid nitrogen.

Analysis of the microarray data from M1.2 mice and WT MRL mice showed that more than 3000 genes or expressed sequence tags were significantly up or down regulated, including more than 500 known genes. Considering the large number of genes that are differentially expressed in the healing tissue as compared to WT tissue, we mainly investigated pathways that are significantly affected during the healing process. The results of the pathway analysis are described in the subsequent section.

3.6.2 **Pathway Analysis of Gene Expression Data from Microarray:** Since point mutations caused by ENU may not produce differences in expression levels of genes, our main aim was to identify affected pathways rather than individual genes. Understanding the role of the differentially expressed genes in the pathways is critical in microarray studies. To thoroughly characterize sets of functionally related genes differentially expressed between mutant mice and WT B6 control mice, we used Onto-Express to classify genes according to the Gene-Ontology (GO) categories: biological process; cellular role; and molecular function. We used a web-based tool, Pathway-Express (freely available as Onto-Tools suite at http://vortex.cs.wayne.edu/Projects.html), to find the most interesting pathways for their input list of genes. The Onto-Tools database integrates different types of genomic data from 19 sequence, gene, protein, and includes Gene Ontology (GO) annotations. After a list of genes is submitted, the system performs a search and builds a list of all associated pathways. A list of pathways for the input list of genes is calculated from the Onto-Tools database. The Pathway-Express first calculates a perturbation factor *PF(g)* for each input gene. This perturbation factor takes into account the (i) normalized fold change of the gene and (ii) the number and amount of perturbation of genes downstream from it. This gene perturbation factor reflects the relative importance of each differentially regulated gene. The impact factor of the entire pathway includes a probabilistic term that takes into consideration the proportion of differentially regulated genes on the pathway and gene perturbation factors of all genes in the pathway. The impact factors of all pathways are used to rank the pathways.

i. **Pathway Analysis of Gene Expression of M1.2D Mutant Mice**

The numbers of genes corresponding to each GO category among the 511 differentially expressed known genes ($p<0.05$) was tallied and compared with the number of genes expected for each GO. Significant differences from the expected were calculated with a two-sided binomial distribution. **Table-22** shows all GO functional classes with a Bonferroni-corrected significance of $p<0.05$, the significance of each class, as well as the number of genes corresponding to each GO functional class identified in our differentially expressed gene list. The functional gene groups demonstrating the most significant representation in our set of differentially expressed genes appear under the biological process ontology and map to the Cell adhesion molecules (CAMs), Axon guidance, and Gap junction. Genes involved in MAPK signaling pathway and Cytokine-cytokine receptor interaction are highly expressed in mutant. Other functional categories significantly represented under the cellular component and molecular function ontologies include genes involved in Tight junction, Leukocyte transendothelial migration, Fc epsilon RI signaling pathway, chemokine signaling, and Focal adhesion.

ii. **Pathway Analysis of Gene Expression of 12137 and 12184 Mutant Mice**

Tables 23 & 24 show number of genes corresponding to various GO categories among the 112 differentially expressed genes (with known function) in 12137 mice as compared to WT mice (n=3). The functional gene groups demonstrating the most significant representation in our set of differentially expressed genes appear prominently under the biological process MAPK signaling pathway, regulation of actin cytoskeleton, cytokine-cytokine receptor interaction, and apoptosis. Consistent with the histomorphometric data, microarray analysis identified some important genes associated with osteoclast differentiation or survival in 12137 mutant mice. Pathway analysis of differentially expressed genes from 12184 mice did not reveal statistically significant pathways (**Table-24**).

Quantitative RT-PCR (qRT-PCR): Changes in gene expression as determined by microarray analysis were independently confirmed by qRT-PCR for selected genes that were significantly up or down regulated and were involved in the osteoclast formation or activity. This confirmation was performed on the cDNA from same bones that underwent microarray analysis. The results of the qRT-PCR of selected genes normalized to expression of the housekeeping *Ppia* gene are shown in **Figure-48**. Interestingly, the expression levels of mRNA of osteoclastic enzyme cathepsin-k (*Ctsk*) and acid phosphatase (*Acp5*) were increased in 12137 mice compared to controls, which was further confirmed by the quantitative RT-PCR (**Figure-48)**. Recent data shows that *Ctsk* plays a key role in osteoclasts apoptosis and senescence, revealing the importance of osteoclasts senescence in bone homeostasis. Data from *Ctsk* deletion mice indicates that osteoclasts lacking *Ctsk* exhibited over-growth both in vitro and in vivo. These abnormalities resulted in an unusually high osteoclast numbers. On the contrary, the over expression of *Ctsk* in pre-osteoclasts induced premature senescence. These findings regarding *Ctsk* function provide insight into the potential mechanism of the high bone density mutant mice and could provide a useful tool to identify the mutant gene.

iii. **Pathway Analysis of Gene Expression of 917 Osteoblasts**

We performed separate pathway analysis for genes differentially regulated in basal osteoblasts and genes that were differentially regulated when osteoblasts were stimulated with 5α-DHT. Approximately 164 genes were differentially expressed in basal osteoblasts from 917 mice as compared to those from WT mice. Similarly, about 179 genes were differentially expressed when osteoblasts were treated with 5α-DHT.

The numbers genes corresponding to various GO category among the 164 differentially expressed known genes ($p<0.05$) at basal level. The number of genes corresponding to various GO category among the 179 differentially expressed known genes ($p<0.05$) under stimulated conditions is shown in **Table-25**.The functional gene groups demonstrating the most significant representation in our set of differentially expressed genes appear under the biological process Phosphatidylinositol signaling system, ECM-receptor interaction, Focal adhesion, TGF-beta signaling pathway. Other functional categories significantly represented under the cellular component and molecular function ontologies included genes involved in GnRH signaling pathway.

The functional gene groups demonstrating the most significant representation in 5α-DHT treated osteoblasts appeared under similar biological process, as

observed in basal osteoblasts such as Phosphatidylinositol signaling system, ECM-receptor interaction, Focal adhesion, TGF-beta signaling pathway. However, genes corresponding to the other functional categories significantly represented under stimulated conditions included genes involved in Cytokine-cytokine receptor interaction and MAPK signaling pathway (**Table-25**). These pathways will provide vital clues for identification of mutant gene and for prioritization of candidate gene to sequence and identify mutation.

3.7 GOAL 6. Identify candidate gene in the chromosomal locus of selected mutant mouse

The progress made under this objective was above and beyond the specific objectives proposed in the grant period 1999-2008. Since we met all the specific objectives, we followed up one potential candidate gene for functional study.

Identification of *Runx1t1* by Microarray Analysis and Candidate Gene Approach: In the Specific Objective 4, we described identification of candidate gene, Runx1t1, for a bone size mutant in 917M in C57BL/6J (B6) background. The runt-related transcription factor 1, translocated to, 1 (cyclin D-related) (Cbfa2t1h) (new symbol *Runx1t1*, other synonyms ETO, MTG8), was approximately six folds higher in skeletal tissues of mutant mice as compared to WT control. We validated the microarray based expression differences by quantitative qRT-PCR, which confirmed that expression of *Runx1t1* was about 2-folds higher in mRNA from skeletal tissues and osteoblasts from 10-week old mutant mice as compared to WT controls. The *Runx1t1* is located at 4.4 cM on chromosome 4, a genomic region within the mutant locus. The *Runx1t1* is human homologue of RUNX1T1, a putative transcription factor. The *Runx1t1* is well expressed in skeletal tissues and osteoblasts from B6 mice (**Figure-49**).

i) **Expression of *Runx1t1* during Proliferation and Differentiation:** To understand the relationship between osteoblast proliferation and *Runx1t1* expression, we analyzed *Runx1t1* levels during proliferative expansion of MC3T3 cells. The cells were grown in cultures in α-MEM containing 10% fetal bovine serum (FBS), growth arrested, and subsequently stimulated to proliferate by adding different amount of FBS (**Figure-50**). Cell numbers were analyzed by counting cells. Total extracts from MC3T3 cells that were incubated with different concentrations of FBS. Cell extracts were used for Western blot with an anti-Runx1t1 polyclonal antibody (Santa Cruz, CA). The western blot analysis indicates decrease in *Runx1t1* expression while expression of cyclin D1 was increased with increasing FBS concentration in cultures. Although molecular weight of *Runx1t1* protein is 64.3 kD, on SDS-Page it appeared between 64 kDa and 98 kDa molecular weight markers (**Figure-50**) under denaturing conditions. This was consistent with the Western blot analysis described earlier for *Runx1t1* null mice. These data indicates that *Runx1t1* levels were increased during reduced cell growth.

ii) To investigate *Runx1t1* expression levels during osteoblast differentiation, we performed two experiments. Bone marrow cells isolated from C57BL/6J mice, washed, and plated at a density of 1.5-2.5x10^6 cells/10-cm^2. When confluent, cells were treated with differentiation medium α-MEM+ β-glycerophosphate and ascorbic acid for 24 days. Cells were collected at 0, 6, 12, 18, and 24 days after initiation of differentiation, washed with PBS, and mRNA extracted using procedures described previously. We measured markers of differentiation such as *Runx2* and osterix and expression of *Runx1t1* by qRT-PCR. The results showed (**Figure-51**) that as

compared to day-0 the transcript levels of *Runx1t1* was mainly suppressed during the days 6-24, with a transient increase on day-12.

iii) In the second experiment, MC3T3 cells were plated at a density of 1.5-2.5x10^6 cells/10-cm^2 and differentiated and cells were harvested as described above. Nuclear extracts were tested with Western blot using antibodies against *Runx2* transcription factor and *Runx1t1*. The expression of *Runx1t1* was similar to those described above for bone marrow derived cells (details not shown). Results of both these preliminary observation indicate that *Runx1t1* is expression was mainly suppressed during differentiation. The physiological significance of these data remains to be elucidated.

iv) **siRNA Knockdown of *Runx1t1* mRNA in MC3T3 Cells:** The specific inhibition of gene by small interfering RNA (siRNA) provides a practical approach to investigate the function of gene in vitro. Consequently, we investigated the effect of suppression of *Runx1t1* gene on osteoblast proliferation and differentiation using pool of four siRNA specific for *Runx1t1* (Dharmacon). A non-targeting siRNA sequence was used as control. MC3T3 cells were plated to a density of 1x10^4 cells/2-cm^2 (proliferation assays) and 1x10^5 cells/10-cm^2 (Western blot) in antibiotic free α-MEM containing 10% FBS and chemically transfected (Dharmafect-1 transfection reagent) using manufacturers suggested protocol. After 24-36 hours, proliferation or differentiation was initiated as described above. The rate of proliferation was measured by AlmarBlur dye uptake as described previously and differentiation was measured by induction of alkaline phosphatase activity. Our results show that transfection of MC3T3 cells with *Runx1t1* siRNA but not control siRNA increased the proliferation significantly in presence or absence of FBS (**Figure-52)**. The transcript levels of *Runx1t1* in siRNA knocked down cells determined by qRT-PCR were 50-70% lower after 24-hours as compared to those from control mice (**Figure-52**). The protein levels were also decreased 48-hours after transfection as determined by Western blot (data not shown). The increased proliferation rate was confirmed by counting cell numbers at different time intervals, which showed cell doubling time was decreased (**Figure-52**). Consistent with these data, inhibition of Runx1t1 by siRNA also increased cell number in primary osteoblasts (**Figure-53**). Our data on induction of alkaline phosphatase activity measure on day-1, day-3, and day-7 did not disclose statistically significant differences (details not shown). Thus our data show that suppression of *Runx1t1* resulted in increased proliferation. Although, a major concern for siRNA application is specificity of the siRNA and their potential "off target" effects, we believe our results may not be influenced by "off target" effects because our phenotype was mainly gain of function and sequence homology search of the *Runx1t1* siRNA sequence did not reveal any significant homology.

v) **Acute Expression of *Runx1, Runx2,* and *Runx3* Transcripts were Not Altered After Suppression of *Runx1t1*:** Since *Runx1* and *Runx2* are essential for osteogenesis in mammals, as shown by gene targeting and mutation studies, we investigated if expression of Runx proteins was altered in response to *Runx1t1* suppression. MC3T3 cells were plated at a density of 1x10^5 cells/10-cm^2 in antibiotic free α-MEM containing 10% FBS and chemically transfected with *Runx1t1* siRNA as described above (n=3 each for *Runx1t1* and control siRNA). Cells were harvested 12-hours after transfection, washed with PBS, and total mRNA was extracted as described previously. *Runx1*, *Runx2*, and *Runx3* expression levels measured by qRT-PCR as described previously (34) were not significantly altered at 12-hour time

period (**Figure-54**). These data suggest that the acute effects of *Runx1t1* on cell proliferation may not be mediated through three Runt-domain containing transcription factors.

vi) **Expression of D-type Cyclins were Increased after siRNA Suppression of *Runx1t1*:** *Runx1* is shown to affect cell cycle progression through G1 phase by directly or indirectly controlling the genes for cyclins D2 and D3. Therefore, we postulated that *Runx1t1* may regulate the osteoblast proliferation by directly inhibiting cell cycle regulatory genes including cyclins D1, D2 and D3. We investigated expression levels of cyclins D1, D2, and D3 12- and 24-hours after the suppression of *Runx1t1*. MC3T3 cell were transfected with Runx1t1 or control siRNA as described above and cells were harvested for qRT-PCR analysis 12-hours and 24-hours post transfection. We observed that expression levels of cyclins D2 and D3 were significantly elevated 12-hours after the transfection of *Runx1t1* (**Figure-55**). After 24-hours, cyclins D1, D2, and D3 were significantly elevated. These data are consistent with increased proliferation phenotype described above.

vii) **Inhibition of Cyclin D1 action was Associated with Increased Expression of Runx1t1:** The D-type cyclins act as sensors for mitogenic growth factors and regulate transit of cells through G1 to S phase. We used a potent inhibitor of Cyclin D1, 2-cyclopentenone, to study if repression of cyclin D1 affected *Runx1t1* expression (41). MC3T3 cell were plated at a density of $1x10^5$ cells/10-cm^2 in α-MEM containing 10% FBS and grown to 60% confluence. The culture medium is aspirated and cells were starved for 48 with α-MEM containing no serum. After 48-hours, α-MEM containing 10% FBS was added and cells were treated with 600 μM of 2-cyclopentenone or vehicle (DMSO) for 24 hours. Cells were harvested for Western blot analysis as described above. Our results indicated that 2-cyclopentenone treatment increased the expression of *Runx1t1*, whereas, expression of cyclin D1 was reduced to undetected levels (**Figure-56**). These data provide further support to our hypothesis on the functional relationship between Runx1t1 and cyclin D1.

viii) **Cloning *Runx1t1* Gene to Study Regulation of D-type Cyclins during Cell Proliferation:**

Since, previous studies have shown that cyclin D3 promoter is activated by *Runx1* in certain cell types; it is possible that *Runx1t1* regulates cell cycle by modulating *Runx1* expression/recruitment. Therefore, we cloned the Runx1t1 gene and proposed to study if over expression of *Runx1t1* would influence the D-type cyclins promoter activity. To clone the *Runx1t1* gene, first total RNA was isolated from mouse bones using RNeasy Total RNA Isolation Kit (Qiagen, Chatsworth, CA, USA) according to the manufacturer's instructions. Approximately, 5 µg of total RNA was then reverse-transcribed into first-strand cDNA by using random and oligo(dT) primers according to the Superscript Preamplification System for First Strand cDNA Synthesis instructions (Life Technologies). One microliter aliquot of the cDNA was used as templates for PCR amplification with primers CCAGAACAGGAGGC ATGAGCC (forward primer) and CTAGCGAGGCGTCGTCTCTA (reverse primer). Amplification was performed using high fidelity *Pfu* polymerase with following conditions: were 94°C (12 min), 39 cycles at 94°C (1 min), 56°C (1 min), 72°C (3 min), and 72°C (10 min). PCR products were separated on 1% agarose gels and stained with ethidium bromide. The PCR results are shown in **Figure-57A** using a

combination of these primers produced expected size bands. After purification with Miniprep (Qiagen) the PCR products were cloned into the pCR TA cloning vector, pCR2.1 (pCR2.1 TOPO; Invitrogen, Inc.). The orientation of the DNA sequence was determined by restriction digests using XbaI, HindIII, and Sal1 restriction enzymes. The orientation of the DNA in the vector was also confirmed by sequencing the construct using primer sets: 1) CCAGAACAGGAGGC and GGTCTCAGTGG GAAGTTAGTAGCT; 2) TGCAAGAAGCTACTAACTTCCC and TTCTTCTTGA CGTGTGCCAT; 3) ACATGGCACACGTCAAGAAG and TGCTGGTTGATGA CTGCTAGAG; and 4) CCAGCAGGAAGACTCCAGTG and CTAGCGAGG CGTCGTCTCTA. The *Runx1t1*-pcR2.1 was amplified, DNA purified, and sub cloned into a pcDNA3.1 vector using HindIII and XbaI restriction enzymes. The orientation of the *Runx1t1* DNA in pcDNA3.1 vector was finally confirmed by restriction digests.

To determine the overe xpression of *Runx1t1*, the MC3T3 cells (mouse osteoblast cell line) were maintained in alpha-MEM medium with 10% fetal bovine serum. Next, the Runx1t1-pcDNA3.1 construct was transiently transfected in MC3T3 cells using Lipofectamine reagent (Invitrogen). After 48 hours the expression of *Runx1t1* protein in transfected MC3T3 cells was studied by western blotting with anti *Runx1t1* antibody. The data presented in **Figure-57B** show the expression of *Runx1t1* protein in transfected MC3T3 cells. Over expression of *Runx1t1* was >100 folds as determined by quantitative real time RT-PCR 12 hours after the transient transfection (**Figure-57C**).

Summary of Functional Characterization of *Runx1t1*: We identified that a putative transcription factor, *Runx1t1*, plays an important role in osteoblast proliferation. We have demonstrated that suppression of *Runx1t1* is coincidental with significant increase in cyclins D2 and D3 during early response and D1, D2, and D3 24-hours after the suppression of *Runx1t1*. These observations indicate that at least in part effects of *Runx1t1* could be mediated by regulation of expression of components of cyclin D pathway. The function of *Runx1t1* in vivo remains obscure, although mice lacking this protein have severe abnormalities of midgut development, leading in most cases to embryonic or early neonatal death. Details of skeletal phenotypes were not reported. In addition to the gastrointestinal defects, sterility was consistently observed in the few male null mutants surviving into adulthood. Since *Runx1t1* was mostly expressed by Leydig cells in the adult testis, it was suggested that male sterility in homozygotes could be due to hormonal insufficiency. Considering that another member of *Runx* family, R*unx2,* is essential for osteogenesis in mammals, as shown by gene targeting (ref) and by its mutations in cases of human cleidocranial dysplasia (ref), it can be speculated that *Cbfa2t1h* also plays important role in osteoblast senescence.

3.8 KEY RESEARCH ACCOMPLISHMENTS

- ***i)*** We optimized ENU dosage, optimized breeding schedule, developed and validated musculoskeletal phenotypic screens for mouse model. We optimized phenotypic measurements to allow for maximal reproducibility and sensitivity.
- ***ii)*** We developed a screening strategy to identify skeletal phenotypes in a large population of F1 and F3 progeny.
- ***iii)*** We produced >1600 F1 and >1200 F3 progeny for screening with skeletal and extra skeletal phenotypes.
- ***iv)*** We identified >50 phenotypic deviants in dominant and recessive screens.

v) We bred >30 phenotypic deviant mice in backcross with wild type mice. We confirmed several binary and quantitative phenotypic deviants in backcrosses. Finally, we have archived three important mutant strains by sperm cryopreservation.

vi) We mapped three mutant strains to putative chromosomal locations. We fine mapped one mutant strain to a narrower region, 12 cM, of chromosome 4.

vii) We used DNA microarray analysis to examine genome wide gene expression pattern in bone from four mutant mice as compared to that of wild type control mice.

viii) We have identified several potential pathways that could be altered in the mutant mice. These pathways would help us in identification of mutant gene.

ix) Using microarray and quantitative RT-PCR techniques, we identified a potential candidate gene, *Runx1t1* that was differentially expressed in the 917M mutant mice as compared to control mice.

x) Using siRNA mediated disruption of gene we studied the role of *Runx1t1* in mouse osteoblasts and identified a hitherto unknown role for *Runx1t1* in mouse osteoblasts. We cloned the *Runx1t1* gene into an expression vector (pcDNA3.1) to further study its role in regulation of cell cycle genes such as D-type cyclins.

3.9 REPORTABLE OUTCOMES

i) Srivastava AK, Bhattacharyya S, Li X, Mohan S & Baylink DJ. Circadian and longitudinal variation in serum C-telopeptide, osteocalcin, and skeletal alkaline phosphatase in C3H/HeJ mice. Bone, 29(4): 2001.

ii) Umemura Y, Baylink DJ, Wergedal JE, Mohan S & Srivastava AK. A time course of bone response to jump exercise in C57BL/6J Mice. J Bone & Mineral Metabolism, 20 (4), 2002.

iii) Li X, Srivastava AK, Gu W, Mohan S, and Baylink DJ. Opposing changes in osteocalcin levels in bone verses serum during the acquisition of peak bone density in C3H/HeJ and C57BL/6J mice. Calcified Tissue International, 71(6), 2002.

iv) Srivastava A K, Mohan S, Wergedal J E & Baylink DJ. A Genome-wide Screening of N-Ethyl-N-nitrosourea Mutagenized Mice for Musculoskeletal Phenotypes. Bone, 33, 179-191, 2003.

v) Srivastava AK, Kapur S, Godfred M, Kapur S, Wergedal J, Mohan S & Baylink DJ. Identification of novel genetic loci for bone size and mechanosensitivity in an ENU mutant exhibiting decreased bone size. J Bone & miner Res, 20(6):1041-50, 2005.

vi) Srivastava AK, Mohan S, Masinde G, Yu H, Baylink DJ**.** Mapping quantitative trait loci that influence blood levels of alkaline phosphatase in MRL/MpJ and SJL/J mice**.** J Lipid Res, 47(1):123-33, 2006.

vii) Mohan S, Chest V, Chadwick RB, Wergedal JE, Srivastava AK. Chemical mutagenesis induced two high bone density mouse mutants map to a concordant distal chromosome 4 locus. Bone, 41(5):860-868, 2007.

viii) Wergedal JE, Ackert-Bicknell CL, Beamer WG, Mohan S, Baylink DJ, Srivastava AK. Mapping genetic loci that regulate lipid levels in a NZB/B1NJxRF/J intercross and a combined intercross involving NZB/B1NJ, RF/J, MRL/MpJ, and SJL/J mouse strains. J Lipid Res, 48(8):1724-34, 2007.

3.10 CONCLUSIONS

i) We developed, validated, and adapted a musculoskeletal screen for mouse model. Through an extensive biological variation study, we determined the optimal sampling time for biochemical measurements. We then synchronized the phenotype screens by performing bone density and biochemical screen under one episode of

anesthesia. Consequently, we have achieved our first primary objective of developing, validating, and optimizing the phenotype screening procedure.

ii) We tested 7 different doses of ENU on seven different batches of male C3H mice. Although these experiments were still under progress, our preliminary results strongly suggest that three weekly injections of 100 mg/kg ENU was effective in producing large number of F1 progeny with mutations (exemplified by visible phenotypes). This accomplished our second main objective of identifying the optimum ENU dosage.

iii) We injected several batches of C3H/HeJ, C57BL/6J, and MRL/MpJ males with ENU dose of 3 X 100 mg/kg to generate ENU founder males. We bred the ENU injected founder males in a breeding scheme to generate about >1600 F1 mice for dominant screening and approximately 80 lines of recessive screening F3 progeny. In addition, we have screened >300 mice to generate normative data. Thus, total number of mice screened was ~3000, and therefore, we have exceeded our goals proposed in this grant.

iv) We have tested the inheritability of >30 phenotypic deviants and confirmed several phenotypic deviants as inheritable mutations. Furthermore, from the mice generated in inheritance-test crosses, we have done extensive characterization of mutant phenotype to explore cellular mechanism responsible for mutant phenotype.

v) We bred four ENU mutant mice to generate >450 F2 mice for mapping four mutant strains. In addition, we bred wild type non-mutagenized mice to generate 330 F2 mice for genotyping. We have genotyped >300 F2 mice using 40-60 genome wide informative markers to find out QTLs harboring mutant gene (s). We performed genome wide mapping of four ENU mutants and identified putative locus for three mutant genes.

vi) We provide evidence that the decrease in bone size observed in ENU mutant male mice could be due to a mutation in gene regulating osteoblast function in terms of proliferation, apoptosis, and response to mechanical stimulus. In addition, linkage analysis indicates that the point mutation is located on a novel allele of Chr 4 because no mouse or human linkage study has described QTL in a corresponding position. Additionally, we identified two mouse mutants with high aBMD, a clinically relevant phenotype. All these mutants were bred through more than five generations. Our mapping data showed that Chr 4 region contains a gene (or genes) that can influence variation in aBMD. Considering the importance of the Chr 4 locus in regulating several important bone strength and density phenotypes, the mutant mice identified in this project provide an attractive resource for identification of the gene at this locus.

vii) To identify the candidate gene in the chromosomal locus established for the bone size mutant mice, we performed DNA microarray analysis to investigate if the global gene expression pattern was altered in bone from mutant mice compared with wild type control mice. We have identified candidate genes or clones that were differentially expressed in mutant mice as compared to control mice. We evaluated various pathways that were affected by the differentially expressed genes for three mutant lines. Therefore, we have completed all four objectives of 'Specific Objective-5' and exceeded the proposed work.

viii) Finally, we identified *Runx1t1* as a potential candidate gene in the chromosomal locus established for the bone size mutant mice, 917M. We rigorously pursued the functional characteristics of this gene and assigned a novel function of *Runx1t1* in osteoblasts. Our data indicates that the Runx1t1 is a potential regulator of osteoblast proliferation. These studies were in addition to the specific objectives proposed during this study period.

ix) In conclusion, we demonstrated for the first time the effectiveness of employing phenotype-driven ENU mutagenesis in the investigation of genetics of osteoporosis. It also illustrates the utility of the ENU mutagenesis approach for generating models for use in genetic studies of osteoporosis where conventional knockout could be lethal. As anticipated, this project was successful in generating mutant mouse resources that will be useful in discerning function of genes that regulate skeletal tissues.

Table – 1. Breeding characteristics of C3H/HeJ male mice injected with different ENU doses.

	Dose (mg/kg x number of inj.)	Total dose	Inj/Sur	No Fertile	Sterile Period	Sterile (After)	No of F1 offspring
1	90 × 4	360	15/1	None	Sterile	Sterile	None
2	90 × 3	270	15/13	7	16-Week	26-Week	141
3	85 × 3	255	15/14	8	16-Week	Term.	101
4	250 × 1	250	20/18	2	15-Week	>40-weeks	65
5	85 × 3	255	45/45	24	15-Week	Term.	196
6	100 × 3	300	15/12	6	20-Week	TBD	48
7	85 × 4	340	15/13	1	30-Week	TBD	3 (Dead)

Table – 2. Response of C3H/HeJ and C57BL/6J mouse strains to 3 X 100 mg/kg dosage of ENU.

	C3H/HeJ (C3H)	C57BL/6J (B6)	MRL/MpJ (MRL)
Percentage of males died before regaining fertility	20%	10%	20%
Return to fertility (Weeks)	20-22	15-20	23.8
Percent males sterile	50%	40%	40%
Average Litter size	4.1	6.6	3.7

Table – 3. Effect of sampling time on biological variation in biochemical markers.

Biochemical marker	Between-individual variance (CV)	Signal to noise ratio
C-telopeptide	20.6 (9-10 AM sample)	2.3
	12.9 (3-4 PM sample)	3.7
Osteocalcin	16.4 (9-10 AM sample)	2.9
	13.3 (3-4 PM sample)	3.5
Skeletal Alkaline Phosphatase	12.9 (9-10 AM sample)	2.4
	12.6 (3-4 PM sample)	2.5

Table – 4. Correlation coefficients between size sensitive parameters measured by PIXImus and pQCT, before and after adjustment for body weight (n=60).

Phenotype & Measurement Technique	**Non-Adjusted Data**		**Adjusted Data**	
	Spearman Correlation Coefficient (r)	**p-Value**	**Spearman Correlation Coefficient (r)**	**p-Value**
	Male/Female			
BMD (PIXImus)	0.65/0.45	<0.0001	<0.02	NS
BMC (PIXImus)	0.74/0.65	<0.0001	<0.02	NS
Bone Area (PIXImus)	0.58/0.62	<0.0001	<0.02	NS
Femur BMD (PIXImus)	0.58//0.63	<0.0001	<0.02	NS
Total CNT (pQCT)	0.70/0.63	<0.0001	<0.02	NS
Total Area (pQCT)	0.65/0.66	<0.0001	<0.02	NS
Periosteal Circumference (pQCT)	0.63/0.63	<0.0001	<0.02	NS
Endosteal Circumference (pQCT)	0.14/0.20	NS		
Cortical Thickness (pQCT)	0.58/0.50	<0.0001	<0.02	NS

Table – 5. Reference range values of bone density and other parameters determined by Dual Energy X-ray Absorptiometery (DEXA) on 6-, 10-, and 16-week old non-mutagenized C3H/HeJ mice

Phenotype	Sex	6-Week Old Mice		10-Week Old Mice		16-Week Old Mice	
		Mean±SD (n=37)	Population Variance (CV)	Mean±SD (n=38-46)	Population Variance (CV)	Mean (n=40)	Population Variance (CV)
Weight (g)	F	17.2±1.6*	9.5	19.7±1.4*	7.2	21.8±1.6*	7.3
	M	21.2±1.7	7.8	24.8±1.5	6.0	28.1±1.5	5.4
Total Body BMD (g/cm^2)	F	0.0391±0.0023	5.8	0.0476±0.0018	3.8	0.0547±0.0018	3.4
	M	0.0411±0.0020	4.9	0.0481±0.0018	3.4	0.0545±0.0018	3.4
Total Body BMC (g)	F	0.298±0.0296*	9.9	0.454±0.0342*	7.5	0.539±0.036*	6.7
	M	0.338±0.030	9.0	0.483±0.030	6.3	0.582±0.038	6.5
Total Body Bone Area (cm^2)	F	7.6±0.5*	6.9	9.54±0.45*	4.7	9.9±0.5*	4.6
	M	8.2±0.6	7.7	10.0±0.40	4.6	10.7±0.52	4.9
Total Body Muscle mass (g)	F	7.4±0.71*	9.7	8.16±1.16*	13.9	10.2±1.5*	14.6
	M	10.2±1.1	9.8	12.8±1.20	9.7	15.7±1.34	8.6
Femoral BMD/CM^2	F	0.0505±0.032*	6.3	0.0678±0.0026*	3.9	0.080±0.003*	4.3
	M	0.0596±0.036	6.1	0.0754±0.004	5.4	0.085±0.006	6.7
Total Body BMD adjusted with Bone Area	F	0.0425±0.025	6.0	0.0462±0.0015	3.2	0.0547±0.0018	3.4
	M	0.0431±0.027	6.3	0.0455±0.0015	3.3	0.0545±0.0018	3.4
Total Body BMC adjusted with Bone Area	F	0.324±0.024*	7.4	0.440±0.024*	5.6	0.515±0.025*	5.6
	M	0.353±0.022	6.1	0.457±0.021	4.6	0.534±0.024	4.6

*Male significantly different from female.

Table – 6. Reference range values of bone density and other parameters determined at mid-diaphysis of tibia by peripheral quantitative computed tomography (pQCT) on 6-, 10-, and 16-week old non-mutagenized C3H/HeJ mice

Phenotype	Sex	6-Week Old Mice		10-Week Old Mice		16-Week Old Mice	
		Mean±SD (n=38)	Population Variance (CV)	Mean±SD (n=38-46)	Population Variance (CV)	Mean±SD (n=40)	Population Variance (CV)
Total BMC (mg/mm)	F*	0.78±0.05	6.6	1.05±0.06	5.8	1.31±0.08	5.9
	M	0.94±0.08	8.5	1.28±0.09	7.1	1.59±0.12	7.3
Total BMD (mg/cc)	F	754±17	2.3	889±23	2.6	978±19	1.9
	M	762±15	1.9	884±16	2.0	954±26	2.7
Total Bone Area (mm^2)	F*	1.03±0.09	8.3	1.19±0.09	7.3	1.34±0.07	5.3
	M	1.23±0.09	7.2	1.45±0.10	7.1	1.67±0.10	6.2
Cortical Density (mg/cc)	F	857±23	2.7	979±26	2.7	1060±16	1.5
	M	889±19	2.1	991±18	1.8	1058±21	1.9
Periosteal Circumference (mm)	F*	3.60±0.15	4.1	3.85±0.13	3.1	4.10±0.11	2.6
	M	3.93±0.14	3.6	4.27±0.15	3.6	4.58±0.14	3.0
Endosteal Circumference (mm)	F*	1.52±0.11	7.2	1.40±0.12	8.5	1.34±0.08	6.3
	M	1.76±0.09	5.1	1.63±0.13	8.0	1.64±0.11	6.5

*Male significantly different from female.

Table – 7. Number of mice tested, phenotypes scored (including visible and musculoskeletal), and inherited mutations identified.

Procedure	C3H/HeJ	C57BL/6J	MRL/MpJ	Total
Screened for Dominant Mode of Inheritance	832	596	197	1625
Screened for Recessive Mode of Inheritance	585	397	24	1205
Abnormal Phenotypes Identified in Primary Screen (dominant as well as recessive screening)	26	43	32	101
Abnormal Phenotypes Confirmed in Secondary Screen	13	21	20	54
Phenotypes Introduced to Backcross with Wild Type Mice	13	16	20	49
Phenotypic Deviants Confirmed (including binary phenotypes) in Backcross	4	4	1	9
Phenotypes Not-inherited in Progeny Testing (including those died or could not mate)	8	5	19	32

Table – 8. List of phenodeviants identified in dominant and recessive screening.

Phenotype (Mice ID)	Description of Phenotype	Mice Strain	ENU Screen
11.16.6.B.M	12% High volumetric BMD	C3H	Recessive
12.14.5.E.A.M	20% Low Area and 15% high total body BMD	C3H	Recessive
Line 2.8.6	10-12% Low total body BMD, BMC, 10-20% low body weight, greasy fur (Fig.-5)	C3H	Recessive
10.14.5.E.M	High Total Body BMD (C3H)	C3H	Recessive
12137	20% High body weight and 15% high body weight adjusted BMD	B6	Dominant
12184	15% High BMD	B6	Dominant
9187	20% High lean body mass	B6	Dominant
917M	17-20% Low BMC, and 10% Low total body bone area	B6	Dominant
12.15.1.C.F	Hip Dysplasia, Also See Fig.-4	B6	Dominant
12.6.4.D.F	Hip Dysplasia, Also See Fig.-4	B6	Dominant
12.13.9.I.F	Hip Dysplasia, Also See Fig.-4	B6	Dominant
14.7.3.B.M	25% Low bone area and BMC	B6	Dominant
Line B2.4	20% High total body BMD	B6	Recessive
Line B7.2	10% High volumetric BMD	B6	Recessive
Line B13.2	10% High volumetric BMD	B6	Recessive
Line B5.1.c	6-10 Folds high Creatinine Kinase	B6	Recessive
Line B3.2.F	High blood cholesterol, HDL and triglyceride	B6	Recessive
B24.3	12-17% High Total Body BMD	B6	Recessive
B19.4	55-90% High Triglyceride	B6	Recessive
B17.2	High FAT Mass Z-Score=6.1, Total Body Bone Area Z-Score=-2.5	B6	Recessive
B3.2	20-30% Low Total Cholesterol, HDL, & TG	B6	Recessive
B20.3E & F	Total Body BMD Z-Score=2.4 to 3.5, Total Body BMC Z-Score=2.4 to 2.5	B6	Recessive
B9.4.I & K	Total Body BMD Z-Score=2.6-4.2, Total Body BMC Z-Score=3.0-4.1	B6	Recessive
B5.4.D	Total Body BMD Z-Score=3.2, Total Body BMC Z-Score=4.2	B6	Recessive
B14.1.E	High FAT Mass Z-Score=4.5	B6	Recessive
B15.3.F	Body Weight Z-Score=-5.8 Low IGF-I	B6	Recessive
B5.3.F	High Cortical Thickness Z-Score=2.0	B6	Recessive
B22.3c, g & e	Body Weight Z-Score=-2.5 to –5.6, Low IGF-I	B6	Recessive
B29.2	30-40% Low Serum Alkaline Phosphatase and Osteocalcin, Total Body BMD Z-Score=1.8	B6	Recessive
B27.2	Total Body BMD Z-Score=-5.0, Total Body BMC Z-Score=-6.8	B6	Recessive
B15.3.F	Body Weight Z-Score=-5.8 Low IGF-I	B6	Recessive
B5.3.F	High Cortical Thickness Z-Score=2.0	B6	Recessive
B22.3c, g & e	Body Weight Z-Score=-2.5 to –5.6, Low IGF-I	B6	Recessive
B29.2	30-40% Low Serum Alkaline Phosphatase and Osteocalcin, Total Body BMD Z-Score=1.8	B6	Recessive
B27.2	Total Body BMD Z-Score=-5.0, Total Body BMC Z-Score=-6.8	B6	Recessive

Table – 9. Selected phenotypic deviants identified in MRL strain of mice and backcrossed to confirm mutation.

ID	Phenotype Observed at 16-Week Confirmation Screen	Number of Mice Produced for Inheritance Testing	Status
M1.2d	STR 1.9 mm, Tibia Midshaft BMD Z-Score=4.2, Trabecular BMD Z-Score=3.7	**76**	Confirmed
M1.9a	STR 1.9 mm	**13**	Not Confirmed
M1.4d	STR 1.7 mm, Tibia Midshaft BMD Z-Score=2.0	**1**	Could Not Breed[a]
M1.4.A	Low Total Body BMC, Z-Score=-3.1	**0**	Could Not Breed
M1.4.B	High Total Body BMC, Z-Score= 2.5, Tibia Midshaft BMD Z-Score=3.8	**15**	Not Confirmed
M1.11b	Low BW Z-Score=-2.1, Total Body BMD Z-Score=-3.7, Total Body BMC Z-Score=-3.1	**0**	Could Not Breed
M1.2.k	High BW Z-Score=2.0, Total Body BMD Z-Score=2.9, Total Body BMC Z-Score=2.4	**0**	Could Not Breed
M1.8.A	High Total Body BMC Z-Score=4.2	**0**	Could Not Breed
M1.8.B	High Total Body BMD Z-Score=3.4, Total Body Bone Area Z-Score=-3.2	**3**	Could Not Breed
M1.9.D	BW Z-Score=3.3, Total Body BMD Z-Score=3.9, Bone Area Z-Score=-5.1	**18**	Not Confirmed
M1.6.A	STR 1.6 mm, High BMD BW Z-Score=3.2, BMD Z-Score=3.7, BMC Z-Score=2.8	**0**	Could Not Breed
M1.9.k	STR 1.1 mm, Total Body BMD Z-Score=3.7, Total Body BMC Z-Score=2.3	**0**	Could Not Breed
M1.5.I	Total Body BMD Z-Score=2.8, Total Body Bone Area Z-Score=-3.1, High Alkaline Phosphatase	**16**	Partially Confirmed
M1.5.k	Total Body BMD Z-Score=3.6, Total Body BMC Z-Score=3.0	**0**	Could Not Breed
M1.2.L	Total Body BMC Z-Score=2.9, Total Body Bone Area Z-Score=2.9	**0**	Could Not Breed
M1.6A	STR 1.6 mm	**0**	Could Not Breed
M1.7A	STR 1.4 mm	**15**	Not Confirmed
M1.14.g	51% High Alkaline Phosphatase	**0**	Could Not Breed
M1.4.F	23% High Blood Triglyceride	**0**	Could Not Breed
M1.14C	Low BMD at Midshaft Tibia Z-Score=-5.8	**0**	Could Not Breed
M1.7.D	STR=1.9	**8**	Could Not Breed

BW= Body Weight, BMD= Bone Mineral Density, BMC= Bone Mineral Content, STR= Soft tissue Regeneration phenotype shown as size of hole in mm (normal values range between 0-5 mm) Z-Score indicates differences in a particular phenotype in terms of SD units from wild type control mice.

[a]A lot of mice could not produce more than one or two litters and therefore we were unable to assess if mutation is inherited or not. A possible reason was that these mice were bred only after secondary screening (when >16-week old) and after 1-2 breeding cycle their productivity declines considerably as they grow older.

Table – 10. Selected phenotypic deviants from recessive screen that were backcrossed to confirm heritability.

No	ID	Phenotype at Repeat Screening or 16-Week Confirmation Screen	Number of F1 & F2 Mice Produced	Number of F3 Mice Screened	Status
1	Line 286 (Agouti Line)	10-12% Low total body BMD, BMC, 10-20% low body weight, fur has greasy appearance (Fig.-5)	91	37	Confirmed But Did Not Breed Well
2	B2.4.C.M	Total Body BMD Z-Score=3.9, Total Body BMC Z-Score=3.0	182	111	Confirmed
3	10.14.5.E.M	High Total Body BMD (C3H)	60	19	Confirmed But Normative Data Shifted (Discontinue)
4	B7.2.AM & BM	Total Body BMD Z-Score=2.5, Tibia Midshaft BMD Z-Score=2.9	80	39	Not Confirmed
5	B7.2.E	High Blood Urea Nitrogen (45 mg/dL)	28	0	Not Confirmed
6	B24.3	12-17% High Total Body BMD	50	4	Not Confirmed
7	B19.4	55-90% High Triglyceride	22	0	IT Testing
8	B17.2	High FAT Mass Z-Score=6.1, Total Body Bone Area Z-Score=-2.5	18	9	Not Confirmed
9	B3.2	20-30% Low Total Cholesterol, HDL, & TG	25	9	Not Confirmed
10	B20.3E & F	Total Body BMD Z-Score=2.4 to 3.5, Total Body BMC Z-Score=2.4 to 2.5	101	21	Confirmed But Did Not Breed Well
11	B9.4.I & K	Total Body BMD Z-Score=2.6-4.2, Total Body BMC Z-Score=3.0-4.1	35	13	Not Confirmed
12	B5.4.D	Total Body BMD Z-Score=3.2, Total Body BMC Z-Score=4.2	62	39	Confirmed
13	B14.1.E	High FAT Mass Z-Score=4.5	18	11	Not Confirmed
14	B15.3.F	Body Weight Z-Score=-5.8 Low IGF-I	57	16	Not Confirmed
15	B5.3.F	High Cortical Thickness Z-Score=2.0	82	25	Partially Confirmed
16	B22.3c, g & e	Body Weight Z-Score=-2.5 to –5.6, Low IGF-I	14	4	Not Confirmed
17	B29.2	30-40% Low Serum Alkaline Phosphatase and Osteocalcin, Total Body BMD Z-Score=1.8	60	16	Not Confirmed
18	B27.2	Total Body BMD Z-Score=-5.0, Total Body BMC Z-Score=-6.8	51	1	Not Confirmed

BMD= BONE MINERAL DENSITY, BMC= BONE MINERAL CONTENT, Z-SCORE INDICATES DIFFERENCES IN A PARTICULAR PHENOTYPE IN TERMS OF SD UNITS FROM WILD TYPE CONTROL MICE.

Table – 11. Selected phenotypic deviants from dominant screening that were backcrossed to confirm heritability, characterize phenotype, and mapped to identify chromosomal location.

No	ID	Phenotype (Strain)	Number of Mice Produced in Backcross	Number of Backcrossed Mice Screened	**Current Status**
1	917M	15-20% Low Total Body Bone Area and BMC (B6)	>450	427	Archived by Sperm Cryopreservation
2	12137	20% High BW & Total Body BMC (B6)	492	492	Archived by Sperm Cryopreservation
3	12184	16% High Total Body BMD & BMC (B6)	341	341	Archived by Sperm Cryopreservation
4	M1.2d	STR 1.9 mm, Tibia Midshaft BMD Z-Score=4.2, Trabecular BMD Z-Score=3.7	172	172	Confirmed But Discontinued Because of Breeding Difficulties

*In this mutant line only male mice were screened after we observed that only male mice were affected

Table – 12. Mean percent difference in body weight adjusted bone area parameters in 16-week old 917M phenotypic deviant mice as compared to wild type control mice.

	Total Body Bone Area (Excluding skull)	Tibia Middiaphysis		
		Bone Area	BMC	Periosteal Circum.
Male (n=21)	-10.4**	-16.9**	-11.7**	-8.8**
Female (n=36)	-2.6*	-5.1*	-1.4#	-2.4*

#p=NS, *p<0.05, **p<0.001 Vs wild type control mice (n=40)

Table – 13. Differences in bone size parameters at tibia midshaft in affected 917M progeny as compared to non-affected littermates.

Phenotype	10-Week*	p-value	16-Week*	p-Value
Total Bone Area	8.8%	<0.001	-9.3%	<0.001
Total BMC	-9.7%	<0.001	-10.4%	<0.001
Cortical Area	-7.3%	<0.001	-8.9%	<0.001
Periosteal Circumference	-4.4%	<0.01	-4.7%	<0.001
Endosteal Circumference	-6.6%	<0.001	-5.5%	<0.001

*Values represents difference in size phenotypes at midshaft tibia in mutant mice (n=52) as compared to littermates (n=72) or WT B6 male mice

Table – 14. Characterization of bone size parameters at femur and tibia midshaft in affected 917M mutant progeny as compared to non-affected littermates as determined by histology.

Phenotype	Femur			Tibia		
	917M (Mean±SD)	WT (Mean±SD)	p-value	917M (Mean±SD)	WT (Mean±SD)	p-Value
Length (mm)	14.8±0.59	15.53±0.46	0.304	17.27±0.83	17.6±1.41	0.194
Total Area (mm^2)	1.69±0.046*	2.04±0.152	0.003	0.87±0.047*	1.09±0.145	0.030
Bone Area (mm^2)	0.81±0.038	0.93±0.107	0.083	0.66±0.043	0.69±0.043	0.284
Marrow Area (mm^2)	0.88±0.009*	1.11±0.102	0.004	0.21±0.057	0.39±0.142	0.055
Periosteal Perimeter (mm)	4.87±0.026*	5.35±0.261	0.012	3.44±0.152	4.09±0.497	0.056
Endosteal Perimeter (mm)	3.61±0.047*	3.99±0.226	0.018	1.64±0.21	2.35±0.56	0.063
Bone Perimeter (mm)	8.48±0.039*	9.34±0.437	0.008	5.08±0.309	6.44±1.01	0.050
Bone Formation Rate (mm^2 x 10^{-3}/day)	1.58±0.68	2.04±0.56	0.277	1.18±0.27	1.09±0.44	0.742

*Values represent difference in size phenotypes at midshaft tibia in mutant mice (n=5) as compared to littermates or WT B6 (n=4-5).

Table – 15. List of suggestive and significant marker pair showing interaction from genome-wide analysis of bone area in 917M B6C3H F2 males.

Chr. Pairs Q1 × Q2	cM Q1	cM Q2	LOD full	LOD int	p-value (Interaction)	LOD Q1	p-value	LOD Q2	p-value
1 × 1	5	40	9.31	5.02	0.0001	3.49	0.0003	0.00	0.9975
1 × 2	45	95	8.78	3.06	0.0070	1.32	0.0481	5.38	0.0000
1 × 4	90	10	12.32	3.18	0.0054	7.62	0.0000	1.16	0.0686
4 × 4	10	80	12.22	3.69	0.0019	0.56	0.2748	7.86	0.0000

T

hreshold for significant full effects (LODfull) was LOD 8.9 (when combined effects of marker pair were significant at $p<0.05$) and threshold for suggestive interaction was LOD 8.7 ($p<0.1$). Threshold for significant interaction (LODint) was LOD 5.6 and threshold for suggestive interaction was LOD 5.1 ($p<0.1$). Q1 and Q2 indicate locus 1 and 2. LODQ1 and LODQ2 indicate LOD score for main effect of locus 1 and locus 2. The cM1 and cM2 indicate centi-Morgan position of locus 1 and locus 2.

Table – 16. Linkage analysis of the body weight adjusted aBMD in mutant mice.

Mutant ID	LOD Score [a]	Peak Location (cM)	95% Confidence Interval (cM)	p-value
12137 (n=164)	3.1	55.0	46-78	0.000779
12184 (n=137)	7.7	70.0	46-72	<0.000001

[a]The cut-off for genome-wide significance at p<0.05 was LOD 3.1. aBMD= Total Body Areal BMD

Table – 17. Linkage analysis of the aBMD when body weight is used as a covariate.

Mutant ID	aBMD LOD Score	Peak Location (cM)	p-value	aBMD LOD Score with Body Weight as Covariate	Peak Location (cM)	p-value
12137 Male (n= 61)	2.6[c]	70.0	0.05652	4.9[f]	60.0	0.000012
12184 Male (n= 71)	3.6[a]	57.4	0.000240	3.7[d]	70.0	0.000187
12184 Female (n= 66)	3.3[b]	70.0	0.000537	4.2[e]	70.0	0.000061

The cut-offs for genome-wide significant (P<0.05) LOD score were [a, b, c] LOD 3.3, [d, e]LOD 3.1, and [f]LOD 3.2. Linkage data for female 12137 mice is not shown because LOD score was below suggestive levels (P<0.10). aBMD=Total Body Areal BMD

Table – 18. List of chromosomes 4 markers that have been used to fine map the chromosomal location of the mutant gene for bone size mutant 917M. Our earlier mapping effort identified a prominent locus in the proximal region of the chromosome 4. Therefore, we have increased the marker density to narrow the mutant interval.

Locus	Chromosome	Genetic Position (cM)
D4Mit149	4	1.0
D4Mit264	4	1.9
D4Mit227	4	3.2
D4Mit50	4	5.4
D4Mit171	4	6.3
D4Mit193	4	7.5
D4Mit172	4	8.6
D4Mit41	4	10.5
D4Mit196	4	12.1
D4Mit237	4	13.3
D4Mit17	4	13.4
D4Mit286	4	14.5
D4Mit91	4	15.6
D4Mit268	4	17.9
D4Mit53	4	19.8
D4Mit80	4	37.7
D4Mit153	4	45.5
D4Mit308	4	57.4
D4Mit203	4	60.0
D4Mit251	4	66.0
D4Mit170	4	66.6
D4Mit209	4	79.4
D4Mit42	4	81.0

Table - 19. List of genes that belong to chromosomes 1 and 4 and are significantly up or down regulated in mutant 917 mice as compared to WT control mice.

This list only includes genes that are differentially expressed between mutant 917M mice as compared to WT mice and are located on chromosome 1and 4 where two QTLs regulating bone size were observed.

Gene Name	Normalized Data	Common		Genbank
H3106E12	5.99	Cbfa2t1h	Chr 4	BG072085
H3087D02	5.48		Chr 4	BG070437
H3068H11	2.84		Chr 4	BG068752
H3062A11	2.76		Chr 4	BG068128
H3045G04	2.38		Chr 4	BG066591
H3155F06	2.22		Chr 4	
H3038H06	2.10		Chr 4	BG066098
H3063H09	1.76		Chr 4	BG068298
H3009E04	1.40	2410043F08Rik	Chr 4	BG063619
H3025H09	1.34	Vamp3	Chr 4	BG064970
H3004B04	1.33		Chr 4	BG063189
H3101C12	1.31		Chr 4	BG071628
H3059H05	1.28	Smp1-pending	Chr 4	BG067938
H3065E11	1.14		Chr 4	BG068443
H3106C04	1.11		Chr 4,10,14	BG072059
H3021G02	1.11		Chr 4	BG064599
H3113A04	0.93	Rps6	Chr 4	BG072620
H3016C08	0.93		Chr 4	
H3145H04	0.92	C1qb	Chr 4	BG075320
H3128E03	0.90		Chr 4	
H3131B04	0.90	Scp2	Chr 4	BG074122
H3022H02	0.89		Chr 4,18	
H3115H06	0.88		Chr 13,17,4	
H3055A12	0.81	Prdx1	Chr 4	BG067497
H3099G06	0.50	Tcea3	Chr 4	BG071507
H3144D01	0.13		Chr 8,4	BG075190
H3064E12	3.376		Chr 1	BG068355
H3037G06	2.374		Chr 1	BG065999
H3064B04	2.243		Chr 1	BG068315
H3146F07B	1.909		Chr 1	BG075390
H3124H10A	1.813		Chr 1	
H3146G02	1.539	Cfh	Chr 1	BG075397
H3125B12	1.463		Chr 1	
H3061H05	1.433		Chr 1	BG068111
H3033A06	1.42		Chr 1	BG065593
H3040G11	1.417		Chr 1	
H3019B03	1.402	Soat1	Chr 1	BG064396
H3056C01	1.347	Fmn2	Chr 1	BG067604
H3146C07	1.314		Chr 1	BG075356
H3140F12	1.212		Chr 1,M	BG074900
H3041A10	1.179		Chr 1	BG066276
H3019A11	0.939	Vps4b	Chr 1	BG064392
H3107E08	0.915	C130074G19Rik	Chr 1	BG072168
H3112E01	0.905	Snrpe	Chr 1	BG072573
H3066F01	0.892	Rgs2	Chr 1	BG068533
H3009C06	0.872	Arpc2	Chr 1	BG063604
H3121A10	0.863		Chr 1	
H3113E11	0.862	LOC226519	Chr 1	BG072670
H3124F03	0.856		Chr 1,14	
H3076A07	0.851	2810031L11Rik	Chr 1	BG069483
H3016F11	0.81		Chr 1,11	
H3130F03	0.808		Chr 1,14	
H3039H04B	0.759	Ipo9	Chr 1	BG066182
H3124G10	0.742	Uxs1	Chr 1	BG073697

Table – 20. Candidate genes and their known functions identified in 917M locus on chromosome 4.

Gene Name, Clone, EST	Position (Mb)	Expression in Bone*	Predicted Function	Difference between Mutant & Control
Rbm12b	12.1	Median	RNA binding activity	0.54
Cbfa2t1h	13.7	Median	Adipocyte cell differentiation, regulation of DNA binding	5.99
Efcbp1	15.0	Median	EF hand calcium binding protein	0.13
Wwp1	19.5	Median	Inhibition of transcription, Epithelial sodium channel (ENaC)	0.28
5730406M06 Rik	21.9	2 Folds	Protein of unknown function	5.48
Map3k7	32.3	Median	TGF-beta receptor signaling pathway	1.29
Mdn1	33.0	Median	ATP binding protein	1.24
Prol2	33.6	Above Median	Receptor activity	0.86
Ddx58	40.4	Median	ATP binding protein	1.38
Chmp5	41.1	Below Median	Molecular function unknown	0.91
BG063189	41.7	Above Median	Protein of unknown function	1.33
Smp1	43.7	Median	Molecular function unknown	1.28
Fbxo10	45.1	Median	Protein binding	0.90
Frmpd1	45.2	Above Median	Signal transduction	1.31
Ppp3r2	49.7	Median, >50 fold in testis	Bone formation, calcium-dependent protein serine/threonine phosphatase activity	2.84

*The expression levels were taken from the web based repository at http://symatlas.gnf.org/SymAtlas/

Table – 21. Selected Genes that are differentially expressed in the skeletal tissues of the 12137 and 12184 mutant mice as compared to those from WT control mice.

Gene Symbol	Fold Change	P-Value	Gene Name	Function
12137 Mutant				
Cox6a2	0.4	0.0076	Cytochrome c oxidase, subunit VI a	functional differentiation of preosteoclasts
Cox7a1	0.6	0.0405	Cytochrome c oxidase, subunit VII a	
Ndrg2	0.4	0.0071	N-myc downstream regulated gene 2	
Pgam2	1.3	0.0065	phosphoglycerate mutase 2	phosphotransferases activity
Cox8b	0.3	0.0053	Cytochrome c oxidase, subunit VIII b	
Ostf1	1.4	0.0040	osteoclast stimulating factor 1	Transcriptional regulation of osteoclasts
Ctsg	1.7	0.0244	Cathepsin G	Cysteine Protease
Fgr	1.3	0.0155	Gardner-Rasheed feline sarcoma viral (Fgr) oncogene homolog	Tyrosine protein kinase
Ctsk	1.5	0.0147	Cathepsin K	Cysteine Protease, degradation of the type I collagen
Acp5	1.6	0.0038	Tartrate resistant acid phosphatase 5	
Clic1	1.3	0.0345	chloride intracellular channel 1	chloride channel activity
Alox5ap	1.3	0.0159	arachidonate 5-lipoxygenase activating protein	development of collagen-induced arthritis
Scap2	1.3	0.0279	src family associated phosphoprotein 2	
12184 Mutant				
Sparc, osteonectin	2.5	0.0350	secreted acidic cysteine rich glycoprotein	Decreased osteoclast and osteoblast cell number
Ctsk	2.4	0.0459	Cathepsin K	Cysteine Protease, degradation of the type I collagen
Col1a2	2.6	0.0312	procollagen, type I, alpha 2	extracellular matrix structural constituent,
Bglap-rs1	3.3	0.0405	bone gamma-carboxyglutamate protein, related sequence 1	Bone mineralization
Acp5	2.1	0.0250	Tartrate resistant acid phosphatase 5	degradation of the type I collagen
Cox7c	0.7	0.449	cytochrome c oxidase, subunit VIIc	
Cox8b	0.4	0.348		
Cox6a2	0.5	0.372	Cytochrome c oxidase, subunit VI a	functional differentiation of preosteoclasts
Ubc	0.9	0.0028	Ubiquitin C	protein modification process

Table – 22. Pathway analysis of genes that are differentially expressed between soft tissue undergoing healing from mutant Line M1.2 and similar tissue from WT MRL mice as control.

Rank	Pathway Name	Impact Factor	# Genes in Pathway	# Input Genes in Pathway	p-value
1	Cell adhesion molecules (CAMs)	230	147	4	0.127
2	Axon guidance	7.0	132	6	0.008
3	Gap junction	6.8	90	3	0.114
4	Tight junction	6.1	117	3	0.198
5	Leukocyte transendothelial migration	6.1	117	4	0.068
6	MAPK signaling pathway	6.0	231	7	0.033
7	Cytokine-cytokine receptor interaction	5.4	241	8	0.014
8	Focal adhesion	5.3	190	4	0.238
9	Fc epsilon RI signaling pathway	5.2	75	4	0.017
10	Colorectal cancer	5.2	77	3	0.080
11	Notch signaling pathway	5.0	46	2	0.121
12	Natural killer cell mediated cytotoxicity	4.9	117	2	0.454
13	Long-term depression	4.8	72	2	0.243
14	GnRH signaling pathway	4.7	93	4	0.034
15	Huntington's disease	4.5	28	2	0.052

Table – 23. Pathway analysis of genes that are differentially expressed between skeletal tissues of Line 12137 and WT B6 mice.

Rank	Pathway Name	Impact Factor	#Genes in Pathway	#Input Genes in Pathway	%PathwayGenes in Input	p-value
1	MAPK signaling pathway	28	231	5	2.165	0.007742
2	Natural killer cell mediated cytotoxicity	18	117	4	3.419	0.001833
3	Regulation of actin cytoskeleton	15	199	4	2.01	0.016658
4	Leukocyte transendothelial migration	11	117	4	3.419	0.001833
5	Toll-like receptor signaling pathway	10	91	3	3.297	0.004755
6	Apoptosis	10	81	4	4.938	3.47E-04
7	Cytokine-cytokine receptor interaction	10	241	5	2.075	0.009424
8	Adipocytokine signaling pathway	9	69	2	2.899	0.01472
9	Complement and coagulation cascades	8	71	3	4.225	0.001939
10	Neuroactive ligand-receptor interaction	8	311	4	1.286	0.082689
12	Focal adhesion	8	190	3	1.579	0.053483
13	Type II diabetes mellitus	6	45	1	2.222	0.043991
14	Regulation of autophagy	6	31	1	3.226	0.022101
15	Insulin signaling pathway	6	133	2	1.504	0.076686
17	Axon guidance	6	132	2	1.515	0.07535
18	Olfactory transduction	5	30	2	6.667	0.001409
19	Amyotrophic lateral sclerosis (ALS)	5	17	1	5.882	0.006918

Table – 24. Pathway analysis of genes that are differentially expressed between skeletal tissues of Line 12184 and WT B6 mice.

Pathway Name	Impact Factor	Input Genes in Pathway	Pathway Genes on Chip	%Pathway Genes in Input	p-value
Olfactory transduction	5.214	1	30	3.3	0.08109
Long-term potentiation	4.734	1	63	1.6	0.1628
Taste transduction	4.454	1	60	1.7	0.15568
Hedgehog signaling pathway	4.405	1	53	1.9	0.13883
Gap junction	4.241	1	90	1.1	0.22428
MAPK signaling pathway	4.211	2	231	0.9	0.13798
Natural killer cell mediated cytotoxicity	3.974	1	117	0.9	0.2813
Wnt signaling pathway	3.696	1	143	0.7	0.33228
Calcium signaling pathway	3.54	1	174	0.6	0.38841
Insulin signaling pathway	3.431	1	133	0.8	0.31311
GnRH signaling pathway	3.412	1	93	1.1	0.23083
Type I diabetes mellitus	3.168	1	63	1.6	0.1628
Regulation of actin cytoskeleton	1.777	1	199	0.5	0.43026

Table – 25. Functional gene groups demonstrating the most significant representation to various pathways in 917M osteoblasts as compared to those from WT mice (basal levels).

Pathway Name	Impact Factor	Genes in Pathway	Input Genes in Pathway	%Pathway Genes in Input	p-value	Sum(PF)
Focal adhesion	25.1	190	13	6.8	<0.0000001	2.31
ECM-receptor interaction	22.2	85	9	10.6	<0.0000001	2.16
TGF-beta signaling pathway	15.8	83	5	6.0	0.0001380	6.89
MAPK signaling pathway	15.7	231	10	4.3	0.0000013	2.15
Cytokine-cytokine receptor interaction	14.5	241	10	4.1	0.0000019	1.30
Colorectal cancer	11.9	77	5	6.5	0.0000966	2.64
Regulation of actin cytoskeleton	9.3	199	6	3.0	0.0012393	2.62
Toll-like receptor signaling pathway	8.2	91	4	4.4	0.0021331	2.07
Complement and coagulation cascades	7.7	71	4	5.6	0.0008499	0.61
Leukocyte transendothelial migration	7.2	117	3	2.6	0.0325579	3.76
Insulin signaling pathway	6.5	133	4	3.0	0.0082109	1.67
B cell receptor signaling pathway	6.4	64	3	4.7	0.0065399	1.33
Apoptosis	6.2	81	3	3.7	0.0124493	1.77
T cell receptor signaling pathway	5.3	94	3	3.2	0.0185010	1.33
mTOR signaling pathway	4.4	49	2	4.1	0.0342293	1.04

Table – 26. Functional gene groups demonstrating the most significant representation to various pathways in 917M osteoblasts treated with 5α-DHT as compared to those from WT mice (treated under identical condition).

Pathway Name	Impact Factor	# Genes in Pathway	# Input Genes in Pathway	% Pathway Genes in Input	p-value
MAPK signaling pathway	33.9	233	13	5.6	0.000066
Focal adhesion	84.8	156	11	7.1	0.000020
Phosphatidylinositol signaling system	42.8	48	3	6.3	0.009703
Cytokine-cytokine receptor interaction	17.4	240	9	3.8	0.009849
Complement and coagulation cascades	15.1	70	5	7.1	0.001392
Toll-like receptor signaling pathway	14.1	94	5	5.3	0.006102
Apoptosis	14.1	90	6	6.7	0.001008
Adherens junction	9.5	76	3	3.9	0.043916
Calcium signaling pathway	8.3	180	4	2.2	0.206820

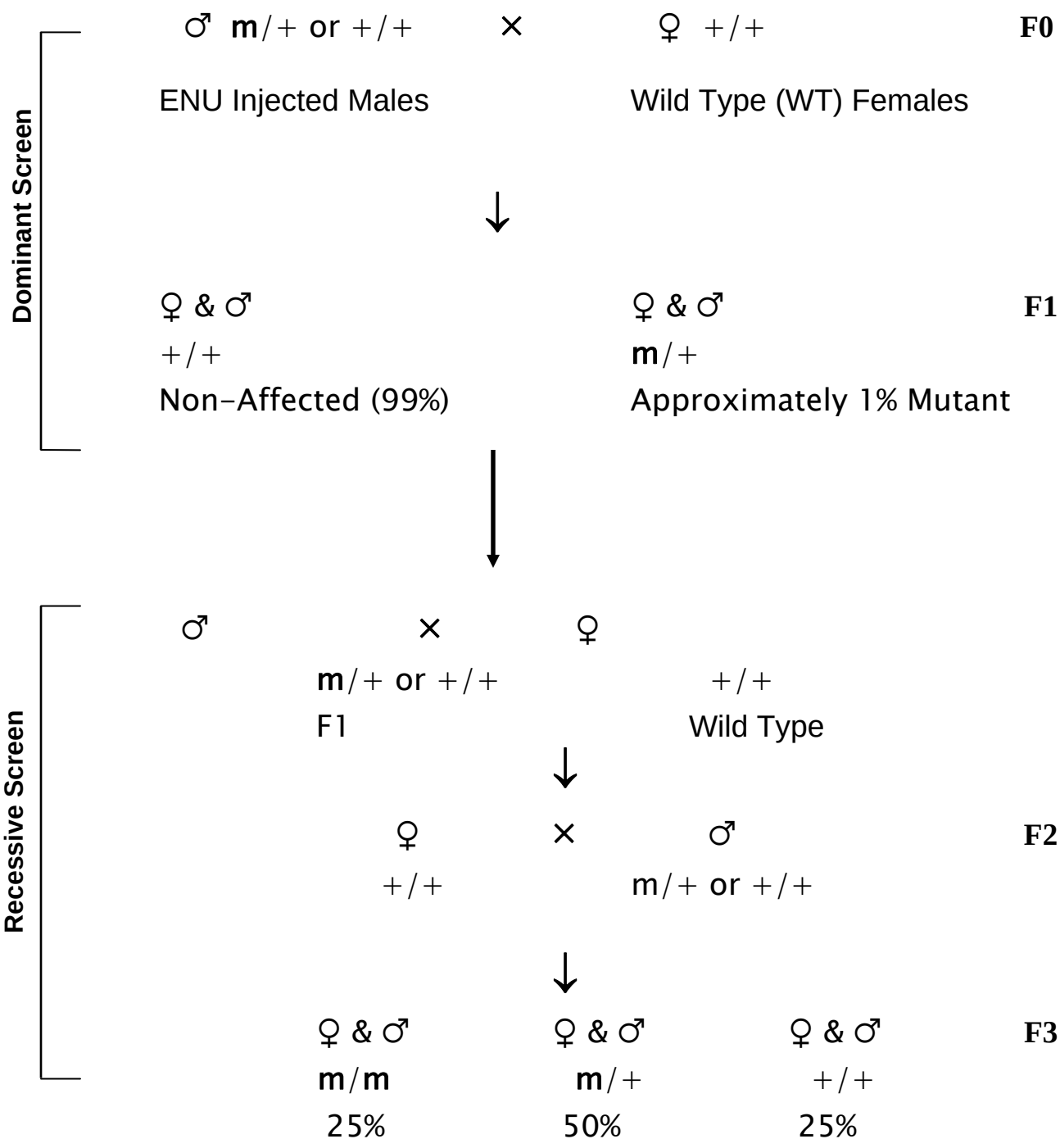

Figure-1. Breeding scheme for generating ENU induced mutations. The breeding scheme incorporates both dominant and recessive screens.

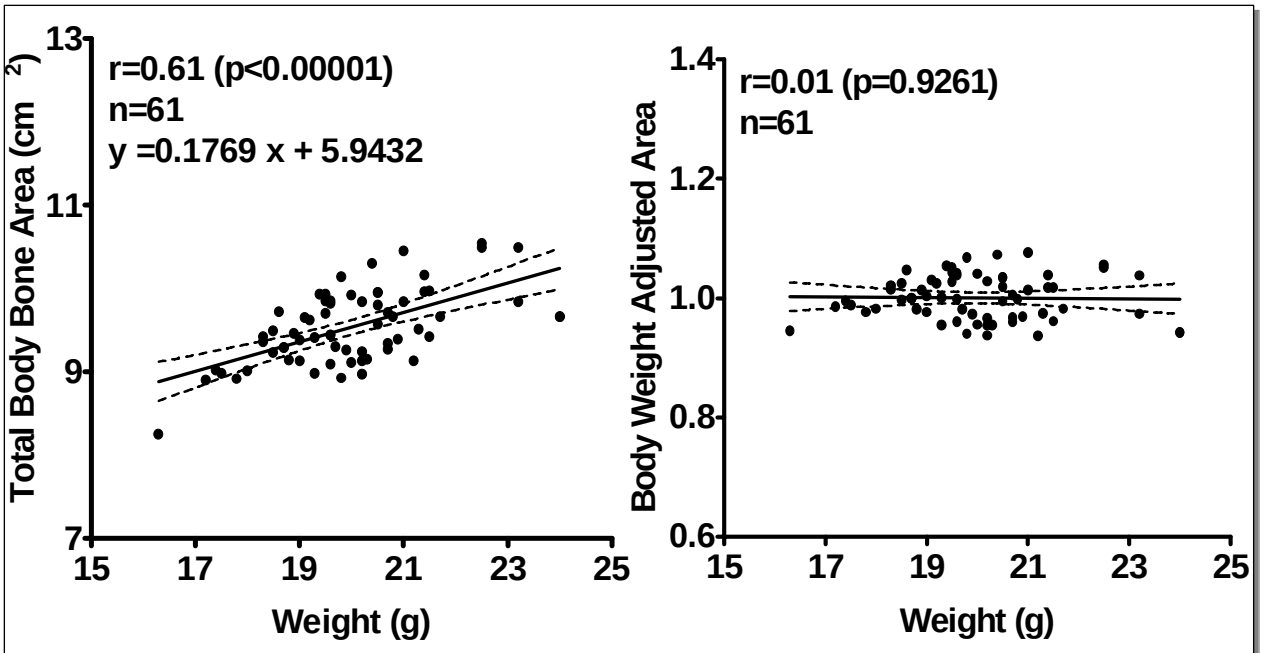

Figure – 2. Bone density, bone mineral content, and bone size measured by DEXA were significantly dependent on body size. Therefore, to identify if the skeletal phenotypes were abnormal relative to body size, we used regression analysis to correct for body size. Data from wild type mice was used to generate regression equation, which was used to adjust for body mass. The body weight adjusted values did not show significant correlation with body weight.

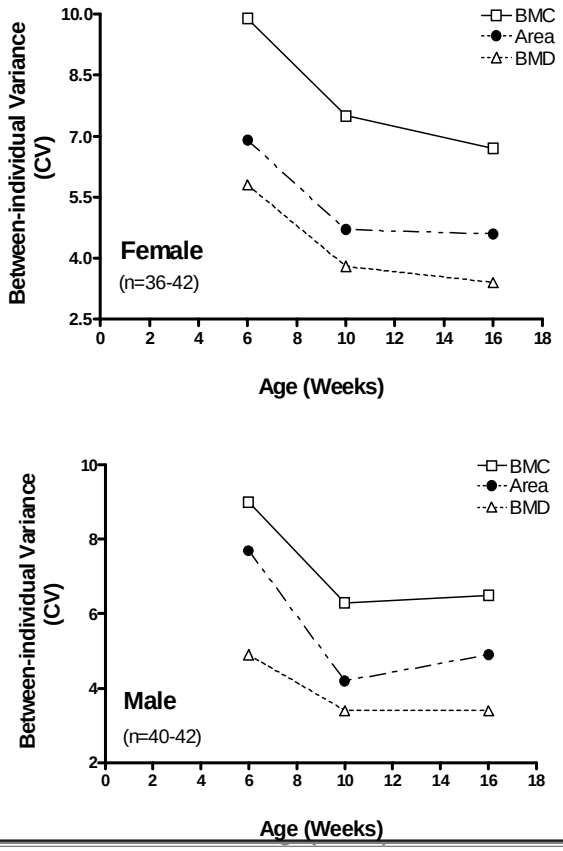

Figure – 3. Population variance in the measurements of bone mineral density, bone mineral content, and bone area as determined by Dual Energy X-ray Absorptiometry (DEXA) of female and male C3H/HeJ mice. The higher CVs at 6-week age would result in classification errors in identifying abnormal phenotype using this technique.

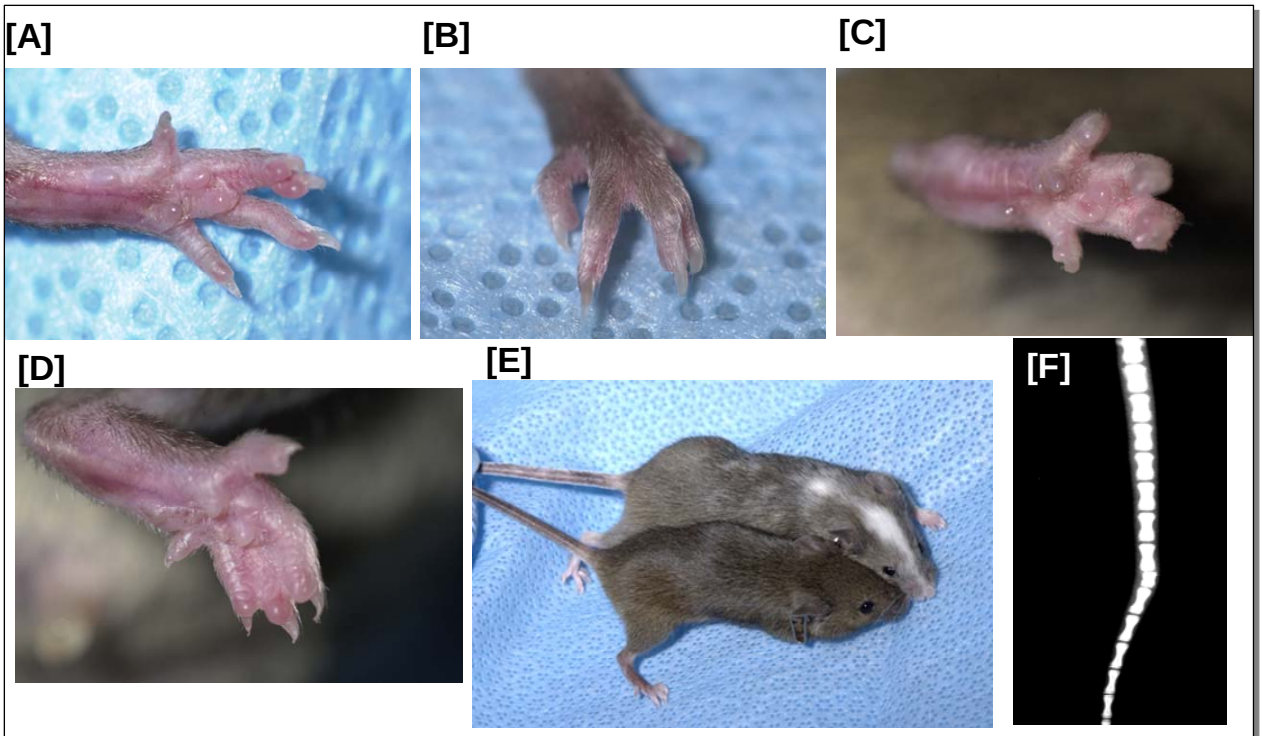

Figure 4. Dominant mutations that result in visible phenotype. Syndactyly was observed in both forepaws and hind-paws of four different C3H mice. Pictures A-C show syndactyly with fusion of digits 2+3; picture D shows fusion of digits 2+3+4. [E]. Mouse with dominant spotting mutation with a wild-type littermate. [F]. Faxitron (X-ray) image of tail portion of a mouse with kinky tail.

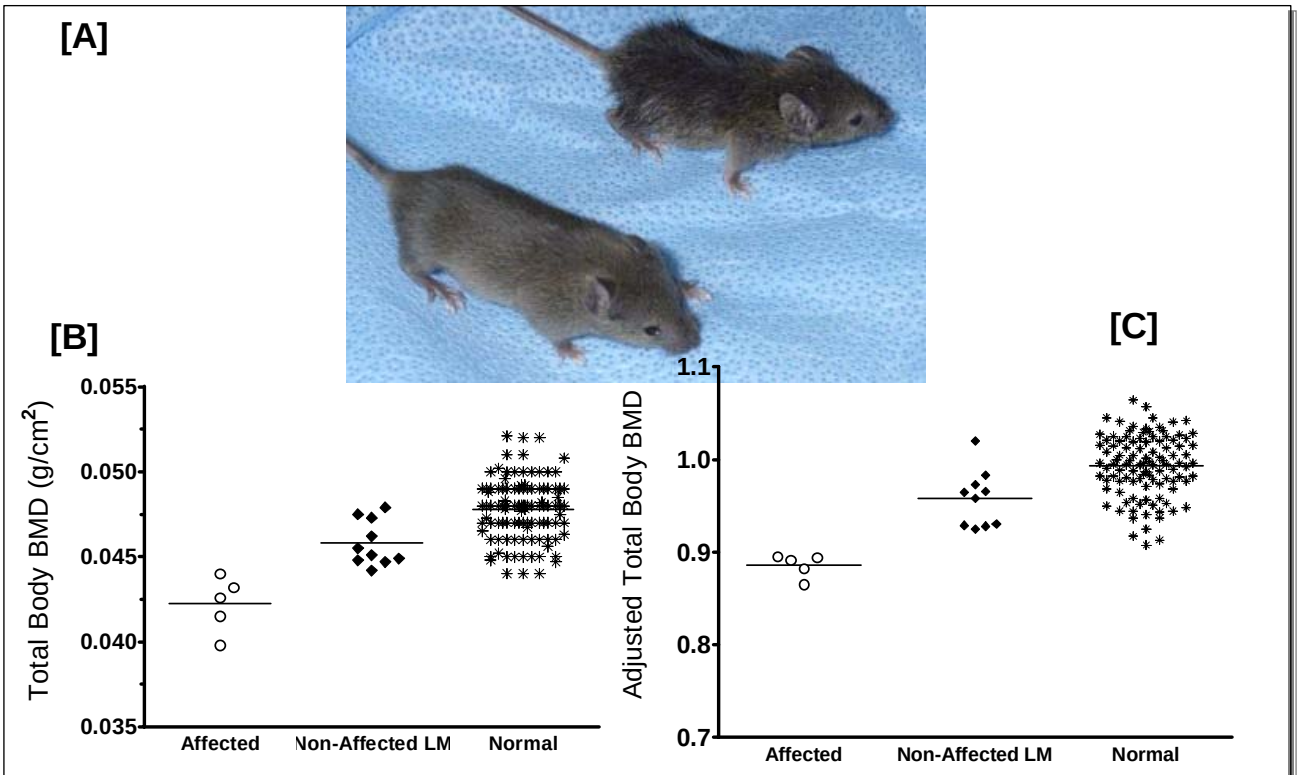

Figure 5. Mutant mice with visible phenotypes detected in F3 progeny in recessive screen. (A) A mutant mice (Right) shown with normal littermate (Left), affected mice appears small (low body weight) and shows fur with greasy appearance early in development (birth to 6-week age). Adult mutants have hairs with increased yellow pigmentation, and low BMD (B & C).

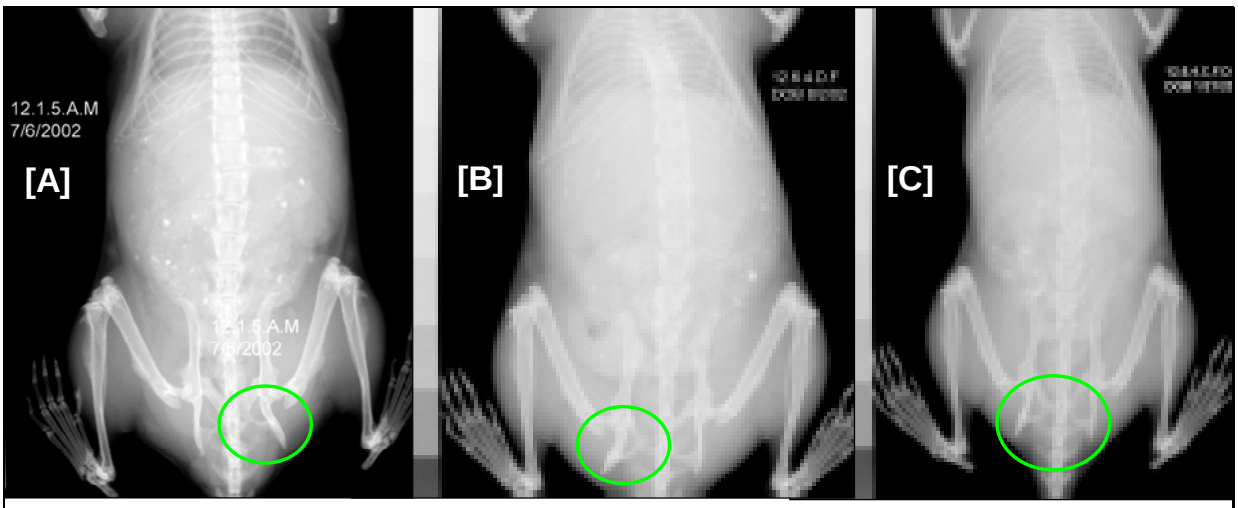

Figure – 6. A & B. Hip dysplasia observed in F1 progeny from dominant screen (B6). C. One of the phenotypic deviant with hip dysplasia (12.6.4) produced progeny that showed that the phenotype was inheritable.

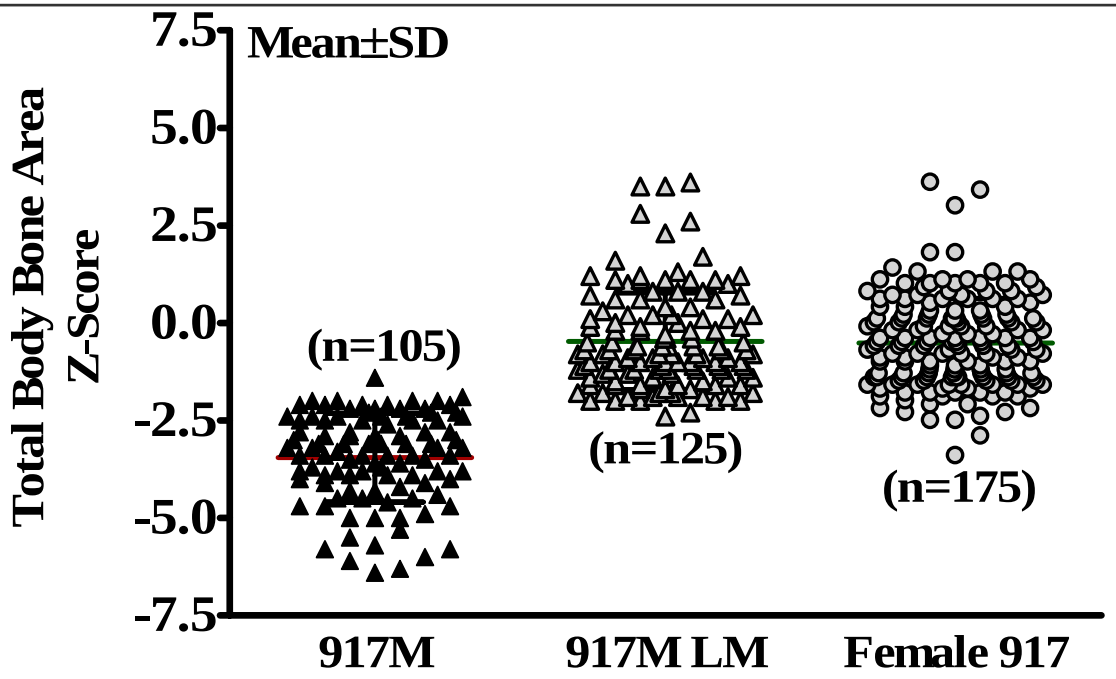

Figure – 7. Identification of ENU mutant with low (10-14%) bone size. Total body bone size (body weight adjusted) expressed as Z-scores (SD units difference from WT mice) in mutant male 917M, and male (917 LM) and female littermates.

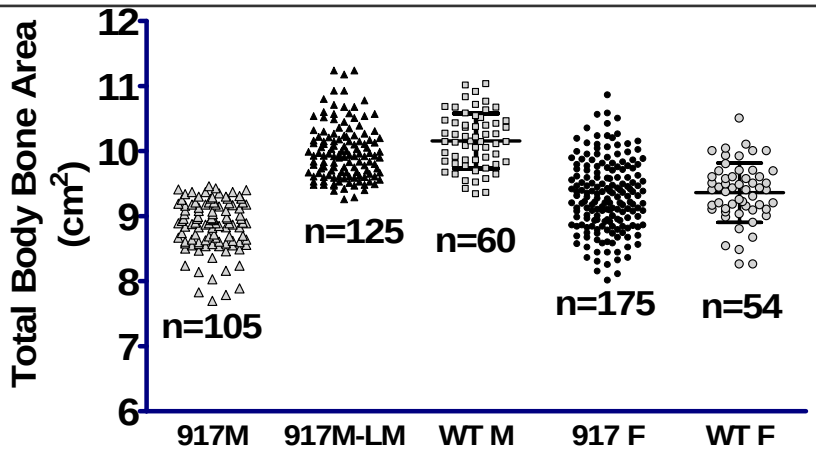

Figure – 8. 917M mutant with decreased bone size in male mice, whereas, females were unaffected. 917M=Mutant Male, 917M LM=Unaffected Male Littermates, 917 F=Female littermates of mutant, WT M & F= Wild type male & female

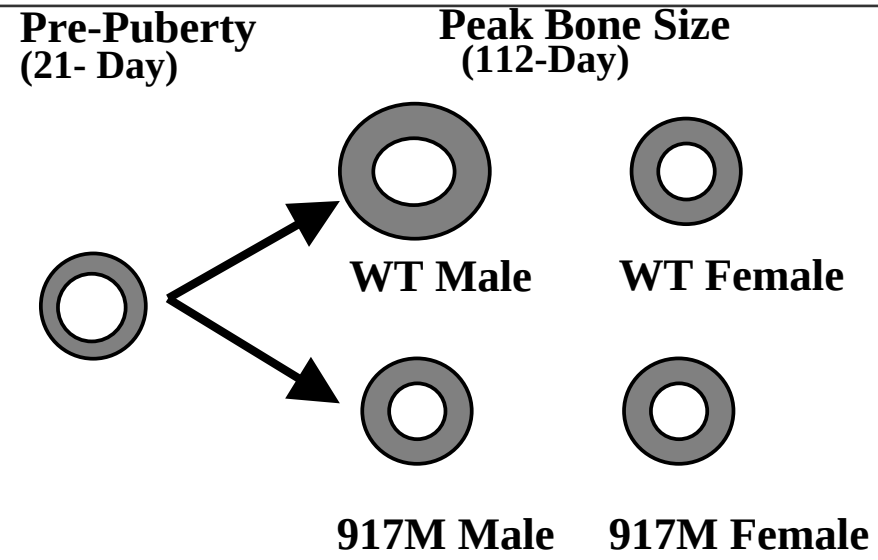

Figure – 9. Gender differences in cross-sectional area development and influence of 917M mutation to reduce the gender difference in bone size.

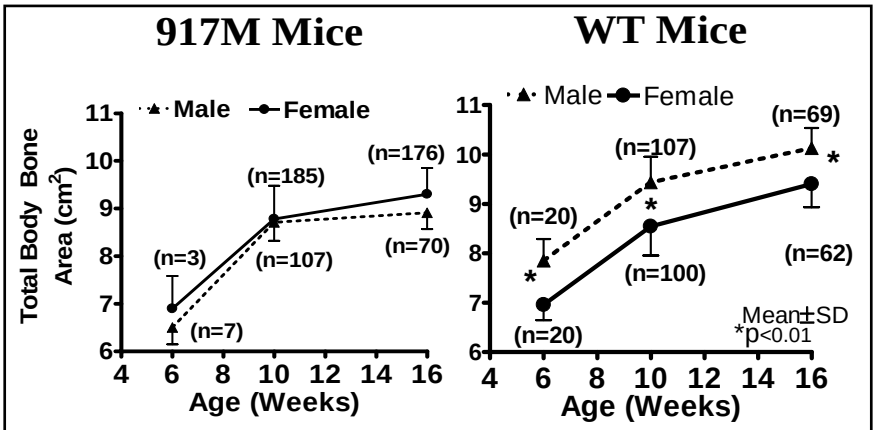

Figure – 10. Total body bone size determined by DEXA in 6-, 10-, 16-week old WT and 917M mutant mice. In mutant mice, the post pubertal increase in bone size is significantly reduced.

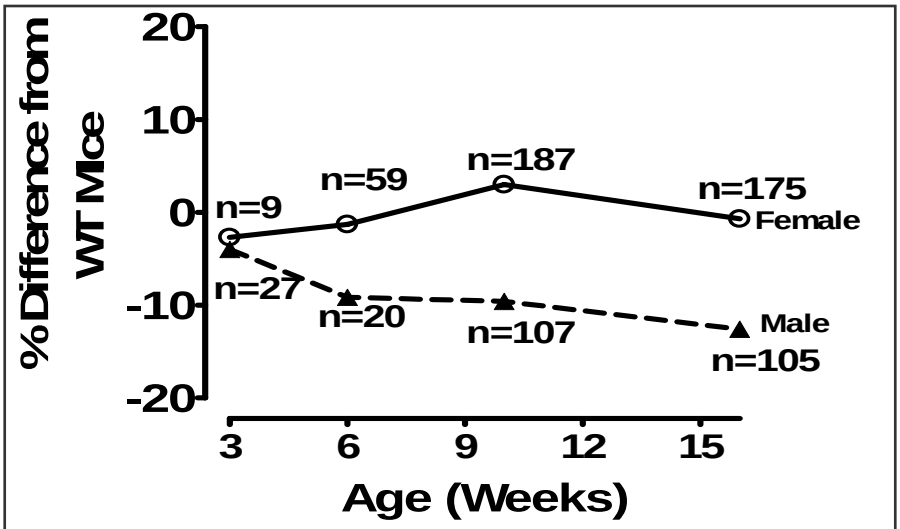

Figure – 11. 917M male mice shows progressively decreased bone area ($p<0.001$ for all data points except 3-week) between ages 3-week and 16–week as compared to age and sex matched wild type (WT) control mice.

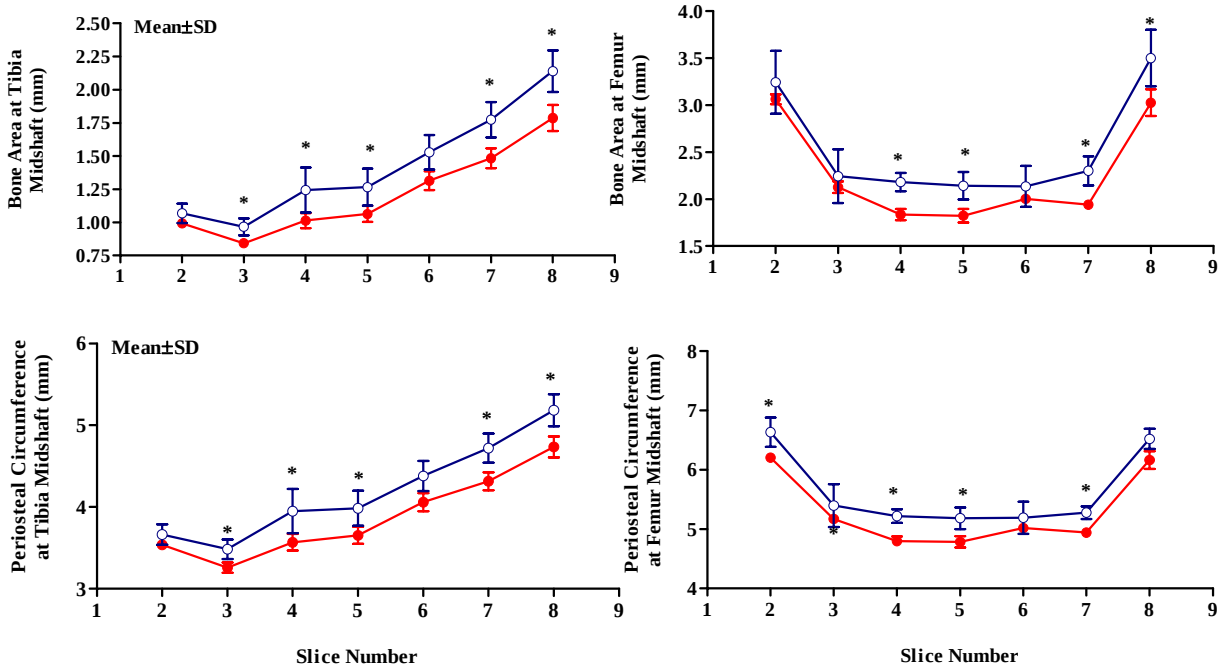

Figure – 12. Ex-vivo bone area measured by pQCT in tibia (left panel) and femur (right panel) of 16-week old 917M male mice. Nine slices covering entire length of the bone (slices 1 & 9 were excluded due to large variation) were scanned. Bone areas of affected 917M male mice were consistently lower over the entire length of tibia and femur as shown with age and sex matched type (WT) mice. *p<0.05 *vs* WT.

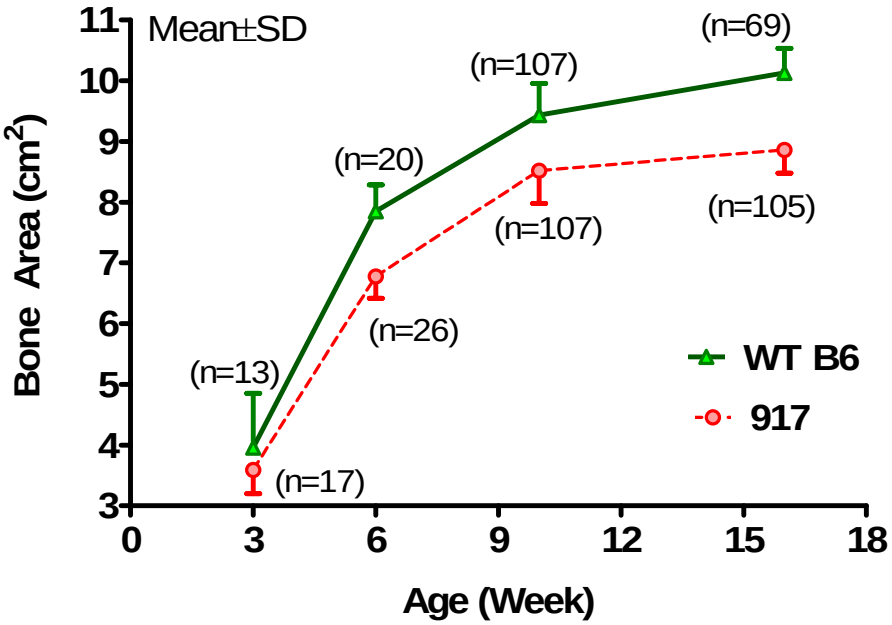

Figure – 13. Longitudinal changes in low bone size phenotype for 917M between 3-16 weeks of age. The y-axis represents total body bone area and x-axis indicates age at which bone area measurements were performed. The 917 data excludes non-affected littermates determined by approximate 2SD cutoff value. The total body bone area were 10-12% lower ($p<0.05$) in mutant mice between 3-week and 16-week age. These data indicates that at 3-week the mutant phenotype was not manifested.

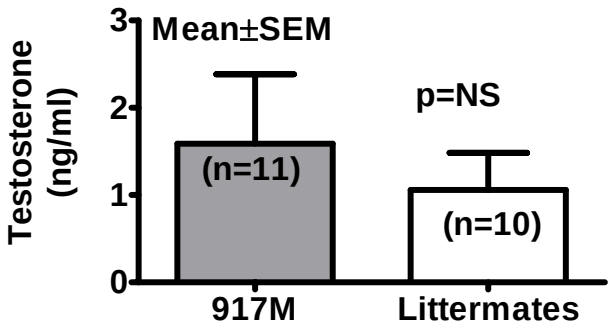

Figure – 14. Serum testosterone levels in 10-week old 917M mice and their non-affected male littermates. The data indicates that serum testosterone levels are not significantly different in 917M mice. The mice were classified as 917M (Z-score, Mean ±SD, 2.9±0.41) and non-affected littermates (Z-score, Mean ±SD, 0.53±1.1) on the basis of total body bone area Z-scores.

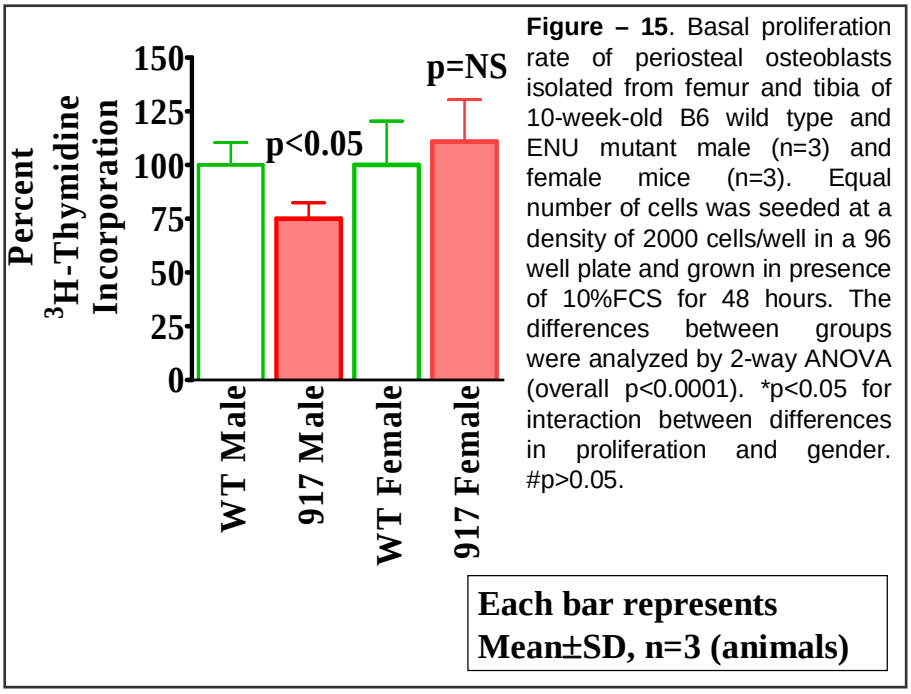

Figure – 15. Basal proliferation rate of periosteal osteoblasts isolated from femur and tibia of 10-week-old B6 wild type and ENU mutant male (n=3) and female mice (n=3). Equal number of cells was seeded at a density of 2000 cells/well in a 96 well plate and grown in presence of 10%FCS for 48 hours. The differences between groups were analyzed by 2-way ANOVA (overall $p<0.0001$). *$p<0.05$ for interaction between differences in proliferation and gender. #$p>0.05$.

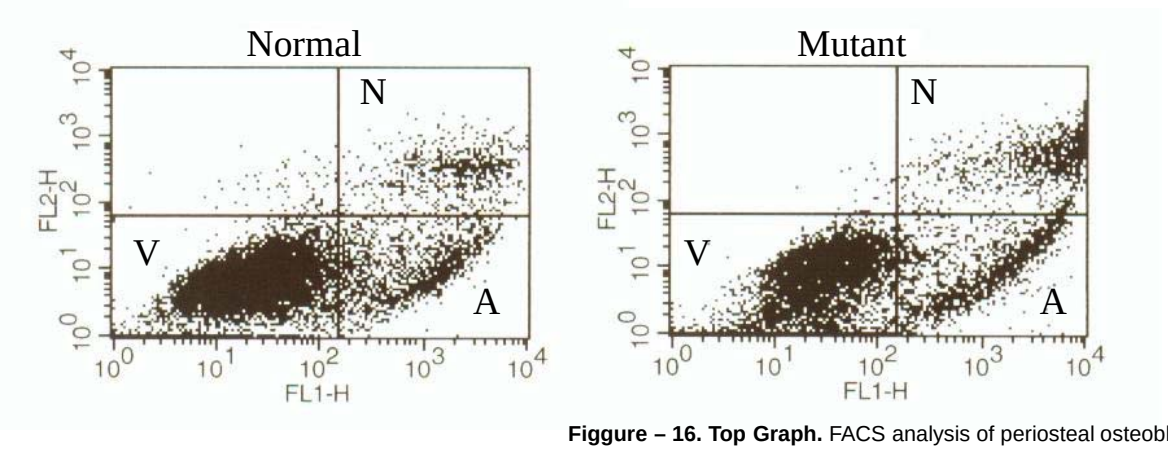

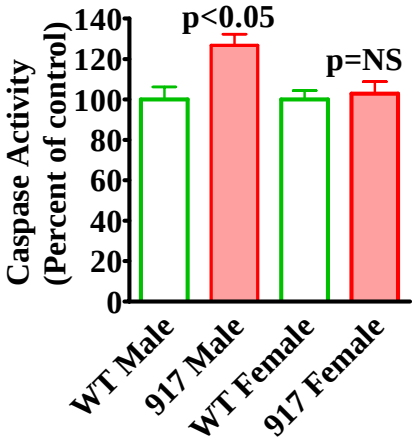

Figgure – 16. Top Graph. FACS analysis of periosteal osteoblasts isolated from femur and tibia of 16-week-old normal and 917M mutant B6 male mice. Periosteal cells from normal and mutant mice were grown with (upper panel) or without 10% FCS (bottom panel) for 24 hours. Cells were then treated with Annexin V conjugated to Alexa Fluor 488 dye and Propidium Iodide for 15 minutes, followed by flow cytometric analysis. In presence of 10%FCS (upper panel) the 917M mutant cells have a higher percentage (10.38%) of apoptotic cells (indicated by an "A") as compared to normal cells (8.85%). When the apoptosis was induced by serum depletion (bottom panel), the 917 mutant cells were found to have 18.67% apoptotic cells as compared to 13.33% apoptotic cells in normal cell population. V=viable cells, N=necrotic cells.

Bottom Graph. Caspase activity in periosteal osteoblasts isolated from 917M male and wild type mice were grown under serum-depleted conditions for 48 hours. WT F=wild type females, 917M FM=female littermates of 917M, WT M=wild type male mice, 917M AM=Affected 917M male mice. *p<0.05 for interaction between differences in proliferation and gender calculated by ANOVA.

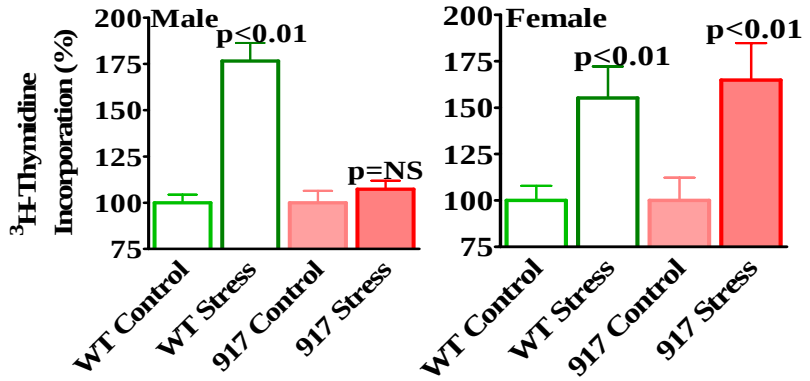

Figure-17. Reduced mechanosensitivity of osteoblasts isolated from 917M mice measured by [^{3}H]-thymidine incorporation in periosteal osteoblasts subjected to a 30-minute steady fluid flow shear strain. The 2-way ANOVA shows that in control mice, sex has no significant differences in response to stress (p-value 0.3345), whereas in 917M littermates, the affected 917M mice has significantly reduced response to shear stress (p-value <0.0001 for interaction). Each bar represents Mean±SD, n=3 (animals)

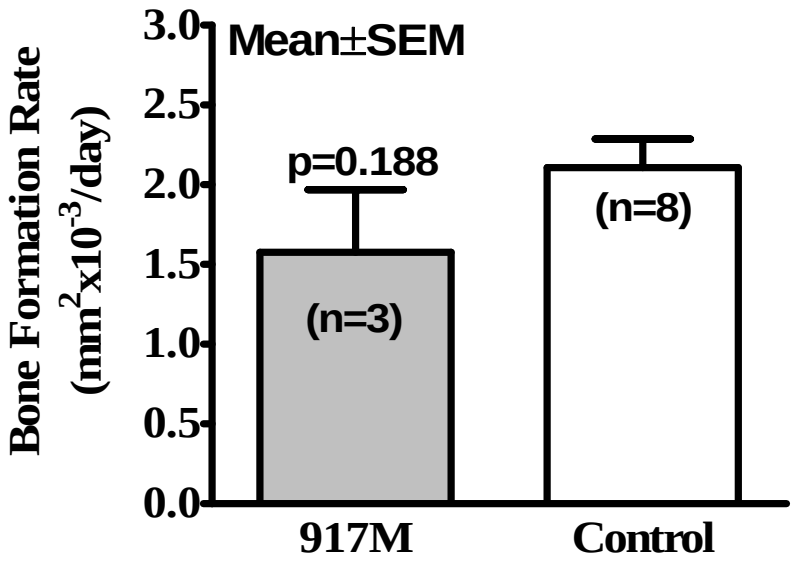

Figure-18. Bone formation rate measured by dynamic histomorphometry at midshaft femur of 917M and control mice (included WT and non-affected littermates)

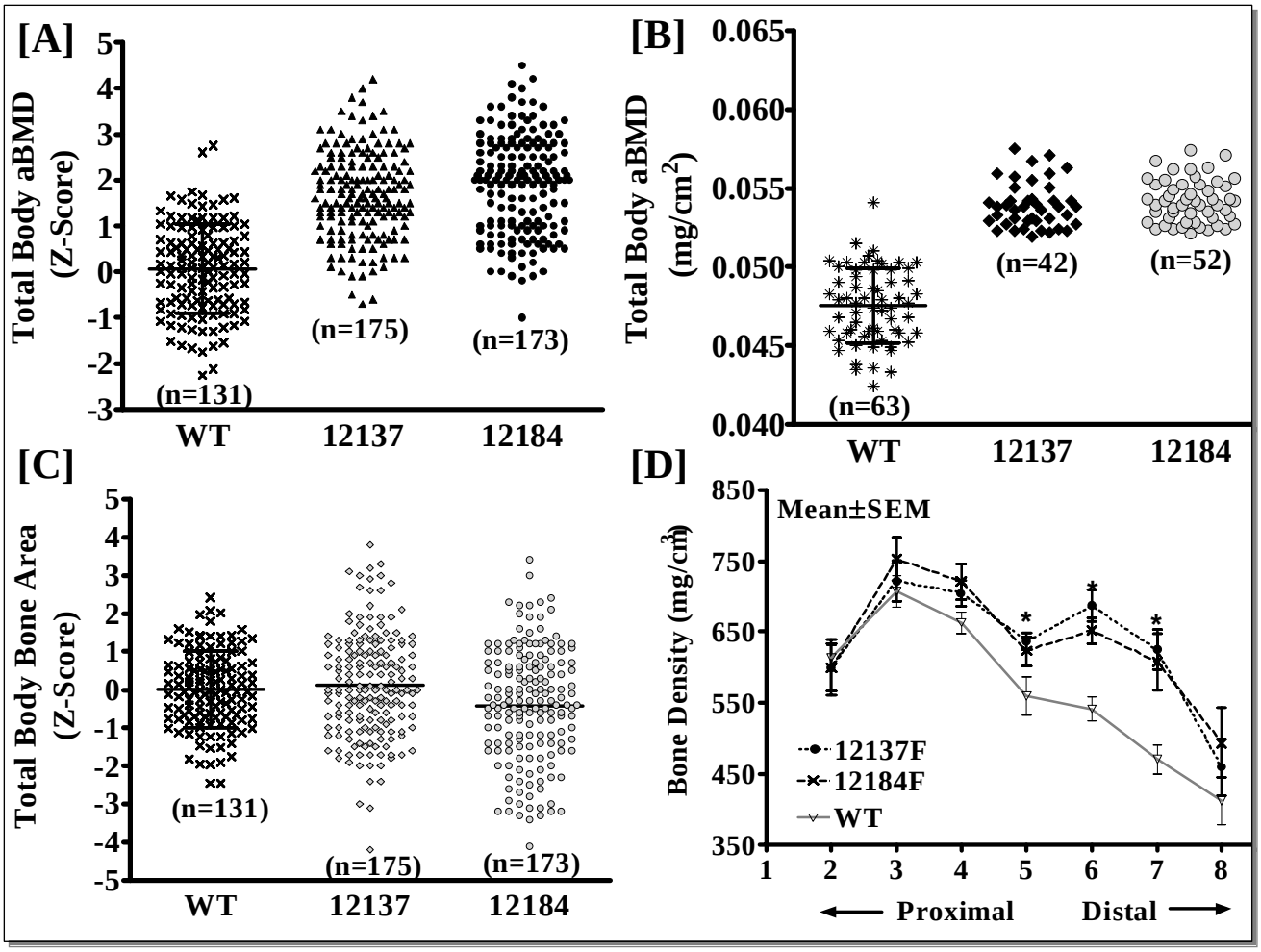

Figure – 19. (A) The total body areal bone mineral density (aBMD) Z-scores of 16-week old progeny from 12137 and 12184 mutant mice including non-affected male and female. The Z-score reflects aBMD differences in SD units calculated from WT mice (n=63-68). The data points include all progeny generated from the two mutant mice including non-affected littermates. **(B)** Representative aBMD data of 16-week old affected 12137 and 12184 female mice. **(C)** The total body bone area Z-scores of 16-week old 12137 and 12184 mice including non-affected male and female. **(D)** Volumetric bone density measured by pQCT in excised femurs of mutant (n=5) and WT mice (n=5). Nine equally distanced slices were collected between proximal and distal end and data from slice-1 and slice-9 were omitted due to large variation.

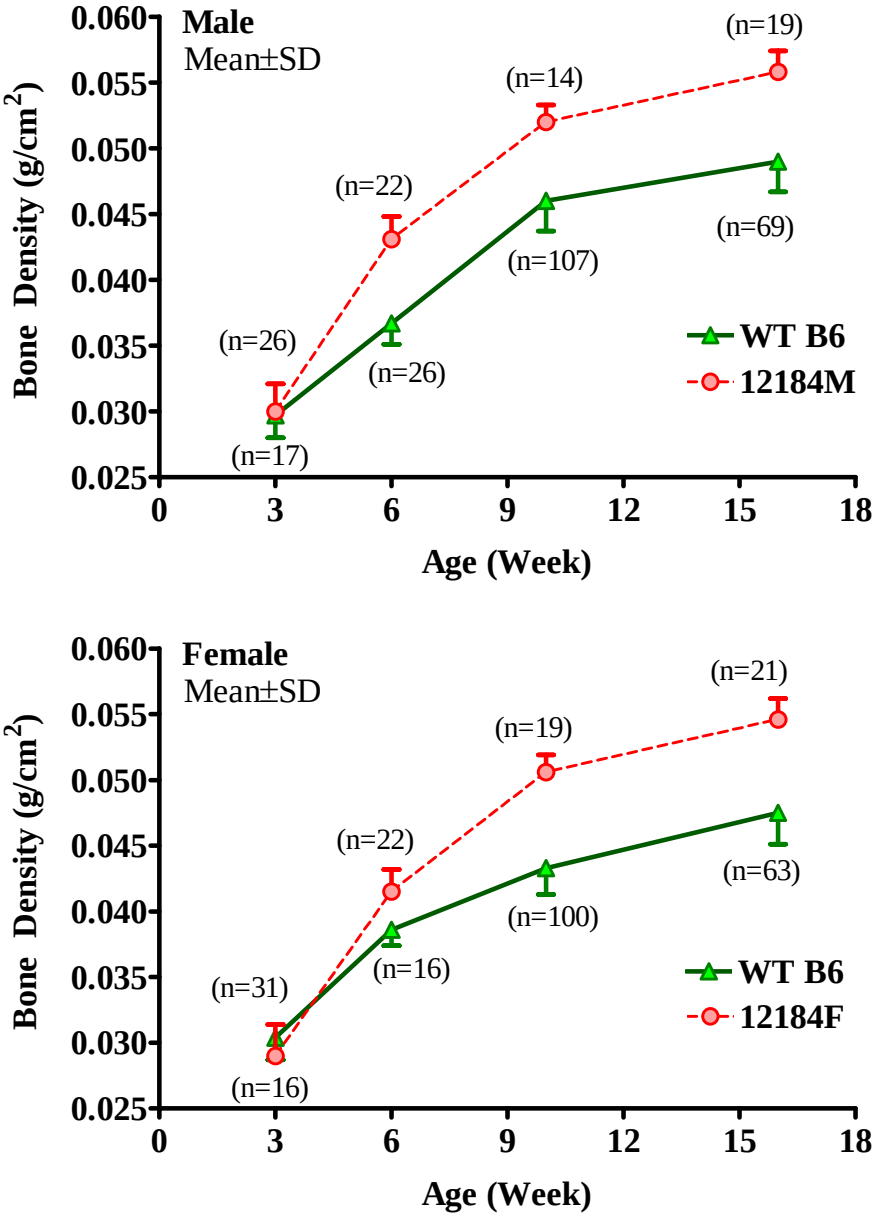

Figure – 20. Longitudinal changes in total body bone density phenotype for male (top panel) and female (bottom panel) 12184 between 3-16 weeks of age. The y-axis represents total body bone density and x-axis indicates age at which phenotype measurements were performed. The data represents 12184 progeny generated during current reporting period. The phenotype data excludes non-affected littermates, which was determined by approximate 2SD cutoff value. The total body bone densities were 10-12% higher ($p<0.05$) in mutant mice between 3-week and 16-week age. These data indicates that at 3-week the mutant phenotype is not manifested.

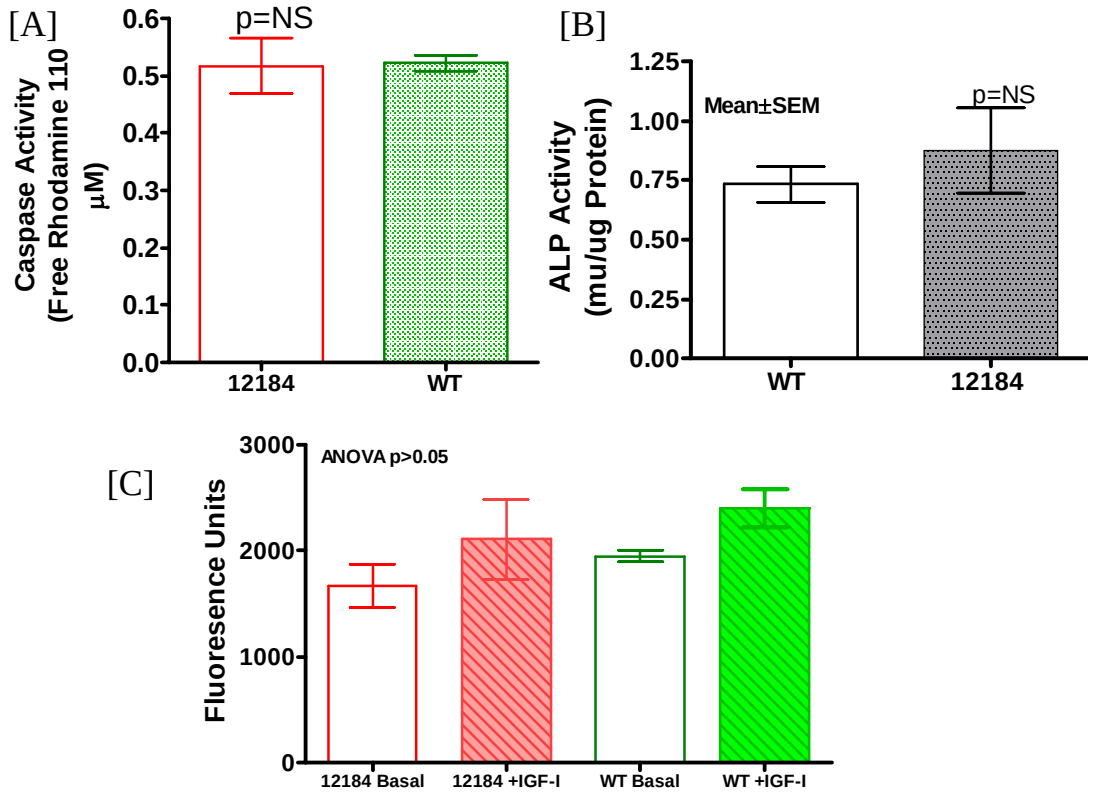

Figure – 21. Characterization of periosteal osteoblast phenotype for mutant with increased bone density (Line 12184). Periosteal osteoblasts were isolated from 10-week old female WT and mutant 12184 mice and grown in cultures. Each experiment was performed with cells from three animals and 3-4 wells were used for cell culture for each animal. Data from 2-4 animals were combined and shown as mean values. No significant differences were observed in basal apoptosis (A), differentiation (B), and proliferation (C) levels of cells from 12184 mice as compared to those from WT mice.

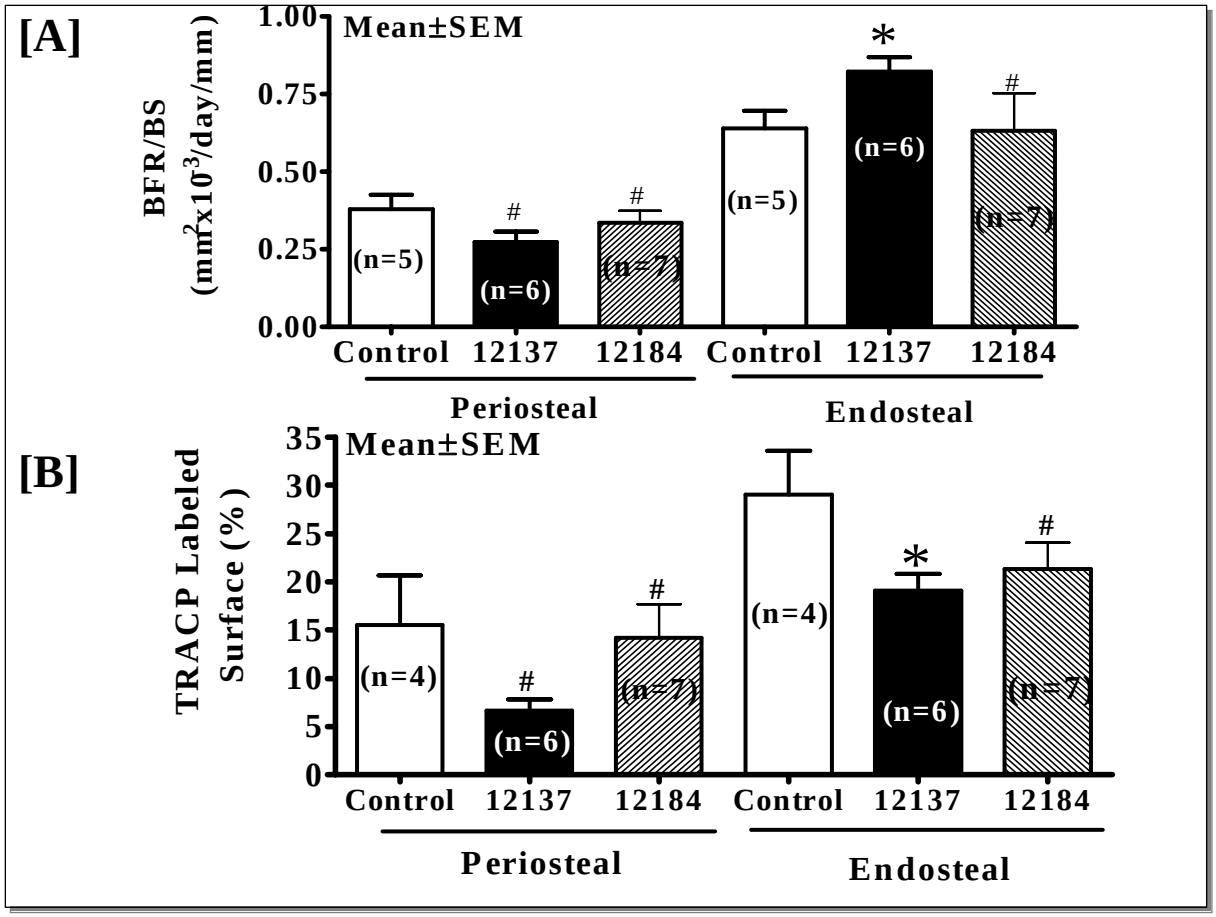

Figure – 22. Histomorphometric measurements to identify cellular mechanisms that determine high bone density phenotype in 12137 and 12184 mutant mice. Comparison of bone formation and resorption rates in female 12137 (black bars), 12184 (grey bars), and control (white bars) mice. **(A)** Dynamic histomorphometric analysis of bone formation rate (BFR) was determined by in vivo dual labeling using calcein and expressed as BFR per bone surface (BFR/BS). **(B)** Static analysis of osteoclast number per mm bone perimeter tartrate resistant acid phosphatase (TRACP) labeled surface. These data provides evidence for diminished osteoclast numbers in both 12137 and 12184 mutant mice. *p<0.05 vs control, #p=NS vs control.

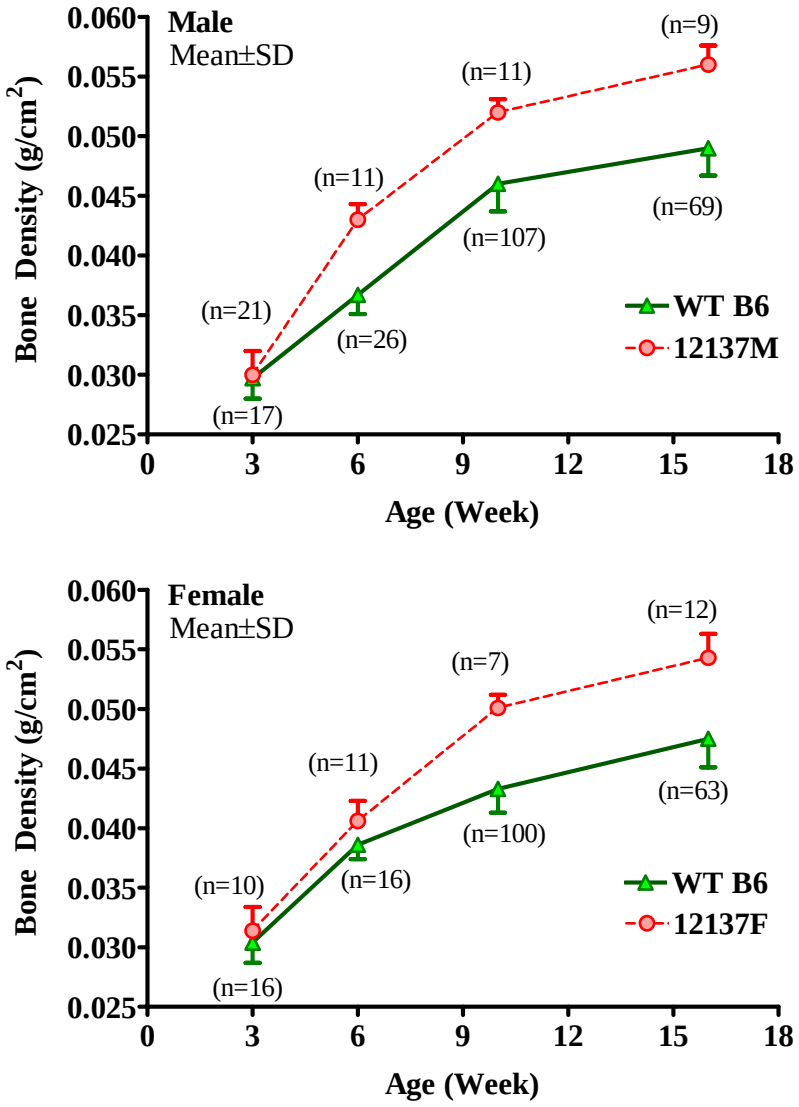

Figure – 23. Longitudinal changes in total body bone density phenotype for male (top panel) and female (bottom panel) 12137 between 3-16 weeks of age. The y-axis represents total body bone density and x-axis indicates age at which phenotype measurements were performed. The data represents 12137 progeny generated during current reporting period. The phenotype data excludes non-affected littermates, which was determined by approximate 2SD cutoff value. The total body bone densities were 10-12% higher ($p<0.05$) in mutant mice between 3-week and 16-week age. These data indicates that at 3-week the mutant phenotype was not manifested.

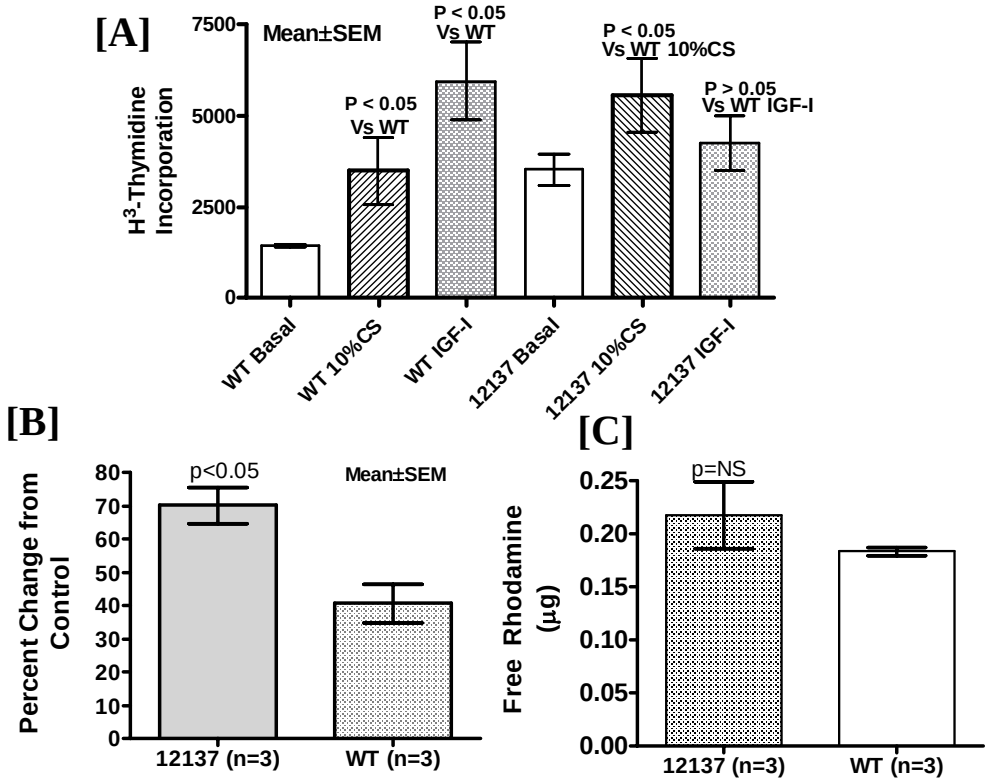

Figure – 24. Characterization of periosteal osteoblast phenotype for mutant with increased bone density (Line 12137). Periosteal osteoblasts were isolated from 10-week old female WT and mutant 12137 mice and grown in cultures. Each experiment was performed with cells from 3-4 animals and 3-4 replicates were used for each animal. Data from three animals were combined and shown as mean values. Our preliminary data indicates higher basal proliferation rate measured by thymidine incorporation in osteoblasts from 12137 mice as compared to WT mice (A). There was a higher increase in proliferation in response to calf serum as compared to IGF-I (A). Basal proliferation rate was also higher when Almar Blue dye was used to measure proliferation rate (B), the y-axis shows percent change in fluorescence units as compared to control. No significant differences were observed in basal apoptosis (C) rate in osteoblasts from 12137 mutant mice, as compared to those

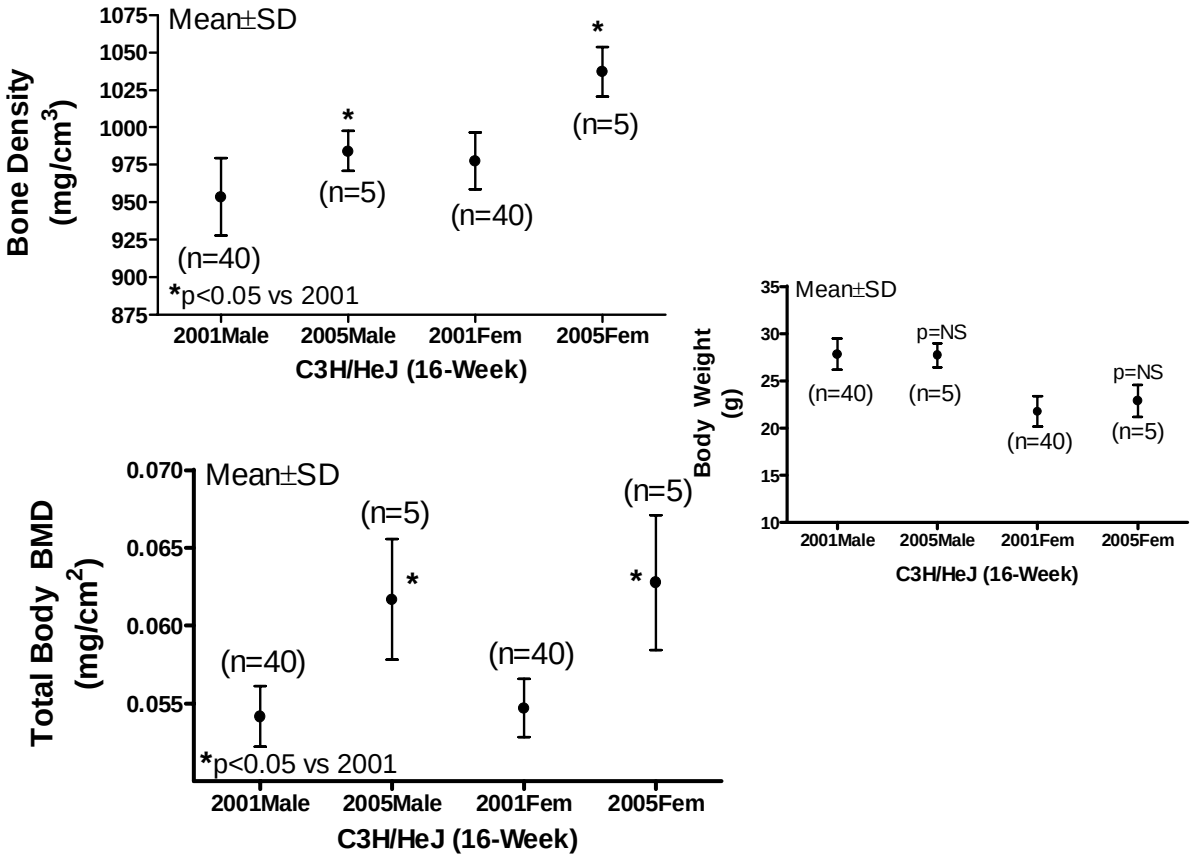

Figure – 25. Shift in normal range values in C3H/HeJ strain of mice acquired in 2001 and those acquired in 2005. The body weights of both male and female were not affected, however, the total body bone density and volumetric bone density was significantly higher in mice obtained in 2005 from The Jackson Laboratory as compared to those obtained in 2001. This shift in bone density and other phenotype compromises the breeding of mutants that are in C3H/HeJ background. A similar comparison in C57BL/6J strain of mice did not show significant differences in BMD and body weights.

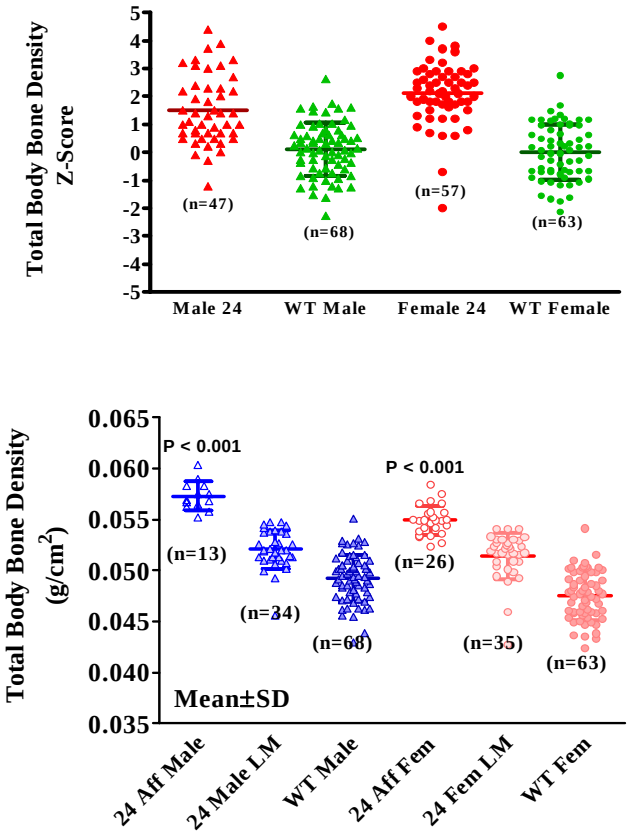

Figure – 26. (Top) Z-scores for total body BMD in 16-week old progeny from male and female B2.4 (referred as Line 24 for simplicity) mutant mice. (Bottom) Total body BMD in 16-week old progeny from male and female B24 mutant mice.

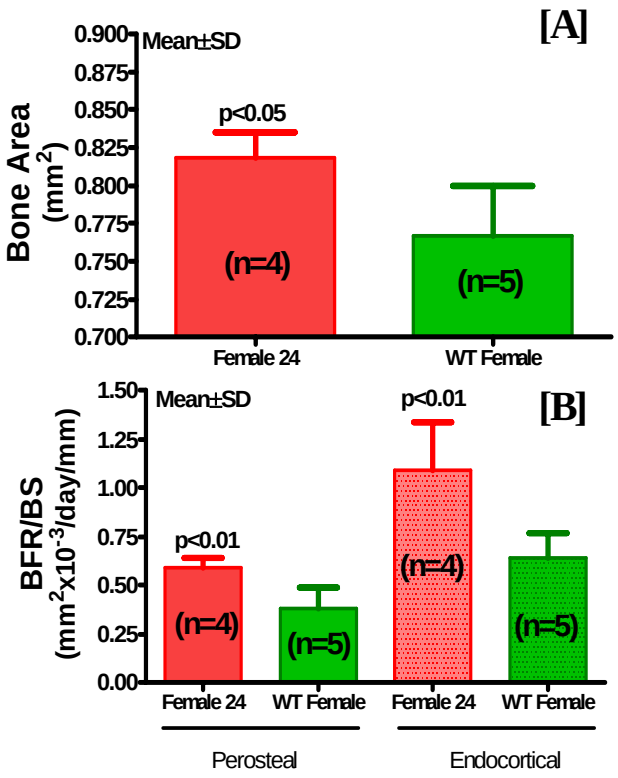

Figure – 27. Histomorphometric measurements to determine high bone density phenotype in Line B2.4 mutant mice Bone area at femur midshaft in 16-week old mutant mice measured by histology (A). (B) Bone formation rate at femur midshaft measured by tetracycline labeling. The histology data suggests that high BMD phenotype is due to increased bone formation at both periosteum and endosteum.

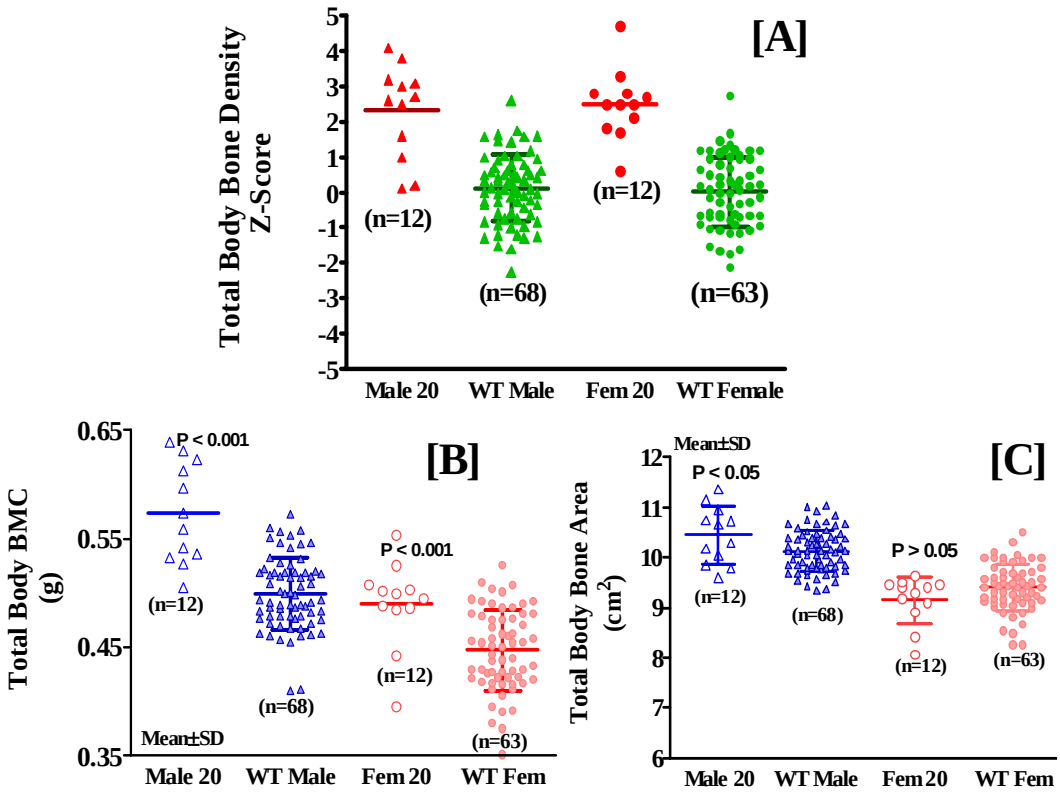

Figure – 28. Skeletal phenotypes for progeny from mutant mice B20.3E (referred as Line 20). Figure A shows Z-scores for total body bone density, affected mice show >10% difference in bone density as compared to age and sex matched WT control mice. The increase in bone density was primarily due to higher total body bone mineral content (B) in females; in males, the bone area was also significantly higher as compared to wild type control male. The x-axis includes progeny from backcrosses including the non-affected littermates. About 25% of the IT progeny were classified as affected.

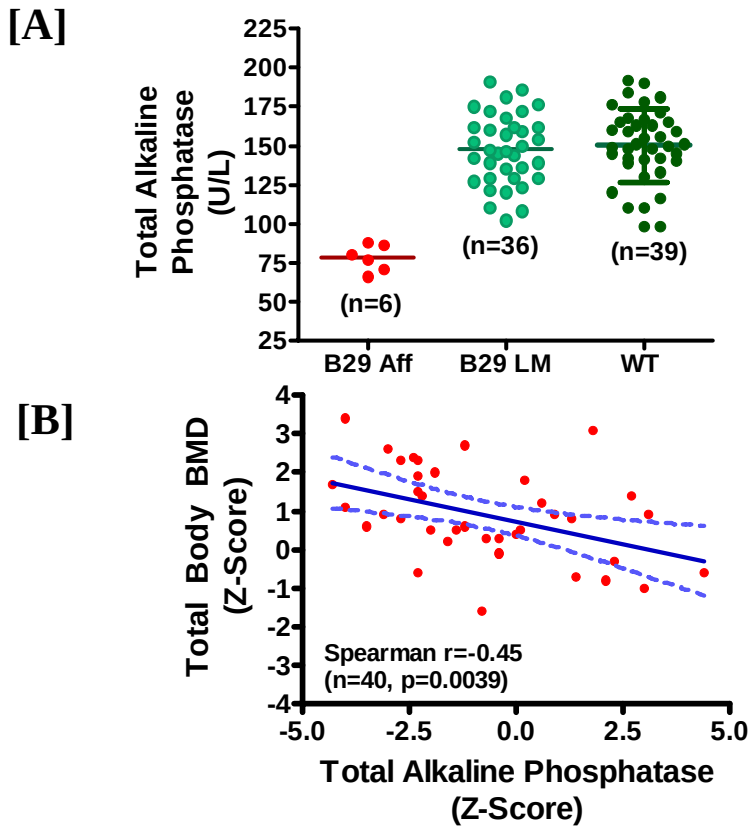

Figure – 29. (A) Total alkaline phosphatase levels in serum from 10-week old progeny from B29.2 mutant (referred as Line 29) mice. The total alkaline phosphatase levels in mutant mice were 3 SD levels lower than WT control mice. Similar results were obtained with serum osteocalcin levels. (B) The bone marker levels negatively correlated with total body BMD. The data points include both male and female progeny from B29.

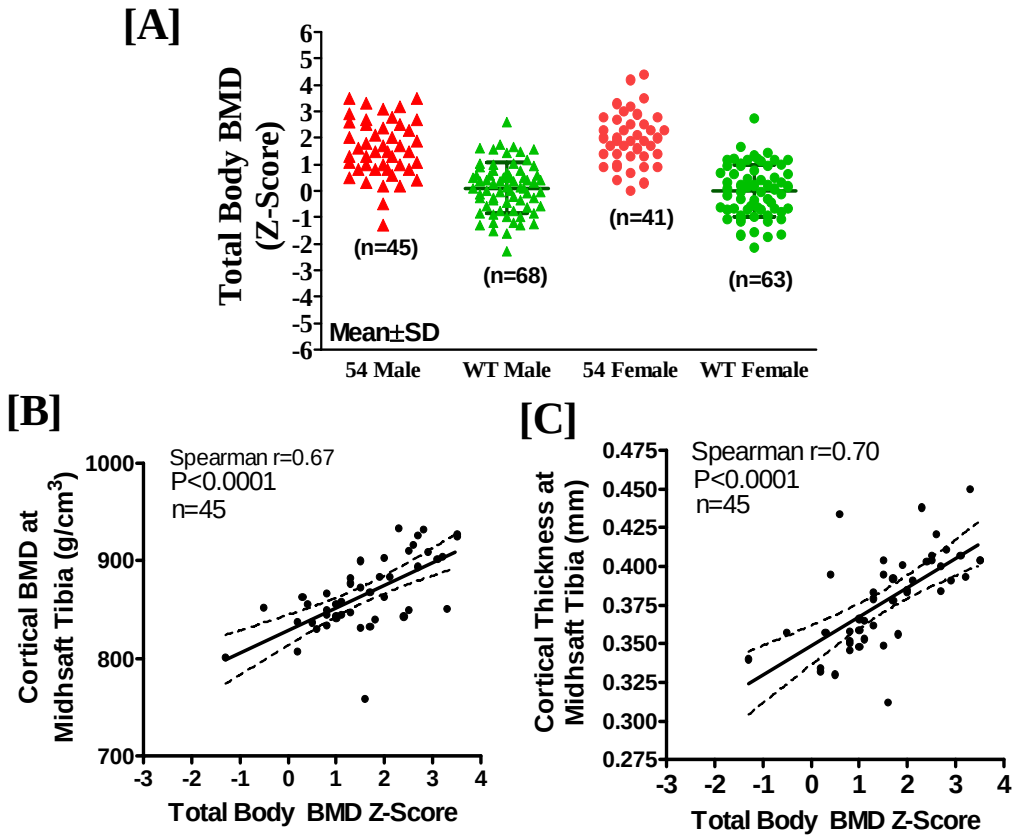

Figure – 30. Z-scores calculated for total body BMD (A) measured by DEXA in 16-week old progeny from B54 male and female mice. The mean BMD Z-score (A) of all affected B54 male and female mice was +2.8 and mean BMC Z-score was +2.1. As expected, approximately 25% mice expressed high BMD phenotype. Interestingly, the total body BMD in B54 progeny correlated positively with volumetric bone density (B) and cortical thickness (C) measured by peripheral quantitative computed tomography (pQCT) at midshaft tibia.

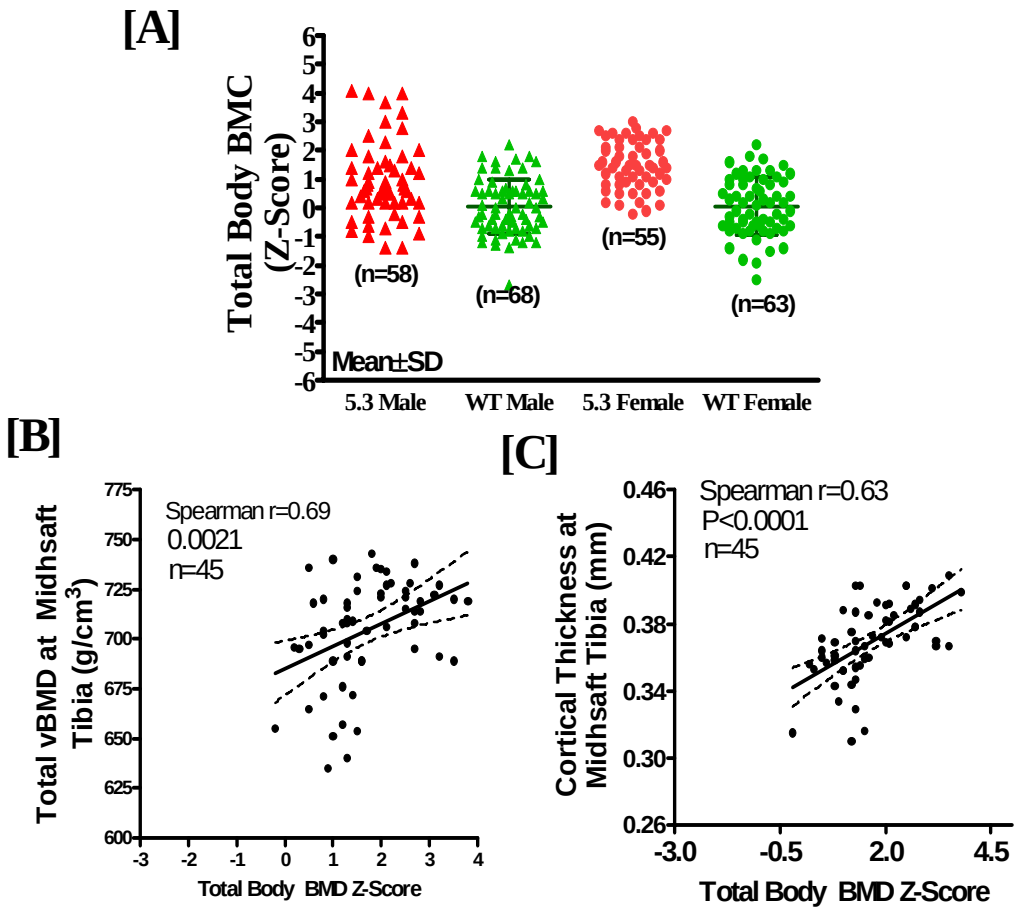

Figure – 31. Z-scores calculated for total body BMD (A) measured by DEXA in 16-week old progeny from B5.3 male and female mice. The mean BMD Z-score (A) of all affected B5.3 male and female mice was +2.0. As observed in Line B5.4, the higher total body BMD correlated positively with volumetric bone density (B) and cortical thickness (C) measured by peripheral quantitative computed tomography (pQCT) at midshaft tibia.

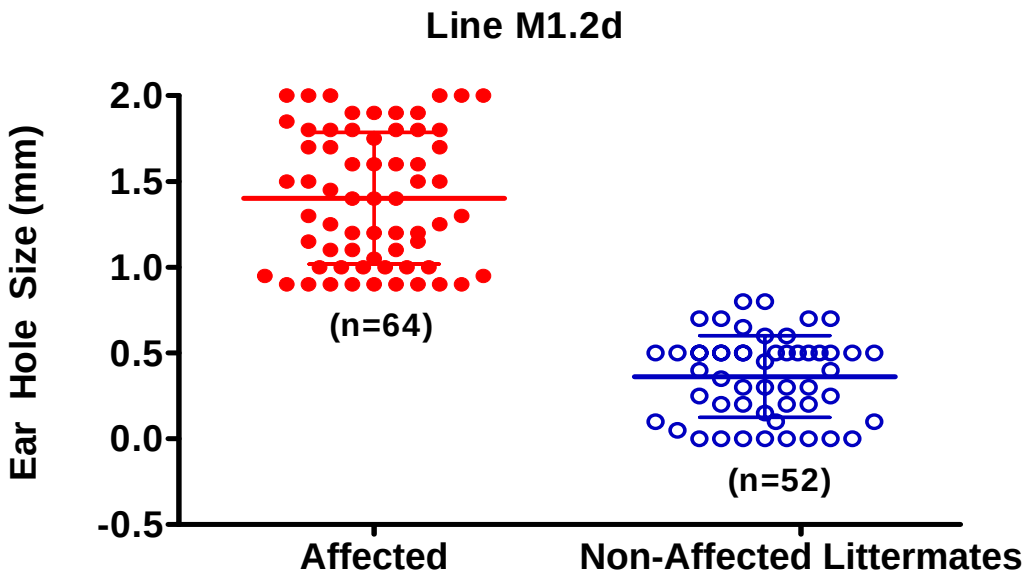

Figure – 32. Phenodeviant with Slow Soft-Tissue Healing (M1.2d). Line M1.2d was identified in a dominant screen using MRL strain of mice; we have generated more than 100 progeny from the original mutant mice and data shows a slower rate of healing of a 2 mm hole punched in ear lobe. Error bars are Mean±SD.

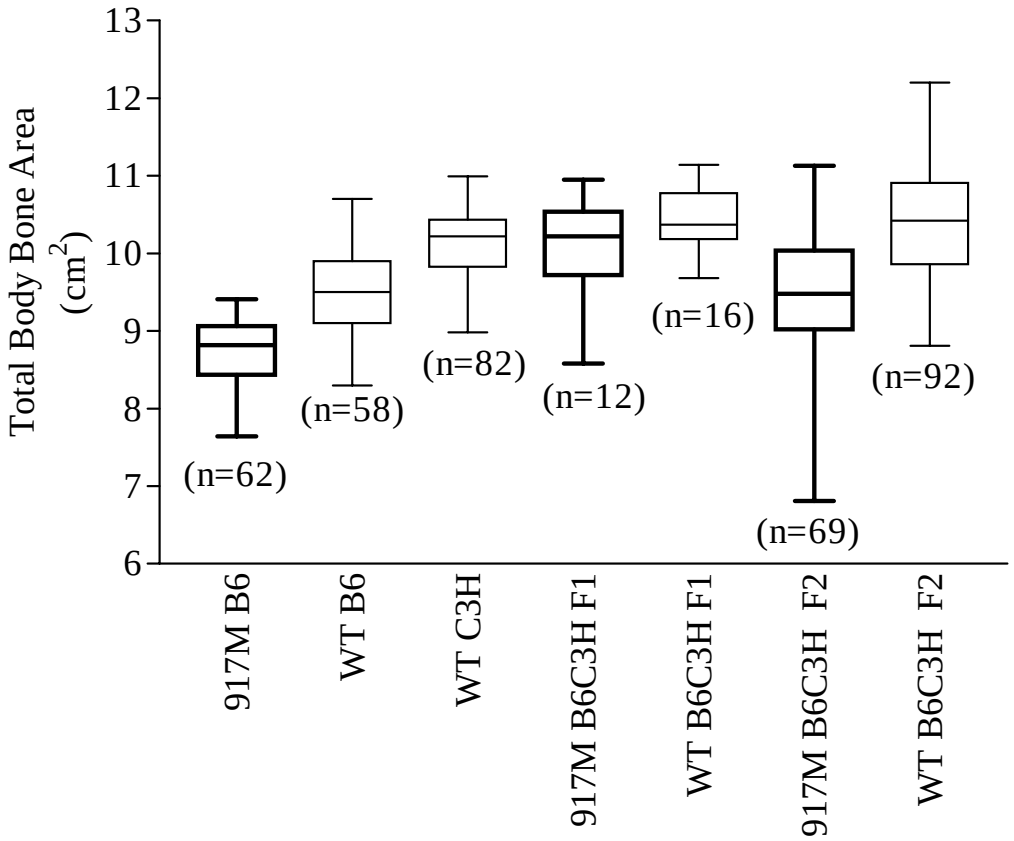

Figure – 33. Total body bone area of 10-week old 917M, wild type (WT) B6 males, WT C3H males, 917M B6C3H F1 male hybrids, WT B6C3H F1 male hybrids, WT B6C3HF2 male hybrids, and 917M B6C3H male F2 mice. The box represents confidence intervals. The box diagram in bold lines represents progeny from mutant mice. Bone area in 917B6, F1 B6C3H hybrids and F2 B6C3H males were significantly ($p<0.05$ by ANOVA) lower than the WTB6, WT B6C3H F1 and WT F2 hybrids.

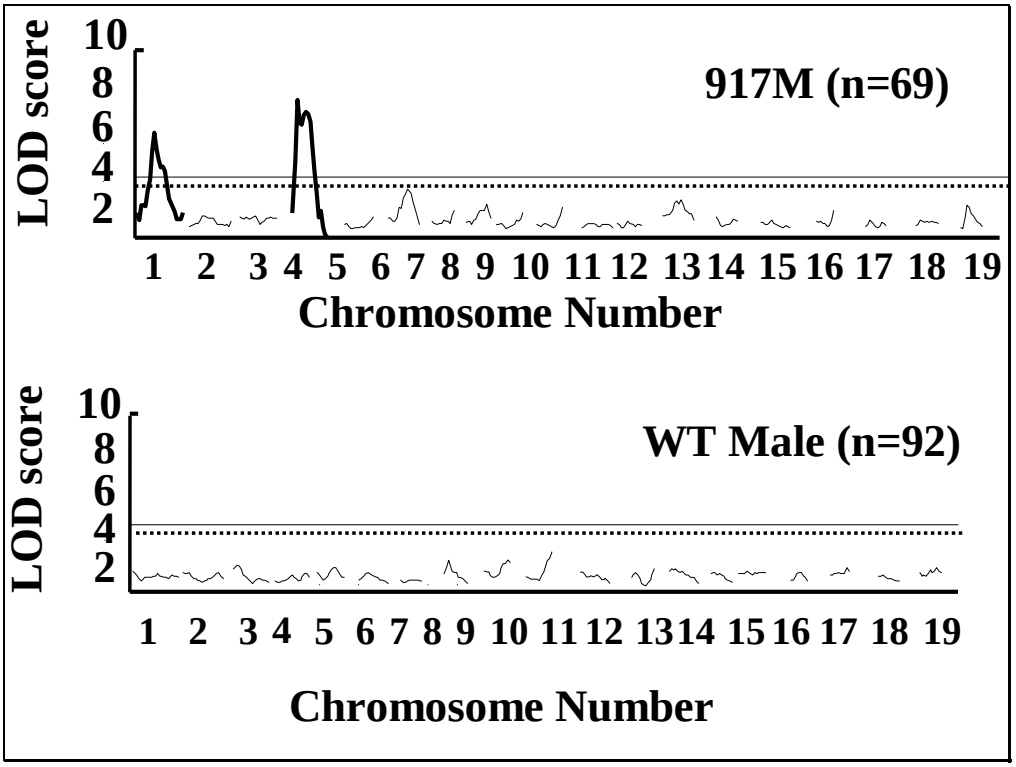

Figure – 34. Mapping chromosomal location of mutation for 917M mutant. The figure shows genome wide main QTL(s) associated with total body bone area (DXA) in 10-week old intercrossed B6C3H F2 males (n=69) generated from mutant mice. The horizontal lines indicate genome-wide error levels of $p<0.01$ and $p<0.05$. Chromosome 1 and 4 harbor loci that significantly affect total bone size in F2 male mice from 917M mutant. The interval mapping was performed by Pseudomarker MAINSCAN program written for the MATLAB programming environment. Since body weight is a strong predictor of bone size traits, we used multivariate analysis with body weight as the covariant to perform interval mapping using. This allows us to delineate the bone size trait from growth related QTLs. The bottom plot shows genome wide main QTL(s) associated with total body bone area in 10-week old intercrossed wild type B6C3H F2 male mice. The horizontal lines indicate genome-wide error levels of $p<0.01$ (solid line) and $p<0.05$ (broken line). The interval mapping revealed no significant linkages in F2 mice generated from wild type B6 (bottom graph).

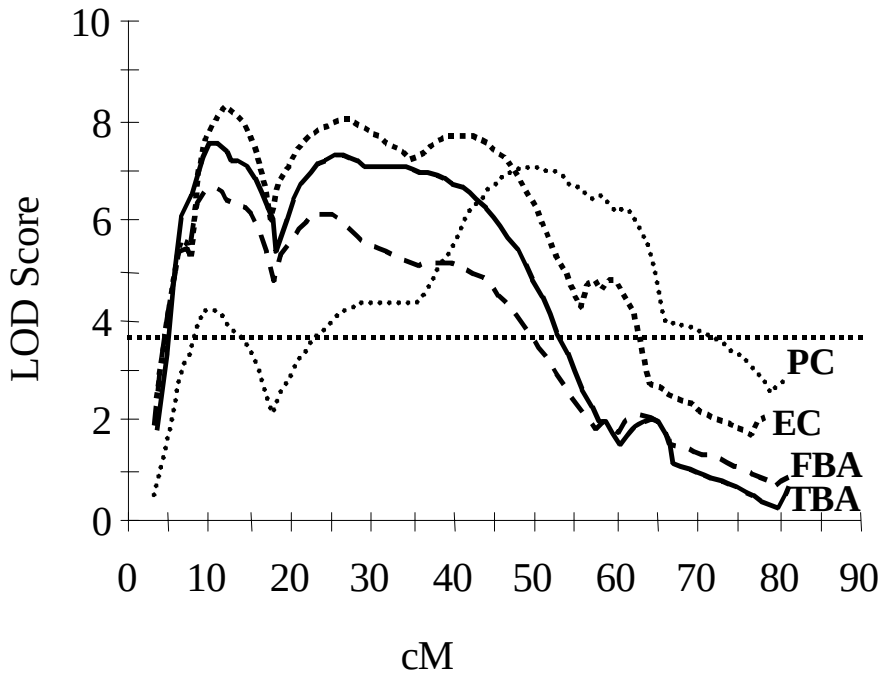

Figure – 35. Fine mapping of 917M mutant. LOD scores of multiple bone size phenotypes for chromosome 4 shown in detail. Dashed horizontal line indicates significance threshold level used at $p<0.05$ for genome wide significance. Several phenotypes were used to identify the locus. PC- Periosteal circumference (pQCT), EC-Endosteal circumference (pQCT), FBA-Femur bone area (DXA), TBA-Total bone area (DXA).

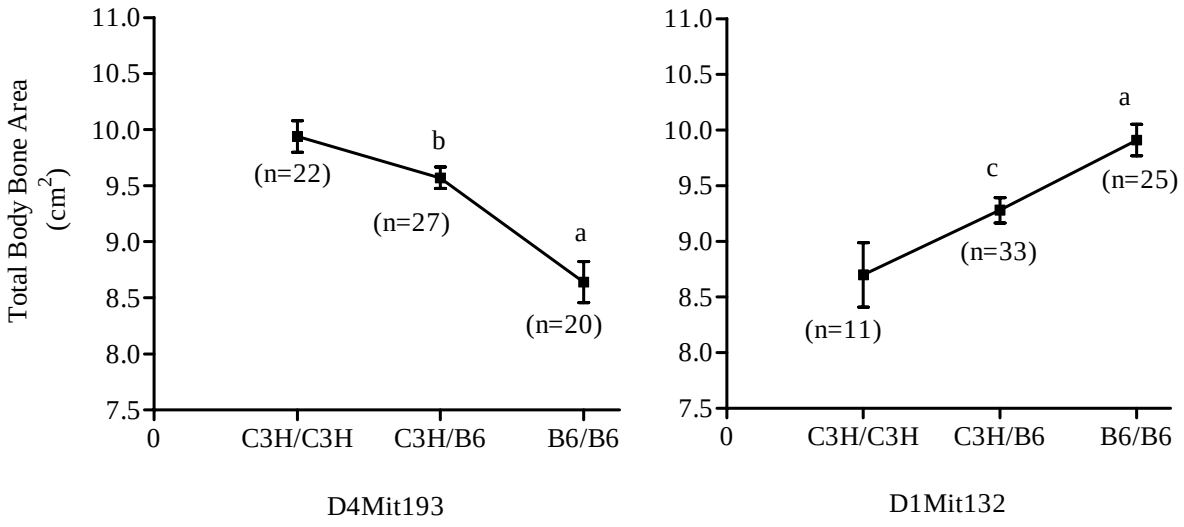

Figure – 36. The main effects of genetic alleles on the mean total body bone area for 197M mutant for markers D4Mit193 (LOD score 6.74) and D1Mit132 (LOD score 3.4). Allele of the Chr 4 interval that was inherited from the B6 parental strain (mutant strain) contribute to a significantly lower bone area than do alleles inherited from C3H. The significant difference between *B6/B6* and *C3H/B6* genotypes suggests that the B6/B6 allele is dominant. Data are presented as mean±SEM and number of animals for each group is indicated in parentheses. a=p<0.001 *vs* C3H/C3H, b=p<0.01 *vs* B6/B6 and p>0.05 vs C3H/C3H, and c=p<0.05 *vs* C3H/C3H and B6/B6 by ANOVA.

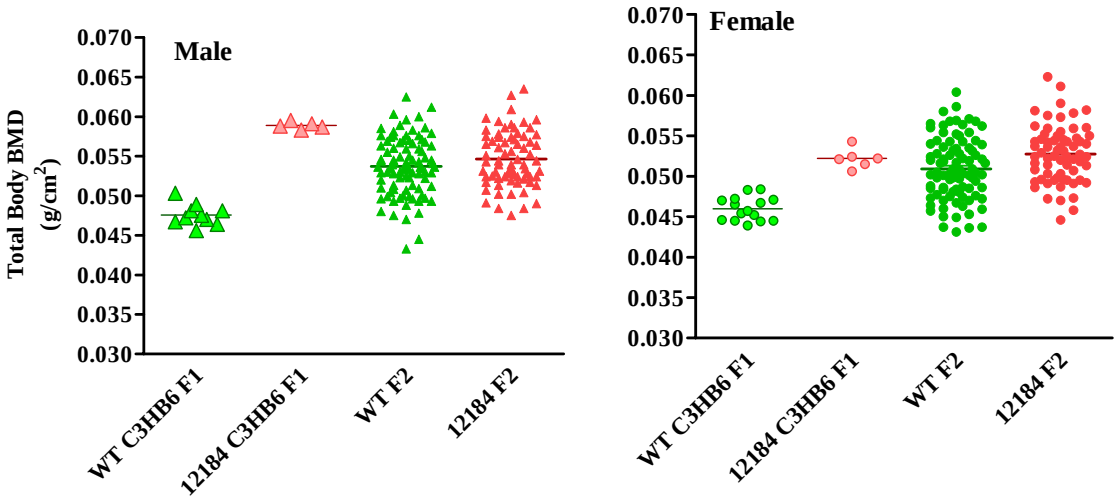

Figure – 37. Generation of F1 & F2 progeny for identification of chromosomal location of high bone density mice (Line 12184). In the current reporting period, we generated several new F1 & F2 mice. This figure shows that the high bone density phenotype was robustly expressed in the F1 mice generated from breeding of mutant 12184 (B6) with C3H/HeJ mice.

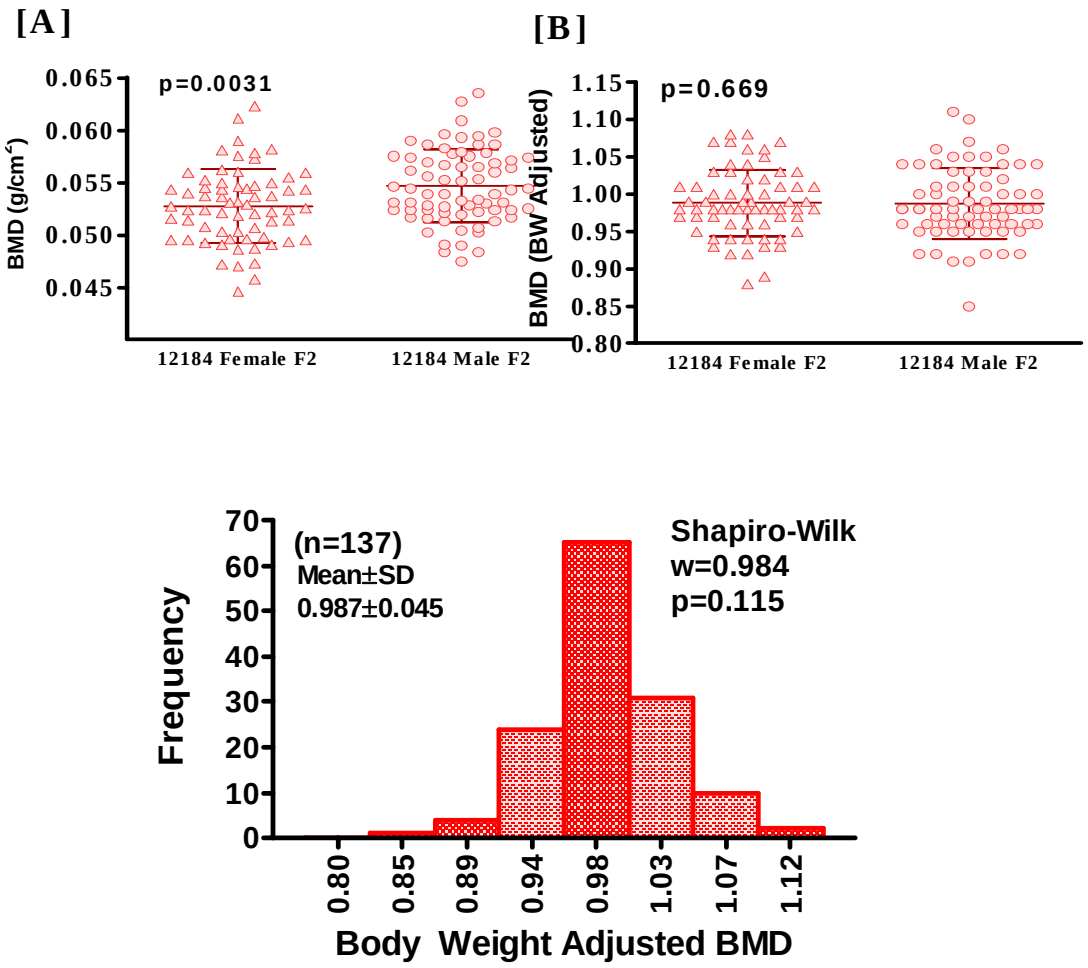

Figure – 38. To identify the chromosomal location of high bone density mutant mice, we used body weight adjusted BMD data from F2 male and female progeny (Line 12184). The top panel (A) shows that total body BMD from male and female F2 mice are statistically different, however, body weight adjusted BMD are similar in male and female F2 mice. Hence, data from male and female F2 could be combined for QTL mapping. The bottom panel shows that the body weight adjusted BMD was normally distributed; therefore, interval mapping could be used to identify QTLs affecting BMD.

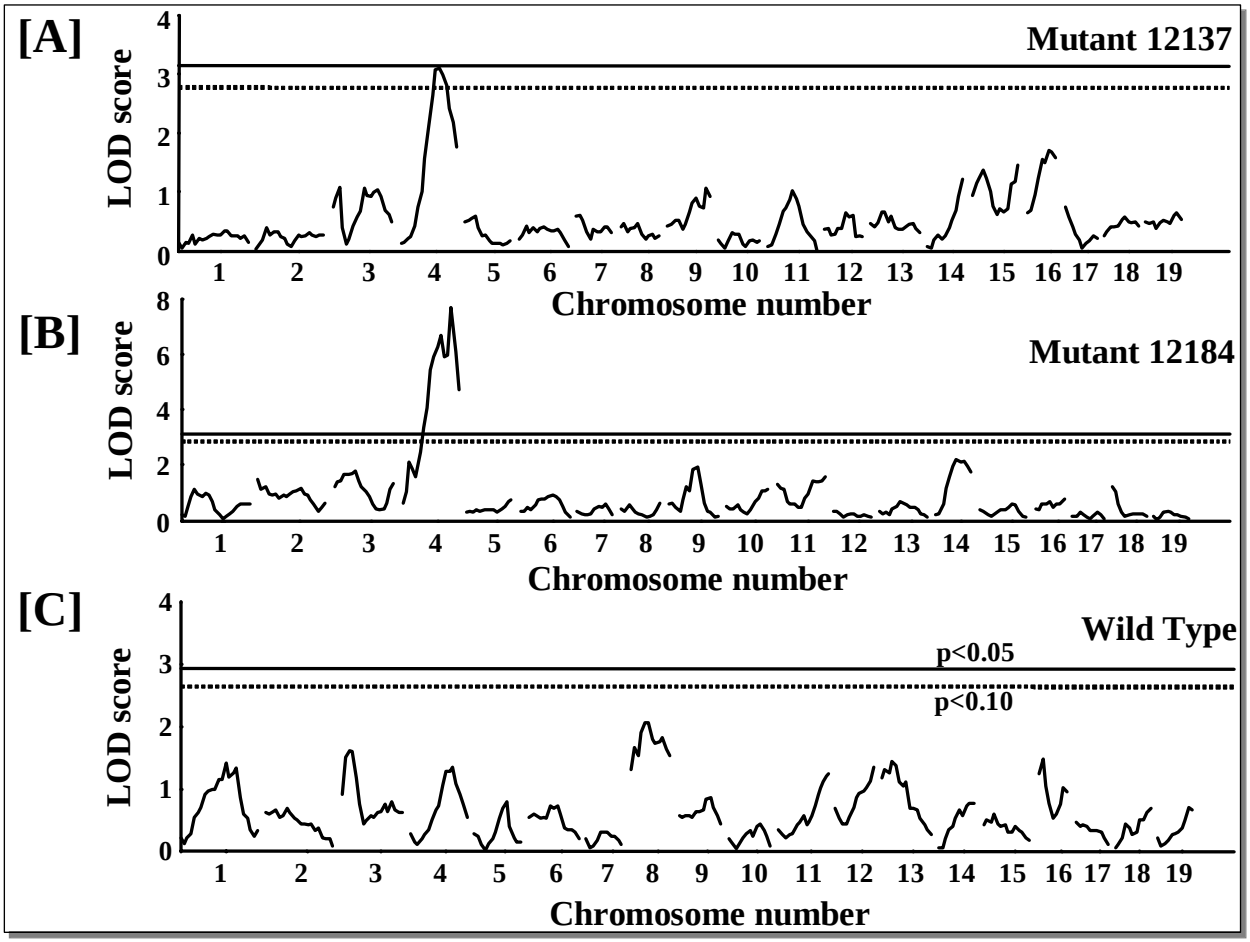

Figure – 39. (A) & (B) Genome wide main QTL(s) associated with body weight adjusted areal bone mineral density (aBMD, measured by DEXA) in 10-week old intercrossed B6C3H F2 mice generated from 12137 (n=164) and 12184 (n=137) mutant mice. **(C)** The bottom plot shows QTLs associated with aBMD in wild type C3HB6 F2 males (n=176). The horizontal lines indicate genome-wide error levels of p<0.1 and p<0.05. Chromosome 4 harbors a locus that significantly affects aBMD in F2s generated from mutant mice, but Chromosome 4 locus was absent in F2 mice from WT mice. Since there was no significant difference in body weight adjusted aBMD between male and female F2 mice, data from male and female mice were combined for interval mapping.

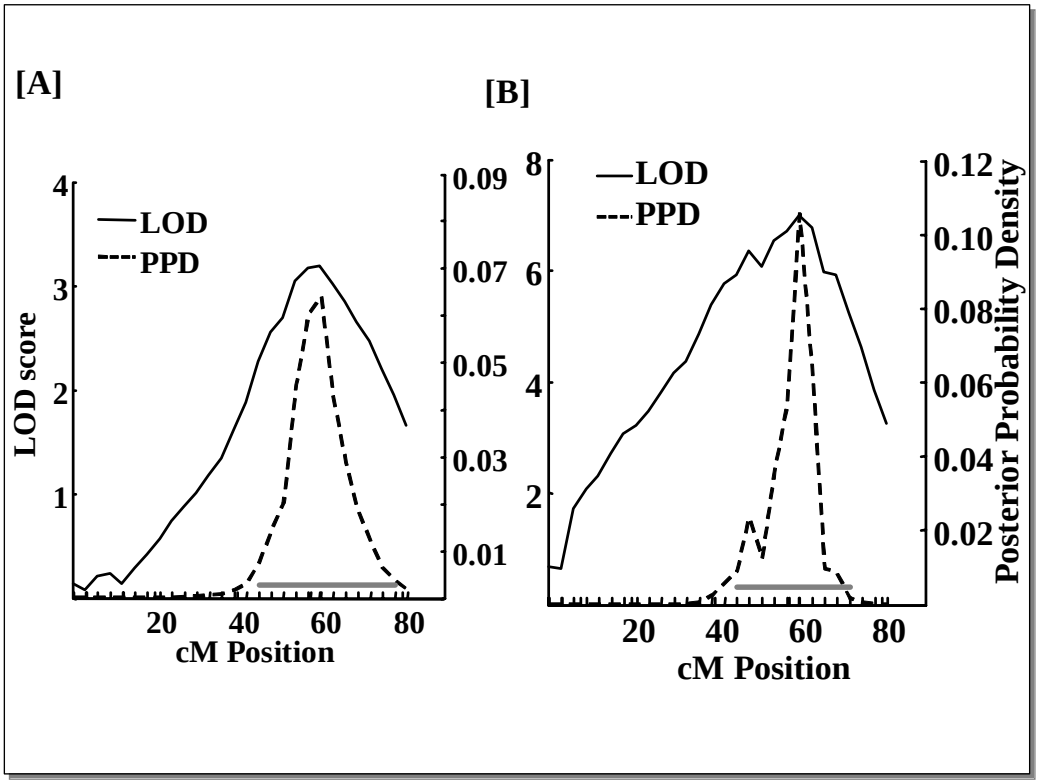

Figure – 40. LOD score and posterior probability density plots (PPD) of the chromosome 4 locus that influenced aBMD in the 12137 (A) and 12184 (B) mutant F2 mice. PPD is a likelihood statistic that gives rise to the 95% confidence intervals, which is indicated by gray horizontal bars. cM, centimorgan.

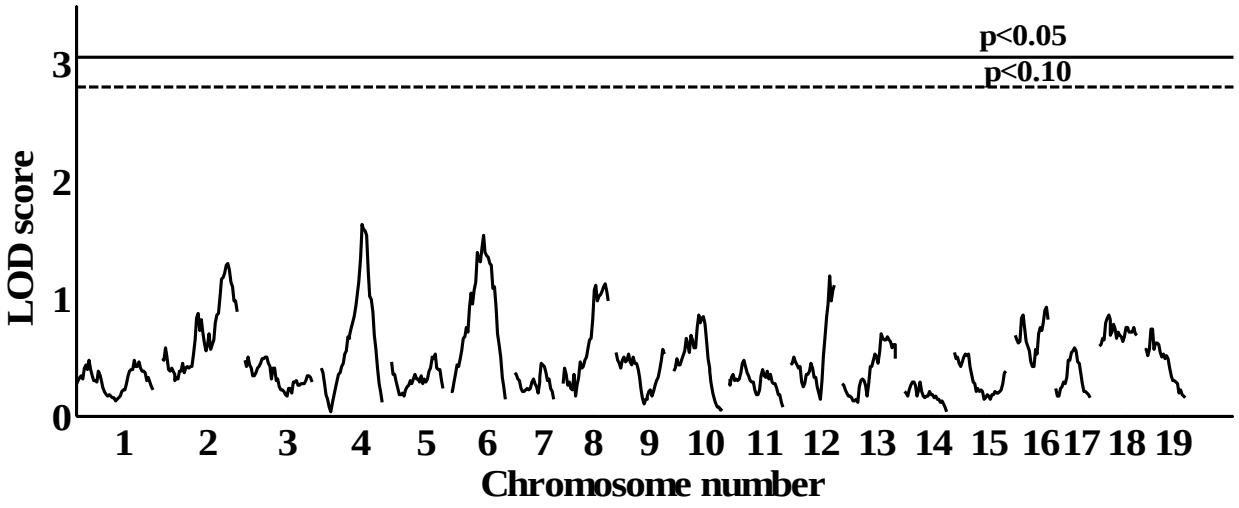

Figure – 41. **Interval mapping results of a recessive mutant line B2.4 with high BMD**. Genome wide main QTL(s) associated with total body bone mineral density (BMD) (measured by DEXA) in 10-week old intercrossed B6C3H F2 female mice (n=97) generated from mutant mice B2.4. The horizontal lines indicate genome-wide error levels of $p<0.05$ (solid line) and $p<0.1$ (broken line). The interval mapping did not disclose significant linkage with any locus. Because the mutation was inherited in a recessive mode and we only mapped a limited number of F2 mice, it could be possible that we have very few mutant mice in the F2 population. Thus, our interval mapping strategy has limited power to detect linkage to a recessive mutation. This was in contrast to dominant ENU mutations where we were able to determine QTLs with only 69 F2 mice.

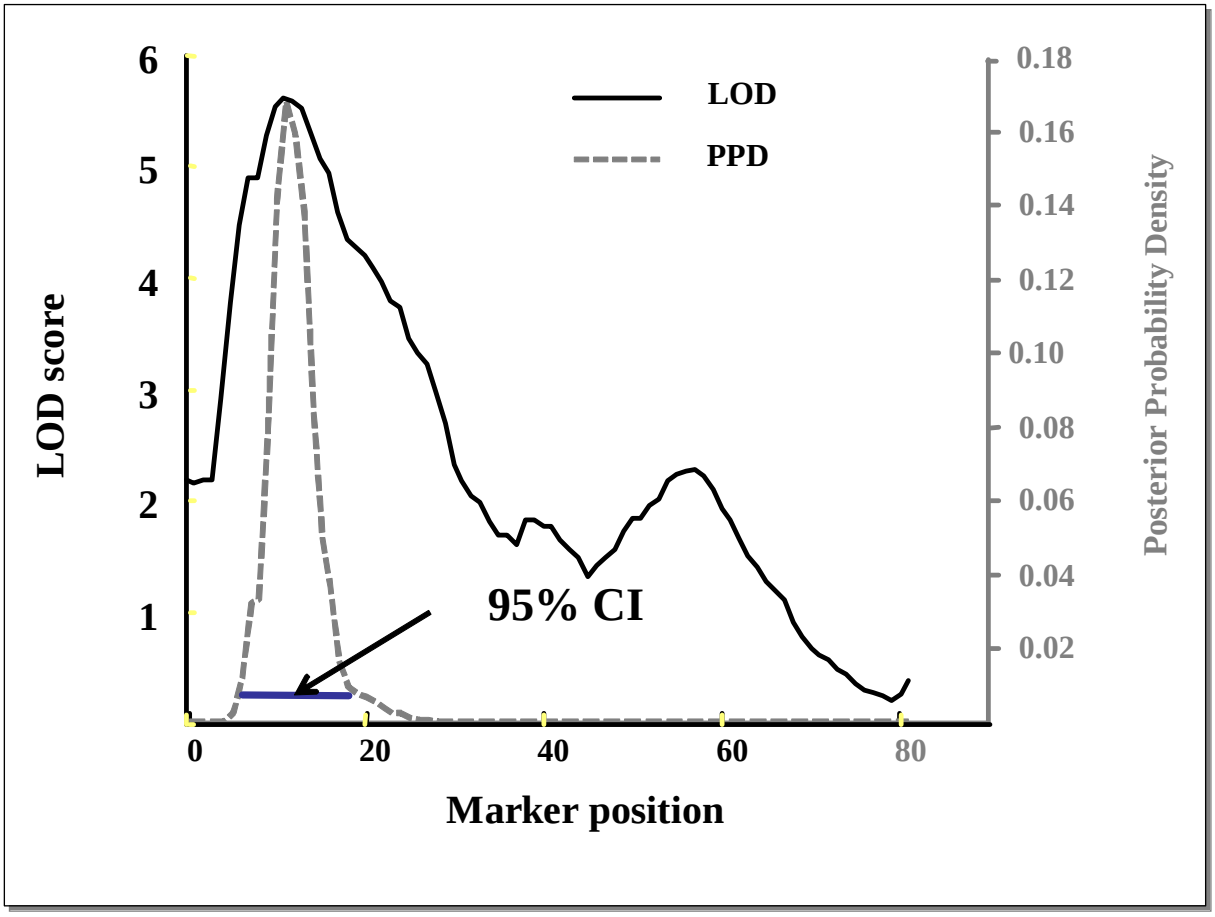

Figure – 42. LOD score and posterior probability density plot (calculated by Pseudomarker) for a major quantitative trait locus (QTL) influencing bone size for the mutant line 917 (the data used for generating this plot was reported in previous reporting period). Posterior probability density is a likelihood statistic that gives rise to the 95% confidence intervals and it is shown as thick black horizontal bar. The 95% confidence interval of 917 mutant locus indicated a large region encompassing 4-18 cM. In the current reporting period we added additional markers in this region and re-genotyped the DNA from 917 F2 mice (n=69). The posterior probability density plot for analysis is shown in next figure.

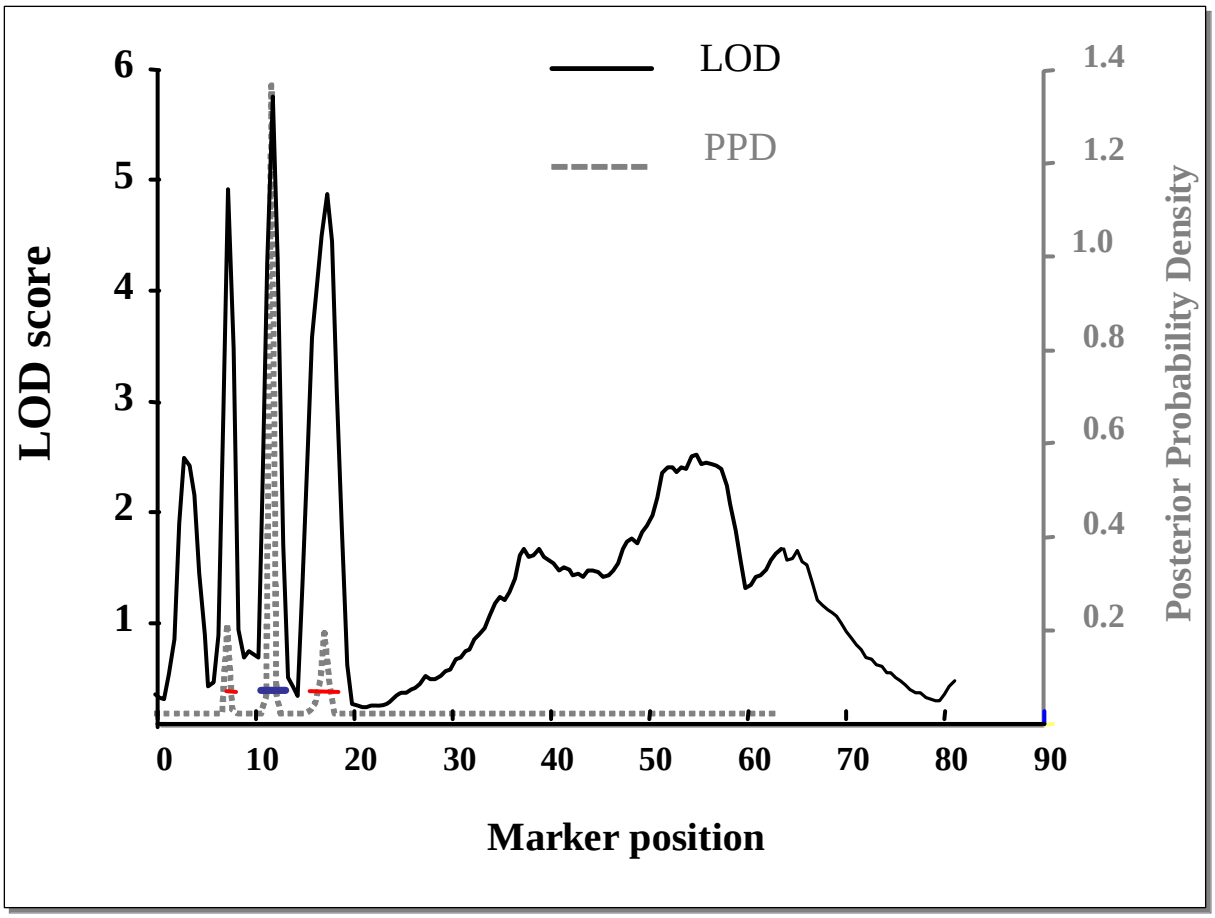

Figure – 43. The posterior probability density plot for a fine mapped region of 917 locus using additional marker. LOD score and posterior probability density plot for a major quantitative trait locus (QTL) influencing bone size for the mutant line 917. Posterior probability density is a likelihood statistic that gives rise to the 95% confidence intervals indicated by black horizontal bar. In the current reporting period we added additional markers described in the **Table-18** in this region and re-genotyped the DNA from 917 F2 mice (n=69). The figure shows that when additional markers were added the proximal peak was resolved into three major peaks, each showing significant LOD scores ($p<0.05$). However, the posterior probability density plot shows that probability of middle peak, located at 10-12 cM, harboring the mutant gene is higher.

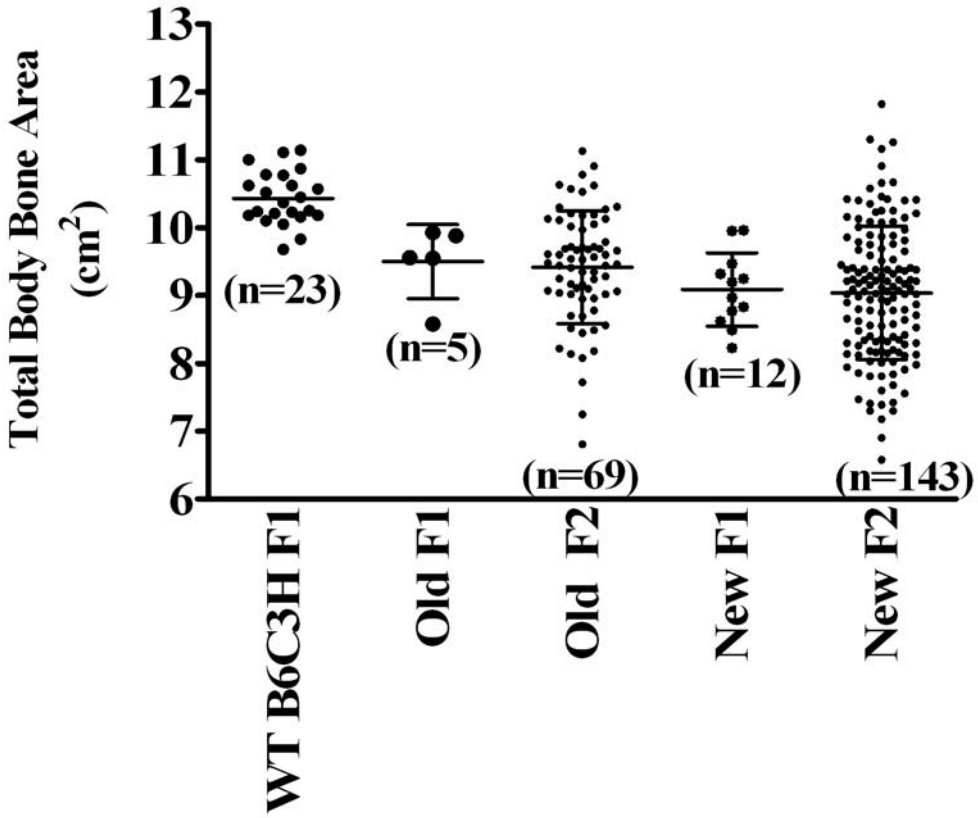

Figure – 44. Generation of F1 & F2 progeny for fine mapping of low bone size mutant mice (Line 917). In the current reporting period, we generated several new F1 & F2 mice. This figure shows that the total body bone size phenotype was comparable to those produced previous reporting periods. The bone area data also shows that bone size is robustly expressed in the F1 mice generated from breeding of mutant 917 (B6) with C3H/HeJ mice.

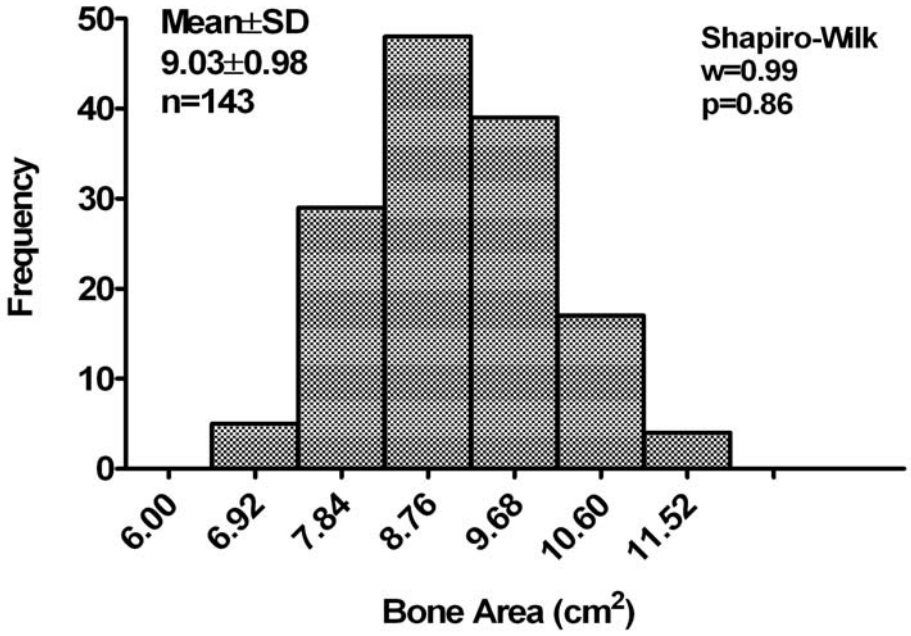

Figure – 45. **Frequency distribution of F2 mice generated for fine mapping of chromosome 4 locus affecting bone size in 917 mutant mice**. The total body bone area data (measured by DEXA) appears to be normally distributed; therefore, interval mapping could be used to identify QTLs affecting bone size.

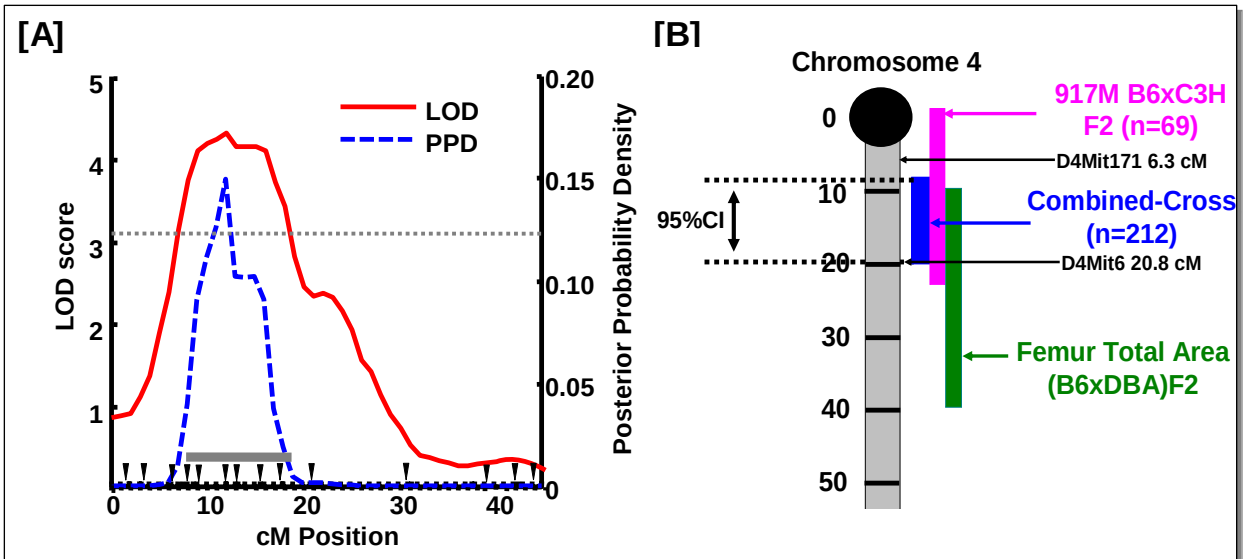

Figure – 46. [A] Fine mapping of 917M locus using 212 F2 males and approximately 14 markers covering the chromosome 4 proximal region. Approximate locations of the markers are shown as bars on x-axis. Posterior probability density is a likelihood statistic that gives rise to the 95% confidence intervals indicated by thick horizontal bar. [B] Diagrammatic illustration of the confidence interval of the 917M locus based on our fine mapping data. Also shown is confidence interval of overlapping locus involved in regulation of bone size.

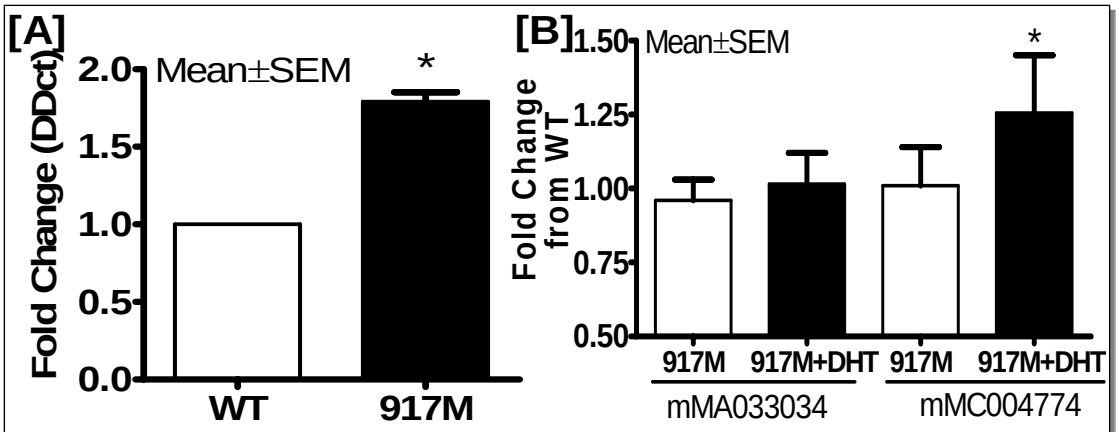

Figure – 47. Validation of microarray data by quantitative RT-PCR using RNA from same samples used for genome-wide microarray screen. [A] The increased expression of Cbfa2t1h gene was confirmed in skeletal tissues from 917M mice as compared to WT control. [B] Figure shows expression of two clones represented in genome-wide microarray analysis of RNA extracted from osteoblasts. A clone representing exon 11 showed increased expression in osteoblasts when treated with 5∝-DHT. The non-normalized data is expressed as fold change over WT osteoblasts. *p<0.05 vs WT.

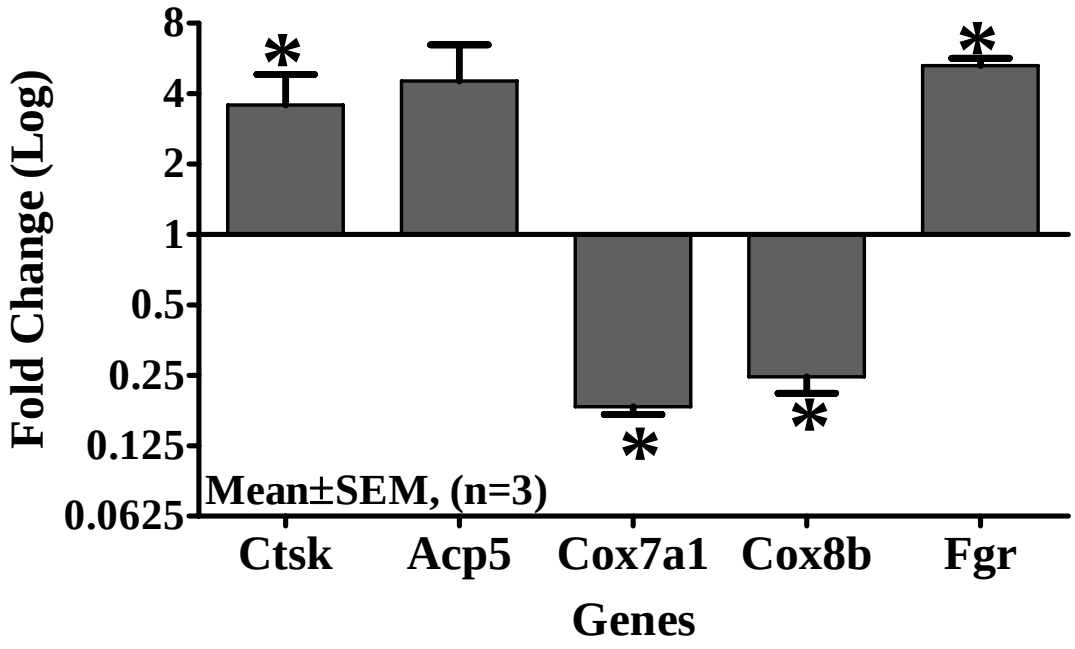

Figure – 48. Fold changes in mRNA levels of selected genes in skeletal tissues of 12137 mutant mice (n=3) as compared to those from WT control (n=3) as assessed by real-time RT-PCR. The mRNA level of each gene was normalized to an expression of a house keeping gene, *Ppia*, and fold change vs WT mice determined by delta delta CT method. *p<0.05 vs WT (p-value for Acp5 was 0.097).

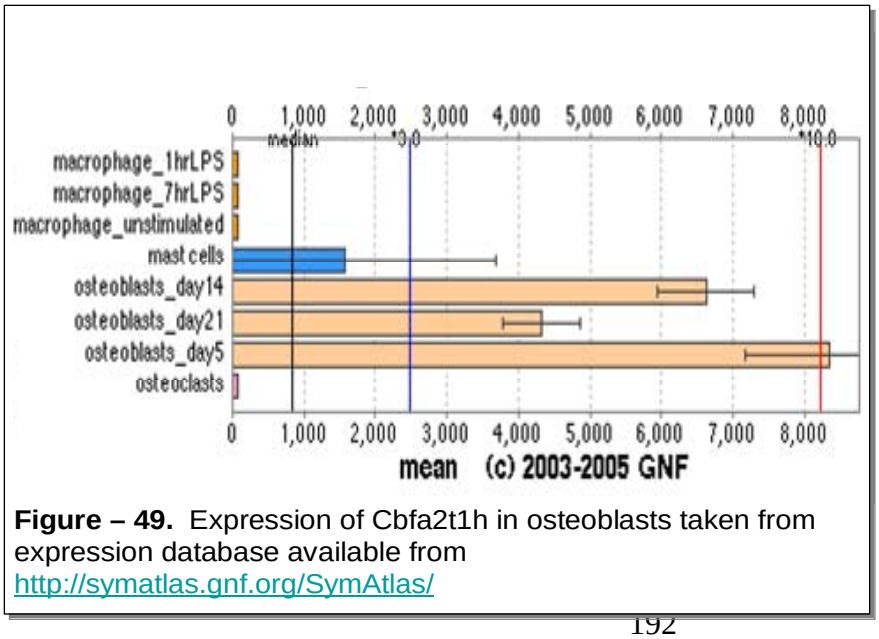

Figure – 49. Expression of Cbfa2t1h in osteoblasts taken from expression database available from http://symatlas.gnf.org/SymAtlas/

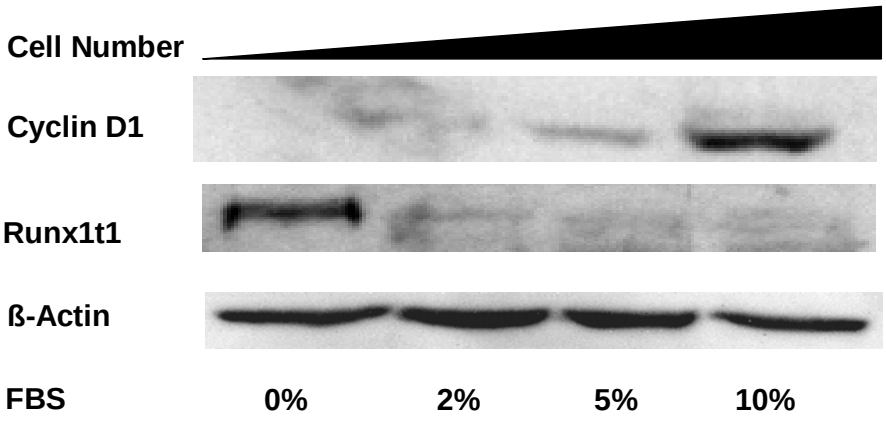

Figure – 50. The expression of *Cbfa2t1h* in MC3T3-E1 cells is inhibited during proliferation. Proliferation in growth arrested MC3T3 cells were initiated by adding varying amounts of fetal bovine serum (FBS). Nuclear extracts from MC3T3 cells incubated with different concentrations of FBS were Western blotted with an anti-Cbfa2t1h polyclonal antibody. The western blot analysis indicates dose dependent decrease in Cbfa2t1h expression while expression of proliferation marker cyclin D1 was increased with increasing FBS concentration in cultures.

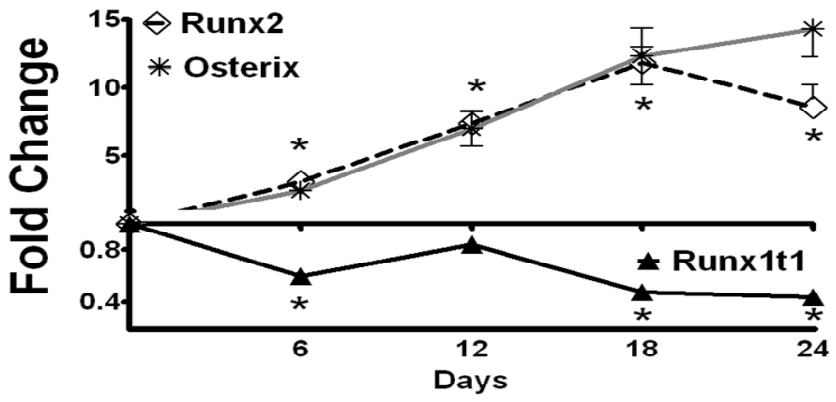

Figure – 51. Expression of *Runx1t1* is decreased during osteoblast differentiation. Bone marrow stromal cells were induced to differentiate from 0 to 24 days as indicated. Total mRNA was extracted and expression levels of *Runx2*, osterix, and *Runx1t1* were measured by qRT-PCR (each bar represents n=6 samples). The mRNA data were calculated as fold changes vs expression at day-0. Error bars: Mean±SD. Expression of Ppia was used to normalize the expression of various genes. (*p<0.05 vs day-0 by ANOVA)

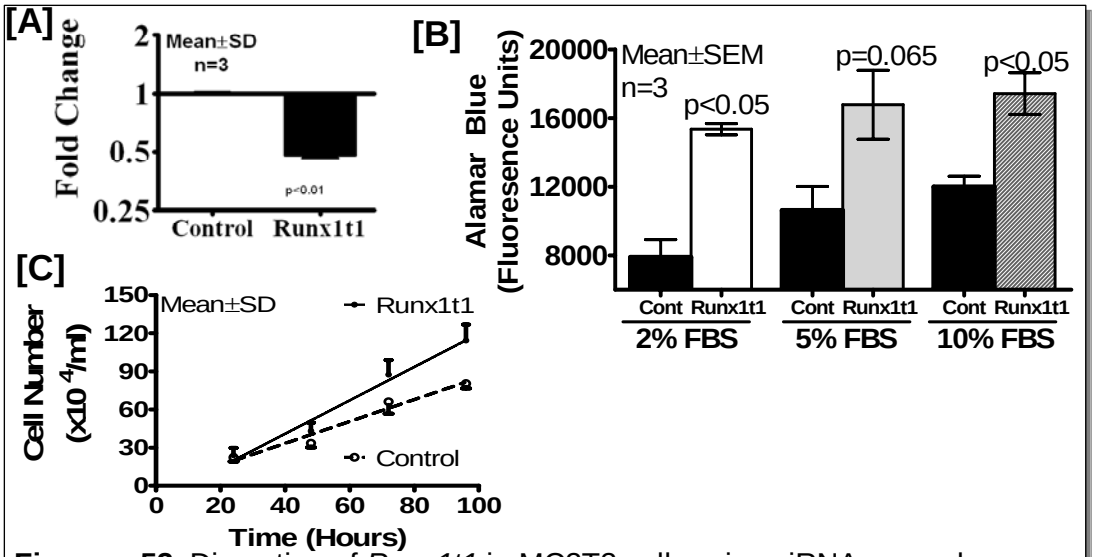

Figure – 52. Disruption of *Runx1t1* in MC3T3 cells using siRNA caused increased proliferation. MC3T3 cells were chemically transfected with *Runx1t1* siRNA. A non-targeting siRNA sequence was used as control. **(A)** The transcript levels of Runx1t1 in MC3T3 cells transfected with control or Runx1t1 siRNA determined by qRT-PCR. **(B)** The rate of proliferation measured by AlmarBlue dye uptake was increased. **(C)** Cell doubling time was decreased in *Runx1t1* disrupted cells as compared to non-targeting siRNA control.

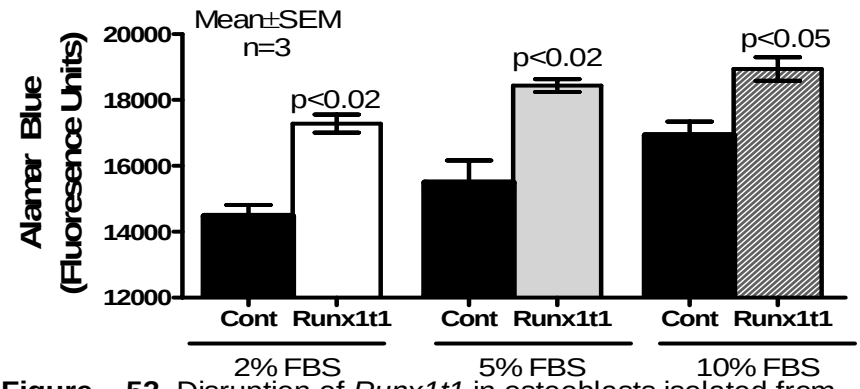

Figure – 53. Disruption of *Runx1t1* in osteoblasts isolated from C57BL/6J (B6) mice using siRNA caused increased proliferation. Periosteal osteoblasts isolated from long bones of B6 mice were grown in cultures and chemically transfected with *Runx1t1* siRNA. Proliferation was initiated 24-36-hours after the transfection in growth arrested cells by adding varying amounts of fetal bovine serum (FBS). A non-targeting siRNA sequence was used as control. These data suggest that disruption of *Runx1t1* in non-transformed wild type cells induces similar phenotype as that observed in MC3T3 cells.

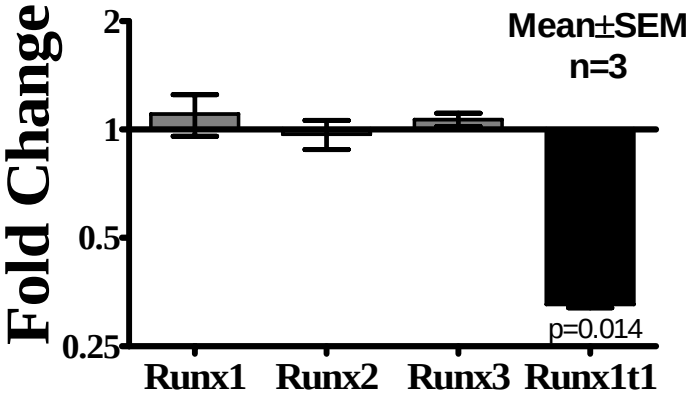

Figure – 54. The expression of Runx1, Runx2, and Runx3 in MC3T3 cells is not significantly altered 12-hours after siRNA induced suppression of *Runx1t1*. Total RNA was isolated from MC3T3 cells 12-hours after transfection. Expression of Runx were determined using qRT-PCR and normalized to expression of *Ppia* mRNA (n=2-3). Suppression of *Runx1t1* was 70%.

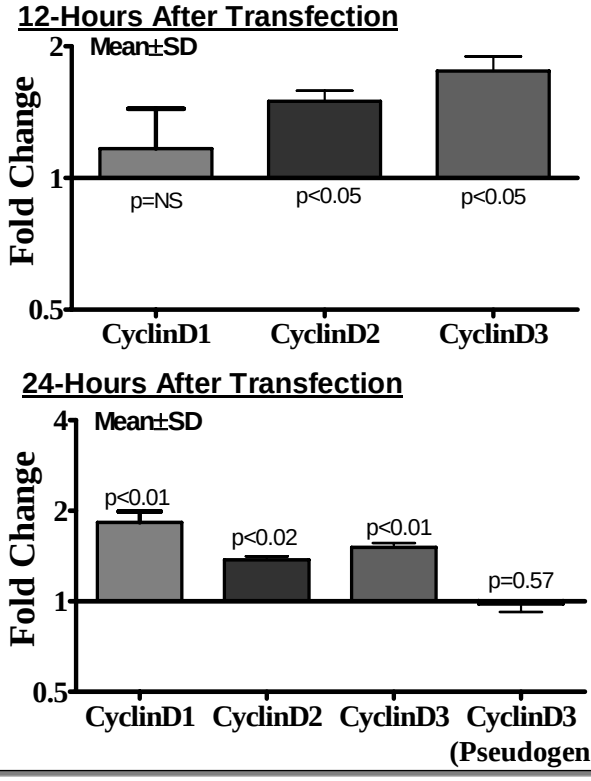

Figure – 55. The expression levels of cyclins D1, D2, and D3 in MC3T3 cells were increased after siRNA induced suppression of *Runx1t1*. Total RNA was isolated from MC3T3 cells 12- and 24-hours after transfection. Expression of three cyclin transcripts were determined using qRT-PCR and normalized to expression of *Ppia* mRNA. After 12-hour cyclins D2 and D3 were significantly increased. Whereas, 24-hours after disruption of *Runx1t1*, cyclin D1 was also significantly elevated. Expression of cyclin D3 pseudogene, where Runx1t1 is translocated in mouse chromosome 4, was not affected. Suppression of Runx1t1 was 50%-70%.

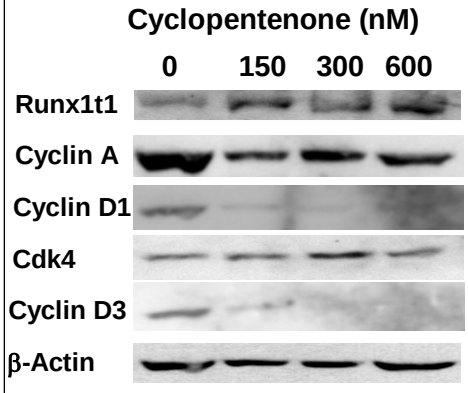

Figure – 56. Effect of inhibition of cell cycle regulatory protein cyclin D1 on expression of *Runx1t1*. Cyclopentenone regulates transit through G1 and S phase of cell cycle by repressing cyclin D1 and A protein levels. MC3T3 cells were treated with 600 μM of 2-cylopentenone and cell extracts were obtained 24-hours after treatment. Cyclin D1 and *Runx1t1* were probed with specific antibodies (Santa Cruz). The Western blot analysis showed that cyclin D1 was undetectable in MC3T3 cells 24-hours after 2-cyclopentenone treatment. Whereas, expression of Runx1t1 was increased, which may be due to loss of feed back regulation of cyclin D1 on *Runx1t1*. These data support our hypothesis that *Runx1t1* directly regulates Cyclins in osteoblasts.

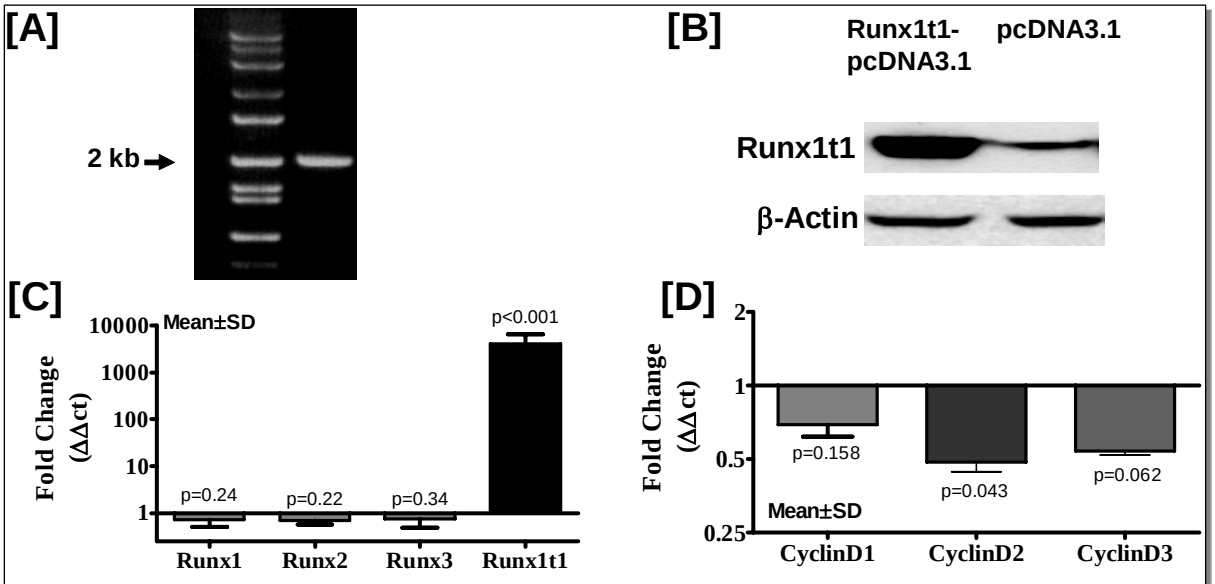

Figure – 57. A. The *Runx1t1* was amplified from mouse bone cDNA. Approximate 2 kb product was purified and cloned in pcDNA3.1 vector. **B.** Transient transfection of mouse MC3T3 cells with *Runx1t1*-pcDNA3.1 vector resulted in several fold higher expression of *Runx1t1* protein (after 48 hours) as determined by western blot analysis compared to control pcDNA3.1 vector. **C & D.** 12 Hours after transient transfection of mouse MC3T3 cells with *Runx1t1*-pcDNA3.1, there was >1000 fold increase in mRNA levels of Runx1t1 and significant decrease mRNA levels of in D-type cyclins.